

# **Processes controlling the evolution of deep moist convection in the summertime West African Sahel**

Miroslav Provd

University of Leeds

School of Earth and Environment

Submitted in accordance with the requirements for the degree of  
*Doctor of Philosophy*

March 2016

The University of Leeds

## Declaration of Authorship

The candidate confirms that the work submitted is his/her own, except where work which has formed part of jointly-authored publications has been included. The contribution of the candidate and the other authors to this work has been explicitly indicated below. The candidate confirms that appropriate credit has been given within the thesis where reference has been made to the work of others.

Chapter 3 includes characterization of cold pools which has been published, with co-authors, in Monthly Weather Review. The reference is **Provod, M., J.H. Marsham, D.J. Parker, C.E. Birch, A Characterization of Cold Pools in the West African Sahel**, MWR, 2016. J. H. Marsham and D.J. Parker supervised the student. C.E. Birch gave advice on methods and ran model simulations (these not used in the publication, but are used throughout the thesis).

This copy has been supplied on the understanding that it is copyright material and that no quotation from the thesis may be published without proper acknowledgement.

The right of Miroslav Provod to be identified as Author of this work has been asserted by him in accordance with the Copyright, Designs and Patents Act 1988.

© 2016 The University of Leeds and Miroslav Provod

## Acknowledgements

Firstly, I would like to express my thanks to my academic supervisors John Marsham and Doug Parker. Their advice, patience and help have been invaluable during the completion of this thesis. John has always been there to answer my questions, give advice and provide prompt feedback on results and gave invaluable guidance during the completion of this thesis. Both John and Doug have provided some great ideas that led to results in this thesis. I would also like to thank Cathryn Birch who ran some of the *Cascade* simulations, the output of which has been used throughout the thesis. Cathryn also promptly and fully answered all the questions I had regarding model output.

Several other members of the School of Earth and Environment provided a great help throughout the PhD. A special thanks goes to Richard Pope, who gave a great help during struggles with code and provided hours of his time to explain and teach me some complex IDL coding. Richard Rigby, in IT support, has always provided great and very prompt help during IT issues. A great thanks also goes to all the current and past people in the office, both for help when it was needed as well as for the great office environment, including: Richard Pope, Becky Jansen, Nsikanabasi Silas Umo, Sarah Dennis, Hannah Walker, Seshagirao Kolusu, Lindsay Lee, John Prytherch, Peggy Achtert, Mark Holden, Kirsty Pringle and Tamsin Farmer. Apologies if I missed out someone. We are a team and I will really miss you!

My family also deserves to be mentioned. My wife, Lucie Provodova, my daughter, Sofia Provodova, my parents, Miroslav Provod and Dana Provodova, and sister, Marketa Provodova, have been all vital to me, not only during this PhD, but throughout my life, providing support of every form. Without your help, this thesis would not be here. Thank you all!!!

## **Abstract**

Deep moist convection and mesoscale convective systems (MCSs) are integral to the West African monsoon and, as the main rain-producing mechanism in the Sahel, are essential to the livelihoods of millions. Current operational forecasting models struggle to predict rainfall with a good precision. It is therefore necessary to study the processes controlling deep moist convection in detail, in order to understand them better and to be able to evaluate simulations to identify errors for future model development. In this thesis properties of cold pools from Sahelian MCSs were characterised from surface observations. It was observed that early season cold pools were stronger and drier, likely due to drier mid-levels before the monsoon onset. The properties of observed cold pools were used to evaluate a Unified Model (UM) convection-permitting simulation. The comparison showed that simulated cold pools are generally weaker than observed. Cold pools and MCS structure were further investigated in two case studies. This enabled an analysis of MCS vertical structure. Processes controlling the diurnal cycle of convection were analysed using observations and UM simulations. This showed that while surface CAPE follows a diurnal cycle with a maximum in the afternoon and minimum in the early morning, elevated CAPE was found to have a nearly opposite cycle, due to advection of high equivalent potential temperature air overnight by the nocturnal low-level jet. In addition, the low-level jet provides low-level wind shear which balances the cold-pool related vorticity and helps to maintain the MCS until morning, when the jet decays and MCSs tend to dissipate. The jet also creates moisture flux convergence overnight, supporting MCSs. Finally, mechanisms underlying storm initiation and regeneration were analysed in UM simulations, showing the roles of soil moisture boundaries, pre-existing cold pools and bookend vortices.

## Table of Contents

<b>Declaration of Authorship .....</b>	<b>ii</b>
<b>Acknowledgements .....</b>	<b>iii</b>
<b>Abstract .....</b>	<b>iv</b>
<b>Table of Contents.....</b>	<b>v</b>
<b>List of Tables.....</b>	<b>viii</b>
<b>List of Figures .....</b>	<b>ix</b>
<b>Abbreviations .....</b>	<b>xix</b>
<b>1. Introduction .....</b>	<b>1</b>
1.1 Motivations and aims.....	1
1.1.1 Thesis structure.....	4
1.2 Literature review.....	5
1.2.1. The West African Monsoon .....	8
1.2.2. Mesoscale convective systems (MCSs) in the West African Monsoon .....	12
1.2.3. Simulations of MCSs in the West African Monsoon .....	30
<b>2. Methods .....</b>	<b>33</b>
2.1 Observational datasets.....	27
2.2 Met-Office Unified Model convection-permitting simulations from the <i>Cascade</i> project .....	30
<b>3. A Characterization of cold pools in the West African Sahel     compared with a convection-permitting model .....</b>	<b>33</b>
3.1 Introduction .....	33
3.2 Methods .....	33
3.2.1 Cold pool detection in observed surface time-series and verification using remote-sensing data .....	33
3.2.2 Selection of monsoon season sub-periods .....	35
3.2.3 Atmospheric tide and diurnal pressure variation .....	36
3.2.4 Statistical evaluation of observed cold-pool properties .....	38
3.2.5 Evaluating cold pools in the 4 km convection-permitting <i>Cascade</i> simulations .....	39
3.3 Characterization of observed and simulated cold pools .....	40
3.3.1 Composite cold pools .....	39
3.3.2 Thermodynamic properties of cold pools .....	41
3.3.3 Role of mid-level dryness .....	57
3.3.4 Cold-pool winds .....	61

3.4 Conclusions .....	69
<b>4. Case studies of two squall-line mesoscale convective systems.....</b>	<b>73</b>
4.1 Introduction .....	73
4.2 Methods .....	78
4.2.1 Data .....	78
4.2.2 Time-to-space conversion .....	79
4.2.3 Vertical profiles .....	81
4.3 Results .....	83
4.3.1 Case study of 22 <sup>nd</sup> July 2006 squall-line MCS .....	83
4.3.2 Case study of 31 <sup>st</sup> July 2006 squall-line MCS .....	95
4.3.3 Preliminary analysis of UM simulation of the 31 <sup>st</sup> July 2006 squall-line MCS .....	106
4.4 Discussion & Conclusions .....	109
4.4.1 Future work .....	111
<b>5. Diurnal cycle of convective storms and their initiation in the Sahel .....</b>	<b>113</b>
5.1 Introduction .....	113
5.2 Methods .....	119
5.2.1 Observational data .....	119
5.2.2 Initiations in <i>Cascade</i> .....	122
5.2.3 Identifications of <i>Cascade</i> cold pools.....	123
5.2.4 Identifications PV anomalies leading to new initiations in <i>Cascade</i> .....	125
5.2.5 2D composites of environmental variables around locations of initiations and rainfall .....	127
5.2.6 Calculating moisture budget around rainfall.....	129
5.3 Results .....	131
5.3.1 Diurnal cycle of deep moist convection.....	131
5.3.2 Diurnal cycle of convective initiations.....	150
5.4 Conclusions .....	167
<b>6. Conclusions .....</b>	<b>171</b>
6.1 Future work .....	176
<b>List of References .....</b>	<b>179</b>

## List of Tables

<b>Table 3.1 The number of cold pools in each sub-period for observations and Cascade.....</b>	<b>Chyba! Záložka není definována. 42</b>
--	---

## List of Figures

<b>Figure 1.1</b> Map of West Africa showing the location of the Sahel (brown). Red dot represent the location of Niamey, Niger. ....	<b>5</b>
<b>Figure 1.2</b> Schematic of the summer monsoon circulation in West Africa. ITD is the location of the Inter-Tropical Discontinuity, AEJ is the African Easterly Jet and the TEJ is the Tropical Easterly Jet (from Lafore, et al., 2011).....	<b>6</b>
<b>Figure 1.3</b> Conceptual model of the kinematic and radar echo structure of a squall-line viewed in a vertical cross section oriented perpendicular to the squall-line (and generally parallel to its motion). Intermediate and strong radar reflectivity is indicated by medium and dark shading, respectively. H and L indicate centres of positive and negative pressure perturbations, respectively. Dashed-line arrows indicate fallout trajectories of ice particles passing through the melting layer (from Houze et al., 1989).	
<b>Figure 1.4</b> Map of West Africa showing the location of the Sahel (brown). Red dot represent the location of Niamey, Niger. ....	<b>14</b>
<b>Figure 1.4</b> An illustration of balances of the positive and negative vorticity produced by the ambient shear and the cold pool, respectively. a) A buoyant parcel with no shear or cold pool creates equal magnitudes of positive and negative vorticity. b) If the negative vorticity produced by the cold pool is greater than the shear produced positive one, the updraft leans backwards. c) If the positive vorticity produced by ambient shear is stronger, the updraft leans forwards. d) If both the negative and positive vorticity are in balance, the updraft is up-right and the MCS is sustained. (Figure from Rotunno et al., 1988) .....	<b>19</b>
<b>Figure 1.5</b> Schematic depicting how a typical vortex tube (horizontal vorticity) contained within (westerly) environmental shear is deformed as it interacts with a convective cell (viewed from the southeast). Cylindrical arrows show the direction of cloud-relative airflow, and heavy solid lines represent vortex lines with the sense of rotation indicated by circular arrows. Shaded arrows represent the forcing influences that promote new updraft and downdraft growth. Vertical dashed lines denote regions of precipitation. (a) Initial stage: vortex tube loops in the vertical as it is swept into the updraft. (b) Splitting stage: downdraft forming between the splitting updraft cells tilts vortex tubes downward, producing two vortex pairs. The barbed line at the surface marks the boundary of the cold air spreading out beneath the storm (from Klemp, 1987).....	<b>21</b>
<b>Figure 2.1</b> Map of West Africa showing the location of AMMA Niamey supersite, located at Niamey International Airport, Niamey, Niger, where all observational data used in this thesis were recorded. (© Google maps).....	<b>29</b>

<b>Figure 2.2</b> An example of an MIT radar long range survey reflectivity at 02:10:08Z on 11 <sup>th</sup> August 2006. This is a single elevation scan performed at an elevation of 0.7°. An approaching squall-line can be seen east of the radar. The echo to the southwest of the radar site is a phantom line created by reflection from a large aircraft hangar.....	<b>30</b>
<b>Figure 2.3</b> Map of the domain for the 4 km convection-permitting UM model run (rectangle). Red dot represents the location of Niamey with the red circle representing the maximum (250 km) range of the MIT radar.....	<b>33</b>
<b>Figure 3.1</b> An example of an observed daily time series as obtained by the surface station at Niamey airport. This time series is for 11 <sup>th</sup> August 2006, when a cold pool crossing was identified at 03:15 Local Time (denoted by vertical red line), which is 02:15 UTC. Black lines denote the borders of the time-window used for the analysis. Solid lines correspond to left-hand axis and dashed lines to right-hand axes. Data recorded every second and averaged at minute intervals.....	<b>37</b>
<b>Figure 3.2</b> Total accumulated rainfall from Niamey ARM surface station data. Red lines separate three sub-seasonal periods used in this study: “Pre-monsoon” (1 <sup>st</sup> June 2006 – 12 <sup>th</sup> July 2006);”Monsoon” (13 <sup>th</sup> July 2006 – 27 <sup>th</sup> August 2006);”Retreat” (28 <sup>th</sup> August 2006 – 30 <sup>st</sup> September 2006).....	<b>39</b>
<b>Figure 3.3</b> Average diurnal pressure variations by month. Solid=June, dotted=July, dashed=August, dash-dot=September).....	<b>40</b>
<b>Figure 3.4</b> An example of an east-west cross-section through surface data at a time output closest to a cold pool passage in the 4-km Unified Model convection-permitting simulation (Cascade). Using a 9.4 m s <sup>-1</sup> velocity, the cross-section is equivalent to a region of time starting at 1 hour before and ending 2 hours after the cold-pool passage. The identified gust front is denoted by vertical pink line. Solid lines correspond to left-hand axis and dashed lines to right-hand axes. 0km location corresponds to the grid-point located at the co-ordinates of Niamey..	<b>43</b>
<b>Figure 3.5</b> An example showing Cascade simulated 1.5m temperature (°C) (shaded) and surface precipitation rate (contour at 2 mm h <sup>-1</sup> ).....	<b>44</b>

<b>Figure 3.6 Composite cold pool obtained from averaging variables of all observed cold pools around the crossing time. Black line is for the whole period, red for the Pre-Monsoon period, blue for the Monsoon and green for Retreat. The vertical pink line shows the cold pool crossing time.....</b>	<b>46</b>
<b>Figure 3.7 As Figure 3.6, but for Cascade. Unlike Figure 3.6, horizontal axis does not represent time, but a spatial west-east cross-section through surface data across the cold pool .....</b>	<b>48</b>
<b>Figure 3.8 Changes in specified thermodynamic variables from observed cold pools: a) Decrease in temperature; b) Increase in pressure; c) Increase in WVMR; d) Increase in mean <math>\Theta_e</math>. Colouring represents the sub-periods (red: Pre-monsoon, blue: Monsoon, green: Retreat). Number of events in each season is normalised to allow a comparison between seasons (see text) with the black line showing total (unnormalised) distributions.....</b>	<b>50</b>
<b>Figure 3.9 As Figure 3.8, but for Cascade .....</b>	<b>53</b>
<b>Figure 3.10 Pressure increases and temperature decreases from the observed cold pools. As Figure 3.9, colours in a) represent the whole period and individual sub-periods. Colouring in (b) represents the time of day (red: 8 – 16 UTC, blue: 18 – 6 UTC, green: 6-8 UTC, there were no events between 16 and 18 UTC). Coloured lines denote best-fit from a least squares method.....</b>	<b>55</b>
<b>Figure 3.11 A Figure 3.10, but for Cascade .....</b>	<b>57</b>
<b>Figure 3.12 As Figure 3.11, but for mixing ratio for a) observations and b) Cascade .....</b>	<b>59</b>
<b>Figure 3.13 As Figure 3.12, but for average mid-level (550-750hPa) <math>\Theta_w</math> depression ((saturated <math>\Theta_w</math>) - <math>\Theta_w</math>) against temperature decrease across leading edge of cold pool.....</b>	<b>59</b>
<b>Figure 3.14 As Figure 3.13, but for Departure from Moist Adiabats (DMA = <math>\Theta_{\text{cold pool}} - \text{mean}(\Theta_w(550 \text{ to } 750 \text{ hPa}))</math>) versus mid-level dryness defined using the difference between mean (<math>\Theta(550 \text{ to } 750 \text{ hPa})</math>) and mean (<math>\Theta_w(550 \text{ to } 750 \text{ hPa})</math>). Diagonal lines represent constant Fractional Evaporational Energy Deficit (FEED) of 100% (black), 67% (blue) and 33% (red).....</b>	<b>59</b>

Figure 3.15 A section of a tephigram showing an example of a graphical representation of mean mid-level (550 – 750 hPa averaged) temperature (T) and dew-point temperature (Td) and associated mean wet-bulb potential temperature ( $\Theta_w$ ) and dry-bulb potential temperature ( $\Theta$ ).  $\Theta_{\text{cold pool}}$  represents an example potential temperature of a cold pool as measured at the surface. Red line represents dry adiabatic descent, blue line represents moist adiabatic descent and the black line is an example possible descent of a cold pool. Departure from Moist Adabat (DMA) is the difference between  $\Theta_{\text{cold pool}}$  and mean mid-level  $\Theta_w$  ..... 61

Figure 3.16 As Figure 3.9, but for observed 3 m (a) wind gusts and (b) mean wind increases ..... 62

Figure 3.17 As Figure 3.15, but for Cascade winds at 4 m ..... 66

Figure 3.18 As Figure 3.16, but for maximum wind at 950 hPa. a) Observed; b) Cascade. The observed values in a) were interpolated from values of two closest levels as provided by the Radar Wind Profiler (with heights of the 950 hPa level obtained from radiosondes and ranging from 310 to 370 metres above ground). ..... 67

Figure 3.19 Relationship between 950 hPa level and 3 m winds for all available values (not only cold pools). a) – d) is for observations, e) – h) is for Cascade. Blue lines are lines of best fit. The times in UTC are: a) 00-06, b) 06-12, c) 12-18, d) 18-24, e) 00-06, f) 06-12, g) 12-18, h) 18-24..... 68

Figure 3.20 As Figure 3.18, but for a) observed and b) Cascade mean wind increase at 950 hPa. Observed winds obtained from wind-profiler data..... 70

Figure 3.21 Observed cold-pool related maximum wind gusts at 3 m against pressure increases at 1.5 m a) and mean wind increases b). Colours represent different times of day (red: 8-17 UTC, blue: 19-6 UTC, green: 6-8 UTC and 17-19 UTC)..... 71

Figure 3.22 As Figure 3.21, but for Cascade. Black lines are best-fit lines for the corresponding observational relationships from Figure 3.21 ..... 72

Figure 4.1 Vertical profiles of the magnitude of wind speed from radiosonde ascents (black) and RWP (red). Radiosondes were released at 05:38 UTC (top), 11:34 UTC (middle) and 17:32 UTC (bottom) with the RWP data being averaged for 05:30 – 06:30 UTC (top), 11:30 – 12:00 UTC (middle) and 17:30 – 18:30 UTC (bottom), all on 31. July 2006..... 85

Figure 4.2 Single elevation (0.7°) MIT radar reflectivity images at: a) 08:30:18 UTC, b) 09:00:10 UTC, c) 10:00:11 UTC and d) 11:00:12 UTC on 22<sup>nd</sup> July 2006. .... 87

**Figure 4.3 Observed surface time series of specified variables time-to-space converted into cross-section based on the east-west propagation of the squall-line on 22<sup>nd</sup> July 2006. Solid lines correspond to the left y-axis, dotted lines to the right y-axis. The cross section is centred at the cold pool edge and corresponds to approximately 5 minutes after the time of the 09:00 UTC radar scan in Figure 4.2. b). Top x-axis is time axis, bottom x-axis shows distance based on conversion..... 88**

**Figure 4.4: Comparison of morning (06:00 UTC, black line) and noon (12:00 UTC, red line) soundings on 22. July 2006 for a) T and Td tephigram, b)  $\theta_e$ .....91**

**Figure 4.5 Differences in a) zonal wind-speed and b) wind direction soundings between the morning (06:00 UTC, black line) and noon (12:00 UTC, red line) radiosonde releases on 22. July 2006..... 93**

**Figure 4.6 Vertical west-east cross-sections through volumetric radar reflectivity at 09:31 UTC on 22<sup>nd</sup> July 2006, centered on Niamey. Overplotted are radiosonde ascents released from Niamey, their locations are specified by the vertical y-axes, where numbers represent height above ground level (km). The position of the ascents is time-to-space converted based on the mean east-west propagation of the squall-line, as discussed in the main text. The radiosonde variables are: Red=temperature ( $^{\circ}\text{C}$ ), Blue=dew-point ( $^{\circ}\text{C}$ ), Green=RH (%), Black=ground-relative zonal wind speed ( $\text{m s}^{-1}$ ). Values to the right of the y-axis are positive and to the left negative (for actual values see previous plots). Horizontal arrows represent the magnitude and direction of the zonal component of ground-relative wind as obtained from the Radar Wind Profiler (RWP). Note the V-shaped white area above 0km is a result of the radar scanning strategy missing the space directly above the radar. 0 km is centered approximately at the gust front crossing. Radiosonde at -150 km has been released at 05:36, radiosonde at +140 km at 12:17 UTC. .... 96**

**Figure 4.7 Same as Figure 4.7., but for storm-relative winds. Times of radar cross-sections are: a) 09:31 UTC, b) 10:31 UTC and c) 11:31 UTC on 22<sup>nd</sup> July 2006. Radiosonde at -150 km in a) released at 05:36 UTC, all other sounding are from radiosonde released at 12:17 UTC..... 98**

**Figure 4.8 Single elevation ( $0.7^{\circ}$ ) MIT radar reflectivity images at: a) 08:00:08 UTC, b) 09:00:03 UTC, c) 12:10:05 UTC and d) 18:20:08Z on 31<sup>st</sup> July 2006. ....101**

<b>Figure 4.9 Observed surface time series of specified variables time-to-space converted based on the east-west propagation of each squall-line. Solid lines correspond to the left y-axis, dotted lines to the right y-axis. a) is centred at the primary cold pool and approximately corresponds to radar in Figure 4.1. b). b) is centred at the secondary cold pool and approximately corresponds to radar in Figure 4.9. c). Top x-axis is time axis, bottom x-axis shows distance based on conversion.....</b>	<b>103</b>
<b>Figure 4.10 Comparison of soundings at a) 06:00 UTC and 12:00 UTC, b) 12:00 UTC and 18:00 UTC, c) 06:00 UTC and 18:00 UTC on 31. July 2006. Comparison of equivalent potential temperature profiles d), zonal wind speed profiles e), and wind-direction profiles f). In a), b) and c), the former time is black and the latter red. In d), e) and f), black is 06:00 UTC, red is 12:00 UTC and green is the 18:00 UTC profile. ....</b>	<b>107</b>
<b>Figure 4.11 As Figure 4.8, but for 08:30:08Z on 31<sup>st</sup> July 2006 for. a) are ground-relative winds, b) are storm-relative winds. Radiosonde has been released at 05:38 UTC. ....</b>	<b>111</b>
<b>Figure 4.12 As Figure 4.13., but for 12:10:08Z on 31<sup>st</sup> July 2006. Winds in a) are ground-relative, in b) storm-relative. Radiosonde has been released at 11:54 UTC.....</b>	<b>113</b>
<b>Figure 4.13 UM model simulation for 11:00 UTC on 31<sup>st</sup> July 2006 showing a) 1.5 m temperature, b) 4 m specific humidity c) zonal vertical cross-sections through the simulated squall-line at 12.8 ° N (as denoted by thick black line in a) and b)) showing temperature and d) specific humidity. In a) and b) contours represent precipitation greater than 2 mm. Arrows in b) represent 4 m windspeed and wind direction. Arrows in c) indicate ground-relative zonal windspeed and direction. Arrows in d) indicate vertical windspeed and direction. Contours in c) enclose regions where the sum of cloud water and/or cloud ice densities is greater than 0.01 kg m<sup>-3</sup>.....</b>	<b>116</b>
<b>Figure 5.1 Mean observed and simulated diurnal cycle of rainfall. Output of various runs from Cascade is shown as specified. The grey area represents the range (minimum and maximum) of rainfall retrieved from satellite products. Figure obtained from Birch et al. (2014) – Figure 3.....</b>	<b>123</b>
<b>Figure 5.2 Mean rainfall rate (mm hr<sup>-1</sup>) by time of day between 1<sup>st</sup> June 2006 and 30<sup>th</sup> September 2006. Shaded area indicates the standard error. Data obtained from surface station in Niamey.....</b>	<b>124</b>

<b>Figure 5.3</b> Number of convective initiations per 15 minutes in 4 km Cascade between 25 <sup>th</sup> July 2006 and 2 <sup>nd</sup> September 2006. Initiations from Taylor et al. 2013.....	125
<b>Figure 5.4</b> Diurnal variations in vertical CAPE (J Kg <sup>-1</sup> ) distributions. Data obtained between 1 <sup>st</sup> June 2006 and 30 <sup>th</sup> September 2006 in Niamey from raw radiosonde data a) and moisture-bias corrected radiosonde data b). .....	129
<b>Figure 5.5</b> As Figure 5.4. a), but using 00, 06, 12 and 18 UTC radiosondes only. ....	130
<b>Figure 5.6</b> Topographic height (m) across the Cascade domain. Dots denote convective initiations (see text) and “plus” symbols indicate initiations within the Sahel subdomain (12–18°N, 12°W–15°E) analyzed later. Figure obtained from Taylor et al. (2013) – Figure 1. ....	131
<b>Figure 5.7</b> An example showing Cascade simulated 1.5 m temperature (°C) (shaded) and precipitation > 0.5 mmh <sup>-1</sup> (contours) for simulation time equivalent to 19:00 (UTC) on 2 <sup>nd</sup> August 2006.....	133
<b>Figure 5.8</b> As Figure 5.7., but for precipitation > 0.5 mm h <sup>-1</sup> (contours), specific humidity (kg kg <sup>-1</sup> ) (shaded) and wind (arrows), the latter two at the 10m level. Times are a) 19:00 UTC on 29 <sup>th</sup> August 2006, b), c) and d) is for 00:00, 04:00 and 07:00 UTC, respectively. ....	124
<b>Figure 5.10</b> Hovmuller diagram of surface rainfall between 10 <sup>0</sup> N and 20 <sup>0</sup> N for the 40day Cascade period. ....	134
<b>Figure 5.9:</b> An example showing surface precipitation > 0.5 mm h <sup>-1</sup> (contours), PV anomalies 10 <sup>-5</sup> (m <sup>-2</sup> s <sup>-1</sup> KKg <sup>-1</sup> ) (shaded) and wind (arrows), the latter two at the 850hPa level.....	135
<b>Figure 5.10:</b> Hovmuller diagram of surface rainfall between 10 <sup>0</sup> N and 20 <sup>0</sup> N for the 40day Cascade period.....	136

<b>Figure 5.11 Frequency distribution of rainfall rate (mm hr<sup>-1</sup>) across all grid boxes in the whole Cascade period. ....</b>	<b>137</b>
<b>Figure 5.12 Cascade accumulated precipitation (m) during the three simulation runs between 1<sup>st</sup> June – 30<sup>th</sup> July (left), 25<sup>th</sup> July and 2<sup>nd</sup> September (middle) and 3<sup>rd</sup> September -30<sup>th</sup> September (right). ....</b>	<b>140</b>
<b>Figure 5.13 (a) Diurnal variations in potential temperature (° C). (b) as a), but with pressure-level mean subtracted (b). Estimated maximum boundary layer height shown by thin horizontal line. Data obtained from Niamey radiosondes between 1<sup>st</sup> June 2006 and 30<sup>th</sup> September 2006.. ....</b>	<b>142</b>
<b>Figure 5.14 a) as Figure 5.13. a), but with respect to height and for greater depth of the troposphere between surface and 12km. b) same as a), but for dry-bulb temperature. c) and d) are same as a) and b) respectively, but with the mean at any given height subtracted from the diurnal cycle. Potential temperature (e) and dry-bulb temperature (f) at 200 m (red), 1 km (blue) and 4 km (green). All data obtained from Niamey radiosondes. ....</b>	<b>143</b>
<b>Figure 5.15 As Figure 5.14. a), but for CIN. Data obtained between 1<sup>st</sup> June 2006 and 30<sup>th</sup> September 2006 from Niamey from radiometer.. ....</b>	<b>145</b>
<b>Figure 5.16 As Figure 5.15, but for wind-speed. b) as a), but considering only soundings within 12 hours prior to an MCS passage, excluding soundings when an MCS passed within the 12 hours prior to their release. Data obtained from Niamey radiosondes between 1<sup>st</sup> June 2006 and 30<sup>th</sup> September 2006.....</b>	<b>146</b>

<b>Figure 5.17 Mean wind-speed at 200 m (red), 800 m (blue) and 3000 m (green) between 1<sup>st</sup> June 2006 and 30<sup>th</sup> September 2006 in Niamey. Data obtained from radiosondes.....</b>	<b>147</b>
<b>Figure 5.18 As Figure 5.16 a), but for equivalent potential temperature (°C) (a) and water vapour mixing ratio (g kg<sup>-1</sup>) (b). Data obtained from Niamey Radiometer between 1<sup>st</sup> June 2006 and 30<sup>th</sup> September 2006. ....</b>	<b>148</b>
<b>Figure 5.19 As 5.4. a), but data obtained from radiometer a). In b), data for temperature and dew-point of the source parcel were taken from radiometer, but data for the environmental profile of temperature was taken from radiosondes. Data provided hourly (averages of 1min data), but averaged to 3-hourly, centred at 00, 03, 06, 09, 12, 15, 18 and 21 UTC.....</b>	<b>149</b>
<b>Figure 5.20 Surface-based (solid) and 600 m above ground (dotted) CAPE by time of day. Data for surface-based parcel obtained from surface station at Niamey airport, data for 600 m parcel and atmospheric profile obtained from radiometer. ....</b>	<b>151</b>
<b>Figure 5.21 Surface rainfall rate (mm h<sup>-1</sup>) by time of day around Cascade points where rainfall exceeds 180 mm h<sup>-1</sup>. Times are as follows: a) 00-03 UTC, b) 03-06 UTC, c) 06-09 UTC, d) 09-12 UTC, e) 12-15 UTC, f) 15-18 UTC, g) 18-21 UTC, h) 21-00 UTC. The number of points used to create the composite is 1874, 1229, 1123, 1367, 4331, 6765, 3037 and 2713 respectively. The colour-scale has been “cut-off” at 10 mm h<sup>-1</sup> in order to be able to see the extent of the rainfall more clearly. ....</b>	<b>154</b>
<b>Figure 5.22 Diurnal cycle of total mean precipitation (blue), mean evaporated water from surface (red) and mean moisture flux convergence (green) in a 200*200 km<sup>2</sup> box around every grid-box with precipitation greater than 180 mm h<sup>-1</sup> assuming stationary rainfall (a), assuming that the area of rainfall is propagating at a speed of 11 m s<sup>-1</sup> from east to west (b). Dotted line is mean difference between moisture input and output by time of day and dashed line is the same, but averaged for the whole day.. ....</b>	<b>156</b>
<b>Figure 5.23 a) as Figure 5.22., but for 5000 randomly selected points. For clarity, mean precipitation in b) and moisture flux convergence in c) is shown again.. ....</b>	<b>158</b>
<b>Figure 5.24 Mean moisture flux convergence in a 200*200 km<sup>2</sup> box around every grid-box with precipitation greater than 180 mm h<sup>-1</sup> by height and averaged over 3-hourly time periods by time day, assuming a MCS is propagating at a speed of 11 m s<sup>-1</sup> from east to west.....</b>	<b>159</b>
<b>Figure 5.25 Mean diurnal variations in a) 0.5 - 1.5 km and b) 0.5 - 2.5 km wind-shear (m s<sup>-1</sup>) between 1<sup>st</sup> June 2006 and 30<sup>th</sup> September 2006 in Niamey. Dotted line is wind-speed at the upper level (1.5 km in a) and 2.5 km in b)) and dashed line is wind-speed at 0.5 km. ....</b>	<b>160</b>

<b>Figure 5.26</b> An example case in Cascade simulation: 1.5m temperature (shaded), 10m specific humidity (coloured contours), 10m wind (arrows) and surface precipitation (black contours). Two contours have been used for specific humidity – yellow shows 9 g kg <sup>-1</sup> and green shows 16 g kg <sup>-1</sup> . Precipitation contour denotes areas where instantaneous precipitation at the hour given is greater than 0.5 mmh <sup>-1</sup> . Times of simulation: a) 18:00 and b) 22:00 on 14 <sup>th</sup> June 2006. c) 02:00, d) 06:00, e) 9:00, f) 12:00, g) 14:00 and h) 18:00 on 15 <sup>th</sup> June 2006. All times are UTC. ....	166
<b>Figure 5.27</b> Composite of 1.5 m temperature (shaded) and 10 m wind (vectors) perturbations centred on points 1 hour before initiations by time of day. The composite is for 00-03, 03-06, 06-09, 09-12, 12-15, 15-18, 18-21 and 21-00 for a), b), c), d), e), f), g) and h), respectively. All times are UTC. Data obtained from Cascade 4km convection-permitting model simulation.. ....	169
<b>Figure 5.28</b> As Figure 5.27, but for Cascade soil moisture. ....	171
<b>Figure 5.29</b> As Figure 5.28, but for Cascade 10 m specific humidity anomaly (composite around convective initiations with mean around 5000 random points subtracted). The composite domain size is 150x150 grid points, or 600x600km.....	175
<b>Figure 5.30</b> Schematics showing a) a vertical plane through a convective storm and the production of positive and negative Potential Vorticity (PV+ and PV-, respectively) due to convective heating and cooling (due to evaporation of rainfall) and the ambient vorticity produced by the African Easterly Jet (AEJ). In b) and c), a horizontal plane shows the production of positive and negative vorticity if the convective heating is b) towards the north above the AEJ and c) towards the south and below the AEJ. ....	176
<b>Figure 5.31</b> As Figure 5.29., but for Cascade potential vorticity 10 <sup>-5</sup> (m <sup>-2</sup> s <sup>-1</sup> K Kg <sup>-1</sup> ) at the 700 hPa level.....	178
<b>Figure 5.32</b> As Figure 5.31, but for Cascade potential vorticity 10 <sup>-5</sup> (m <sup>-2</sup> s <sup>-1</sup> K Kg <sup>-1</sup> ) at the 700 hPa level around points where rainfall rate is greater than 180 mm h <sup>-1</sup> . ....	183
<b>Figure 5.33</b> Cascade 850 hPa PV 10 <sup>-5</sup> (m <sup>-2</sup> s <sup>-1</sup> K Kg <sup>-1</sup> ) (shaded), precipitation (contours) and 10m wind (arrows). a)-h) are for 10:00-17:00 UTC respectively.....	189
<b>Figure 6.1</b> A conceptual model of the identified processes and their importance for the observed diurnal cycle of deep moist convection in the West African Sahel.....	198

## Abbreviations

<b>2D</b>	<b>2 Dimensional</b>
<b>AEJ</b>	<b>African Easterly Jet</b>
<b>AMMA</b>	<b>African Monsoon Multidisciplinary Analysis</b>
<b>AMS</b>	<b>American Meteorological Society</b>
<b>ARM</b>	<b>Atmospheric Radiation Measurement</b>
<b>CAPE</b>	<b>Convective Available Potential Energy</b>
<b>CIN</b>	<b>Convective Inhibition</b>
<b>E2008</b>	<b>Engerer <i>et al.</i> (2008)</b>
<b>ECMWF</b>	<b>European Centre for Medium Range Weather Forecast</b>
<b>EL</b>	<b>Equilibrium Level</b>
<b>IHOP</b>	<b>International H<sub>2</sub>O Project</b>
<b>IOP</b>	<b>Intensive Observation Period</b>
<b>ITCZ</b>	<b>Inter-Tropical Convergence Zone</b>
<b>ITD</b>	<b>Inter-Tropical Discontinuity</b>
<b>ITF</b>	<b>Inter-Tropical Front</b>
<b>LFC</b>	<b>Level of Free Convection</b>
<b>LIDAR</b>	<b>Light Detection and Ranging</b>
<b>LLJ</b>	<b>Low-Level Jet</b>
<b>LNB</b>	<b>Level of Neutral Buoyancy</b>
<b>MCS</b>	<b>Mesoscale Convective System</b>
<b>MCC</b>	<b>Mesoscale Convective Complex</b>
<b>MIT</b>	<b>Massachusetts Institute of Technology</b>
<b>NWP</b>	<b>Numerical Weather Prediction</b>
<b>OCS</b>	<b>Organized Convective System</b>
<b>PBL</b>	<b>Planetary Boundary Layer</b>
<b>RHI</b>	<b>Range Height Indicator</b>
<b>ROP</b>	<b>Radar Observing Period</b>

<b>RKW</b>	<b>R</b> otunno <b>K</b> lemp <b>W</b> eisman theory
<b>SAL</b>	<b>S</b> aharan <b>A</b> erosol <b>L</b> ayer
<b>TRMM</b>	<b>T</b> ropical <b>R</b> ainfall <b>M</b> easuring <b>M</b> ission
<b>UK</b>	<b>U</b> nited <b>K</b> ingdom
<b>UM</b>	<b>U</b> nified <b>M</b> odel
<b>USA</b>	<b>U</b> nited <b>S</b> tates of <b>A</b> merica
<b>WAM</b>	<b>W</b> est <b>A</b> frican <b>M</b> onsoon

# Chapter 1

## Introduction

### 1.1 Motivation and aims

The West African Monsoon delivers a great majority of the annual rainfall to the Sahel. In the Sahel 80-90% of rain is produced by deep moist convection in the form of Mesoscale Convective Systems (MCSs) (Redelsperger *et al.*, 2002). The processes controlling moist convection in the Sahel are poorly understood. Current operational global and regional forecasting models struggle to simulate Sahelian deep moist convection accurately (Agusti-Panareda, *et al.*, 2010), primarily because many important processes and features of the convection, such as cold pools, are poorly captured (Marsham *et al.* 2011b, Marsham *et al.*, 2013a). These incorrect representations are a cause of major biases in the Sahara in the global Unified Model (UM), such as biases in overall thermodynamics (Garcia-Carreras *et al.* 2013) as well as dust uplift (Heinold *et al.* 2013). Because convection is together with its cold pools part of the monsoon (Marsham *et al.*, 2013a) this affects the overall simulated monsoon circulation (Marsham *et al.*, 2013a, Birch *et al.*, 2014).

Compared with, for example, the Great Plains of the USA, there are far fewer studies concentrating on the understanding of structure of deep moist convection over the Sahel and its interaction with the environment, this is partly due to the lack of direct observations before AMMA in 2006. Many features such as cold pools, atmospheric stratification, wind-shear, soil moisture distribution or internal flows within convection are important and influential on convective evolution and diurnal cycle, because they control the initiation and deepening of convection. The convection itself is then important for the overall monsoon circulation (e.g. its cold pools ventilate the Saharan Heat Low (Garcia-Carreras *et al.*, 2013; Marsham *et al.*, 2013b). Given that Sahelian deep moist convection is understudied when compared to USA convection, it is of interest to assess whether the particular environmental conditions as well as dynamical states of MCSs in West Africa result in similar statistics. As far as the author of this thesis is aware, there are several case studies of West-African MCSs, but only a handful of

them concentrate on internal dynamical properties of MCSs (e.g. Barthe, *et al.*, 2010; Chong, 2010; Schwendike *et al.*, 2010; Taylor *et al.*, 2010; Guy, *et al.*, 2011; Lothon, *et al.* 2011).

In addition, there is a great societal need for improvement of rainfall forecasts in the Sahel. Rainfall in the Sahel has a large year-to-year variability (e.g. Rowell *et al.* 1995) and drought conditions can occur frequently, persisting for several years in some cases. An example is a severe drought that affected the region between the 1970s and 1990s, culminating in 1984 (e.g., Nicholson 1980; Nicholson *et al.* 2000; Janicot *et al.*, 2008, Salack *et al.*, 2014). This was attributed to positive land-atmosphere feedback processes and desertification (Charney, 1975) or remote effects of SST anomalies (Giannini, *et al.* 2003; Mohino *et al.* 2011). Most countries that are located in the Sahel region are among the poorest in the world and their agriculture is greatly affected by drought, so that long lasting droughts have led to famine conditions in the past (Mertz *et al.*, 2012 and references therein), resulting in great economic problems as well as loss of life. Better forecasts of rainfall are imperative for the preparedness and adaptation of population.

One of the major issues in West Africa has always been the shortage of data to be assimilated into forecasting models (Roehrig, 2013), which significantly contributes to inaccurate rainfall predictions. More observational data has been added into assimilations in the last decade (Tompkins *et al.*, 2005; Faccani *et al.*, 2009; Agusti-Panareda *et al.*, 2010), which has led to improvements, but these being mostly influential on a one-day scale (Agusti-Panareda *et al.*, 2010). Furthermore, significant improvements have been detected mainly on the synoptic scale (e.g. Vanvyve *et al.*, 2008), but forecasts of smaller spatial-scale or shorter-lived events, such as deep moist convection, still face significant challenges (Ruti *et al.*, 2011). This further reinforces the need to better understand processes related to deep moist convection and its interaction with the environment.

The African Monsoon Multidisciplinary Analysis (AMMA) Special Observing Period (SOP) took place during the summer monsoon of 2006 and progressed our understanding of the West African Monsoon through unprecedented collection of observational data (Redelsperger *et al.* 2006). Documentation of MCSs was one of the key components of AMMA and the data obtained during the field campaign currently provide the most detailed and complete dataset for moist convection in West Africa (Redelsperger *et al.* 2006).

A large scale overview of the summer monsoon of 2006 has been presented by Janicot *et al.* (2006). Their study concludes that the monsoon season of 2006 in the Sahel was characterized by near normal convective activity, except for an excess of rainfall north of 15° N. Another difference with respect to average was that monsoon onset was delayed by ~10 days (Janicot *et al.* 2006), leading to drier soil moisture anomalies until mid-July, which were then offset by wet anomalies in August and September. Because the excess of rainfall north of 15° N was within one standard deviation of the overall 1965-2006 mean, this monsoon season can be taken as representative with respect to the long term average.

The large dataset obtained during AMMA enabled an evaluation of regional and global forecasting models (Hourdin *et al.* 2010), concluding that models generally fail to represent deep moist convection and its diurnal cycle correctly and this was one of the main identified sources of error. Convection-permitting simulations at 1.5, 4, 12 and 40-km resolutions were subsequently provided by the *Cascade* project and these together with observational data from AMMA present the most detailed and complete dataset of observations and simulations to date of moist convection in West Africa (Redelsperger *et al.* 2006; Lebel *et al.* 2009; Parker *et al.* 2008; Marsham *et al.* 2011 and others).

Given these issues and the datasets available, this thesis addresses deep moist convection over the West African Sahel. The thesis aims to:

- (1) improve scientific understanding through quantitative characterisation of the structure of Sahelian deep convective systems
- (2) evaluate convection-permitting simulations, understanding reasons for model errors
- (3) describe, quantify and understand some of the most important processes that control the initiation and subsequent development of Sahelian convection
- (4) improve our understanding of the interaction of Sahelian deep moist convection with its environment, the properties of which vary during a diurnal cycle

By addressing these aims, the thesis will ultimately help future improvement in forecasts of rainfall.

### 1.1.1 Thesis structure

Chapter 1 is a literature review summarizing current knowledge of the West African Monsoon, deep moist convection and its organization, structure of Mesoscale Convective Systems, processes controlling the initiation and organization of deep moist convection and the interaction of deep moist convection with the synoptic scale. Current issues with simulation and forecasting of deep convective storms in West Africa are also discussed.

Chapter 2 describes all the instruments used to collect observational data and the *Cascade* project Unified Model (UM) simulations used in this study. Research techniques performed for the analysis in subsequent chapters are also described.

Chapter 3 presents a climatology of cold pools and their properties in Niamey, Niger. The sub-seasonal variations in cold-pool properties are also investigated and the role of mid-level dryness on these is assessed. Finally, cold pools in *Cascade* project simulations are evaluated and their properties are compared to the observed.

In Chapter 4, two squall-line MCS case studies are chosen and their dynamics is researched by the use of remote sensing and surface data. Structural features in these are identified and described. At the end, a Unified Model simulation of one of the cases is briefly evaluated.

Chapter 5 explores environmental processes that control the diurnal cycle of convection, its initiation and associated rainfall. The results of Chapter 5 are split into two parts. The first part uses primarily observed data in order to study diurnally varying changes in the vertical profile. In the second part data from convection-permitting simulations from the *Cascade* project are utilized to study the diurnally changing relative importance of processes by compositing around convective initiations and mature MCSs. This is achieved with both the use of observational datasets as well as through convection-permitting simulations from the *Cascade* project.

Chapter 6 draws conclusions from our research of processes controlling deep moist convection in the West African Sahel. Contributions of this study to our understanding of processes that influence deep convection and

Mesoscale Convective Systems in the Sahel are discussed. Future work based on our results is suggested.

## 1.2 Literature Review

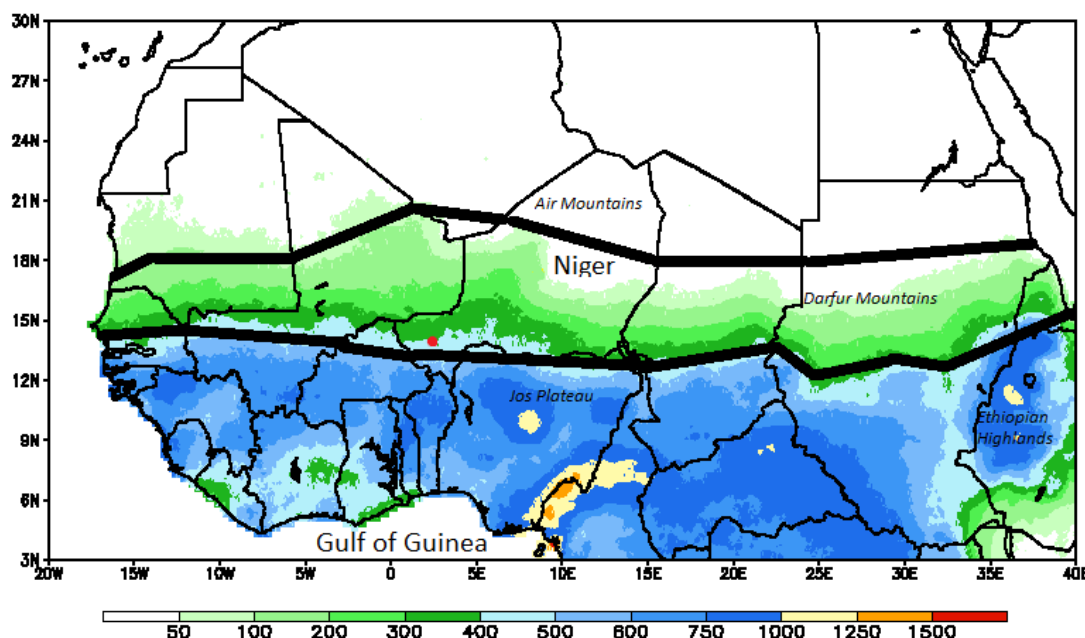


**Figure 1.1:** Map of West Africa showing the location of the Sahel (bordered by thick black lines). Coloured shading represents mean 1995-2006 annual precipitation (mm) Red dot denotes the location of Niamey, Niger. Precipitation based on NOAA/CPC RFE Climatology Method.

The Sahel is located in tropical Africa, being approximately 8000 km across west to east ( $\sim 20^\circ \text{W}$  to  $40^\circ \text{E}$ , see Figure 1.1) and it is a transition zone between the Sahara Desert (north) and the Sudanian Savannas (south) (spanning  $\sim 13^\circ \text{N}$  to  $18^\circ \text{N}$ ). Annual rainfall in the Sahel ranges from  $\sim 50$  to  $\sim 500$  mm, a great majority of which occurs in most of the Sahel during the West African monsoon between late May and September. Niamey, the capital of Niger (see red dot in Figure 1.1), has been one of the supersites during AMMA and all observational data used in the thesis has been collected at this supersite.

### 1.2.1 The West African Monsoon

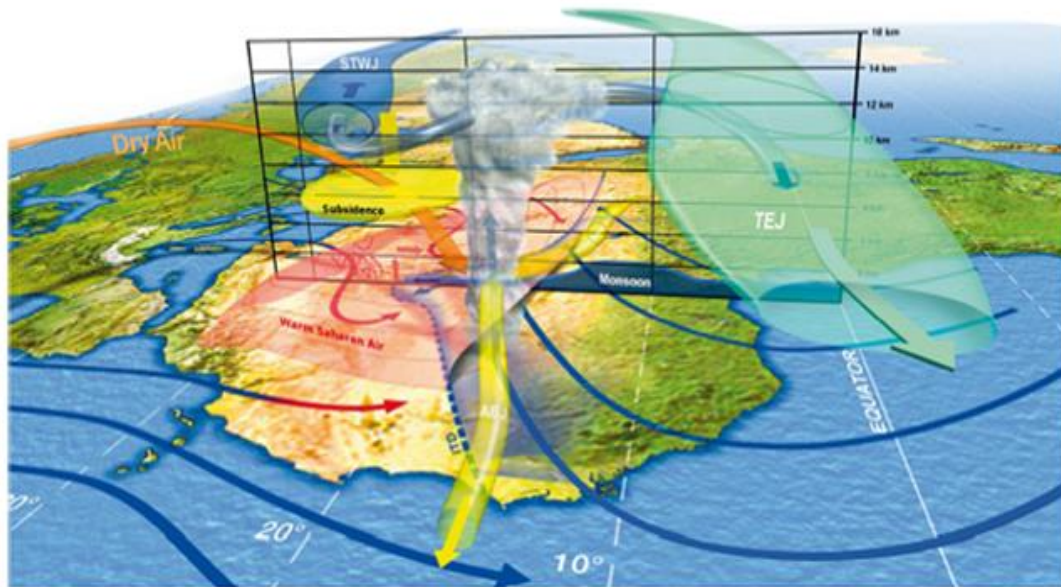


**Figure 1.2:** Schematic of the summer monsoon circulation in West Africa. ITD is the location of the Inter-Tropical Discontinuity, AEJ is the African Easterly Jet and the TEJ is the Tropical Easterly Jet (from Lafore, et al., 2011).

The West African Monsoon (WAM) occurs between late May and September each year, although there are year to year variations in both the onset and retreat. Figure 1.2 shows a graphical representation of the monsoon structure. The monsoon is driven by a surface heat-low (the Saharan Heat Low, SHL) that forms over west Sahara due to high soil and air temperatures and a dust layer absorbing shortwave solar radiation (Bounoua and Krishnamurti, 1991). The SHL, together with the pressure gradient between the Gulf of Guinea and the Atlantic, causes south-westerly low-level winds from the Gulf of Guinea to the Sahel, which bring moisture northwards (Figure 1.2). The onset of the WAM is influenced by the dynamics of the SHL (Sultan and Janicot, 2003a,b; Drobinski *et al.*, 2005; Ramel *et al.*, 2006; Sijikumar *et al.*, 2006), which influences the moisture budget in West Africa (Parker *et al.*, 2005). Strengthening of this heat low usually reinforces the monsoon flux and is often followed by a monsoon surge (Couvreur, *et al.* 2009). Such a surge consists of warm and moist air, which meets very dry and hot Saharan air and hence forms the inter-tropical front/discontinuity (shown as ITD in Figure 1.2). The ITD has long been recognized as a fundamental feature of the West African monsoon (Hamilton

and Archbold 1945; Eldridge, 1957) and is sometimes referred to as the Inter-Tropical Front (ITF). It is defined as a line where 2 m dew-point temperature drops below 15°C (Flamant, *et al.* 2007). Between approximately surface and ~700 hPa, the ITD slopes upward to the south at inclinations of between 1:100 to 1:400 (Hastenrath and Lamb 1977; Hastenrath 1991) and is an upper boundary of the monsoon air (Lele and Lamb, 2010).

In the evening hours, boundary-layer stabilization leads to the formation of a nocturnal low-level jet (LLJ) (Parker *et al.*, 2005b). The LLJ in the Sahel is a region of enhanced south to south-westerly winds above the stable nocturnal boundary layer. The moisture advection to the south of the ITD is dependent on the existence of this nocturnal Low Level Jet (LLJ), which is the main meridional transporter of moist air from the Gulf of Guinea to the Sahel (Parker *et al.*, 2005b). Lothon *et al.*, (2008) showed the importance of this process and subsequent mixing of moist air by the diurnal turbulent boundary layer throughout a large depth of the troposphere. This monsoon circulation is important in sustaining deep moist convection (Peyrille and Lafore, 2007b), which forms to the south of the inter-tropical front as it requires both heat and moisture (Figure 1.2).

The summertime thermodynamic stratification in the Sahel and neighbouring Sahara features a two-layer structure in the low levels, with well-mixed Planetary Boundary Layer (PBL) located below a very dry Saharan Air Layer (or sometimes called Saharan Aerosol Layer; SAL) (Karyampudi *et al.*, 1999; Berthier *et al.*, 2006). This is shown as “Warm Saharan air” in Figure 1.2. In the summer, seasonally increasing south-westerly monsoon winds advect moist high equivalent potential temperature ( $\Theta_e$ ) low-level air into the Sahel, which undercuts this dry mid-level Saharan Air Layer (SAL; Parker *et al.* 2005a). The SAL is characterised by almost dry adiabatic lapse rates, which together with the low-level moisture results in large quantities of Convective Available Potential Energy (CAPE).

CAPE is a measure of how much thermodynamic energy could be potentially released by moist convection in lifting a parcel from the surface layer or any other given layer before it reaches its Equilibrium Level (EL). On a tephigram, CAPE is the integral of the difference between the temperature of an adiabatically rising air parcel and the temperature of the environment. Equation (1) shows a mathematical expression of CAPE. In equation 1,  $T_{vp}$  is temperature of the source parcel,  $T_{ve}$  designates environmental temperature,

$g$  is acceleration due to gravity,  $z$  represent height, LNB is Level of Neutral Buoyancy and LFC is Level of Free Convection:

$$CAPE = \int_{LFC}^{LNB} g \frac{T_{vp} - T_{ve}}{T_{ve}} dz \quad (1)$$

Convective Inhibition (CIN), sometimes referred to as a “lid”, is “the energy needed to lift an air parcel vertically and pseudo adiabatically from its originating level to its level of free convection (LFC)” (AMS glossary, 2016). CIN is another important parameter influencing if and when deep moist convection occurs, because rising air parcels need to overcome CIN and reach their level of free convection for deep convection to be initiated and sustained (Duvel, 1989). Environments characterized by high CAPE and high CIN are favourable for the development of strong deep moist convection as the high CIN enables temperature and moisture to build up below the inhibition, further increasing CAPE for parcels originating below the CIN. The condition for strong deep moist convection is however the ability of surface parcels to penetrate the CIN as if CIN is not penetrated, no convection occurs. Equation (2) shows a mathematical expression for CIN (AMS glossary, 2016), where it is assumed that the environment is in hydrostatic balance and that the pressure of the parcel is equal to environmental pressure. In equation 2,  $T_{vp}$  is the virtual temperature of the source (lifted) parcel and  $T_{ve}$  designates the virtual temperature of the environment:

$$CIN = - \int_0^{LFC} g \frac{T_{vp} - T_{ve}}{T_{ve}} dz \quad (2)$$

If convection erodes CIN and reaches the level of free convection, primary initiation occurs. There are several mechanisms that can provide localised triggering for the CIN to be overcome. The dominant mechanism for the erosion of CIN and primary convective initiation is low-level lifting (Trier, 2003; Fink, *et al.*, 2006; Laing, *et al.*, 2008; Guy, *et al.*, 2011), but other mechanisms such as heating or synoptic-scale forcing by African Easterly Waves in the Sahel (Thorncroft, 1995) can play a significant role. Low-level lifting is generally caused by thermally induced mesoscale circulations, which can provide low-level moisture convergence. Studies from various locations around the world confirmed that contrasting surface features organized on length scales of several tens of kilometres can be a focus of such convergence (Anthes, 1984; Chen and Avissar, 1994; Emori, 1998). These include orographic features, which provide an elevated heat source (Barthlott *et al.* 2006). Horizontal temperature and moisture gradients within the boundary layer can also be a cause of low-level convergence (Comer, *et al.*, 2007), where initiation is preferred over the warmer surface (Emori 1998; Carleton *et al.* 2001), typically at the downstream edge of the

warm surface (e.g. Taylor *et al.*, 2011). Such gradients can be formed by horizontal gradients of soil moisture content as well as variations in vegetation (e.g. Segal and Arritt, 1992; Taylor *et al.* 1997b; Koster *et al.* 2004; Dixon *et al.* 2013). These surface properties influence the planetary boundary layer (Taylor *et al.* 2010) by partitioning of the incoming energy into sensible and latent heat fluxes, which induces horizontal temperature gradients.

The meridional temperature gradient on the ITD results in a thermal wind, which is normally located near 700 hPa (Burpee, 1972; Kalapureddy *et al.*, 2010). This is the African Easterly Jet, which is marked by the yellow arrow and AEJ in Figure 1.2 and translates approximately between 5°N and 16°N on a 1-2 week time scale (Ferreira and Rickenbach, 2009). Wind speeds in the African Easterly Jet range from ~9 (wet conditions) to 15 m s<sup>-1</sup> (dry conditions) (Hsieh and Cook, 2005). There are, however, many open questions surrounding the generation, maintenance, variability and location of the AEJ – e.g. Cook (1999) showed with the use of a Global Climate Model that the temperature gradient alone does not explain the formation of the African Easterly Jet and that gradients in soil moisture are also important. A study by Thorncroft and Blackburn (1999) shows that the equivalent potential temperature gradient (baroclinic instability) at the origin of the jet is caused by dry convection occurring in the Saharan Heat Low to the north and also by deep convection occurring in the ITCZ to the south.

The African Easterly Jet plays an important role in the organization of MCSs (Houze and Betts, 1981; Diedhiou *et al.*, 1999) as it provides mid-level vertical wind shear (Mohr and Thorncroft, 2006). Due to barotropic instability, waves and oscillations form on the African Easterly Jet. These are known as African Easterly Waves (Pytharoulis and Thorncroft, 1999; Hsieh and Cook, 2008), which propagate west across the Sahel and West Africa. They are important for the modulation of convection and are the major synoptic scale variation that occurs in the Sahel. Relations between annual rainfall and variability of the African Easterly Jet have been found (e.g. Newell and Kidson, 1984), but their importance is unknown.

### **1.2.2 Mesoscale Convective Systems (MCSs) in the West African Monsoon**

Initially, primary initiation of deep convection in the Sahel results in discrete small-scale convective storms (Dione *et al.*, 2014) that can, under certain conditions, organize and grow upscale to form a group of convective cells, which initiate, propagate and dissipate in an organised fashion (Vila *et al.* 2008). Three phases of a convective storm were identified in The

Thunderstorm Project, which was performed in the USA (Byers, 1949), these being the cumulus stage when convective clouds initiate, grow and accumulate water through an updraft containing vertical wind speeds of 1-3  $\text{ms}^{-1}$ ; the mature stage when the updraft is still present, but rainfall begins to form a downdraft through evaporational cooling and melting; and the dissipating stage where downdraft dominates and the convective storm breaks up. More convective storm-cells can interact with each other and if they do so in an organized way, then such a group of cells is referred to as a Mesoscale Convective System (MCS). According to AMS glossary (2016), a Mesoscale Convective System is “a cloud system that occurs in connection with an ensemble of thunderstorms and produces a contiguous precipitation area on the order of 100 km or more in horizontal scale in at least one direction. A MCS exhibits deep, moist convective overturning contiguous with or embedded within a mesoscale vertical circulation that is at least partially driven by the convective overturning.”

Mesoscale Convective Systems form an integral part of the West African Monsoon (Redelsperger *et al.* 2002; Diongue *et al.* 2002; Marsham *et al.* 2013a). They account for 80-90% of the annual rainfall in most of the Sahel (Omotosho, 1985; Mathon *et al.* 2002; Redelsperger *et al.*, 2002; Fink *et al.*, 2006). MCSs in the Sahel often organize into propagating squall lines (Hamilton *et al.* 1945; Aspliden *et al.* 1976; Houze *et al.*, 1989; Chong, 2010; Birch *et al.* 2014), which can propagate over great distances (e.g. Fortune, 1980). A squall-line is a MCS characterised by a line of convective cells at its leading edge and a trailing stratiform precipitation following, although the stratiform precipitation can lead the convective line in some cases. The convective line is typically several hundred kilometres, but can be up to 1000 km in length (Rowell and Milford, 1993) and is normally preceded by a gust front related to its cold-pool edge (Engerer *et al.* 2008). Some MCSs can be composed of multiple squall-lines (Fortune, 1980).

### ***The general diurnal cycle of deep moist convection and MCSs***

In general, the diurnal cycle of deep moist convection features a maximum in the afternoon or evening over land (Gray and Jacobson, 1977; Dai and Trenberth, 2004; Dai, 2006). However, certain areas such as mountain basins (Ohsawa *et al.* 2001) or regions with flat orography, but in a proximity to mountain ranges, can exhibit a nocturnal or even early morning maximum. The diurnal cycle over land is mainly driven by diurnal changes in solar heating of the land, but the exact mechanisms dominating this cycle are not well understood (Bechtold *et al.* 2004; Yuan *et al.* 2013; Folkins *et al.* 2014).

Perhaps the most influential parameter for deep moist convection is CAPE as it is the energy available to convection. If there is no CAPE there can't be any convection. Theoretically, convective precipitation cycle should

be strongly related to the cycle of CAPE, but this is not always the case. There are several studies that confirm a strong positive correlation between CAPE and convective precipitation, such as Zawadzki *et al.* (1981) for eastern Canada or Monkam (2002) for tropical Atlantic and northern Africa. There are, however, other studies that have reported a negative correlation between convective rainfall and CAPE (e.g. McBride and Frank, 1999). Adams and Souza (2009) pointed out that in such correlation studies it is important to note the timing of the CAPE measurements, as an average time of CAPE measurement being after a convective event can easily lead to negative correlation. They have also concluded that a phase lag always exists between measured CAPE and the occurrence of rainfall.

Convective initiation is the first stage of any developing convective storm or MCS. Parsons (2006) performed a detailed review of various initiation processes leading to deep moist convection during the International H<sub>2</sub>O Project (IHOP) (Weckwerth, *et al.*, 2004), which was performed in the Great Plains of the USA, and the conclusion of their study was that boundary layer convergence is often a precursor to initiation. It was further summarized that initiating convection is sensitive to the strength of the boundary layer convergence, the shear, and the spatial variability of moisture (Weckwerth and Parsons, 2006; Cooper, *et al.*, 1982). Weckwerth *et al.*, 2008 analysed several well observed initiating convective cells and noted several features that occur before initiation of convection. These include: mesoscale low pressure region, a dry line and interacting outflow boundary, internal gravity waves and horizontal convective rolls. These findings were supported by several case studies, including Kalthoff *et al.*, 2009 and by Wilson *et al.*, 1992.

Hodges and Thorncroft, (1997) show that convective systems in West Africa are initiated over elevated terrain during peak heating and then grow and propagate westwards, driven by the African Easterly Jet. Rickenbach *et al.*, (2009) tracked MCSs reaching Niamey (see Figure 1.1) backwards using IR satellite imagery and concluded that there are several places where they are likely to be initiated, most frequently over the Air Mountains and Jos Plateau to the east and north-east of Niamey. Other studies, such as Laing and Fritsch, (1993), suggest that Niamey MCSs originate most frequently over Jos Plateau, Darfur Mountains and the Ethiopian Highlands (see Figure 1.1. for locations of mountains ranges). Nesbitt and Zipser (2003) found that MCSs over West Africa reach their mature stage between about midnight and 3am Local Time. Similar results were confirmed by Newman and

Heinselman (2012). This leads to the time of diurnal maximum in convective activity shifting westwards with a delayed phase of arrival of these systems (Laing *et al.* 2008). The role of topography however is also very important for the lysis (dissipation) of MCSs since topography provides a barrier that the propagating MCS have to overcome (Laing *et al.* 2008).

Existing MCSs that have persisted overnight can weaken during the following morning, but then undergo various stages of re-generation or can cause related secondary initiation (Peters and Tetzlaff, 1988). The processes leading to new initiation or re-intensification are related to gravity waves (e.g. Mapes 1993; Birch *et al.* 2013), cold pools (Thorpe *et al.* 1982; Tompkins, 2001), and line-end vortices as well as localised convective moistening of the atmosphere (Nicholls and LeMone 1980; Randall and Huffman 1980). Hodges and Thorncroft (1997) used data over both tropical Africa and the tropical Atlantic Ocean. In agreement with other studies they found that convective systems over West Africa exhibit strong diurnal cycles in contrast to storms over East Africa. Their main observed difference was a tendency for storms to be longer-lived and travel larger distances in the west of tropical Africa as compared to east Africa. This was hypothesized to be due to stronger African Easterly Jet and hence flow and shear in the west, which both organize storms to keep them longer-lived as well as steers them faster westwards, which accounts for their greater distances travelled during their lifecycles. Also, Hodges and Thorncroft (1997) concluded that the greater equivalent potential temperatures as well as potential instabilities were likely playing a role in the greater longevity of the systems in the west. According to Rickenbach *et al.*, (2009), 20 out of 28 studied squall-lines propagated westwards while the rest came to Niamey from either north-east or south-east and only one squall-line came from the northerly direction.

Laing *et al.* (2008) studied the propagation and diurnal cycle of MCSs in north tropical Africa and concluded that each MCS travels on average 1000 km and lasts 25 hours. Generally, the faster propagating systems had longer lifetimes. Their calculated phase speeds ranged between  $\sim 10$  and  $20 \text{ m s}^{-1}$  with a mean of  $\sim 12 \text{ m s}^{-1}$ , which agrees with Rickenbach *et al.*, (2009), who concluded that mean speed of propagation ranges from  $\sim 5$  to  $25 \text{ m s}^{-1}$ , being generally faster than the mean propagation speed of African Easterly Waves of  $\sim 8 \text{ m s}^{-1}$ . The actual propagation direction was to the west-southwest with an average southward propagation speed  $\sim 3\text{-}4 \text{ m s}^{-1}$  slower than westward propagation (Laing *et al.* 2008).

It has been shown that strong relationship exists between land surface properties and precipitation over West Africa (Koster *et al.* 2004; Taylor and Ellis 2006). During the initiation stage, convection tends to form preferably over inhomogeneities in the boundary layer (Clark *et al.* 2003; Taylor *et al.* 2003; 2007). In semi-arid regions, such as the Sahel, these are often caused by varying soil moisture. The Bowen ratio ranges between 0.2-0.3 over wet surfaces, but can exceed 1 over dry surfaces. When convection organizes into mature MCSs, it tends to propagate and be more intense over moister surfaces (Clark *et al.*, 2003; Alonge *et al.*, 2007). This is because moister land surface is normally associated with more CAPE due to enhanced latent heat flux during daytime hours, which moistens the boundary layer and enhances equivalent potential temperature (Williams and Renno 1993; Kohler *et al.*, 2010). This creates positive rainfall intensity feedbacks between subsequent convective systems (Taylor *et al.* 2007; Taylor and Lebel, 1998; Koster *et al.* 2004; Gantner and Kalthoff, 2010; Taylor and Clark, 2001). These feedbacks were investigated and confirmed by Clark *et al.* (2003; 2004) and Alonge *et al.* (2007), who used a cloud-resolving model. It was shown by Clark *et al.* (2003) that the more buoyant convective cells over moister surface have advantage as they are lifted to their level of free convection and they also suppress cells in their surroundings. Contrasting results were presented by Taylor and Ellis (2006), who found a negative feedback between soil moisture and precipitation.

### ***The structure and dynamics of typical squall-line MCSs***

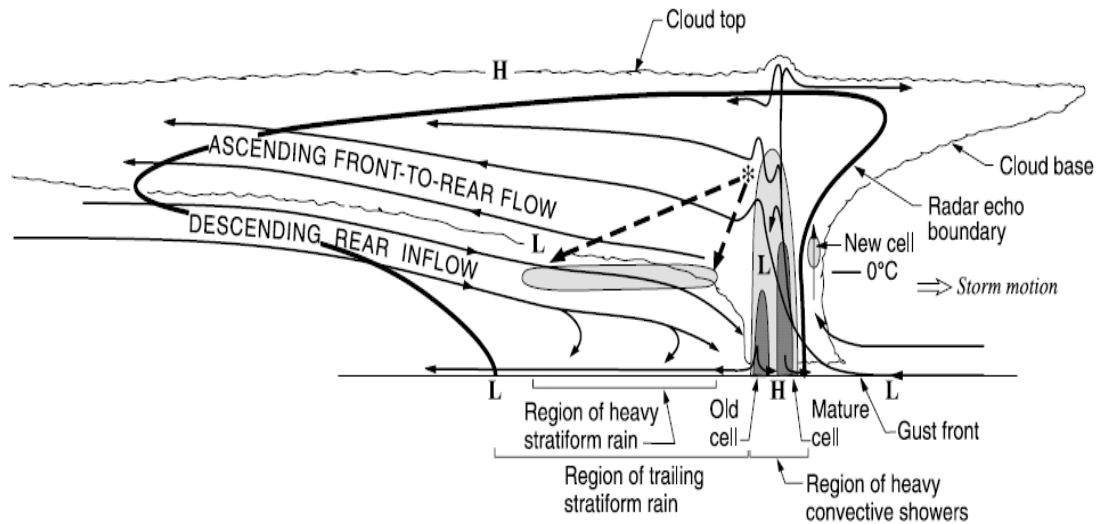


**Figure 1.3:** Conceptual model of the kinematic and radar echo structure of a squall-line viewed in a vertical cross section oriented perpendicular to the squall-line (and generally parallel to its motion). Intermediate and strong radar reflectivity is indicated by medium and dark shading, respectively. H and L indicate centres of positive and negative pressure perturbations, respectively. Dashed-line arrows indicate fallout trajectories of ice particles passing through the melting layer (from Houze et al., 1989).

Figure 1.3 shows a general structure of a squall-line MCS, which comprises of a region of heavy convective precipitation on the front side with a trailing stratiform rain. The overall circulation features a descending rear inflow (the Rear-Inflow Jet) formed partly as a result of dry mid-level air (Smull and Houze 1987). Above the melting layer, the descent of this inflow is mainly dynamically driven by mechanical subsidence caused by the vigorous updrafts in the convective region while below the melting layer it is driven by microphysical processes due to melting and evaporation of precipitation (Biggerstaff and Houze 1993). Therefore, MCSs with large stratiform precipitation areas are generally associated with mesohigh development (Houze 1993) and strong surface winds as a result of momentum transport by the rear inflow jet. This descent below the melting layer is unsaturated (Zipser, 1977) and feeds the cold pool (Zipser, 1969; Chong, 2010) that converges at its gust front with the Low-Level Jet, where it creates a convergence line, which is conducive to new storm cell development (Moncrieff 1981; Coniglio et al., 2010; Marsham et al., 2011) maintained by a release of moist absolute instability (Bryan and Fritsch 2000). As the squall-line MCS matures, these new cells then join the main line of cells (Houze, 1976; Houze, 1977) and bring air upwards, which feeds the ascending front-to-rear flow and the stratiform rain region (Biggerstaff

and Houze 1993; Braun and Houze 1994; Houze 2004). This front-to-rear flow balances the Rear Inflow Jet (Parker and Johnson, 2004).

### ***Cold pools***

Evaporation and sublimation of hydrometeors (as well as melting) is important in the process of creating negative buoyancy (and Downdraft CAPE, which is the potential maximum kinetic energy increase a downdraft can attain due to evaporational cooling; Gilmore and Wicker, 1998). Due to the presence of mid-tropospheric dry air masses in the arid environment of the Sahel, latent cooling of precipitation from mature MCSs caused by such processes is supportive of the formation of a cooler than environment downdraft (Redelsperger and Lafore, 1988). This cooler air then reaches the surface and spreads out as a density current (also called a gravity current) – the cold pool (Charba, 1974; Mueller and Carbone, 1987). The cold pool is associated with strong surface wind gusts, convergence, shear and dynamical lift at its leading edge (Charba, 1974; Knupp and Cotton, 1982; Rotunno and Klemp, 1985; Rotunno *et al.*, 1988; Moncrieff and Liu, 1999; Weisman and Rotunno, 2004). Cold pools can create a haboob, which is important for dust uplift (Sutton, 1925), and are often accompanied by precipitation.

Together with the ambient wind shear, the cold pool helps to lift surrounding air parcels through the inhibition to their level of free convection, where they can exploit the large amounts of CAPE (e.g. Dione *et al.*, 2014) and create new convective cells, further organizing the MCS (e.g. Roca *et al.* 2005). This new cell generation however strongly depends on many properties of the cold pool such as its depth, speed, temperature, ambient thermodynamic profile, etc. (Fovell and Tan, 1998). New storms can also be triggered by a collision of two mature cold pools (Droegemeier and Wilhelmson, 1985a, 1985b; Tompkins, 2001). Wilson and Schreiber (1986) concluded that new convective storms are likely to form within 0-20 km of a moving boundary, 15 km of a stationary boundary and 5 km from colliding boundaries. Overall, cold pools play an important role in organizing and maintaining deep moist convection and are an integral part of MCSs (Thorpe *et al.* 1982; Rotunno *et al.* 1988; Fovell and Ogura 1989; Szeto and Cho 1994a, b).

Cold pools produced by MCSs are however important for a number of other reasons as well. They can influence future convective evolution

through their thermodynamic effects (e.g., Zipser 1977; Tompkins, 2001; Taylor *et al.* 2007) by providing boundaries that can lead to local convergence and penetration of CIN. Cold pools also transport substantial amounts of cold air northwards, ventilating the Saharan Heat Low by advection (Marsham *et al.* 2013; Garcia-Carreras *et al.* 2013). They are responsible for around 50% of summertime dust uplift in the Sahel & Sahara (Knippertz *et al.*, 2007; Marsham *et al.* 2008a,b; Marsham *et al.* 2011b; Knippertz and Todd, 2012; Heinold *et al.* 2013; Marsham *et al.* 2013b) due to intense rain and strong winds being associated with them.

### ***Cold pool properties as observed by Engerer et al. (2008)***

Perhaps the largest observational study of cold pool properties to date is based in the USA over Oklahoma and was performed by Engerer *et al.* (2008; hereafter E2008). Their study investigated 39 squall line MCSs by using data from 110 mesonet stations across the state of Oklahoma and obtained 1389 time series of cold pool related variables. The cold pool quantities studied by E2008 were decreases in potential and equivalent potential temperature, pressure rises, changes in wind direction and maximum wind gusts. The focus of their study was on the evolution of cold pool properties during five life-cycle stages of MCSs (given as first storms, MCS initiation, mature MCS, and MCS dissipation) as well as comparison of the observed cold pool characteristics with idealised model simulations.

The major findings of E2008 include the identification of the greatest decrease in surface potential temperature for the initial “first storms” stage of the MCSs while at later stages in the lifecycle, lower decreases of potential temperature were observed. The mean potential temperature decrease for the “first storms” stage was calculated to be 9.8 K with a reduction in the mean decrease by about 1 K for each subsequent life cycle stage down to 5.6 K for the “MCS dissipation” stage. E2008 attributed much of this decrease to the average timing of each life-cycle stage as “first storms” tend occur in late afternoon local time, the systems tend to mature before midnight and dissipate after midnight, which means that environmental temperature (potential temperature) decreases as the system ages. It was found by E2008 that environmental temperature decreases on average by 8 K while that of the cold pool only by 2 K throughout the life-cycles of the systems. This shows that cold pools are less susceptible to diurnal temperature variations than the environment. Cold pools are not affected as much by radiation due to extensive cloud amounts associated with the parent MCSs, but it is affected by the downdraught, the temperature of which depends on mid-level temperature and dryness, whereas the

environment is affected by sensible heat flux (solar radiation and irradiation to space). E2008 also found that equivalent potential temperature is reduced by cold-pool passages and the magnitude of the reduction also decreased as the MCSs aged. For the first storms, the mean reduction was 21.6 K while at dissipation it was found to be only 13.9 K.

In addition to the cold-pool related temperature decrease getting smaller as the systems age, E2008 found that the related magnitude of the pressure increase was rising as MCSs age. E2008 concluded that if the cold-pool related pressure rise is due to hydrostatic equilibrium, the depth of the cold pools must be increasing as the MCSs age and grow upscale. This may however be biased as the temperature reduction could be masked at the surface later at night by the presence of a stable surface layer, which may not get completely eroded by the cold pool. Typical values of cold pool depth as estimated by E2008 were found to vary between ~300 metres for the shallowest cold pools and up to more than 3 km for the deepest ones. The greatest mean maximum wind gusts occurred during the mature stage while the weakest during the dissipation stage with the mean maximum wind gusts being over  $15 \text{ m s}^{-1}$  for all the life-cycle stages. Regarding the propagation speed of cold pools, it varied between  $\sim 0.5 \text{ m s}^{-1}$  and  $\sim 13 \text{ m s}^{-1}$ .

E2008 compared the observed cold pool characteristics with those of an idealised model simulation and found that real cold pools were colder than those represented by the model. E2008 varied the microphysics scheme and compared the outputs. Simulations that did not use ice processes had warmer/less representative cold pools than those that used ice processes. The average reduction of equivalent potential temperature for simulations that did not use ice processes was found to be only 8.2 K. Both of the ice and no ice simulations created on average warmer and moister cold pools than what was observed in reality during E2008's study. It was suggested by E2008 that the temperature discrepancy could be caused by the fact that most models have their lowest level 200 m above ground where temperature differences associated with cold pools are less prominent.

### ***Gravity waves and bores and their role in MCS organization***

Gravity waves and bores can be created by the updraft or by the cold pool/gravity current and then spread away from the storm along some form of a waveguide, e.g. a stable nocturnal boundary layer (e.g. Crook and Miller, 1985; Rottman and Simpson, 1989; Knupp, 2006; Bretherton and

Smolarkiewicz, 1989). Best conditions for such gravity-wave production is when small-amplitude waves spread at a faster speed along the low-level nocturnal inversion than the speed of the cold pool (Haase and Smith, 1989a, b). Such gravity waves can either suppress or enhance further initiation (Mapes, 1993; Liu and Moncrieff, 2004) and are often responsible for secondary storm initiation (Birch *et al.*, 2013). Williams and Renno, (1993) have analysed tropical thermodynamic soundings and have shown that much of tropical atmosphere is conditionally unstable. Therefore, only a small vertical displacement of the airmass by a gravity wave or a cold pool can easily initiate secondary convection. This can be distant from the primary MCS as gravity waves can propagate over great distances, especially in the tropics where the effect of the Coriolis force is reduced (Liu and Moncrieff, 2004). The secondary initiated convection is initially organized by the gravity wave, but eventually forms its cold pools, which generally become the most important factor in further organization (Stensrud and Fritsch, (1993, 1994a, b); Anabor *et al.*, 2009).

#### ***Wind shear and its role in MCS organization (RKW and TMM theories)***

Vertical wind shear intensity ( $\Delta U$ ) is important for the organisation and sustaining of MCS, especially in case of squall-lines (Barnes and Sieckman, 1984). There are various theories that relate and compare the importance of vertical wind shear at different levels of troposphere to the organization of convection. The interaction of wind-shear produced vorticity with that produced by a cold pool (C) is generally agreed to be favourable. Several studies have investigated the interaction of a cold pool and its environment (e.g. Benjamin, 1968), but in a non-sheared environment. A set of simulation studies on the dynamics of cold pools and their interaction with environmental wind shear was performed by Weisman and Klemp, (1984), Rotunno, *et al.* (1988), and Weisman *et al.* (1988), which has been further broadened again by Weisman and Rotunno, (2004) and Weisman and Rotunno, (2005).

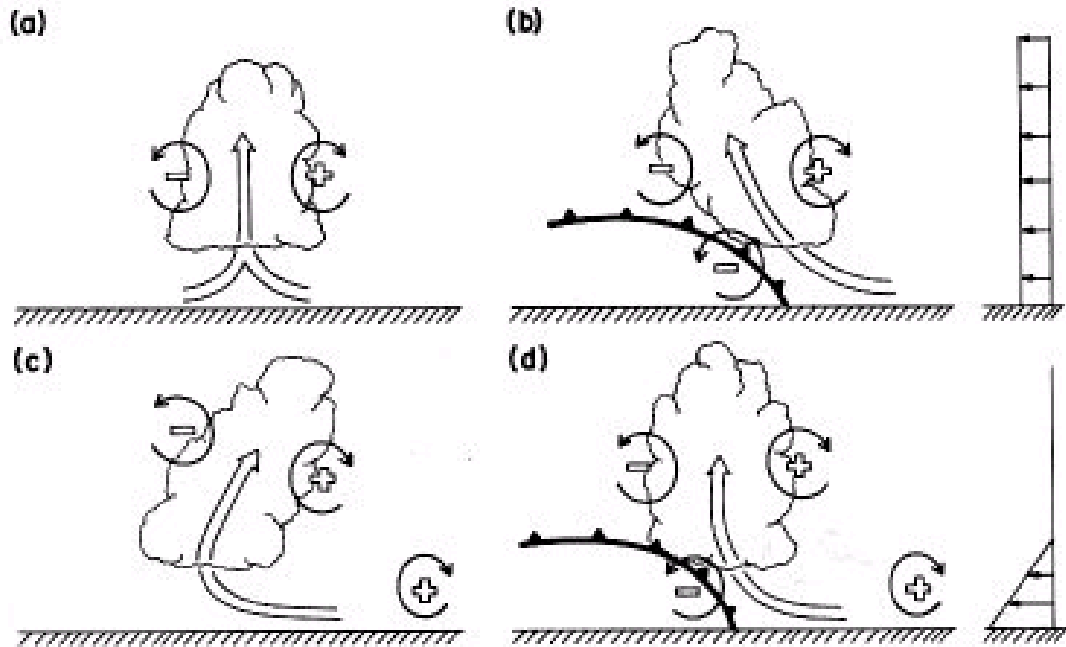


**Figure 1.4:** An illustration of balances of the positive and negative vorticity produced by the ambient shear and the cold pool, respectively. a) A buoyant parcel with no shear or cold pool creates equal magnitudes of positive and negative vorticity. b) If the negative vorticity produced by the cold pool is greater than the shear produced positive one, the updraft leans backwards. c) If the positive vorticity produced by ambient shear is stronger, the updraft leans forwards. d) If both the negative and positive vorticity are in balance, the updraft is up-right and the MCS is sustained. (Figure from Rotunno et al., 1988)

Based on their theoretical and modelling results, a new theory (“RKW”, or “Rotunno Klemp Weisman theory”) was developed (Weisman and Klemp, 1984; Rotunno, et al., 1988; Weisman et al., 1988). In summary, cold pool interacts with the component of the ambient wind shear (Figure 1.4), the vector of which is normal to the squall-line orientation. The relative strengths of the shear and cold pool are important in maintaining the squall-line as well as in determining how organized and long-lived the squall-line will be. If there is no cold pool or shear, convective cells are upright (Figure 1.4 a)), but their precipitation eventually cuts off their updraft. If a cold pool is present with no shear, or the shear is much weaker, the negative vorticity produced by the cold pool causes the squall-line to lean up-shear (backwards) (Figure 1.4 b)). On the other hand, if wind shear is present without a cold pool (or cold pool is much weaker), the positive vorticity of the wind shear leads to down-shear tilt of the squall-line (Figure 1.4 c)). Either of these cases eventually leads to weakening or dissipation of the squall-line. If both wind shear and cold pool are present and resulting vorticities

approximately balance each other, then the convective cells are oriented upright and this is called “the optimal state” of a squall line in RKW (Figure 1.4 d)).

In the optimal state, the squall-line MCS is maintained for a long time as long as CAPE is available with strongest updraft velocities and greatest condensation (Weisman *et al.* 1988; Weisman *et al.* 2004; Bryan and Parker 2006). In fact, Weisman (1992) has shown a model of how a typical squall-line may transit between these stages throughout its lifecycle. Initially, there is no cold-pool and hence down-shear oriented system is formed (Figure 1.4 c)). When a cold pool forms and strengthens, the “optimal state” is eventually reached (Figure 1.4 d)) and if the cold-pool intensity outgrows that of the shear, the system becomes up-shear oriented and weakens (Figure 1.4 b)). While the “optimal state” is the most favourable state for intensification of squall-lines and their maintenance, it is not a requirement for a squall-line to be sustained (Fovell and Ogura, 1989).

There is, however, a large debate about the validity of the RKW theory and several authors have found results contradicting it. An example is Stensrud *et al.* (2005), who found that not all properties of the squall-line were maximised when vorticities related to the cold pool (C) and the wind shear ( $\Delta U$ ) were approximately equal. In their simulations, rainfall intensity was maximised at  $C/\Delta U$  of approximately 0.5 while surface winds associated with squall-lines were maximised at  $C/\Delta U$  of approximately 1.8. Bryan *et al.* (2006), however, concluded that the simulations used to form the basis of RKW theory were run using a model where issues with vertical diffusion scheme near the surface were identified, hence overestimating C, but that the actual theory is still valid.

Another important theory for squall-line organization is the precursor to RKW, the TMM theory (Thorpe, *et al.*, 1982). TMM adds more importance to the shear at mid-levels and deep cold pool production. Based on the TMM theory, the low-level inflow is also important, but not due to providing positive vorticity that balances the cold pool vorticity, but because it opposes the cold pool, slows it down and prevents it from spreading too far away from the storm system. Lafore, *et al.*, (1990) also suggests that the balance of low-level shear and cold pool vorticity is not the most important factor and that the baroclinic vorticity along the edge of the cold pool is not significant and propagates towards the rear of the system along the top of the cold pool.

### **Bookend vortices and their role in MCS organization**

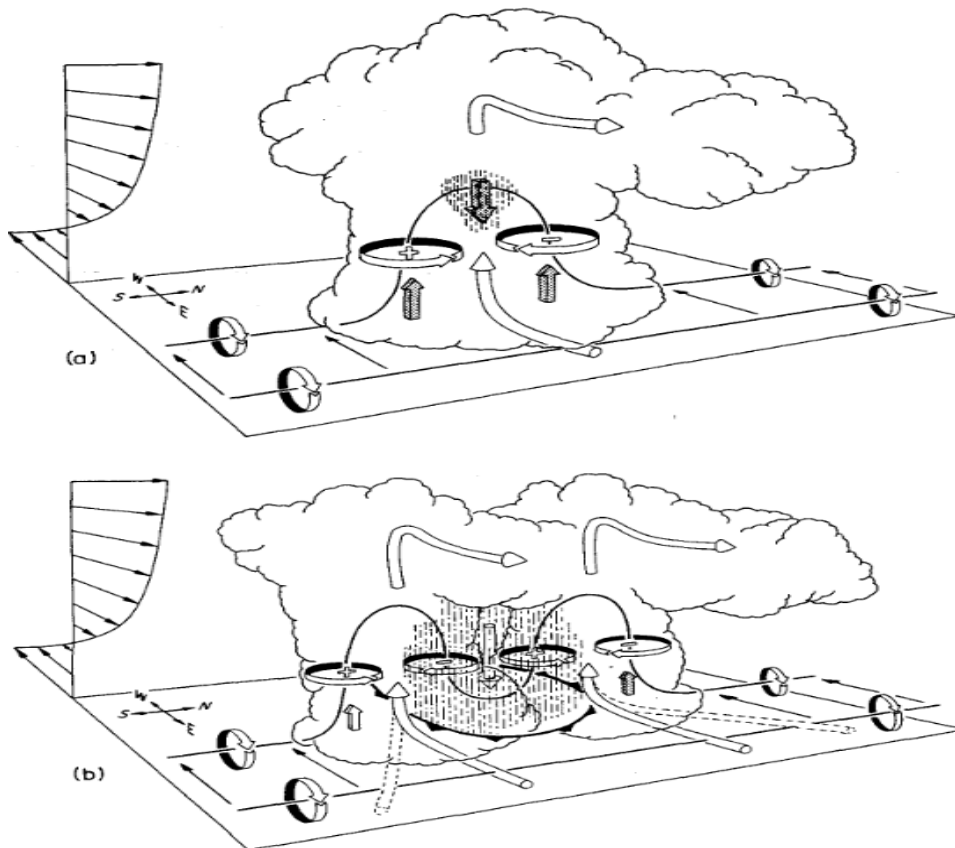


**Figure 1.5:** Schematic depicting how a typical vortex tube (horizontal vorticity) contained within (westerly) environmental shear is deformed as it interacts with a convective cell (viewed from the southeast). Cylindrical arrows show the direction of cloud-relative airflow, and heavy solid lines represent vortex lines with the sense of rotation indicated by circular arrows. Shaded arrows represent the forcing influences that promote new updraft and downdraft growth. Vertical dashed lines denote regions of precipitation. (a) Initial stage: vortex tube loops in the vertical as it is swept into the updraft. (b) Splitting stage: downdraft forming between the splitting updraft cells tilts vortex tubes downward, producing two vortex pairs. The barbed line at the surface marks the boundary of the cold air spreading out beneath the storm (from Klemp, 1987).

Many squall-line MCSs feature bowing segments (described as “bow echoes”), which are typically associated with long swathes of severe wind gusts. These bowing segments are nearly always associated with regions of opposing vorticity on their northern and southern ends, being described as “bookend vortices”. Weisman (1993) identified such bookend vortices in a simulation study of severe long-lived bow echoes and described their genesis and role in the simulation. Bookend vortices are generally

formed by tilting and stretching of environmental wind-shear produced vorticity. Such vorticity is initially ingested into a forming updraft and forms a couplet of oppositely oriented vorticity within the updraft (Figure 1.5 a)). When a downdraft begins to form, a splitting of the initial cell occurs (Figure 1.5 b)), where both splitting cells contain regions of opposing vorticity in their updrafts and downdrafts. The forming cold pool spreads ahead of the splitting cells, eventually forcing a line of convective cells to be formed along its length. A squall-line MCS eventually evolves. The vorticity couplet within the updrafts dissolves and weakens due to the linear updraft organization while the vorticity within the downdraft expands in size while its magnitude is preserved. This vorticity eventually evolves into the vortex pair of the “bookend vortices”. Weisman (1993) also investigated the role of baroclinic vorticity creation along parcel trajectories, but concluded that the role of environmental-shear produced vorticity being ingested, tilted and stretched by the MCS is significantly more important. Bookend vortices play an important role in the dynamics of squall-line MCSs as they focus and enhance the Rear Inflow Jet along their axis of symmetry, which enhances dynamically forced convection on the leading edge of the line and helps to sustain the bow echo.

### ***Types of Sahelian Mesoscale Convective Systems***

Mesoscale Convective Systems can be separated into several groups based on their size and organization. MCSs are typically characterized by a convective region, often organized linearly along some form of convergence, and a stratiform region. The location of the stratiform region with respect to the convective region can differ. It can trail the convective region, be parallel to it or it can lead it (Parker and Johnson 2000). Under certain conditions, MCSs grow into larger, longer lasting and slower propagating Mesoscale Convective Complexes (MCCs), which usually result in more precipitation per event. Machado *et al.* 1998, or Mathon and Laurent (2001) concluded that the lifetime of MCSs is proportional to their size. The first numerical criteria that could be used to distinguish different types of MCSs from satellite observations were given by Maddox (1980), who initially separated these into Mesoscale Convective Complexes (MCCs) and regular MCSs based on their size where MCCs had larger area of cloud top temperature below a certain value (based on satellite observations) than MCSs. This was however not very applicable to distinguish different characteristics of MCSs in the Sahel as MCCs

contribute to only about 15 % of cloud cover there and the fraction of MCCs to all MCSs is very small (Mathon and Laurent, 2001). Therefore, new criteria were given by Mathon, *et al.*, (2002) in order to define another subset of MCSs, one which produces the majority of rainfall in the Sahel. These were named Organized Convective Systems (OCSs) or squall-line MCSs and were distinguished from other MCSs by a cluster of cloudiness at a temperature of 213 K or less that persists for at least three hours and moves at an average speed of at least  $10 \text{ m s}^{-1}$ . These squall-line MCSs (OCSs) feature organized updrafts and downdrafts over a large area and were found to be one of the most efficient rain-productive systems. In their study, Mathon *et al.*, (2002) found that squall-lines account for 78% of cloud cover of all the MCSs, but represent only 12% of the total number of all MCSs. On average, MCSs in West Africa have an area ranging between  $2 \times 10^5$  and  $3 \times 10^5 \text{ km}^2$  (Laing and Fritsch, 1993).

When MCCs and OCSs were compared by Mathon, *et al.*, (2002), the average rain production was found to be 19 mm and 14.7 mm, respectively. However, there were only 3 MCCs and 19 OCSs on average per rainy season, which shows that OCSs (squall-line MCSs) are not as rain efficient as MCCs. The infrequency of MCCs however makes them accountable only for 16% of the yearly rainfall on average while OCSs (squall-line MCSs) were estimated to be responsible for 91% of the yearly rainfall near Niamey. It was concluded by Mathon *et al.* (2002) that while the intensity of all the MCSs is largely variable, they are fast-moving and hence don't affect one region for an extended period of time. Therefore, the yearly rainfall in West Africa at a specific location is more sensitive to the yearly frequency of MCSs rather than to their intensity.

### ***African Easterly Waves, the African Easterly Jet and MCSs***

African Easterly Waves are oscillations within the African Easterly Jet, forming perturbations in potential vorticity (Reed *et al.* 1977) and originating from localised forcing (Thorncroft *et al.* 2008). They are one of the most important synoptic scale variations that are often related to deep moist convection and MCSs (Kiladis *et al.* 2006). African Easterly Waves can generate new convection (Fink, *et al.*, 2006), interact with existing MCSs or modulate their organization (Payne and McGarry, 1977; Fink and Reiner, 2003; Lavaysse, *et al.*, 2006). They form due to barotropic instability produced by meridional and low-level vertical thermal gradients driven by the Saharan Heat Low (Burpee, 1972; Reed *et al.*, 1977; Thorncroft, 1995) as

well as vorticity and thermal gradients associated with the African Easterly Jet (e.g. Burpee, 1972). African Easterly Waves are important even outside of West Africa as they are known to initiate tropical cyclones (hurricanes) downstream (Thorncroft and Hodges, 2001; Chronis *et al.* 2007; Chen, *et al.*, 2008).

Several more or less complex models describe the structure of African Easterly Waves. Three sources are dominating our knowledge of these – the GATE data (Reed *et al.* 1977), analyses from numerical simulations (Diedhiou *et al.* 1999) and theoretical models (e.g. Thorncroft and Hoskins, 1994a, b). Reed *et al.*, (1977) and Payne and McGarry (1977), show a model of African Easterly Waves being an oscillating set of troughs and ridges along the African Easterly Jet, which affect convection by their relative positive or negative vorticity advection. Based on Reed *et al.*, (1977), African Easterly Waves originate west of 20 °E, propagate westwards at a mean phase speed of 6-8 m s<sup>-1</sup> and slow down to ~5 m s<sup>-1</sup> upon reaching the Atlantic. They have a mean wavelength of 2000-4000 km and occur with a period of about 3-5 days (see also Burpee, 1972; Thorncroft and Hodges, 2001; Lavaysse *et al.*, 2006; Hsieh and Cook, 2005). Bain, *et al.*, (2011) suggested a more complex model analysing horizontal variations in potential temperature and moisture resembling that of fronts in extra-tropical systems and suggest that future research into the internal structure of African Easterly Waves is needed in order to improve our understanding of their influence on deep moist convection.

Since the frequencies of the passages of MCSs and African Easterly Waves are similar (about 2-5 days) it was hypothesized that there could be a relation between them. Several studies focus on the relationship between African Easterly Waves and MCSs, such as the location and motion of MCSs with respect to African Easterly Waves. Fink and Reiner (2003) showed that most MCSs in Niamey occurred on the western side of the westward propagating African Easterly Wave, where northerly flow organized them by providing wind shear (Peters and Tetzlaff, 1988). The initiation of MCSs is however generally observed in the tail (eastern) side of the African Easterly Wave or in the ridge behind, which is believed to be due to southerly flow on the rear of the wave advecting moist airmass at low levels (Schrage, 2006). Other studies, such as Barnes and Sieckman, (1984) or Duvel, (1990) concluded that the position of MCSs relative to the African Easterly Wave depends on the relative speed of propagation of convection with respect to the African Easterly Wave. Studies from different

parts of the world that are affected by tropical easterly waves (similar to African Easterly Waves) suggest that maximum in tropical convection and rainfall is maximised ahead of the trough (e.g. Petersen, *et al.*, (2003) for east tropical Pacific).

There have been many other studies trying to understand the importance of the relationship of African Easterly Waves and MCSs in West Africa. In all studies below, African Easterly Waves have been tracked using ECMWF reanalysis data and MCSs have been identified in passive microwave rain rate retrievals. African Easterly Waves are known to initiate MCSs, particularly over the West African coast and most often in August and September (Fink and Reiner, 2003). Payne and McGarry, (1976) studied the phase relation of the African Easterly Waves to MCSs and their position with respect to troughs and ridges by studying 160 MCSs at 3h intervals. Their results have shown that convective cloud was most prominent ahead and at the troughs axis with a great reduction at and ahead of the ridge axis. Most of the convective cloud (MCSs) travelled through less than one half of the wavelength of the whole African Easterly Wave, which was also concluded by Reed *et al.* (1988). Also, Payne and McGarry, (1977) show that there was some convection distributed throughout the whole wave, some of which was well to the north of the centre of the wave in the negative vorticity regime, which well agrees with the findings of Ferreira and Rickenbach, (2009) or Guy and Rutledge, (2011). In general, squall-line MCSs propagate at a speed of  $\sim 16 \text{ m s}^{-1}$  (Peters and Tetzlaff, 1988), which is nearly twice as fast than both the wind speeds in the African Easterly Jet and the phase speed of the African Easterly Wave. At such speed, squall-line MCSs move westwards relative to the wave, propagating into the ridge ahead of it before dissipating.

In their study, Ferreira and Rickenbach, (2009) concluded that there are 2 preferential tracks for the African Easterly Waves, one near  $15^\circ \text{N}$  (northern AEWs) and one to the south near  $\sim 5^\circ \text{N}$  (southern AEWs). The southern AEWs were found to have a period of 6-9 days and were more active later in the monsoon season (August-September). Ferreira and Rickenbach, (2009) concluded that there are structural differences of the MCSs related to northern or southern AEWs. The main of these was the ratio of the leading edge convective to the trailing stratiform homogeneously distributed rainfall. While the difference in the mean total rainfall was not statistically significant, the systems occurring in the positive vorticity regime associated with northern AEW had a significantly greater percentage of

rainfall produced by the trailing stratiform rain as opposed to the ones associated with southern AEWs that produced more convective rain. This was attributed to the mean pre-storm CAPE, the magnitude of which was slightly over  $1000 \text{ J kg}^{-1}$  for northern AEWs while it was almost  $2000 \text{ J kg}^{-1}$  before the MCSs associated with southern AEWs. Using satellite data from a 13-year period of TRMM, Guy and Rutledge, (2011) also concluded that MCSs associated with northern AEWs have larger areas/fractions of rainfall associated with the stratiform region of the MCS (based on surface observations from Niamey, Niger) and that there are differences in microphysics (ice and water liquid mass). Guy *et al.*, 2011 concluded that African Easterly Wave- related MCSs have structural and durational differences from non-African Easterly Wave-related MCSs, mainly in the form of greater convective and stratiform rainfall activity. There are several hypotheses that increased solar heating due to fewer clouds in the negative relative vorticity regime over Niamey present during southern AEWs would be responsible for the higher pre-storm CAPE. On the other hand, positive relative vorticity regimes in Niamey associated with northern AEWs were more favourable for stratiform rainfall production due to moister atmosphere and greater large scale forcing. Several studies (e.g. Mounier *et al.*, 2008) suggest that most years have one preferred track of African Easterly Waves while only a few have almost equal number of northern and southern AEWs.

MCSs were found to create positive feedbacks on the African Easterly Waves (Cornforth *et al.* 2009). They are associated with vertical transports of momentum (Moncrieff, 1992), moisture and heat (Lafore *et al.*, 1998). They also produce vorticity, which can have a positive feedback on the African Easterly Wave and reinforce cyclonic rotation (Barthe, *et al.*, 2010). Berry and Thorncroft (2005) presented a case study, where an African Easterly Wave was likely triggered by a MCS and this wave then triggered further new MCSs during its propagation over West Africa. The overall interaction between MCSs and African Easterly Waves, however, is complicated as there are various processes involved and understanding them individually as well as their interactions presents a great challenge (Redelsperger *et al.*, 2002a; Peyrille *et al.*, 2007a, b).

### **1.2.3 Simulations of MCSs in the West African Monsoon**

As already mentioned in section 1.1.1., the representation of deep moist convection in the simulations of West African Monsoon is currently a great challenge for models. (Thorncroft *et al.*, 2003; Augusti-Panareda *et al.*, 2010). Deep moist convection is often parameterised in the simulations, which leads to incorrect representation of many properties of convection and MCSs. Atmospheric models involving convective parameterization generally struggle to simulate the diurnal precipitation cycle correctly, with the over land peak generally occurring around local noon, being in phase with the diurnal cycle in CAPE. In addition, parameterizations tend to produce the rainfall too light over a great area rather than isolated intense convective rain events (Dirmeyer *et al.*, 2012).

The convective parameterisation scheme used in global circulation models often uses low-level convergence (Tiedtke, 1989) as a parameter to simulate convection and related precipitation. Most convective parameterization schemes use CAPE closure approximation and the phase difference between CAPE and convective precipitation is important in accurate timing of convective rainfall (Tompkins, 2001; Adams and Souza, 2009). There is however a lack of understanding of the processes related to CAPE (Folkins *et al.* 2014) and the peak in simulated precipitation is often several hours early when compared to observations (Yang and Slingo, 2001; Neale and Slingo, 2003; Dai and Trenberth, 2004). In the last several years, there has been a large effort to improve convective parameterization schemes with the transition from shallow convection to deep convection was identified as the most important factor in the diurnal cycle (Hohenegger and Stevens, 2013). Entrainment of dry-air into the convective plume is a very important process in reducing the buoyancy of such a plume and one that can delay the onset of convection, hence being important in the diurnal cycle of convective precipitation (Bechtold *et al.* 2004; Derbyshire *et al.* 2004). Simulations representing entrainment correctly also featured more realistic values of CAPE and related strength of modelled convection (Zhang, 2009). Correct representation of convective organization is another feature, which has positive effects on simulated diurnal cycle of convection, as it also delays convective rainfall over land (Folkins *et al.*, 2014).

A specific set of simulations for West Africa for the period of the West African Monsoon of 2006, when AMMA IOP took place, has been run as part of the *Cascade* project. These simulations were using the UK Met Office Unified Model (UM) and were run as convection permitting, initially for a 40-day period (25<sup>th</sup> July – 4<sup>th</sup> September), this being extended to a 120-

day period covering the months of June, July, August and most of September 2006 at horizontal resolutions of 1.5, 4 and 12 km (Pearson *et al.* 2010). The 12 km horizontal resolution was too large to resolve individual convective clouds or cold pools correctly, but was good enough to resolve larger MCSs and squall-lines. Features such as rainfall rates and the circulations were usually over predicted while the cold pools were too weak and developed slowly (Marsham *et al.* 2011). The runs used a standard MetUM setup (Lean *et al.* 2008). In addition, parameterised deep convection runs at horizontal resolutions of 12 and 40 km were performed.

## Chapter 2

### Methods

#### 2.1 Observational datasets

Deep moist convection and processes controlling its initiation and evolution have been investigated by using both observational datasets as well as a simulation performed by a convection-permitting Unified Model (*Cascade* project). Here we describe datasets used throughout this thesis, with methods specific to Chapters 3 to 5 given in each Chapter.



**Figure 2.1:** Map of West Africa showing the location of AMMA Niamey supersite, located at Niamey International Airport, Niamey, Niger, where all observational data used in this thesis were recorded. (© Google maps).

Niamey was one of the supersites during the AMMA Intensive Observing Period (IOP) in 2006 when a second deployment of ARM (Atmospheric Radiation Measurement) mobile facility was implemented at the Niger Meteorological Office at Niamey International Airport. The ARM facility consisted of both direct and remote sensing instruments. A meteorological surface station was recording surface conditions. Remotely sensed data included a C-Band Doppler Radar, Radar Wind Profiler,

Radiometer, as well as vertically pointing radars/lidars (these were not used for the purpose of this thesis). All observational data used in this study has been obtained at the AMMA Niamey supersite (Figure 2.1).

### **MIT Doppler radar**

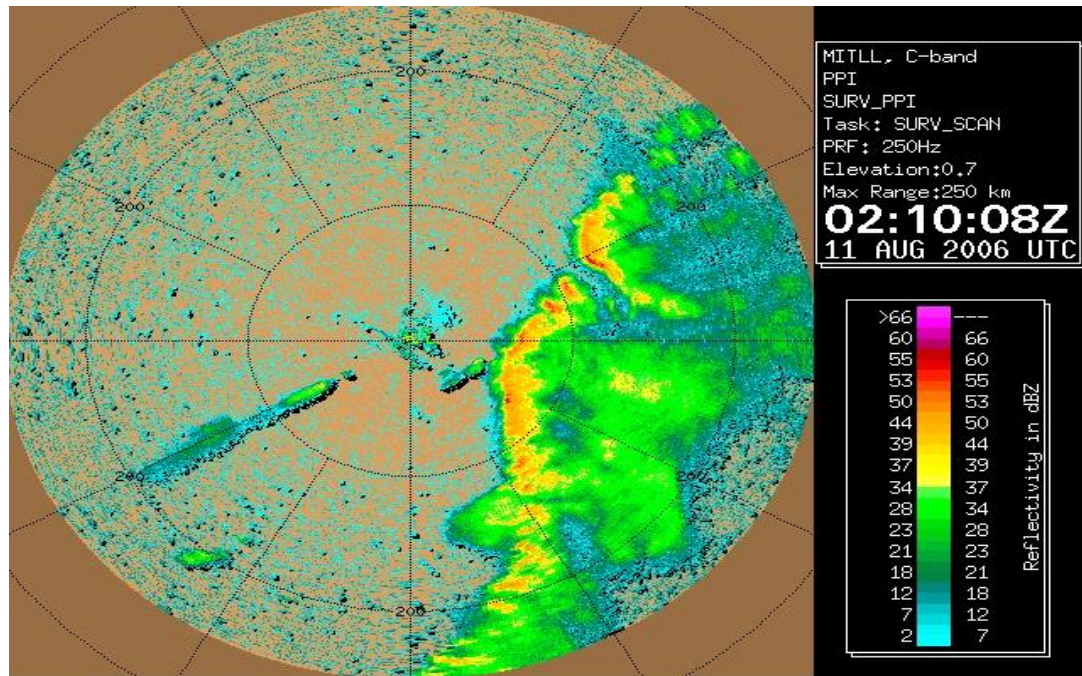


**Figure 2.2:** An example of an MIT radar long range survey reflectivity at 02:10:08Z on 11<sup>th</sup> August 2006. This is a single elevation scan performed at an elevation of 0.7°. An approaching squall-line can be seen east of the radar. The echo to the southwest of the radar site is a phantom line created by reflection from a large aircraft hangar.

The MIT WR-73 C-Band ( $\lambda = 5.30$  cm) ARM Precipitation Doppler radar is a Doppler weather Radar, owned by Massachusetts Institute of Technology and operated by the Weather Radar Laboratory (Russel *et al.*, 2010). This radar was deployed near Niamey, Niger (13.4915° N, 2.1698° E, 224 m latitude) (Chong, 2010) during AMMA. Scans were recorded at 10-minute intervals during the AMMA Radar Observing Period (AMMA ROP), which ran from 5<sup>th</sup> July until 27<sup>th</sup> September 2006. During the ROP a total of over 11,250 volumes was recorded (Rickenbach *et al.* 2009). The radar scanning strategy included a 360° long-range survey at lowest elevation angle of 0.7° and maximum recorded range of 250 km, three-dimensional volume scan composed of 15 elevation angles out to 150 km horizontal radius and occasional RHI scans. The resolution of the radial distance along

the beam is 1.5 km with angular resolution of  $2^\circ$  and variable vertical resolution. In this thesis, radar reflectivity has been used primarily for the purpose of identification of various regions within MCSs with rainfall rate obtained from surface station.

The radar is an active remote sensing instrument, emitting a pulse of radiation and analysing the return from precipitation-forming particles (e.g. droplets) suspended in the air. The radar outputs reflectivity, which is proportional to  $R^6$ , where  $R$  is radius of the particles and the reflectivity can be related to precipitation intensity. In addition, the Doppler radar is able to compute the component of velocity of droplets along the scanning radial based on the Doppler Shift of the returned radio wave (this was not used in this study). More details regarding this radar can be found in Russell *et al.*, 2010.

The MIT radar has also been used during previous studies. This includes the radar operating on board the R/V Gilliss during the Global Atlantic Tropical Experiment (GATE) (see Geotis, 1978), during International Winter Monsoon Experiment (WMONEX) (see Houze Jr *et al.* 1981), Down Under Doppler and Electricity Experiment (DUNDEE) (see Rutledge, *et al.*, 1992), Tropical Ocean Global Atmospheres/Coupled Ocean Atmosphere Response Experiment (TOGA COARE) (see Rickenbach and Rutledge, 1998) and in Pan-American Climate Study (Yuter and Houze, 2000). An example of an MIT radar image at an elevation of  $0.7^\circ$  can be seen in Figure 2.1. This shows radar reflectivity of an approaching squall-line to the east of the radar. Radar reflectivity, which is proportional to precipitation intensity, shows heavy precipitation being detected along linear segments on the front side of the squall-line. This is followed by moderate precipitation further east.

### ***ARM Mobile Facility surface meteorological station***

The ARM (Atmospheric Research Measurement) Climate Research Mobile Facility (Ackerman and Stokes, 2003) was deployed at Niamey airport at the same location (within hundreds of meters) as the MIT radar, and provided one-minute-resolution surface meteorological data. The data used for the purpose of this study consist of 1 m pressure (resolution of 0.1 hPa with an accuracy of 0.15 hPa), 2 m temperature (resolution of 0.001  $^\circ\text{C}$  and accuracy of 0.115  $^\circ\text{C}$ ), surface rainfall (resolution of 0.01  $\text{mmhr}^{-1}$  and accuracy of 0.05  $\text{mmhr}^{-1}$ ), 2 m moisture (resolution of 0.1% and accuracy of 0.155%), 3 m wind speed and direction (resolution of 0.001  $\text{ms}^{-1}$  with an

accuracy for wind speed of  $0.135 \text{ ms}^{-1}$  or 3%, whichever is greater, and for wind-direction of  $0.2^\circ$ ), and visibility at 2 m (resolution of 1 m and accuracy of 1 m or 4% of the distance, whichever is greater) (all accuracies and resolutions obtained from “ARM Surface Meteorology Systems Handbook”). All data were averaged at 1 minute intervals, except pressure and visibility, where readings were taken every minute. These were available for the duration of the whole AMMA SOP and grant key information at a single point regarding surface conditions in the vicinity of MCSs.

### ***Radiosoundings***

For the duration of the AMMA SOP, radiosondes were released from Niamey airport (13.4915° N, 2.1698° E, 224 m altitude) every day at 00:00, 06:00, 12:00 and 18:00 UTC. Two types of radiosondes were released, the Vaisala RS80A and the Vaisala RS92. Generally (but not as a rule), the RS92 radiosondes were used for the 00:00, 06:00, 12:00 and 18:00 UTC releases, where a radiosonde was released between 15 and 30 minutes prior to the given time (e.g. a 12:00 UTC radiosonde was released at ~11:40 UTC). Some days (21<sup>st</sup> – 30<sup>th</sup> June and 1<sup>st</sup> – 15<sup>th</sup> August) had additional radiosonde releases at 03:00, 09:00, 15:00 and 21:00 UTC. At these times, the RS80A radiosondes were normally used, but again, there were several exceptions to this. There were also days when radiosonde releases were missing. The radiosonde ascents provide vertical profiles with approximately 10 m vertical resolution of pressure, temperature, dew point temperature, relative humidity, wind-speed and wind-direction. Biases in dew-point temperature and relative humidity data have been identified in soundings provided by both RS92 and RS80A radiosondes. These were in the form of overestimation or underestimation of moisture, which was related to the sensor being affected by solar radiation (Agusti-Panareda *et al.*, 2009).

A number of studies have used the ARM data and the MIT radar in the past. Slingo *et al.* (2008) used ARM data together with satellite data obtained as part of the RADAGAST experiment to study seasonal changes in surface variables and precipitation. Kollias *et al.* (2009) studied the seasonal behaviour of precipitation in response to changes in surface variables and the atmospheric profile by the use of ARM surface data and radiosondes. Lothon *et al.* (2011) used the MIT radar together with surface data to analyse a gust front produced by a locally initiated small-scale thunderstorm complex. Giangrande *et al.* 2012 used the MIT radar as well as radiosondes from Niamey (in addition to other supersites elsewhere in the

world) to study vertical air motions and microphysical properties of precipitation producing systems.

### ***Radiometer***

During AMMA a vertically pointing radiometer was installed at the location of the surface station in Niamey, providing continuous retrievals of the vertical distributions of temperature, water vapor, and cloud liquid water from the ground up to 10 km for all non-precipitating conditions. The advantage of the radiometer over radiosondes is its continuous (time step of 1 minute) and instantaneous retrieval of the atmospheric profile. The disadvantage compared to radiosondes is poorer vertical resolution with 50 vertical layers ranging in thickness from ~100 m near the ground to approximately 1000 m near the top of the troposphere. In addition, radiometer can be attenuated in conditions of heavy precipitation and due to these disadvantages, it was generally used as a supplementary data source compared to radiosondes or to avoid biases, which were present in radiosonde data.

## **2.2 Met-Office Unified Model convection-permitting simulations from the Cascade project**

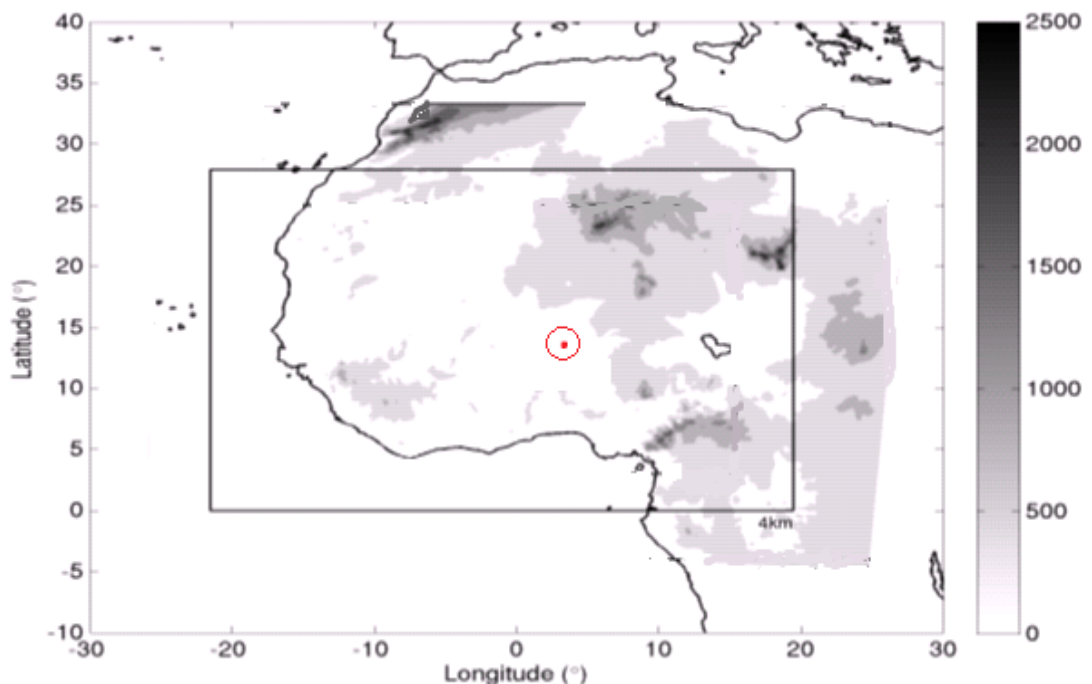


**Figure 2.3:** Map of the domain for the 4 km convection-permitting UM model run (rectangle). Red dot represents the location of Niamey with the red circle representing the maximum (250 km) range of the MIT radar.

The Met-Office Unified Model (UM) (Walters *et al.*, 2011) is a fully coupled ocean-atmosphere numerical model, and can be used for global as well as regional domains (Davies *et al.*, 2005; Staniforth *et al.*, 2006). UM simulations were performed as part of the *Cascade* project for 144 days starting on 1<sup>st</sup> June 2006, with diagnostics output at hourly intervals. The *Cascade* model domain is centred on West Africa and also covers parts of the adjoining oceans (Figure 2.3), using rotated coordinate system with the north pole at 79° N 180° W (Davies *et al.*, 2005). The results of Pearson *et al.*, 2010, show that diurnal timing as well as the organization of convection is best performed by the 4 km convection-permitting model. For this reason, the 4km model output was used for the purpose of analysis in this study.

The framework for the 4 km simulation domain was carried out with the version 7.1 of the UK Met Office Unified Model (UM) (Marsham *et al.* 2011). The simulations are ‘convection-permitting’, which means that the convective parameterisation is switched off or that the closure time scale of the parametrized convection is increased for high CAPE (Birch *et al.* 2014). It has 70 vertical levels with the lowest level at 2.5 m, with vertical grid spacing of approximately 300 m at a height of 1 km and 900 m at a height of 10 km. The 4 km domain is forced at the boundaries by an outer 12 km domain. The 4 km domain is based on high-resolution configurations, which was originally developed for the United Kingdom by Lean *et al.* (2008). The 12 km domain has 38 levels, is forced at the boundaries by European Centre for Medium-range Weather Forecast (ECMWF) analyses and employs the standard UM convective bulk-plume parameterisation scheme with a CAPE closure (Gregory and Rowntree, 1990). The 4 km simulation features three component cloud microphysics (prognostic liquid, ice and rain) and horizontal 2D Smagorinsky mixing. The simulations have a semi-Lagrangian, semi-implicit and non-hydrostatic formulation and a terrain following co-ordinate system (Davies *et al.* 2005). Many processes are parameterized, such as the surface (Essery *et al.*, 2001), the boundary layer (Lock *et al.* 2000) and mixed-phase cloud microphysics (Wilson and Ballard, 1999). The model fields are available at hourly intervals. See Lean *et al.* (2008) or Pearson *et al.* (2010) for more details of the model configuration and evaluation.

Several studies have used the output from *Cascade* model runs with various outcomes. Marsham *et al.* (2011) used *Cascade* simulations to study simulated dust emissions due to cold pools (haboobs) and winds associated with the low-level jet breakdown, which depends on the strength of the Saharan Heat Low. Their results concluded that simulations with parametrized convection underestimate dust uplift from haboobs, but overestimate dust uplift associated with the Saharan Heat Low induced flows, resulting in reduced dust emissions on days with active convection. Marsham *et al.* (2013) compared two *Cascade* simulations of the same resolution, but with parametrized and explicit convection schemes. They concluded that the intensity, location and timing of convection was better represented in the explicit convection scheme and that improved parametrizations in NWP models would better represent rainfall in West Africa. Birch *et al.* (2014) used outputs from several models, including versions of *Cascade* simulations at various resolutions, both convection-permitting and parametrized. They conclude that parametrized convection runs incorrectly trigger and simulate convection, which creates feedbacks and reinforces the error in moisture advection and hence the location of the most intense rainfall in the Sahel.

## Chapter 3

# A Characterization of cold pools in the West African Sahel compared with a convection-permitting model

### 3.1 Introduction

This Chapter presents a climatology of near-surface properties of mesoscale convective system (MCS)-related cold pools observed in the West African Sahel during the 2006 West African Monsoon, during AMMA. This climatology is used to evaluate cold pools in Unified Model convection-permitting simulations from the *Cascade* project in order to assess the ability of *Cascade* to simulate cold-pools and their properties correctly.

The approach taken in this study was based on an observational study of cold-pool properties over Oklahoma, USA, performed by Engerer *et al.* (2008; hereafter E2008). Their study investigated 39 squall-line MCSs by using data from 110 mesonet stations across the state of Oklahoma and obtained 1389 time series of cold pool related variables. The cold pool quantities studied by E2008 were decreases in potential and equivalent potential temperature, pressure rises, changes in wind direction and maximum wind gusts associated with a gust front passage. The focus of their study was on the evolution of cold pool properties during life cycles of MCSs as well as comparison of the observed cold pool characteristics with idealised model simulations. Further details regarding the study of E2008 are given in Chapter 1. Given that the study by E2008 was based on mid-latitude MCSs in the USA, it is of interest to assess whether the particular conditions of MCSs in West Africa result in comparable distributions of cold pool properties. This assessment was performed in this Chapter for a study period spanning from 1<sup>st</sup> June to 30<sup>th</sup> September 2006 for both observations and *Cascade* in order to cover cold pools from the pre-monsoon onset until the monsoon retreat. In addition, a sub-seasonal cold-pool characterization has been done by splitting the monsoon season into three sub-periods to enable evaluation of seasonal evolution of MCS-related cold pool properties. The main purpose of this chapter is to provide a baseline of cold pool strengths in West-African MCSs and an insight into related processes to serve as a guidance in future modelling work.

Section 3.2. describes the observational and model data sets and the analysis method. Section 3.3. focuses on climatology of cold-pool properties such as thermodynamic variables and wind changes, their seasonal variations and evaluates these in *Cascade* simulation. In addition, role of

mid-level dryness is investigated. Section 3.4. summarizes the results and discusses their implications.

## 3.2 Methods

### 3.2.1 Cold-pool detection in observed surface time-series and verification using remote-sensing data

In this study, a very similar approach to E2008 has been applied to allow comparison between West African MCS cold pools and E2008's results from the USA. E2008 subjectively identified cold-pool crossing times and then objectively quantified changes in surface station variables from the 30 minutes preceding the cold pool crossing to the two hours subsequent to the crossing. The 30 minute time window used to detect pre-storm maxima and minima in surface variables used by E2008 was not always long enough to capture these in Niamey, mainly in case of pressure as the pre-storm minimum was on average 52 minutes ahead of the cold pool. Therefore, in this study, the pre-storm time window was extended to 1 hour before the cold pool arrival time.

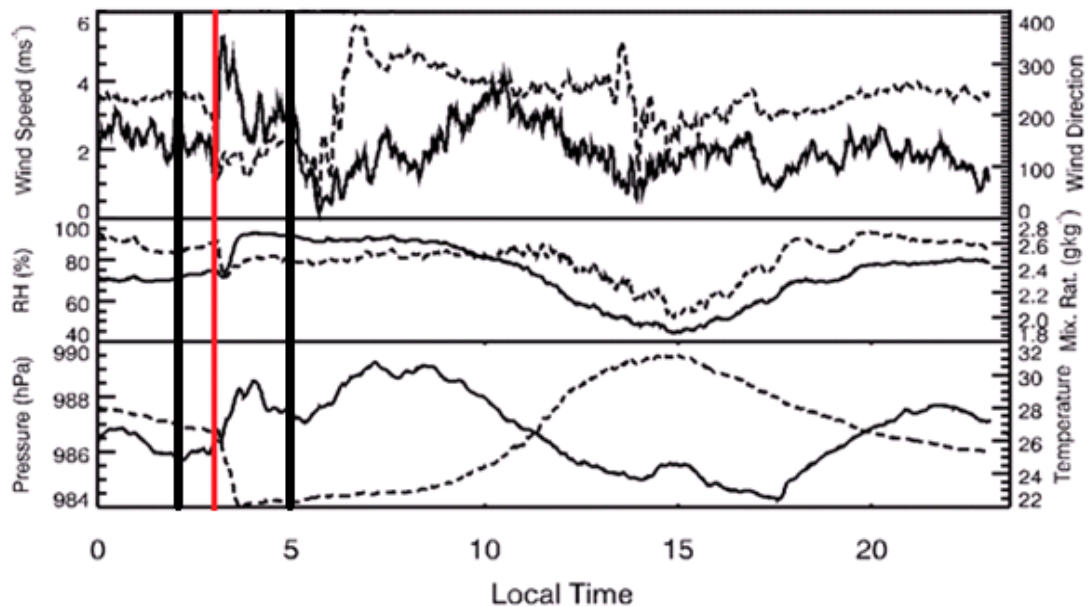


**Figure 3.1:** An example of an observed daily time series as obtained by the surface station at Niamey airport. This time series is for 11<sup>th</sup> August 2006, when a cold pool crossing was identified at 03:15 Local Time (denoted by vertical red line), which is 02:15 UTC. Black lines denote the borders of the time-window used for the analysis. Solid lines correspond to left-hand axis and dashed lines to right-hand axes. Data recorded every second and averaged at minute intervals.

Cold pool crossings are associated with a sudden change in wind direction (Engerer *et al.* 2008) and as in E2008 the wind direction change was considered as the main factor in the identification of crossing times (e.g. Figure 3.1). Times of sudden wind direction changes were subjectively identified and counted as potential cold pools. In order for the wind direction change to be sudden, it must have happened within 5 minutes and been of at least 30-degree magnitude. Because a wind direction change may, however, be associated with features other than cold pools, e.g. dust devils (Tratt *et al.*, 2003), or gravity waves (Cram *et al.*, 1992b, Birch *et al.*, 2013), the other surface variables and remote sensing data were also considered as specified below.

The change in wind direction must have occurred within 30 minutes of a wind gust and changes in temperature and pressure to be counted as cold-pool related. The magnitude of the gust must have been at least 1.5 times greater than the mean wind speed in the 30 minutes before the gust and temperature must have dropped by at least 1 °C (e.g. Figure 3.1). It is not likely, but possible, that something other than a MCS cold pool in the Sahel would cause these changes in pressure, temperature and wind. Because of this limitation of using surface data only, all the identified cold pools were verified by considering images from the MIT radar or satellite (outside of the ROP). This verification has been done subjectively based on inspection of radar/satellite images to see whether a MCS has been present in the vicinity of Niamey at the time of the cold pool passage.

### **3.2.2 Selection of monsoon season sub-periods**

Based on previous studies (e.g. Barnes & Sieckman, 1984; Marsham *et al.* 2008), it was hypothesised that cold-pool intensity in Niamey is not consistent throughout the monsoon season. The reason for this was related to the observed and in previous studies reported varying environmental conditions throughout the season. Because total accumulated rainfall varies throughout the season – both in terms of rainfall accumulated per event and overall seasonal accumulated rainfall – the fraction of rainfall evaporated into the parcel, which feeds the cold pool, as well as the environmental dryness was not expected to be constant throughout the season.

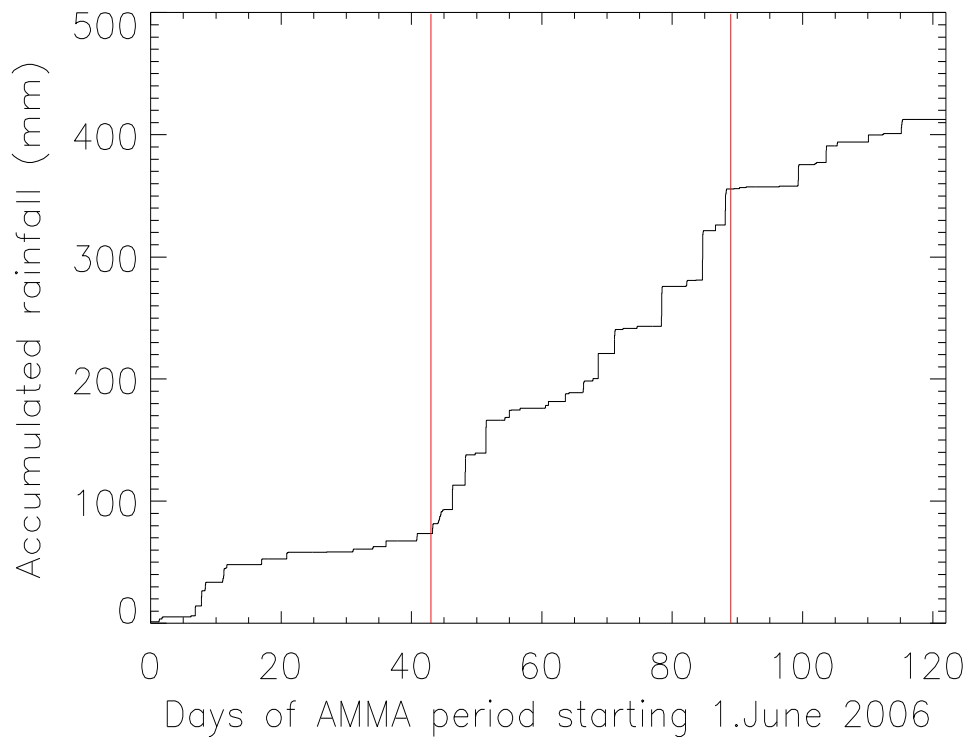


**Figure 3.2:** Total accumulated rainfall from Niamey ARM surface station data. Red lines separate three sub-seasonal periods used in this study: “Pre-monsoon” (1<sup>st</sup> June 2006 – 12<sup>th</sup> July 2006); “Monsoon” (13<sup>th</sup> July 2006 – 27<sup>th</sup> August 2006); “Retreat” (28<sup>th</sup> August 2006 – 30<sup>st</sup> September 2006).

In order to study the seasonal evolution of cold pools, the monsoon season of 2006 was divided into three sub-periods based on the seasonal evolution of rainfall at Niamey (Figure 3.2). The monsoon onset in 2006 was estimated to have been on 10<sup>th</sup> July (Janicot *et al.* 2008). The sub-period boundaries were set based on subjectively-identified changes of slope in the observed time-series of accumulated rainfall (clearest for pre-monsoon to monsoon) and were selected and defined as: “Pre-monsoon” (1<sup>st</sup> June 2006 – 12<sup>th</sup> July 2006), “Monsoon” (13<sup>th</sup> July 2006 – 27<sup>th</sup> August 2006) and “Retreat” (28<sup>th</sup> August 2006 – 30<sup>th</sup> September 2006), although they are not based on any formal definition of monsoon onset. Out of the 38 cold pools identified in this study, 22 occurred in the ‘monsoon’ sub-period with 8 in the ‘pre-monsoon’ and 8 in the ‘retreat’ sub-periods.

### 3.2.3 Atmospheric tide and mean diurnal pressure variation

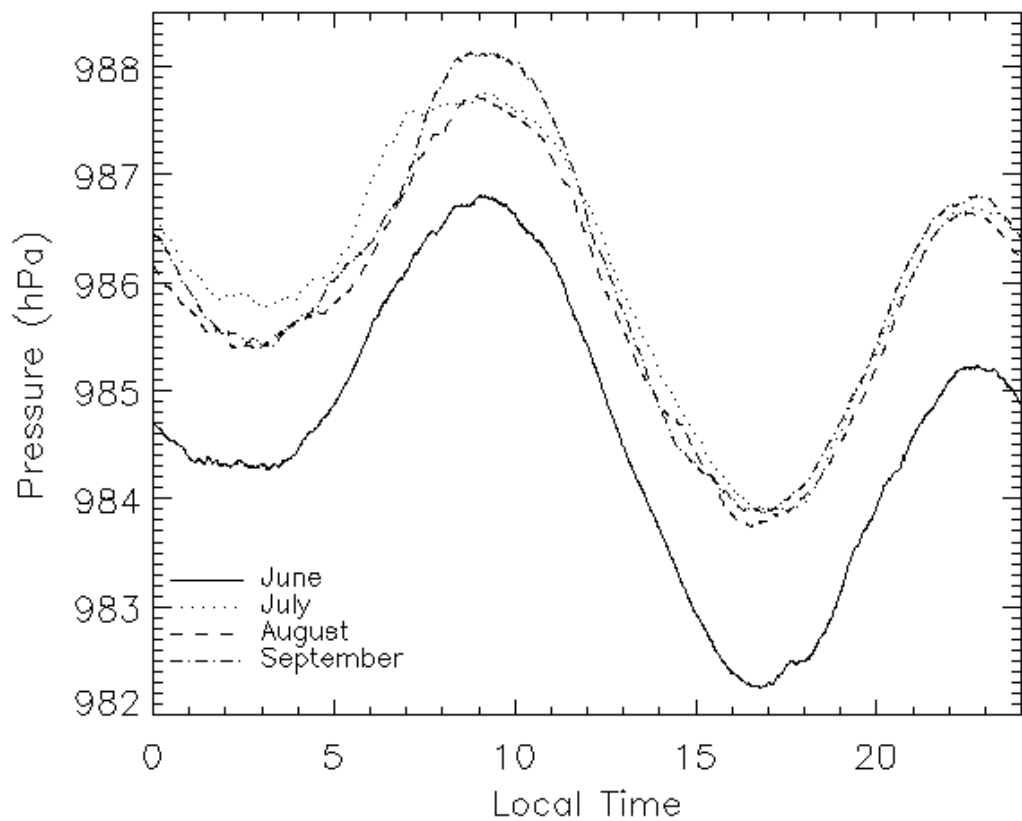


**Figure 3.3:** Average diurnal pressure variations by month. Solid=June, dotted=July, dashed=August, dash-dot=September.

The effect of diurnal pressure variation on representation of cold-pool related pressure changes was considered. Unmodified pressure data were analysed and then the average diurnal pressure variation has been calculated for each month. This was taken off each daily curve in order to remove the contribution from the mean diurnal pressure variation (on the order of 2-3 hPa), which is largely a result of atmospheric tides (Miyoshi, *et al.*, 2012) that are independent of the MCSs (Figure 3.3). The average diurnal pressure variation does however include cold pools, because there is a diurnal cycle in cold pools (Rickenbach, *et al.*, 2009). The magnitude of cold-pool related changes can be greater than that of diurnal tides, but unlike diurnal tides, cold-pool related pressure changes are temporary, infrequent (frequency on average of 0.32 per day) and incoherent. Therefore, subtracting the average diurnal pressure variation averaged over ~30 days from each daily curve includes a partial subtraction of cold-pool induced perturbations as well, but due to their relative infrequency and incoherency, these mean cold-pool perturbations are expected to be smaller than effects from atmospheric tides when averaged for the period of one month. Some of the minor perturbations

in Figure 3.3 may therefore be related to cold pools. Cold-pool related pressure changes were studied both with and without the subtraction of these diurnal pressure variations. The difference in results was, however, marginal and therefore the cold-pool related pressure variations obtained from the unmodified daily curve without the subtraction of the diurnal tide were used in the analysis.

### **3.2.4 Statistical evaluation of observed cold-pool properties**

Following the approach of E2008, the cold pool related changes in surface variables were calculated for: (1) increase in pressure (the maximum after the cold-pool minus the minimum before), and (2) decrease in temperature (maximum before minus the minimum after). For (3) equivalent potential temperature ( $\Theta_e$ ), cold pools could give an increase or a decrease, and often short-lived fluctuations complicated any method based on minima and maxima; therefore, unlike E2008, changes in mean from the period spanning 1 hour before the cold-pool crossing-time to the period spanning 2 hours after the crossing were calculated. In addition, unlike E2008, (4) change in water vapour mixing ratio (WVMR) and (5) increase in mean wind speed were also calculated. For WVMR, the mean value in the hour before the cold pool was subtracted from the minimum value in the 2 hours after (so positive values show moistening). The minimum after the passage was used rather than maximum as there was often a sharp minimum just following a cold pool passage, that was often followed by an increase that reached greater than pre-cold pool magnitudes within the 2 hours, but which was likely not primarily related to the cold pool crossing (e.g. Figure 3.1). The mean value in the 1 hour before the cold pool was used rather than a maximum in order to take into account the sometimes sharp fluctuations in WVMR that were likely related to turbulence and mixing. In addition, maximum wind gust associated with the cold pool was obtained by taking maximum wind speed in the 2 hours after the cold pool crossing (as in E2008).

For a majority of the studied cold pools, the cold-pool-related changes in surface variables were coincident or nearly coincident. There were, however, several cases where this was not the case and hence it was difficult to define the cold pool crossing time. This was most frequent in case of wind direction changes, where in several cases there were multiple wind direction changes of more than  $30^\circ$  within  $\sim 2$  hours of a wind gust, but none coincided with the actual wind gust. These were likely related to waves propagating faster than the cold pool from the parent storm. In such cases either the time of the closest wind direction change to the gust or the time of the actual gust was taken as the crossing time, based on whichever was closest to the temperature drop. Because of this there is clearly uncertainty in the cold pool

crossing times, but E2008 show the objectively determined changes are generally robust to the precise crossing time used.

Using the radar, the storms generating the cold pools were separated subjectively into isolated storms and larger organized convective systems (MCSs; spanning at least 100km as defined by American Meteorological Society, 2016). The main difference between the methods of E2008 and this study is that MCS lifecycle stage differentiation was not used. This would provide a great challenge in West Africa because there was only one radar available in the Sahel, which does not provide enough information to be able to decide on the lifecycle stage as it often covers only a fraction of the MCS. Unlike in E2008, data was separated by sub-periods in order to perform the sub-seasonal characterization as discussed in section 3.2.2.

### **3.2.5 Evaluating cold pools in the 4 km convection-permitting *Cascade* simulations**

In order to make the test of the 4-km UM *Cascade* runs as fair as possible, an identical approach to the observational data analysis, unless stated, was performed when evaluating *Cascade* simulations. While all the observed surface data was output every minute, UM diagnostics were only available at hourly intervals, which made the resolution of cold pools in the obtained model time-series poor. Therefore, a space-to-time conversion was performed to convert a west-east cross-section through Niamey at each hour into a virtual 'time-series' for the purpose of having more frequent data for the evaluation, in this implicitly assuming that the system does not change much during the hourly crossing time. The conversion has been performed based on the following criteria: *Cascade* simulations have a 4-km grid-spacing. The mean propagation speed of the parent MCSs that produced all the detected cold pools was  $9.4 \text{ m s}^{-1}$  and it was assumed that a cold pool moves at a very similar speed to the parent MCS. The average time a MCS would take to travel 4 km equals 7-min. In this process it was assumed that cold pools did not change significantly with time and their speed of propagation was uniform.

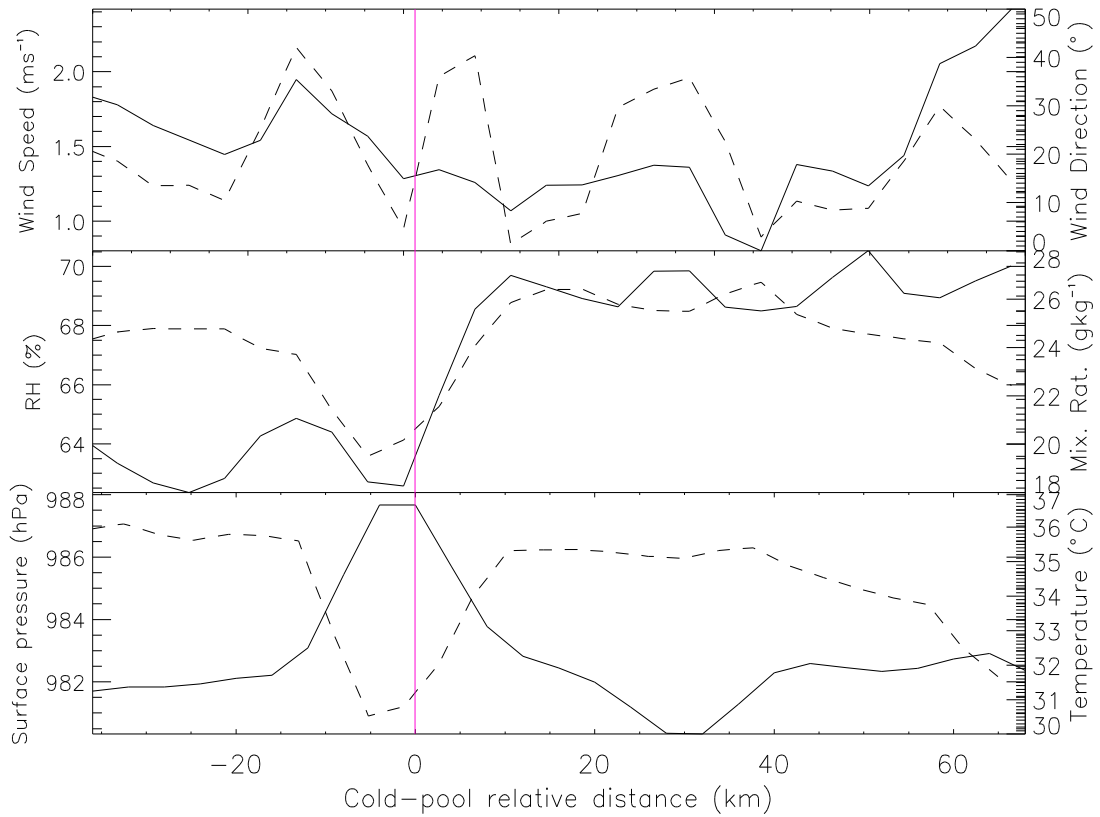


**Figure 3.4:** An example of an east-west cross-section through surface data at a time output closest to a cold pool passage in the 4-km Unified Model convection-permitting simulation (*Cascade*). This cross-section is for 10<sup>th</sup> August 2006, when a simulated cold pool crossing was identified at 10:00 Local Time (denoted by vertical red line), which is 09:00 UTC. Using a 9.4 m s<sup>-1</sup> velocity, the cross-section is equivalent to a region of time starting at 1 hour before and ending 2 hours after the cold-pool passage. The identified gust front is denoted by vertical pink line. Solid lines correspond to left-hand axis and dashed lines to right-hand axes. 0 km location corresponds to the grid-point located at the co-ordinates of Niamey.

The space-to-time conversion was performed for every cold pool on a west-east spatial cross-section at a time when the identified cold pool was at the closest distance from the location of Niamey (e.g. cross-section in Figure 3.4 – note that times and locations of simulated cold pools were not identical to observed cold pools and Figure 3.4 is the closest cold pool in time at Niamey to the observed cold pool in Figure 3.1). This conversion provided an equivalent of a model output being approximately every 7-min, which is at much higher frequency than the hourly *Cascade* diagnostics. This increased the density of data points by approximately 9 times compared with the hourly outputs. For a fair evaluation of the model all observational data have been smoothed by a 7-min running mean to create a similar averaging in time and space. Regarding the sub-seasonal evaluation, the same three sub-periods (pre-monsoon, monsoon and retreat) with identical date boundaries as for observations were used for *Cascade*.

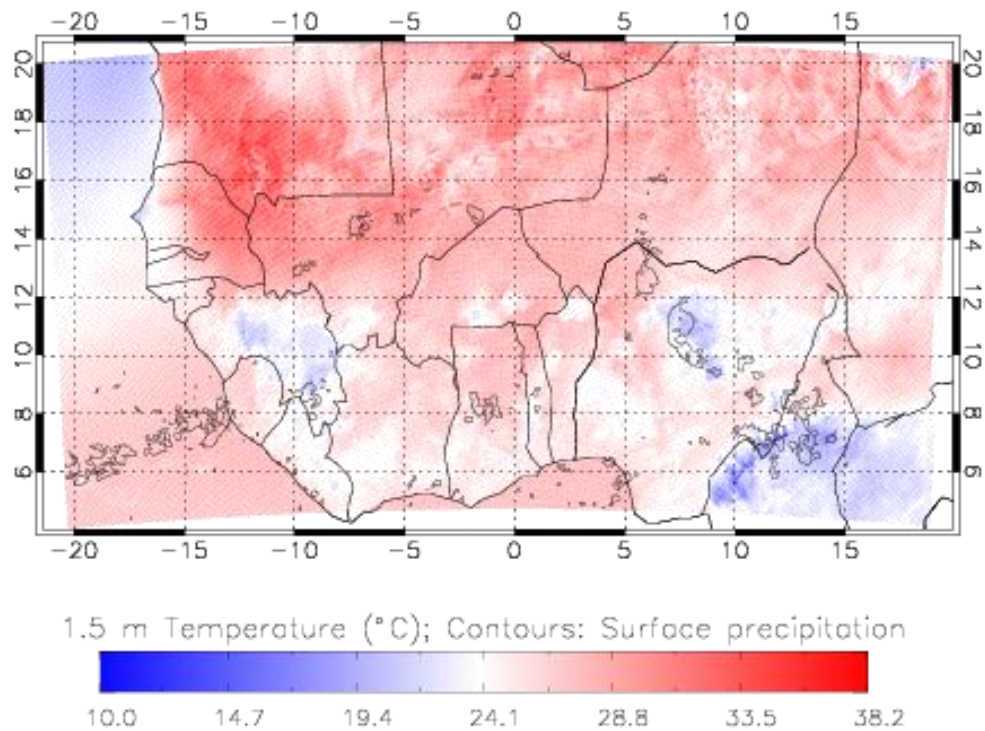


**Figure 3.5:** An example showing *Cascade* simulated 1.5m temperature ( $^{\circ}\text{C}$ ) (shaded) and surface precipitation rate (contour at  $2\text{ mm h}^{-1}$ ).

Due to the temporally limited output from *Cascade* (even after the above described conversion), it was difficult to distinguish ‘sudden’ changes associated with cold pools in the time series. However, unlike in case of observations, *Cascade* simulations provide full 3-D data and cold pools could easily be detected by the use of 1.5 m temperature data and surface precipitation (see example in Figure 3.5). Therefore, *Cascade* cold pools were subjectively detected from plots such as the example in Figure 3.5. A criterion that precipitation of the parent MCS must cover an area of at least 25 grid points (100km) in the longest direction (e.g. Figure 3.5) has been used in order to avoid cold pools produced by local isolated convection.

All the identified cold pools were then verified in the ‘time-series’ derived from the space to time conversion, where all detected cold pools had to pass similar criteria to the observed cold pools. The change in wind direction associated with the visually detected potential cold pool must have occurred within 20 kilometres of a wind gust (local maximum in wind-speed). The magnitude of the gust, like in case of observed cold pools, must have been at least 1.5 times greater than the mean wind speed in the 20 kilometres before the gust and temperature must have dropped by at least  $1^{\circ}\text{C}$  within 40km of the gust (e.g. Figure 3.4).

### 3.3 Characterization of observed and simulated cold pools

During the study period, 38 cold pools were detected in the observations. Of these, 33 were squall-line MCSs (having a continuous line being at least 100 km in length and having reflectivity of at least 35 dBz along at least 50% of its length), 4 were non-squall-line MCSs, one was a propagating cold pool from a freshly dissipated MCS (seen in satellite imagery but out of radar range) and 4 were from local non-MCS convection (there were many isolated convective storms in the range of the MIT radar, but their cold pools rarely crossed Niamey). The 4 cold pools related to the isolated convection gave very limited statistics and since this study focuses on cold pools produced by organised MCS's, data from these 4 cases were not used in the analysis. Therefore, 38 observed cold pools were used in the analysis together with 42 MCS-related cold pools identified in the model data.

	<b>Observations</b>	<b>Cascade</b>
<b>Pre-monsoon</b>	<b>8</b>	<b>12</b>
<b>Monsoon</b>	<b>22</b>	<b>14</b>
<b>Retreat</b>	<b>8</b>	<b>16</b>

**Table 3.1:** *The number of cold pools in each sub-period for observations and Cascade.*

The seasonal evolution of the number of cold pools is shown Table 3.1. The pre-monsoon period was 42 days long with the monsoon and retreat periods being 50 and 30 days long, respectively. On average, there was an observed cold pool crossing Niamey once every 5.3 days in the pre-monsoon period, every 2.3 days in the monsoon period and once every 3.8 days in the Retreat period. In *Cascade* the cold pool frequency was one every 3.5, 3.6 and 1.9 days for Pre-monsoon, Monsoon and Retreat sub-periods respectively. For observations the cold-pool frequency agrees with the seasonal evolution of rainfall (see Figure 3.2). A peak in rainfall (steepest increase in accumulated rainfall) is observed during the monsoon sub-period and more than half of observed cold pools occurred during that sub-period. In *Cascade*, cold pools are almost evenly distributed throughout the pre-monsoon and monsoon sub-periods with greatest frequency in Retreat sub-period.

### **3.3.1 Composite cold pools**

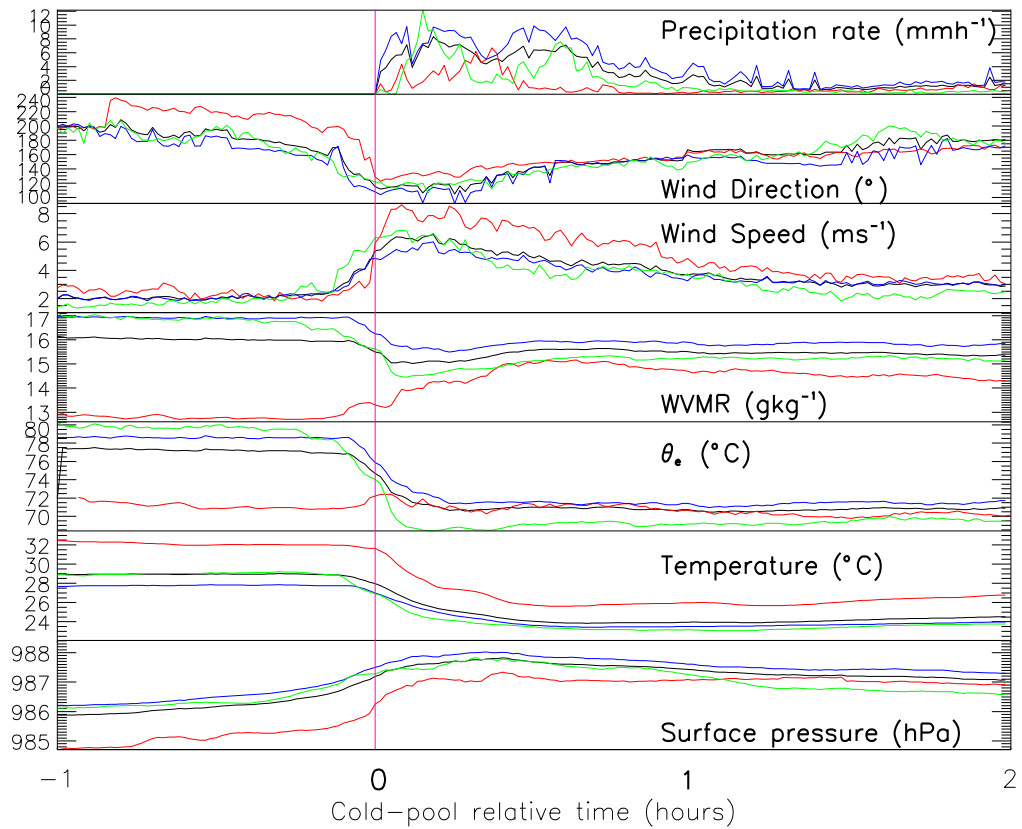


**Figure 3.6:** Composite cold pool obtained from averaging variables of all observed cold pools around the crossing time. Black line is for the whole period, red for the Pre-Monsoon period, blue for the Monsoon and green for Retreat. The vertical pink line shows the cold pool crossing time.

Figure 3.6 shows composites of observed surface variables, centred on cold pool crossing time. The mean standard errors for the individual all-season (black lines) variables are: 0.7 hPa for pressure, 1.5 °C for temperature, 1.8 °C for equivalent potential temperature, 0.9 g kg<sup>-1</sup> for WVMR, 1.1 m s<sup>-1</sup> for wind-speed, 12° for wind direction and 1.7 mm hr<sup>-1</sup> for rainfall. The “composite cold pool”, (over the entire observation period, black lines), was accompanied by a decrease in temperature of 5.3 °C. As expected, the cooling of the cold pool brings a pressure increase, the magnitude of which was 1.9 hPa. The wind maximum related to the cold pool passage had a magnitude of 6.5 m s<sup>-1</sup> in the composite, with the wind rotating from approximately 200 to 120 degrees, consistent with southwesterly monsoon flow changing to a more easterly wind from MCS moving from east to west. Rainfall intensity increased rapidly to a maximum about 15 minutes after the cold pool passage with a second peak approximately 45 minutes after the passage. The weaker precipitation behind the first peak corresponds to the “weak echo” in the radar observations, between stratiform rain and the main line of convective cells. WVMR decreased after the initial passage and stayed low throughout the first “convective rainfall” maximum. Approximately 30 minutes after the cold pool passage, there was a small increase of WVMR (accompanied by an increase in relative humidity, not shown). Although only around 0.5 g kg<sup>-1</sup>, this change is larger than the mean standard error in the 30

minutes after the cold pool in the composite of cold-pool changes (not shown) and this temporary decrease followed by an increase was observed in 26 out of 38 cases. The increase was coincident with the second “stratiform” rainfall peak. This drying and moistening coincidence with the rainfall suggests that there may be a descent of dry mid-level air towards the surface occurring during the convective rainfall, while later evaporation of stratiform rain increases WVMR (this is confirmed in Chapter 4). Since all the changes associated with cold pools are always greater than the mean standard error over the 2 hours (excluding sub periods with lower number of events), it can be concluded that the mean magnitudes of changes obtained here are representative of a typical case.

Figure 3.6 shows that cold-pool related changes are different across the sub-periods. Pre-monsoon cold pools are generally stronger, associated with greater pressure increases, temperature decreases and stronger winds. Precipitation is less intense and shorter-lived, mainly for the second “stratiform” peak, which supports the idea that drier mid-levels enhance evaporation and more latent heat is used, creating colder and possibly deeper cold pools. Furthermore, the related changes in equivalent potential temperature and WVMR vary. The statistical significance of these seasonal differences is investigated in later sections. All values given below are means and standard deviations. The composite pre-monsoon cold pool caused a long-lived WVMR increase of  $2.5 \text{ g kg}^{-1} \pm 0.8 \text{ g kg}^{-1}$ , while during the monsoon and retreat there are long-lived decreases of  $1.5 \pm 0.2 \text{ kg}^{-1}$  for monsoon and  $2.7 \pm 0.5 \text{ kg}^{-1}$  for retreat. This shows that pre-monsoon cold-pools are transporting moisture into the lowest layers of the Sahelian atmosphere whereas later on, the boundary layer is much moister and cold pools mix drier mid-level air downwards. Equivalent potential temperature changes were small with a pre-monsoon cold pool passage. In contrast, there is a sharp and long-lived decrease in equivalent potential temperature in the monsoon and retreat sub-periods, with the decrease during the retreat being greater than during the monsoon ( $11.9 \pm 1.0^\circ\text{C}$  and  $7.8 \pm 4.8^\circ\text{C}$  for retreat and monsoon respectively). The very small pre-monsoon change in equivalent potential temperature suggests that the cold-pool airmass is not different to that of its environment. The most likely explanation would be a deep boundary layer before monsoon onset, where the downdraft mainly moistens and cools the boundary layer airmass, which causes equivalent potential temperature to remain nearly unchanged.

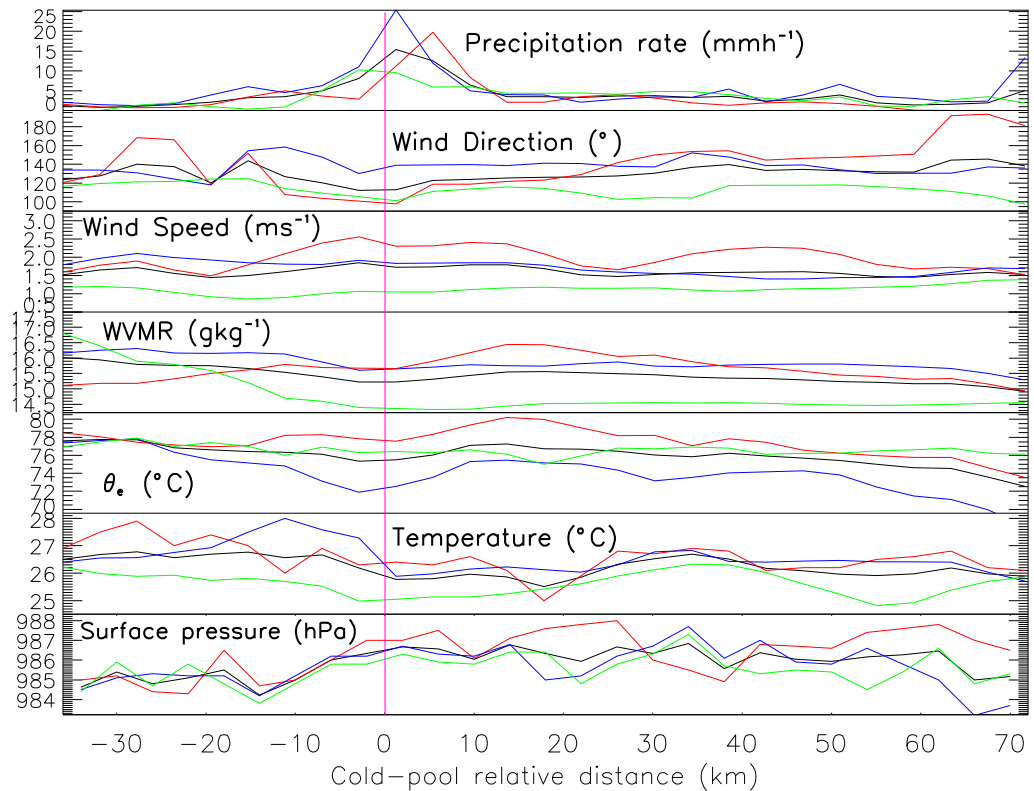


**Figure 3.7:** As Figure 3.6, but for *Cascade*. Unlike Figure 3.6, horizontal axis does not represent time, but a spatial west-east cross-section through surface data across the cold pool.

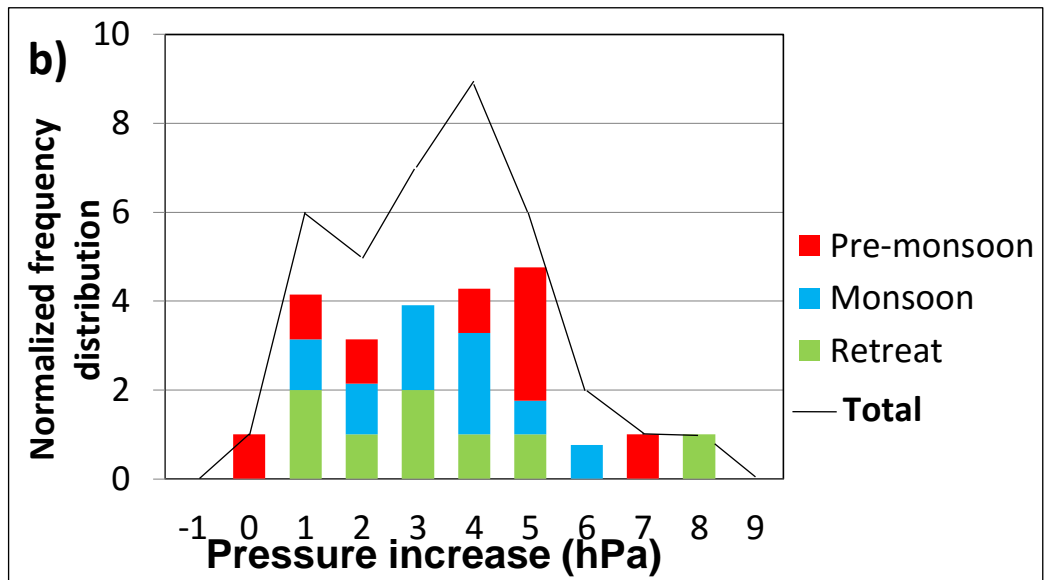
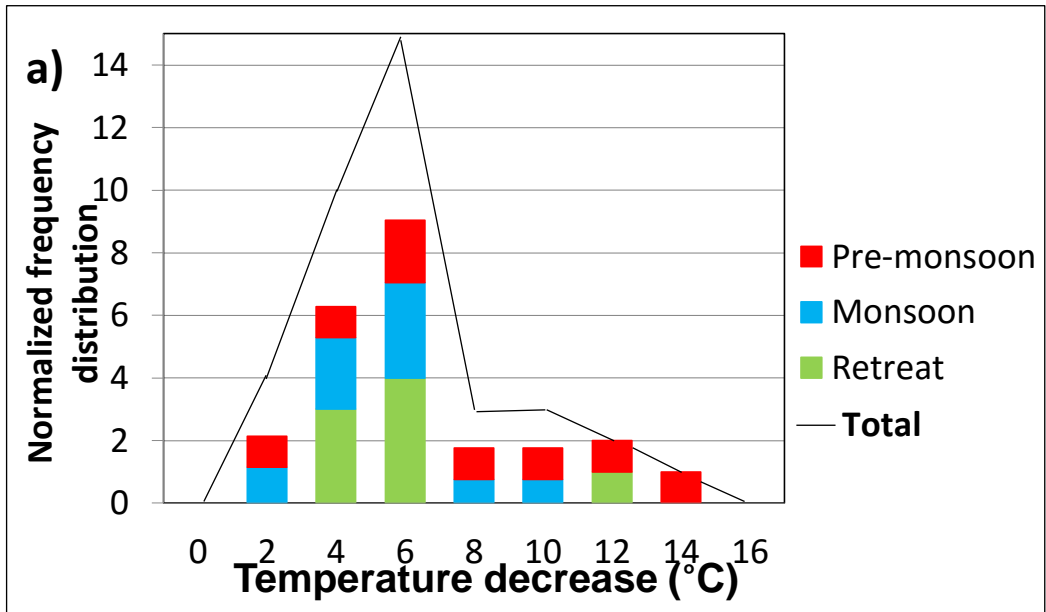
Figure 3.7 shows the composite horizontal surface conditions across cold pools in *Cascade*. In the model composite, the general cold pool signatures are captured, at least to some degree. The difference to observations is much smoother appearance of cold-pool related changes, which reflects the greater uncertainty for defining the cold-pool leading edge in *Cascade*. Magnitudes of cold-pool induced changes are lower than in the observed mean cold pool. The *Cascade* composite cold pool features a pressure increase of 1.7 hPa, temperature decrease of 0.9°C, equivalent potential temperature decrease of 5.5 °C, WVMR decreasing by 1.0 g kg<sup>-1</sup> and mean precipitation rate peaking at 15 mm h<sup>-1</sup>. There is a small peak in mean wind with a maximum wind speed of ~2.0 m s<sup>-1</sup> and a wind direction change of 35.1°.

There were differences between the *Cascade* and observed composites. While pressure increase is similar to the observed (1.9 hPa for observed vs 1.6 hPa for *Cascade*), the mean *Cascade* cold pool had much lower magnitude of temperature decrease (1.1 °C) when compared to the 5.3 °C drop in observed mean temperature. This would imply a much deeper mean cold-pool in *Cascade* due to hydrostatic equilibrium, but caution must be taken as hydrostatic equilibrium assumes a well-mixed cold pool and its environment. While the cold pool may be well-mixed, the environmental surface layer features a stable layer overnight and a super-adiabatic layer during the day. In addition, there are various other dynamical processes that can influence pressure changes. *Cascade* does not capture some details such as the temporary reduction in WVMR followed by an increase as in case of

the mean observed cold pool. This is likely smoothed-out in the cross section. *Cascade* rainfall in the composite cold pool is generally 2-2.5 times more intense than observed, which is consistent with previous studies (e.g. Birch *et al.* 2014), and generally features one peak rather than continuous precipitation seen in observed composite cold pool. This reflects the lack of stratiform rain in *Cascade* (UM model), consistent with Stein *et al.* (2015).

There are also some variations between observed and *Cascade* cold pools on a sub-seasonal scale. As in the observations, pre-monsoon cold pools are associated with stronger pressure perturbations, but the difference in magnitude when compared to observations is much lower. *Cascade* pre-monsoon cold pools are also accompanied by the strongest winds, which shows that the seasonally stronger cold pools in *Cascade* have been simulated to some degree. WVMR of the *Cascade* composite cold pool temporarily increases in pre-monsoon, decreases in monsoon and sharply decreases during the retreat sub-period. This agrees with observations except that the increase in pre-monsoon is only temporary. During pre-monsoon the composite cold pool caused, as in observations, a temporary equivalent potential temperature increase of nearly 2 °C magnitude. This temporary increase of equivalent potential temperature in the boundary layer would need further work to be explained, perhaps using tracers of cold-pool air to identify its source region. This temporary change, however, has been much longer, lasting only ~5 minutes in observations, but nearly 2 hours when converted to time in *Cascade*. The magnitude of a decrease in equivalent potential temperature during monsoon and retreat in *Cascade* is  $6.0 \pm 0.7$  °C and  $2.2 \pm 0.2$  °C respectively. Wind speed is much lower in all *Cascade* sub-periods than in observations. The rainfall structure of *Cascade* MCSs has a mean peak several kilometres behind the gust front crossing with the peaks for the whole period and sub-periods slightly offset, which will act to reduce the overall mean peak. The greatest rainfall rates are observed in the monsoon sub-period while retreat has the lowest. The individual peaks between sub-periods are displaced from each other, which could however be a result of lower resolution of data output in *Cascade* (see section 3.1.4) as all three peaks are within two grid-points from each other.

### 3.3.2 Thermodynamic properties of cold pools



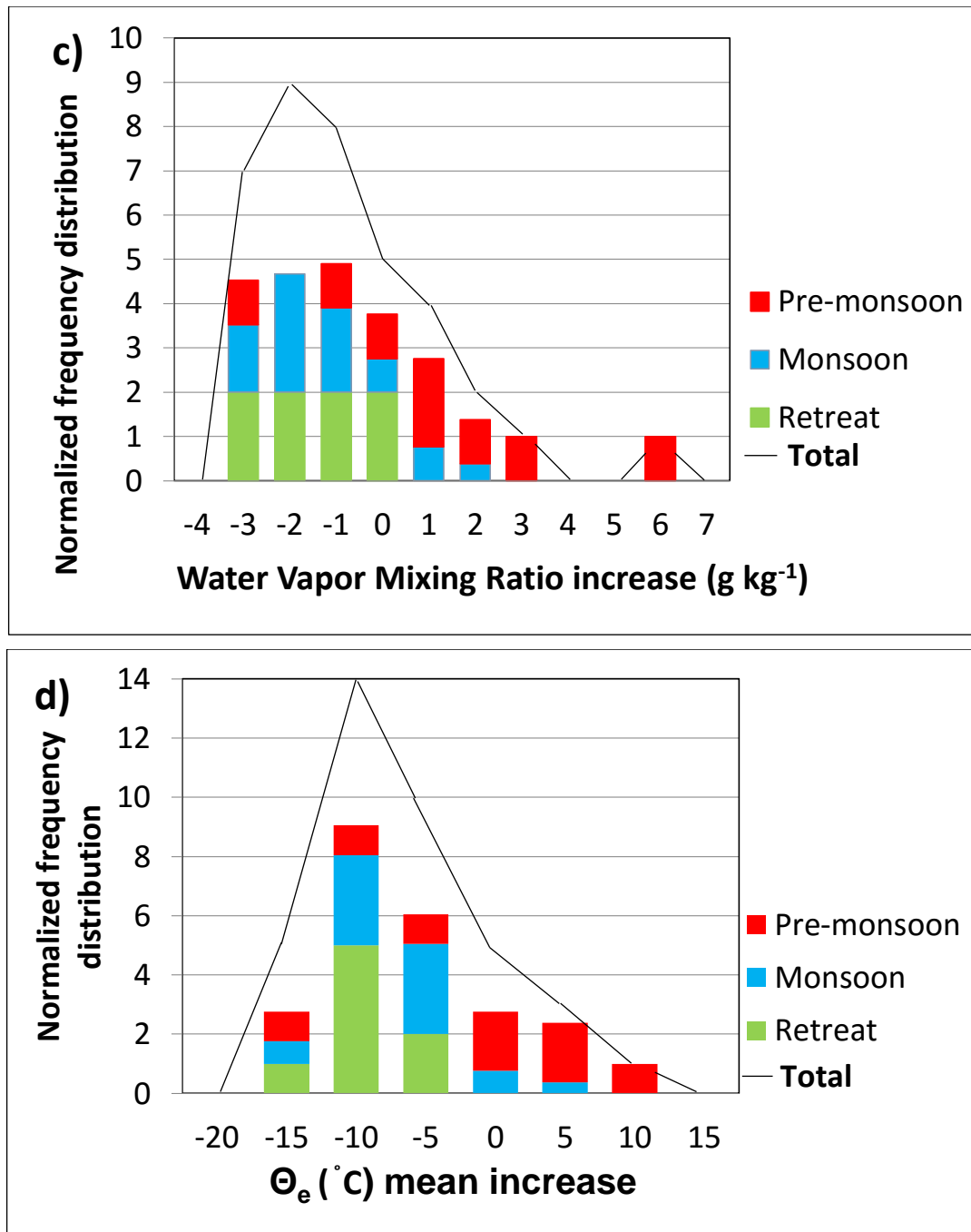


**Figure 3.8:** Changes in specified thermodynamic variables from observed cold pools: a) Decrease in temperature; b) Increase in pressure; c) Increase in WVMR; d) Increase in mean  $\Theta_e$ . Colouring represents the sub-periods (red: Pre-monsoon, blue: Monsoon, green: Retreat). Number of events in each season is normalised to allow a comparison between seasons (see text) with the black line showing total (unnormalised) distributions.

Figure 3.8 shows bar plots of the normalised frequency distribution of several cold pool properties and their seasonal variations. The bars are normalized to allow comparison between sub-seasons and account for the

different numbers of cold pools identified in the three sub-periods. There were 8 events each in “pre-monsoon” and “retreat” and 22 in “monsoon”; therefore “monsoon” was normalised by multiplying the number of events by 8/22 to allow comparison. The black line which shows the frequency distribution over all three sub-periods therefore only overlies the top of the bar plots when there are no “monsoon” events in that bin.

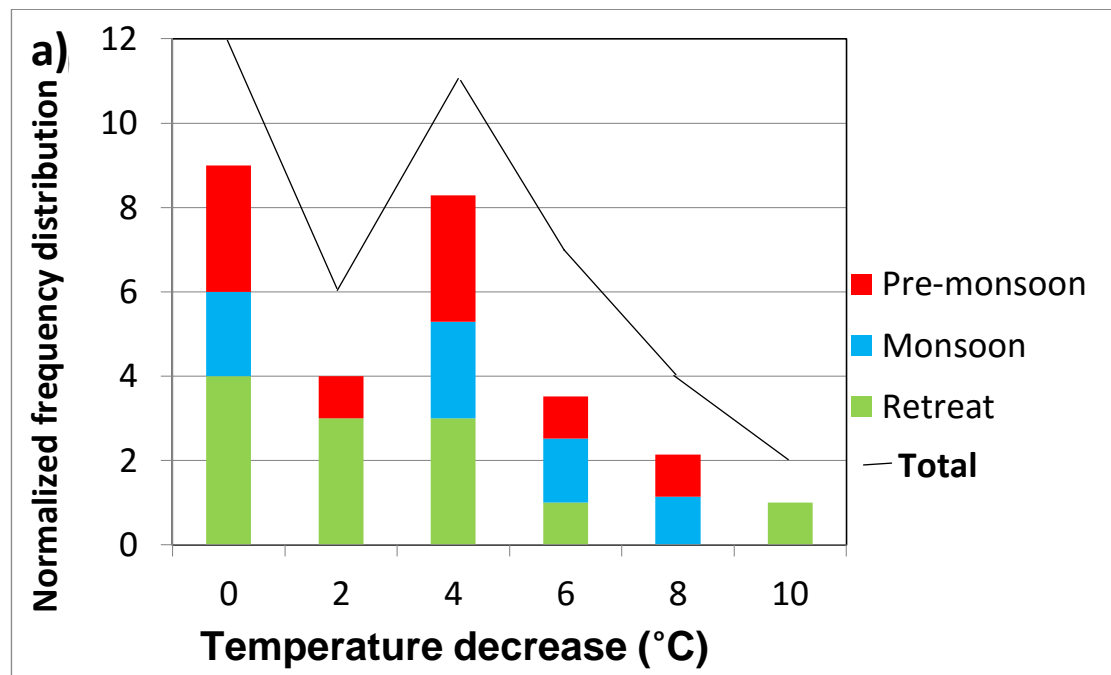
A temperature decrease between 1.8 °C and 13.6 °C was observed for all cold pool passages (Figure 3.8 a). The whole seasonal distribution is skewed however, with a broad peak between approximately 3 °C and 7 °C and only 3 events of temperature decrease greater than 11 °C. The distribution of pressure increase in Figure 3.8 b) is also skewed, ranging from 0.4 to 8.1 hPa, with most events between 1 and 4 hPa. These values are larger than the pressure increase in the cold pool composite in Figure 3.6, because the timing of the maximum and minimum pressure relative to the gust-front differs between cold pools. This is a limitation of the composite as minima and maxima occur at relatively different times from the time of crossing; partly because cold pools propagate at different speeds and also because for any system the maxima/minima are located at different positions relative to the gust front.

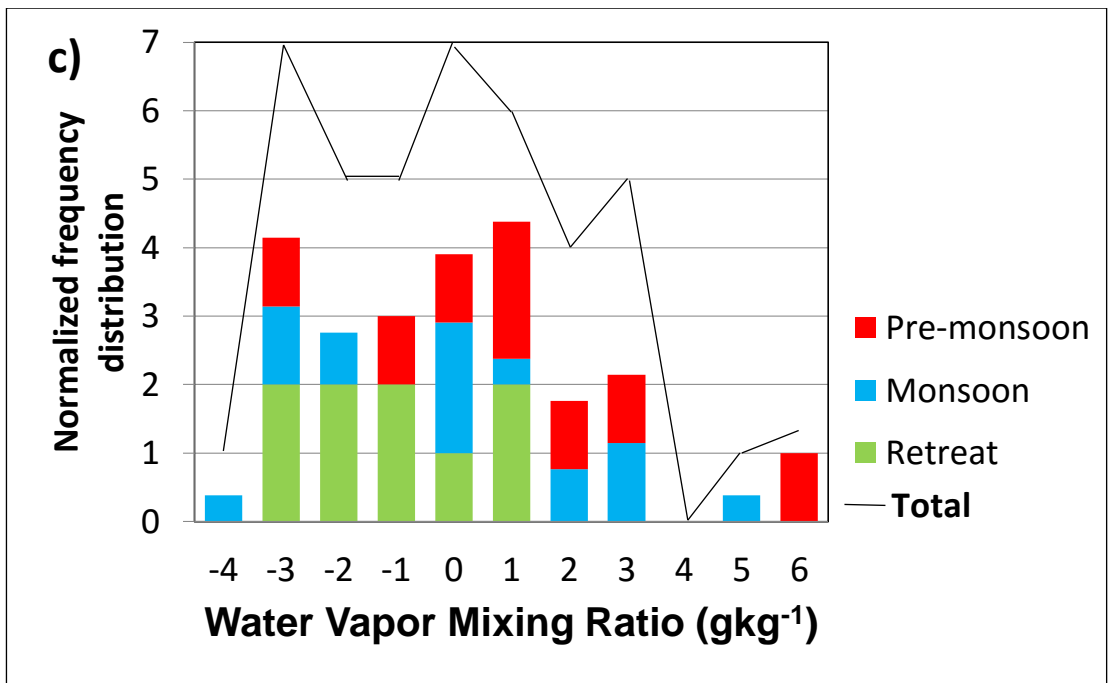
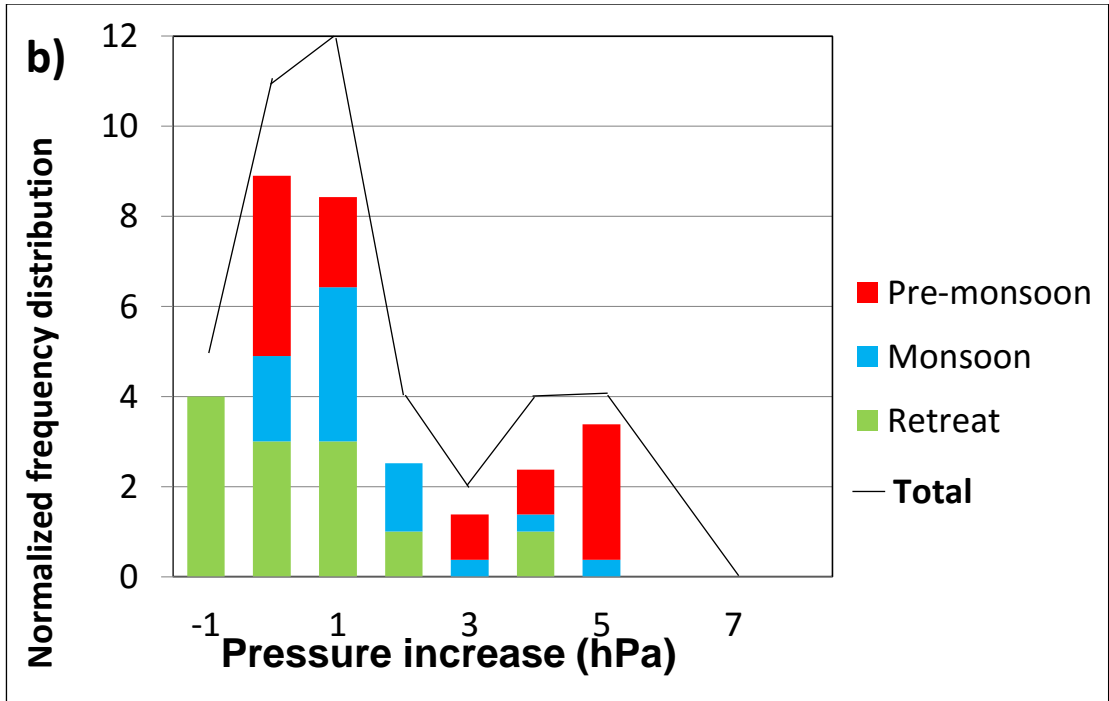
Figure 3.8 c) shows that the majority of cold pools led to a drying, but 10 cold pools (27%) led to an increase in WVMR. This change ranged from -3.5 g kg<sup>-1</sup> to +6.1 g kg<sup>-1</sup>. Most events gave a decrease in mean  $\Theta_e$  with the greatest decrease being -12.6 °C, but several events show an increase, with the largest being +8.7 °C (Figure 3.8 d). It was found that the three cold pools with greatest WVMR increases were closest to rain, but no overall relationship could be concluded between the WVMR change and its proximity to rainfall.

Regarding seasonality, there was a tendency towards greater pressure increases and temperature decreases in the pre-monsoon sub period when compared to the whole season (mean observed changes were 4.4 hPa for pre-monsoon compared to 3.7 hPa overall and 7.8 °C compared with 6.7 °C overall). The differences in pressure and temperature changes between sub-seasons were, however, not statistically significant at the 90% level. Humidity changes from cold pools also varied across the sub-periods, with WVMR tending to increase in pre-monsoon, but tending to decrease in the rest of the season (observational means of +1.1 g kg<sup>-1</sup> for pre-monsoon compared with -0.6 g kg<sup>-1</sup> overall). Mean equivalent potential temperature both increased and decreased in the pre-monsoon, but nearly always decreased in the remainder of the observation period (mean observational changes of -2.2 °C compared with -9.6 °C). Decreasing equivalent potential temperature is caused by transport of dry air from the Saharan Air Layer by convective downdrafts. Several increases of boundary layer equivalent potential temperature were observed with night-time cases, presumably

related to high equivalent potential temperature air advected by the low-level jet above dryer (lower equivalent potential temperature air) stable night-time boundary layer. A cold pool eroding such stable layer would also transport this higher equivalent potential temperature to the surface. The observed seasonal differences in changes in equivalent potential temperature and WVMR were significant at the 90% level.

The pre-monsoon difference is consistent with drier mid-levels during the pre-monsoon period that promote more evaporation (or sublimation) and hence greater associated moistening, cooling and greater pressure increases, although the differences were only statistically significant for the moistening (see Figure 3.8). It is also consistent with Garcia-Carreras, *et al.* (2013) who shows that cold pools carry moisture northwards into the Sahara from the Sahel during the pre-monsoon period.





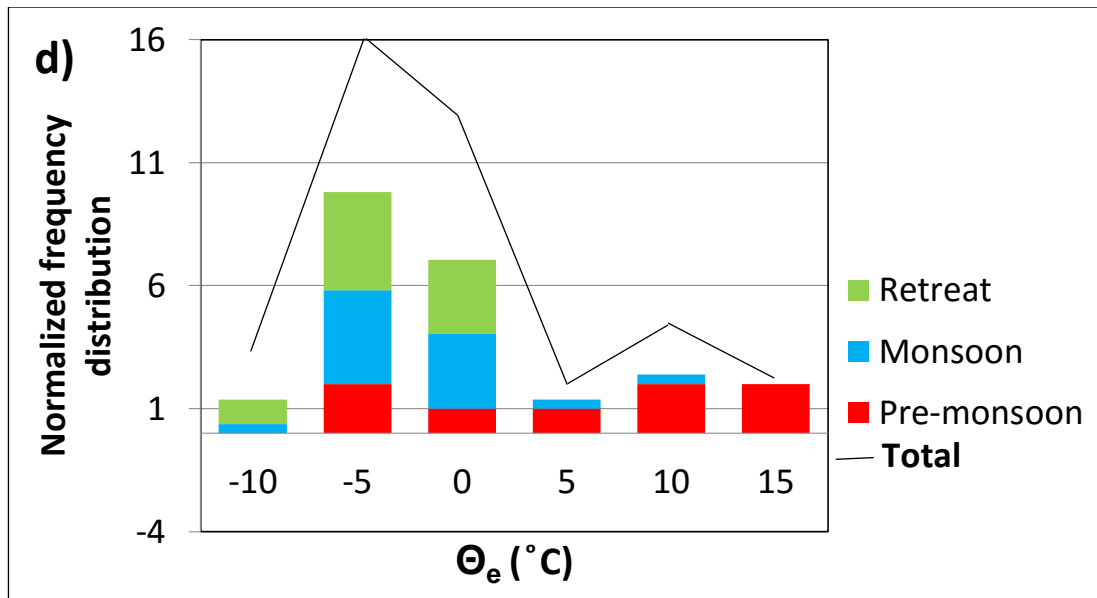


**Figure 3.9:** As Figure 3.8, but for Cascade.

The *Cascade* model results (Figure 3.9) give generally smaller magnitudes of changes related to cold pools than observations for most thermodynamic variables, but the difference is not as high as that of the composite. This again shows that greater uncertainty in gust front location in *Cascade* is smoothing out cold pool signatures in the composite. *Cascade* cold pools are associated with cooling up to 10.1°C, with most in the range of 2 to 6 °C (Figure 3.9 a)). The mean decrease of temperature across a cold pool in *Cascade* is 3.37 °C, whereas the observed mean decrease is 5.92 °C. The lower mean decrease of temperature in *Cascade* agrees with the lower magnitude of cold-pool related temperature decrease seen in the *Cascade* composite cold pool. The largest pressure increases were near 6 hPa, with the majority being below 2 hPa (Figure 3.9 b)), whereas observed cold-pool pressure increases ranged mostly between 2 and 6 hPa. 5 out of 42 cold pools were associated with a pressure decrease, unlike those observed. All the decreases were of a magnitude smaller than 1 hPa and were possibly related to a pre-cold pool passage of a bore or gravity wave.

Figure 3.9 c) shows that the range of simulated cold-pool related WVMR perturbations is similar to observations, but *Cascade* has more wet cold pools than were observed (43% of all). Equivalent potential temperature both increased and decreased in *Cascade* with 57% of cold pools having an increase (Figure 3.9 d)), which is consistent with the finding that *Cascade* has more wet cold pools than observations, where only 18% of cold pools have an increase. The magnitudes of equivalent potential temperature change range from -10 °C to 15 °C, which is similar to observations (-15 °C to 10 °C). These magnitudes in *Cascade* are larger than those in the composite cold-pool in Figure 3.7, which is due to the fact that increases and decreases in equivalent potential temperature even out, which is another limitation of the composite.

The observed stronger pre-monsoon cold pools were captured to some degree in *Cascade*, where values of mean pressure increase and temperature decrease for the pre-monsoon period were found to be 2.9 hPa and 4.4 °C respectively (compared with 1.5 hPa and 2.8 °C for the whole season). Observed cold pools were stronger in the pre-monsoon sub-period, but the magnitudes of changes were greater overall (4.4 vs 3.7 hPa and 7.8 vs 6.7 °C for pressure and temperature for pre-monsoon and overall, respectively). The differences in pressure and temperature changes between sub-seasons were not, as in the observations, statistically significant at the 90% level. In *Cascade*, no statistically significant changes of WVMR increases were found across the sub-periods, but a mean of  $-1.3 \text{ g kg}^{-1}$  during retreat contrasts with the overall mean of  $0.6 \text{ g kg}^{-1}$ . *Cascade* pre-monsoon increase in  $\Theta_e$  has a mean of 7.3 °C with an overall decrease of -1.7 °C. The difference between the population of pre-monsoon cold pools and the overall population is significant at the 90% level regarding changes in  $\Theta_e$ .

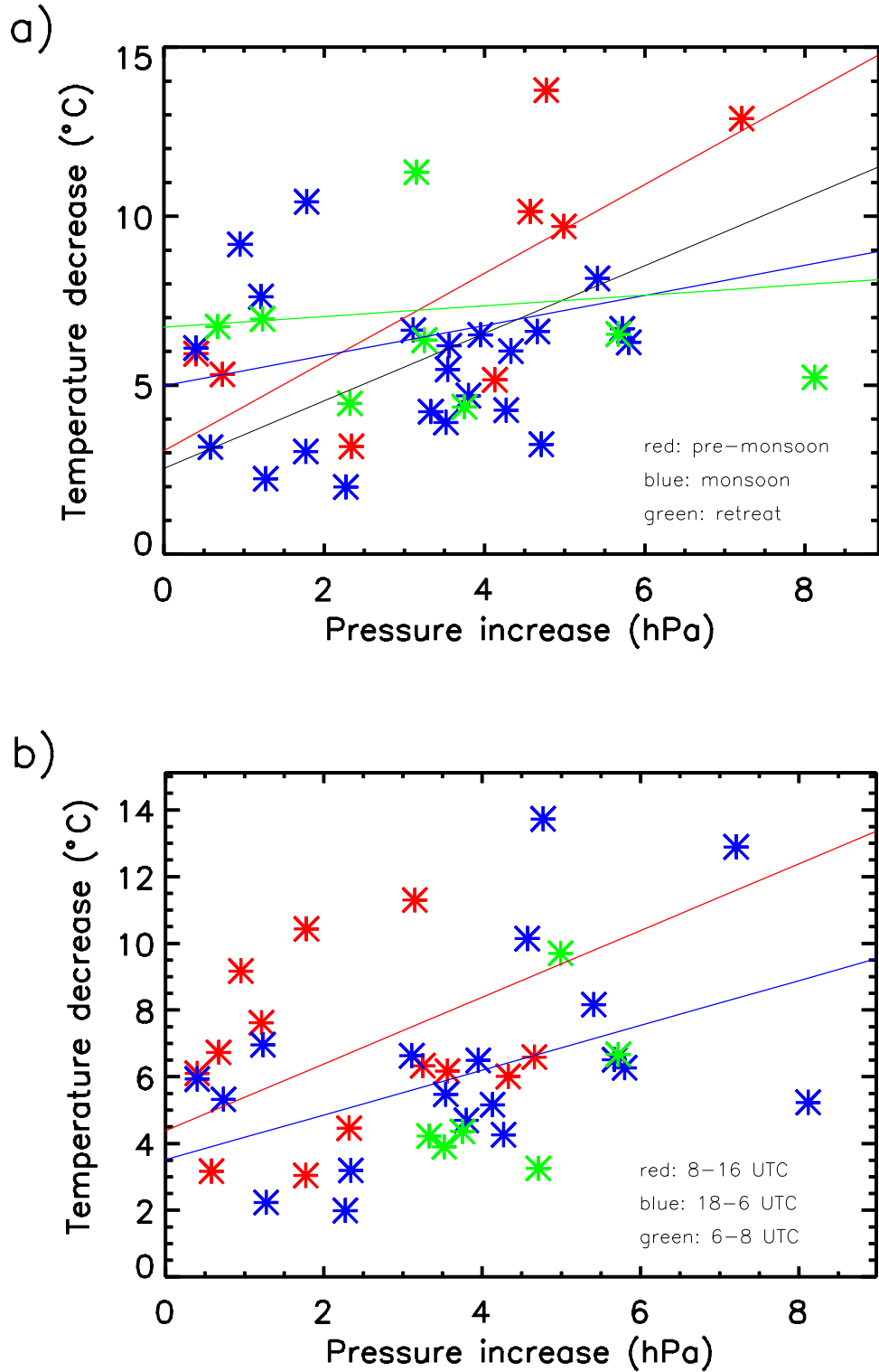


**Figure 3.10:** Pressure increases and temperature decreases from the observed cold pools. As Figure 3.9, colours in a) represent the whole period and individual sub-periods. Colouring in (b) represents the time of day (red: 8–16 UTC, blue: 18–6 UTC, green: 6–8 UTC, there were no events between 16 and 18 UTC). Coloured lines denote best-fit from a least squares method.

Figures 3.10 a) and 3.10 b) show that in observations colder cold pools give larger pressure increases, as expected. The relationship has a weak correlation of 0.3 (statistically significant at  $p < 0.1$ ). Higher correlation of 0.6 (statistically significant at  $p < 0.1$ ) was obtained for pre-monsoon cases only, but it needs to be noted that there are only 8 cases in pre-monsoon period, which is approximately 20% of the full sample. Monsoon and retreat sub-periods had only weak correlations of 0.08 and -0.2 respectively (not statistically significant). This is due to the larger scatter and higher number of events than in the pre-monsoon period. A paired t-test was used for calculation of all significances of correlation.

The overall distribution in Figure 3.10 a) is similar to that shown in Figure 8 of E2008, except that a small percentage of cold pools in E2008 study (1.5%) had either larger pressure increases or temperature deficits. Based on the total number of data points and the data points with temperature decrease greater than 14 °C or pressure increase greater than 7 hPa in E2008, we would expect approximately 0.6 data-points with magnitudes of at least 14 °C or 7 hPa for temperature decrease and pressure increase respectively to be found in our study if magnitudes of cold pool properties in Niamey were identical to those in Oklahoma. The fact that there were no such cold pools in our study, however, is not statistically significant at the 0.05 significance level to conclude that cold pools in Niamey are weaker in terms of temperature decrease and pressure increase when compared to Oklahoma. Approximately 40 times larger data-set would be needed to make any conclusions about the occurrence of such strong cold pools in Niamey when compared to Oklahoma. Note that MCSs tend to be observed at a particular point in their lifecycle in Niamey. This was often either in a mature or dissipating stage, although difficult to differentiate at times due to only one radar data source and attenuation by rainfall as already discussed. Hence, stronger cold pools may be observed elsewhere in West Africa. This is a limitation of this observational study, which was, by necessity, confined to one spatial point.

Observed night-time cold pools are generally associated with higher values of pressure increase for a given temperature decrease than day-time ones (Figure 3.10 b)). The reason for this is likely the fact that at night the boundary layer tends to be stable due to nocturnal cooling and during the day the surface layer is unstable. The magnitude of the cold pool related change in temperature aloft is therefore greater than observed at the surface at night, and less during the day (Davies *et al.* 2005). The cold pool may also flow on top of the stably stratified surface layer at night (Heinold *et al.* 2013; Marsham 2011a), significantly reducing the temperature decrease measured at the surface. However, both small and large decreases in surface temperature in Figure 3.10 b) show that at least some of downdrafts at Niamey routinely reach the surface despite the presence of a nocturnal inversion. Figure 3.10 b) shows that pressure increases greater than ~5 hPa occurred only at night or in the morning (before 8am), which is consistent with E2008 and likely the result of deeper cold pools associated with maturing/dissipating MCSs and the known tendency for large organised systems at night over Niamey (Rickenbach *et al.* 2009). The correlation for daytime events was 0.25 and for night-time events 0.43 (both statistically

significant  $p < 0.1$ ). A contributing factor to the lower daytime correlation may be the variations in the super-adiabatic boundary-layer near the surface and related overestimation of the temperature decrease by several degrees in some cases.

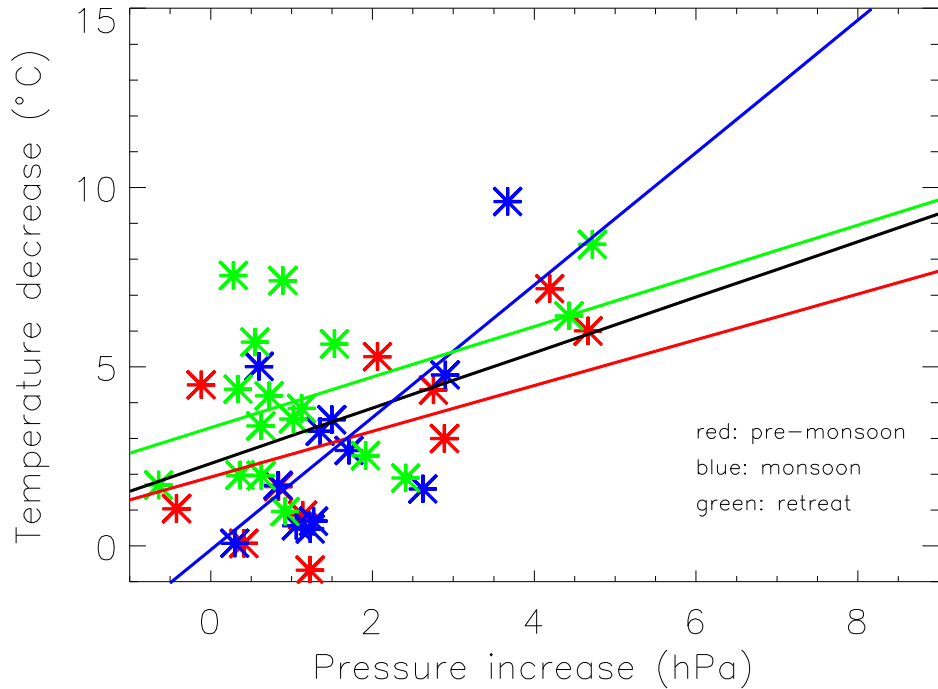


**Figure 3.11:** A Figure 3.10, but for Cascade.

Cold pools in *Cascade* exhibit, as in observations, a positive relationship between pressure increases and temperature deficits (Figure 3.11), as expected. The overall correlation for *Cascade* is 0.46 (statistically significant  $p < 0.1$ ), which is greater than for observations. Unlike observations, *Cascade* correlations are more similar among the different sub-periods; 0.50 for pre-monsoon, 0.68 for monsoon and 0.43 for retreat period cold pools (all statistically significant  $p < 0.1$ ).

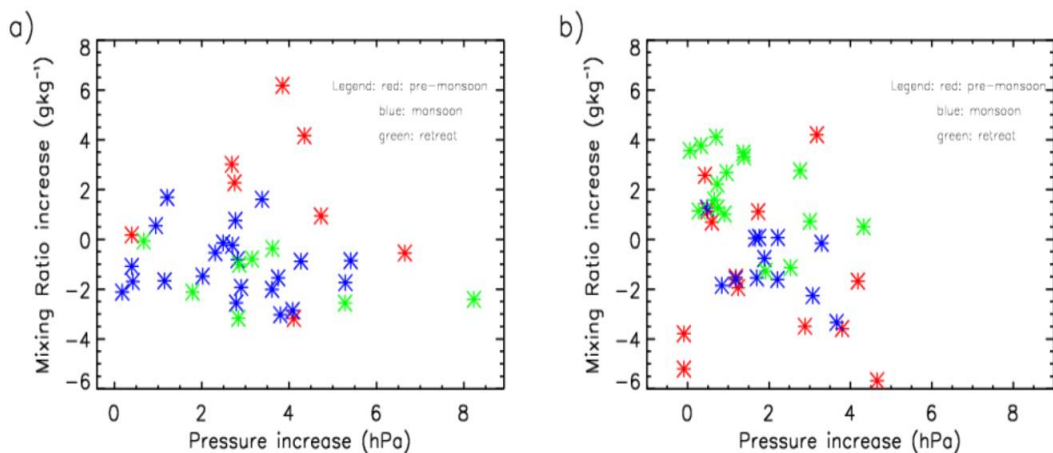


**Figure 3.12:** As Figure 3.11, but for mixing ratio for a) observations and b) *Cascade*.

In order to see whether more evaporation into the air parcel feeding the cold pool, which is responsible for greater pressure increases via greater cooling (see e.g. Figure 3.11), is also related to the amount of moisture the cold pool actually transports into the region, the relation between cold pool moisture (WVMR) and pressure increase was investigated. This relation (Figure 3.12 a)) shows that there is a large amount of scatter, implying no clear correlation. There were no weak and moist or strong and moist cold pools, but the relatively dry cold pools were associated with a range of pressure rises. In *Cascade*, there is a weak tendency for intense cold pools with larger pressure increases to be drier (Figure 3.12 b)), with a correlation of 0.41 overall and 0.56 if pre-monsoon cases are not counted (both correlations statistically significant at  $p < 0.1$ ). The overall trend in *Cascade* is consistent with either a strong contribution of dry mid-level air to these strong cold pools, or perhaps a tendency for dry mid-levels to cause strong cold pools. The role of mid-level dryness in determining cold pool properties is investigated in the next section.

### 3.3.3 Role of mid-level dryness

Dry mid-tropospheric air masses can be ingested into MCSs and these dry intrusions can strongly modulate convective activity (e.g., Yoneyama and Fujitani 1995; Brown and Zhang 1997; Yoneyama and Parsons 1999). It was therefore hypothesised that the stronger cold pools in the pre-monsoon period may be caused by seasonally drier mid-levels in that period (Marshall *et al.* 2008; Barnes and Sieckman 1984). We test this hypothesis using a one-dimensional conceptual model, where radiosonde data were used to quantify mid-level dryness for each cold pool using  $\Theta_w$  (wet-bulb potential temperature) depression (i.e. difference between  $\Theta$  and  $\Theta_w$  averaged between 550 and 750 hPa) using the nearest pre-storm sounding. These soundings were between 38 minutes and 5 hours 52 minutes before the cold pool crossing. As a result of these long gaps between the radio-sounding and the cold pool in some cases the applicability of the one-dimensional model may be limited by significant horizontal gradients and transports. Despite this limitation, these were the best mid-level data available.

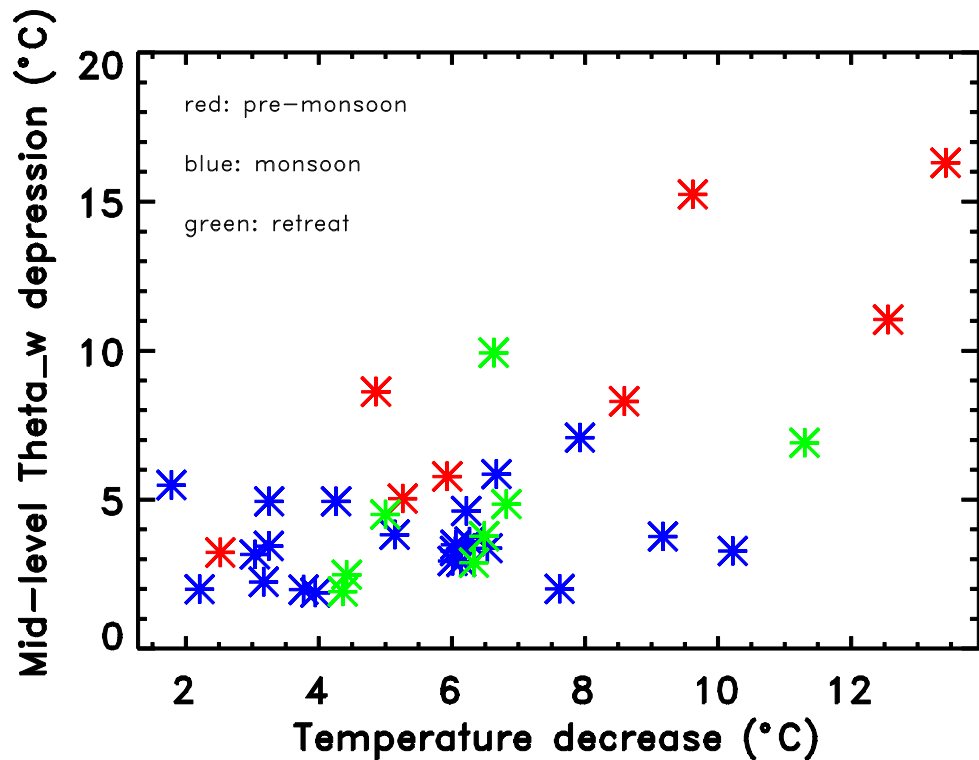


**Figure 3.13:** As Figure 3.12, but for average mid-level (550-750hPa)  $\Theta_w$  depression ( $(\text{saturated } \Theta_w) - \Theta_w$ ) against temperature decrease across leading edge of cold pool.

Figure 3.13 shows the relation between mid-level  $\Theta_w$  (wet-bulb potential temperature) depression (differences between saturated  $\Theta_w$  and  $\Theta_w$  averaged between 550 hPa and 750 hPa level) and surface cooling associated with a cold pool. The  $\Theta_w$  depression indicates the dryness of midlevels. A positive relationship between this and the surface cooling would show that dryer midlevels are associated with colder cold pools, likely due to enhanced evaporation of rain in dry mid-level air. The  $\Theta_w$  depressions range from 1.9 °C to 16.3 °C. Pre-monsoon period  $\Theta_w$  depressions tend to be larger, associated with driest mid-levels, while monsoon period  $\Theta_w$  depressions tend to be lowest and associated with least dry mid-levels. There is a positive relationship between  $\Theta_w$  depressions and the surface cooling from a cold pool (correlation of 0.6). This relationship is the strongest during the pre-monsoon sub-period (correlation of 0.8) and weakest during the monsoon sub-period (correlation of 0.4), showing that mid-level dryness is most important for the temperature of the cold pool in the pre-monsoon sub-period. Other microphysical effects such as melting and sublimation may be more important in the monsoon as well as retreat sub-periods. There are no cases associated with a large  $\Theta_w$  depression and low  $\Delta T$ ; however, small  $\Theta_w$  depression cases were associated with an approximately 8 °C range of  $\Delta T$ , especially during the monsoon and retreat periods. This relation supports the hypothesis that drier mid-levels tend to produce colder cold pools by stronger evaporational cooling.

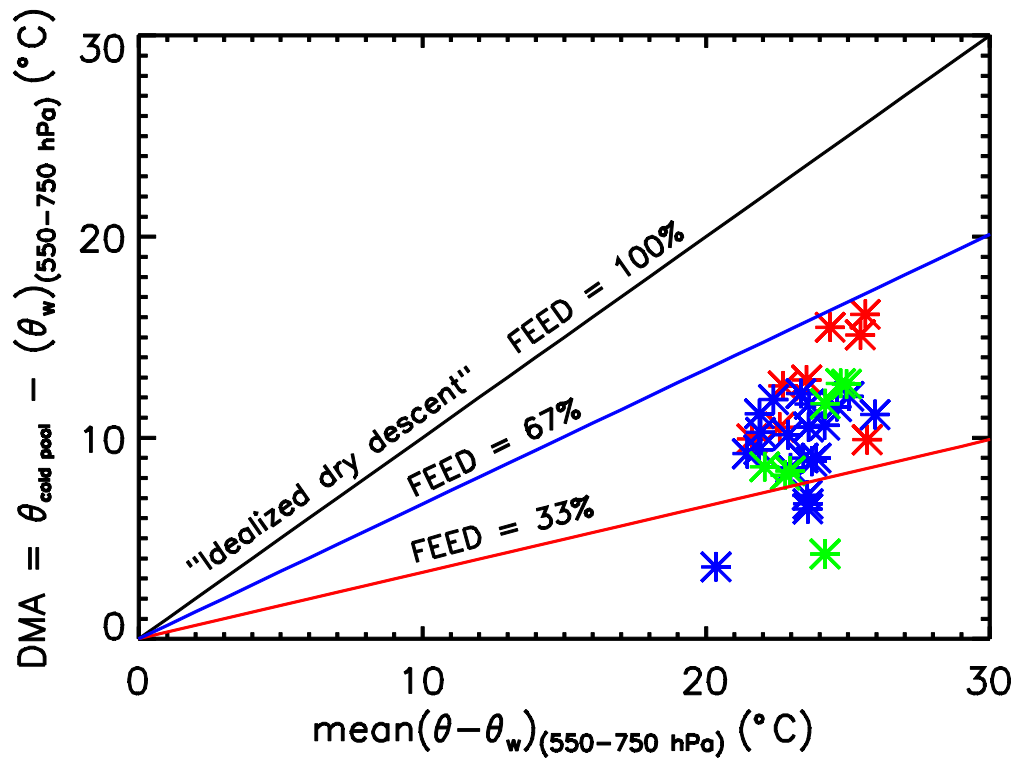


**Figure 3.14:** As Figure 3.13, but for Departure from Moist Adabat ( $DMA = \Theta_{cold\ pool} - \text{mean}(\Theta_w(550\ \text{to}\ 750\ \text{hPa}))$ ) versus mid-level dryness defined using the difference between  $\text{mean}(\Theta(550\ \text{to}\ 750\ \text{hPa}))$  and  $\text{mean}(\Theta_w(550\ \text{to}\ 750\ \text{hPa}))$ . Diagonal lines represent constant Fractional Evaporational Energy Deficit (FEED) of 100% (black), 67% (blue) and 33% (red).

Figure 3.14 shows how close observed cold pool temperatures are to idealised descents of mid-level air. In this figure, we plot “departure from moist adiabat” (DMA), defined as

$$DMA = \Theta_{cold\ pool} - \text{mean}(\Theta_w(550\ \text{to}\ 750\ \text{hPa})) \quad (3)$$

Against mid-level dryness defined using the difference between mean potential temperature and wet-bulb potential temperature in the 550 to 750 hPa layer. Therefore Figure 3.14 shows how the cold pool potential temperature minus the wet-bulb potential temperature of mid-levels (y-axis) depends on the mid-level  $\Theta_w$  depression. If mid-level air was cooled by evaporation of precipitation and descended whilst being kept saturated by continued evaporation then the air would descend moist adiabatically and the cold pool potential temperature would equal the mid-level  $\Theta_w$  (y-axis value equals zero in Figure 3.14). In contrast, if mid-level air instead descended completely dry-adiabatically then the potential temperature of the cold pool would equal the potential temperature of the mid-levels and data would lie on the one-to-one line in Figure 3.14. Therefore, how far the data are from the one-to-one towards the x-axis line in Figure 3.14 is a measure of the degree of saturation in the idealised one-dimensional descent. We therefore refer to the y-axis as the “Departure from Moist Adabat” (DMA) and the ratio of both axes as the “Fractional Evaporational Energy Deficit” (FEED), with the one-to-one line of FEED = 100%.

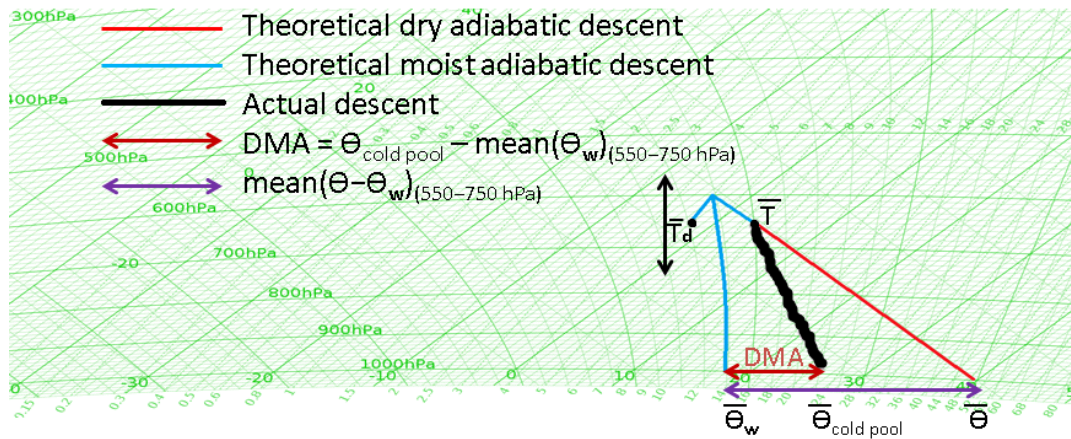


**Figure 3.15:** A section of a tephigram showing an example of a graphical representation of mean mid-level (550 – 750 hPa averaged) temperature ( $T$ ) and dew-point temperature ( $T_d$ ) and associated mean wet-bulb potential temperature ( $\Theta_w$ ) and dry-bulb potential temperature ( $\Theta$ ).  $\Theta_{cold\ pool}$  represents an example potential temperature of a cold pool as measured at the surface. Red line represents dry adiabatic descent, blue line represents moist adiabatic descent and the black line is an example possible descent of a cold pool. Departure from Moist Adibat (DMA) is the difference between  $\Theta_{cold\ pool}$  and mean mid-level  $\Theta_w$ .

The values in Figure 3.14 can also be related to the energetics of the downdraught. For a fixed pressure of source air (Figure 3.15), the potential energy of cooling by evaporation is approximately proportional to the area between the red and blue lines in Figure 3.15 (the energy is proportional to the tephigram-area bounded by the  $\Theta_w$  line of saturated descending air and the theta-line for unsaturated descending air, and here we approximate this by a triangle). As noted above, if FEED is zero, then the downdraught is fully saturated in its descent, and we could regard DCAPE (Downdraught Convective Available Potential Energy) to be a good measure of the downdraught potential energy released.

Figure 3.14 shows that  $\Theta_{cold\ pool}$  values are never equal to mid-level  $\Theta_w$  values, with the moistest cold pool having DMA of 3.6 °C, confirming that no cold pool in our study was formed by the theoretical, perfectly moist adiabatic descent of mid-level air. In contrast, the highest value of DMA is 16.1 °C. All data points lie below the line of FEED of 67% and the lowest data point has a FEED of 17.6%. The overall relationship suggests that drier mid-levels are related to greater DMA and FEED (correlation between DMA and mid-level  $\Theta_w$  depression is 0.5 with  $p < 0.001$ , correlation between FEED and mid-level  $\Theta_w$  depression is 0.03 with  $p < 0.89$ ). This suggests that the ability of precipitation to keep the descending parcel saturated decreases with drier mid-levels, which may be due to greater mixing of dry air or insufficient availability of precipitation to be evaporated into the descending parcel. Pre-monsoon data points have generally greater percentages of FEED and lie closer to the FEED of 67% line. This is not statistically significant, but suggests that the drier atmosphere in the pre-monsoon period may lead to drier descents.

### 3.3.4 Cold-pool winds

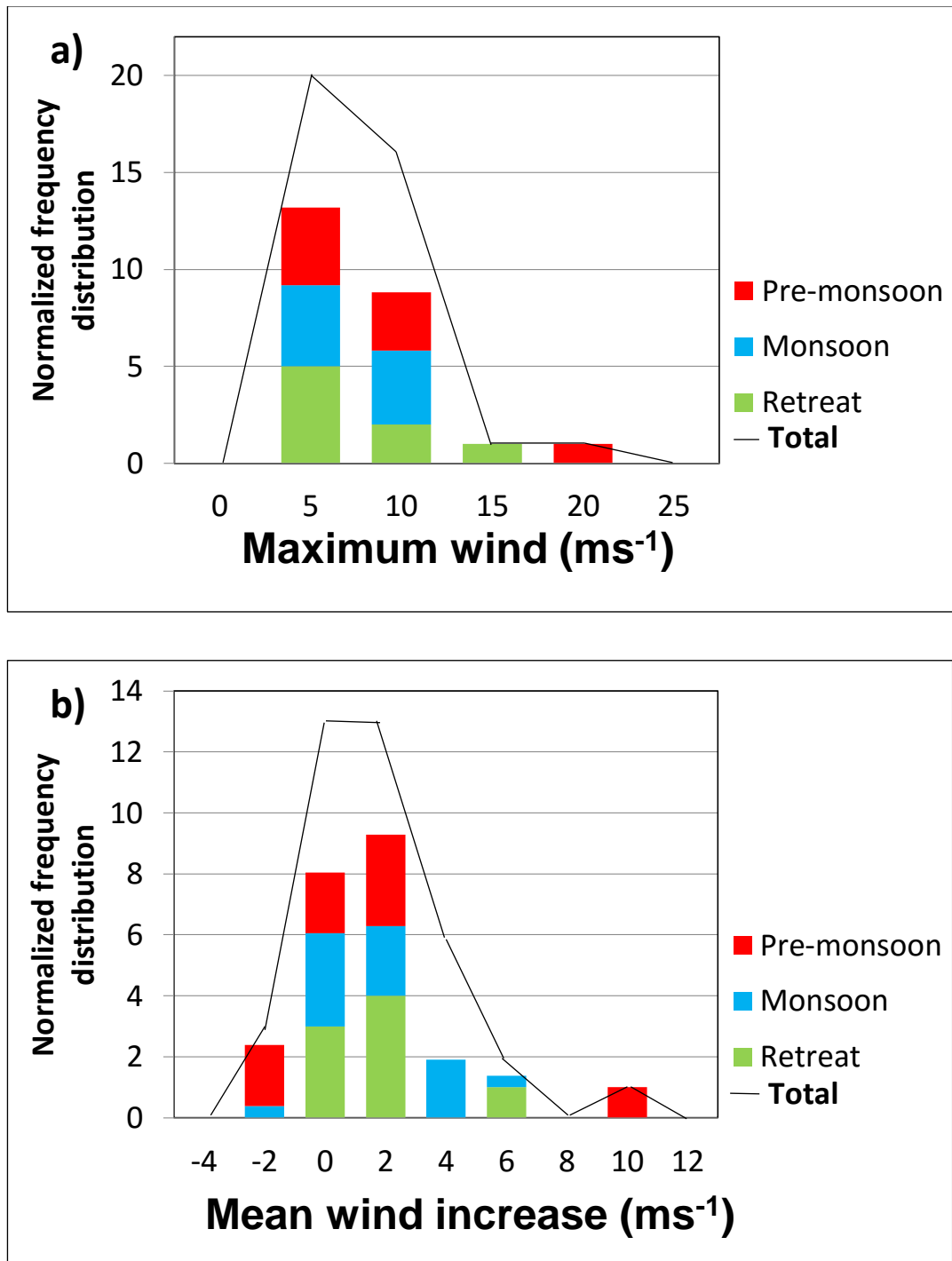
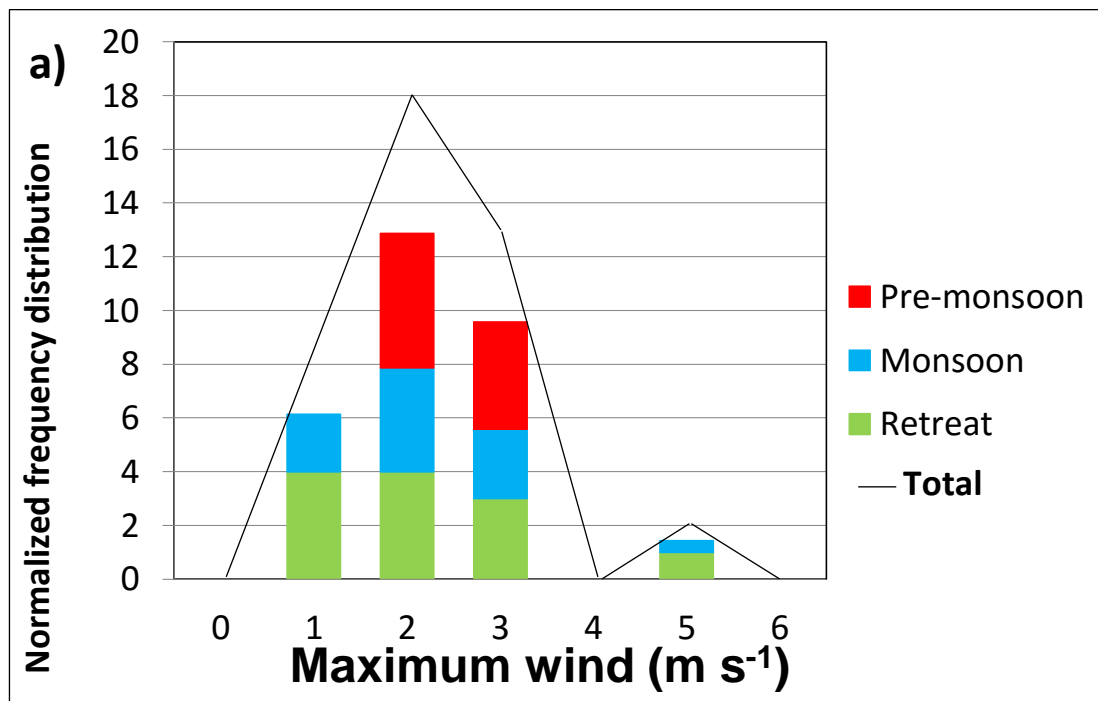


**Figure 3.16:** As Figure 3.9, but for observed 3 m (a) wind gusts and (b) mean wind increases.

The observed maximum wind gusts range from 3.4 to 21.4  $\text{m s}^{-1}$  with most cold pools having gusts between 2.5 and 12.5  $\text{m s}^{-1}$  (Figure 3.16 a)). The mean wind can either increase (30 cases) or decrease (8 cases) during a cold pool passage, with the magnitudes of increase generally between 0

and  $6 \text{ m s}^{-1}$ , with the greatest value of increase being  $9.8 \text{ m s}^{-1}$  (Figure 3.16 b)). The magnitudes of the decreases were  $2.3 \text{ m s}^{-1}$  and less and were always associated with a mean decrease of the general environmental wind speed. Magnitudes of maximum gusts as well as changes in mean wind generally agree with previous studies (e.g. Addis *et al.*, 1984; Saxen and Rutledge, 1998, E2008). There are some higher values observed in E2008, but as already discussed in section 3.1.2., approximately 40 times larger dataset would be needed to make any conclusions.

The mean for maximum wind gusts in the pre-monsoon period was  $10.1 \text{ m s}^{-1}$ , which was greater than that in the monsoon and retreat periods ( $7.6$  and  $7.5 \text{ m s}^{-1}$  respectively). This difference was, however, not statistically significant. There were comparable mean wind-speed changes ( $+1.4$ ,  $+1.6$  and  $+1.4$  for pre-monsoon, monsoon and retreat respectively). The mean pre-monsoon gusts were strongly affected by a single strong event on 17<sup>th</sup> June, when the highest gust of  $21.4 \text{ m s}^{-1}$  was recorded. If this case was removed, then the mean pre-monsoon gust decreases to  $8.5 \text{ m s}^{-1}$ , which is still higher than other sub-periods, but again not significantly.



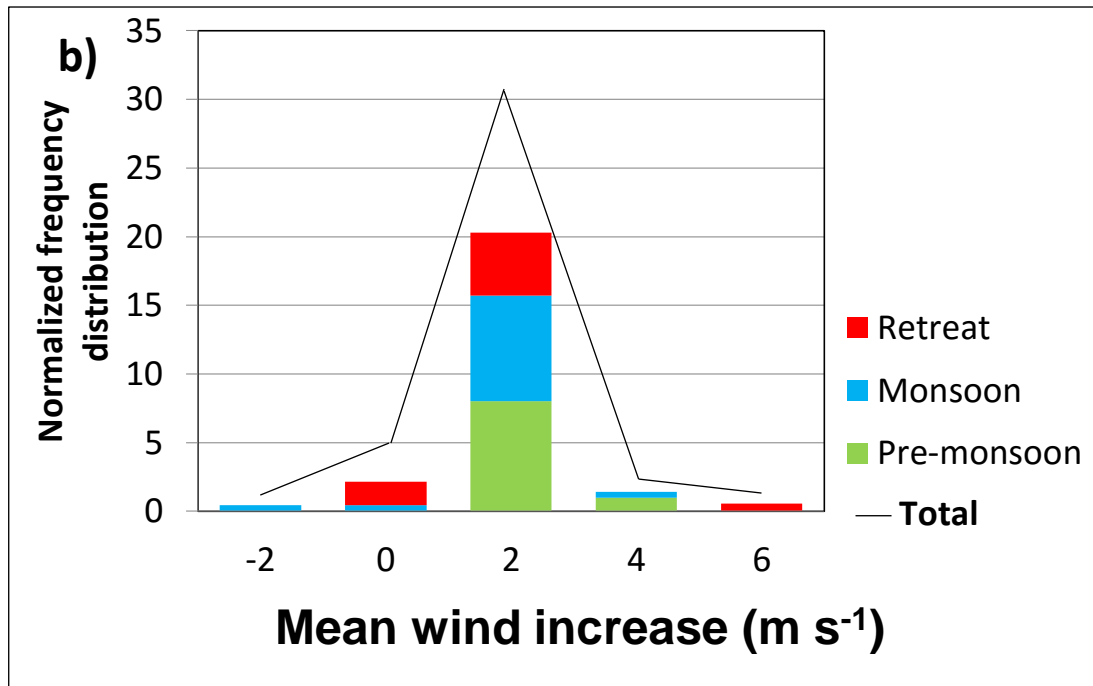


**Figure 3.17:** As Figure 3.16, but for Cascade winds at 3 m.

Figure 3.17 a) shows that simulated cold-pool related maximum winds in *Cascade* are lower than in observations (see Figure 3.16 to compare). While over 90% of observed cold pools had maximum 3 m wind gusts of over 6 m s<sup>-1</sup>, with one event of 21.4 m s<sup>-1</sup>, *Cascade* cold pools didn't have any 3 m winds over 6 m s<sup>-1</sup>, with all except 2 cases (95 %) being below 4 m s<sup>-1</sup>. The lower magnitudes of maximum winds in *Cascade* may be explained by weaker cold pools with weaker pressure gradients, a surface roughness error in the *Cascade* runs (hypotheses examined later in this section) or the fact that turbulence, being a sub-grid phenomenon, is parameterized (not resolved) in *Cascade* and the 7-min smoothing of the observations to convert 1-min data to 4-km grid-scale for comparison with the model is approximate (see Section 3.2.5.).

The modelled increases in mean 4-m winds from cold pools are also underestimated compared with observations. While three observed mean wind increases had a value greater than +6 m s<sup>-1</sup>, *Cascade* mean increases never went above that value. While an increase in mean wind speed is normally expected with a passage of a cold pool due to the gusty nature of majority of cold-pool passages, several cases were associated with a mean decrease. *Cascade* modelled mean wind speed changes were negative in 5 out of 42 cases with the passage of a cold pool whereas observed mean wind speeds decreased in 8 out of 38 cases.

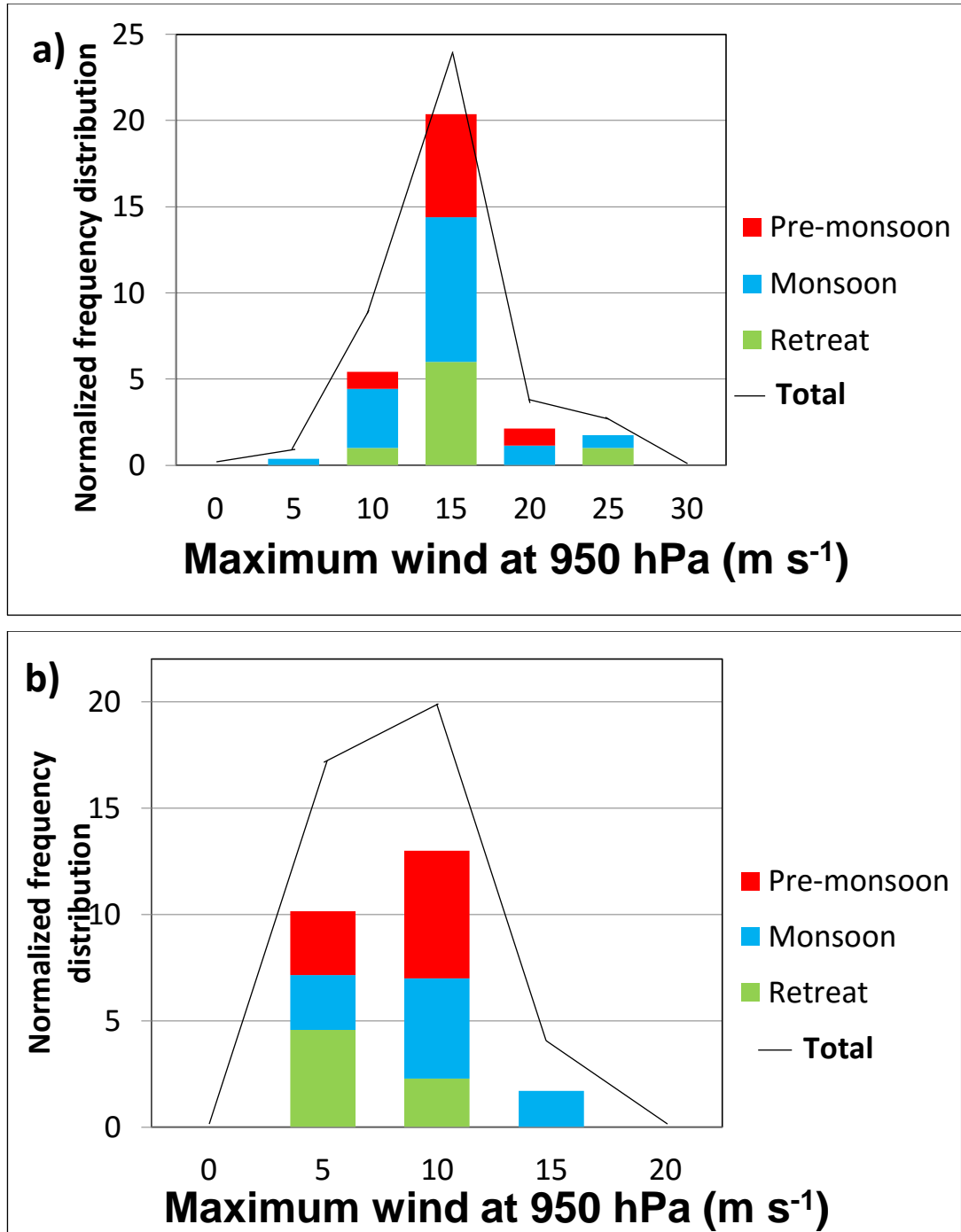


**Figure 3.18:** As Figure 3.16, but for maximum wind at 950 hPa. a) Observed; b) Cascade. The observed values in a) were interpolated from values of two closest levels as provided by the Radar Wind Profiler (with heights of the 950 hPa level obtained from radiosondes and ranging from 310 to 370 metres above ground).

It was hypothesised that the underestimation of winds in Cascade has been caused by errors in surface roughness. This hypothesis was tested by comparing observed and modelled cold-pool related mean wind changes at 950 hPa level. Winds at 950 hPa level were obtained from the Radar Wind Profiler. Since Radar Wind Profiler provides winds at height levels, a pressure profile was taken from the nearest radiosonde ascent and winds

from Radar Wind Profiler were interpolated to 950 hPa. At this level, surface roughness effects should be much smaller than at 4 m (see Figure 3.18). An improvement in underestimation of maximum wind by the model can be seen at this level, although *Cascade* still underestimates maximum winds by approximately 30%.

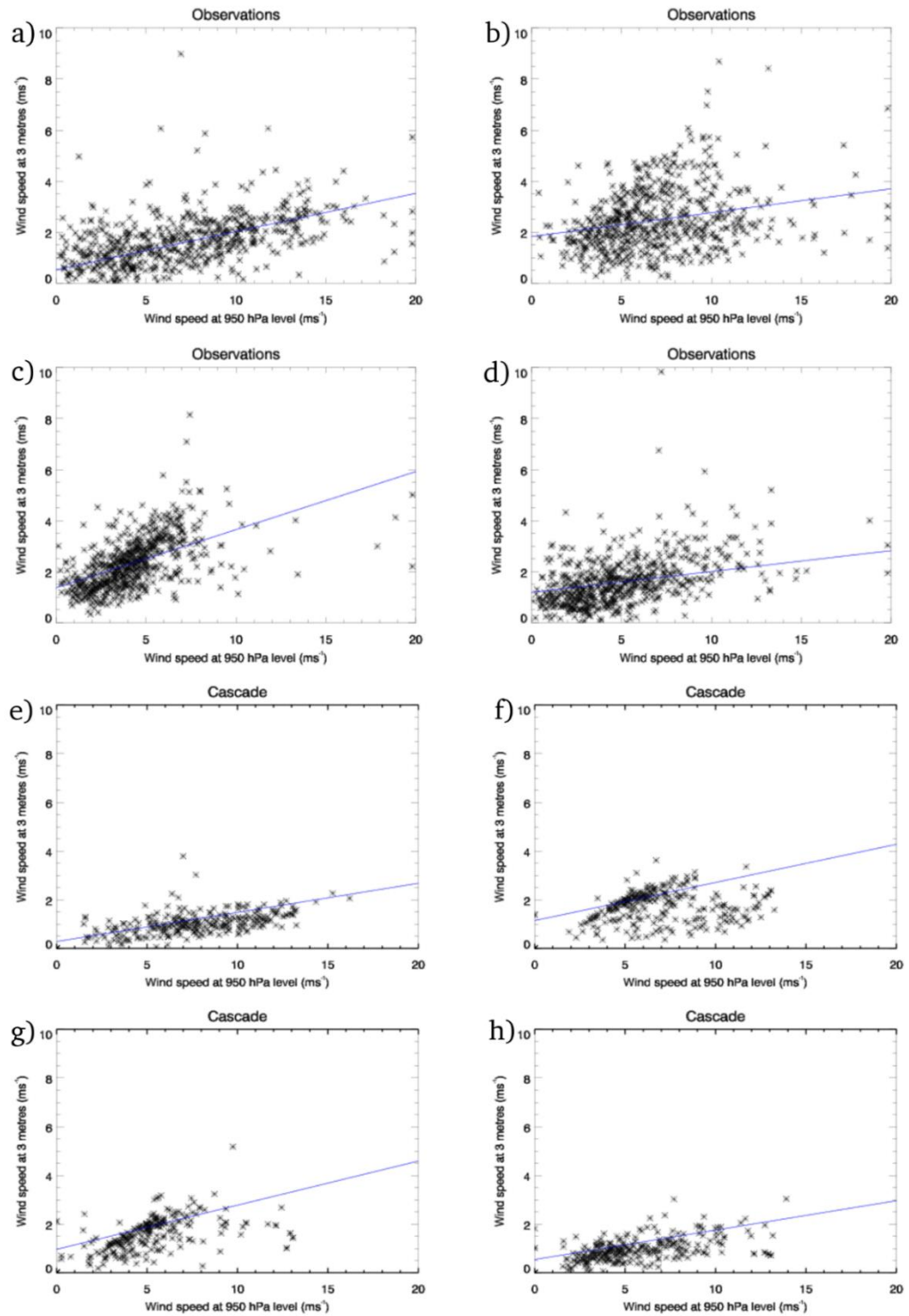


**Figure 3.19:** Relationship between 950 hPa level and 3 m winds for all available values (not only cold pools). a) – d) is for observations, e) – h) is for Cascade. Blue lines are lines of best fit. The times in UTC are: a) 00-06, b) 06-12, c) 12-18, d) 18-24, e) 00-06, f) 06-12, g) 12-18, h) 18-24.

Figure 3.19 compares all available values (i.e. at all times, not only for cold pool events) of 3 m wind speeds against 950 hPa level wind speeds and shows that *Cascade* wind speeds at both levels are generally lower than those observed. The lowest level for wind in *Cascade* is at 4 m above ground and these 4 m winds were interpolated to 3 m using winds at 4 m and 13 m, assuming a log-profile of wind speed with height. Mean 3 m wind speeds for all times of day were 1.6 and 2.2 m s<sup>-1</sup> for *Cascade* and observations respectively. At the 950 hPa level, mean winds were 5.4 m s<sup>-1</sup> and 5.9 m s<sup>-1</sup> for *Cascade* and observations respectively. This shows that *Cascade* underestimates winds at 3 m by approximately 30%, but by less than 10% at 950 hPa level.

Different times of day in Figure 3.19 feature a different amount of scatter. Greatest scatter (or lowest correlation) is observed in the 06-12 (morning) time period (Figures 3.19 b) and f)) and smallest scatter in the 12-18 (afternoon) time period (Figures 3.19 c) and g)) for both observations and *Cascade*. Greatest scatter in the morning is due to the breakdown of the nocturnal low-level jet in that time period, which is located near 950 hPa. Points early in that period, when the low-level jet is still active and there is a stable layer near the surface, would be expected to have stronger 950 hPa winds for a given 3 m wind. Points later in that period (before noon) would be expected to have weaker 950 hPa winds for a given 3 m wind as the atmosphere is normally well-mixed by that time up to 950 hPa and there is no low-level jet anymore. This changing relationship within the time period is therefore responsible for the scatter. In addition, the low-level jet is a narrow region of strong winds, which can fluctuate with height. Therefore, when it is normally present (overnight), there is larger scatter due to the vertical gradient of wind speed associated with the low-level jet. Low scatter and generally weaker winds in the afternoon (Figures 3.19 c) and g)) are a result of strong mixing, which is responsible for a stronger relationship between these two levels.

The 12-18 UTC time-frame (Figures 3.19 c) and g)) is the most useful for our test of roughness in *Cascade* due to the strongest mixing and greatest influence of the drag due to surface roughness on the whole layer. During the 12-18 UTC time frame, lines of best fit for observations have steeper gradient (0.31) (Figure 3.19 c)) than *Cascade* (0.25) (Figure 3.19 g)). This shows that *Cascade* underestimates surface winds by approximately 20%, suggesting that there is an issue with surface roughness, or possibly mixing in *Cascade*. The underestimation of both surface and 950 hPa wind increases and wind gusts associated with cold pools is however greater and the issue with surface roughness does not explain the whole difference. To draw more specific conclusions, further research into this issue is needed.

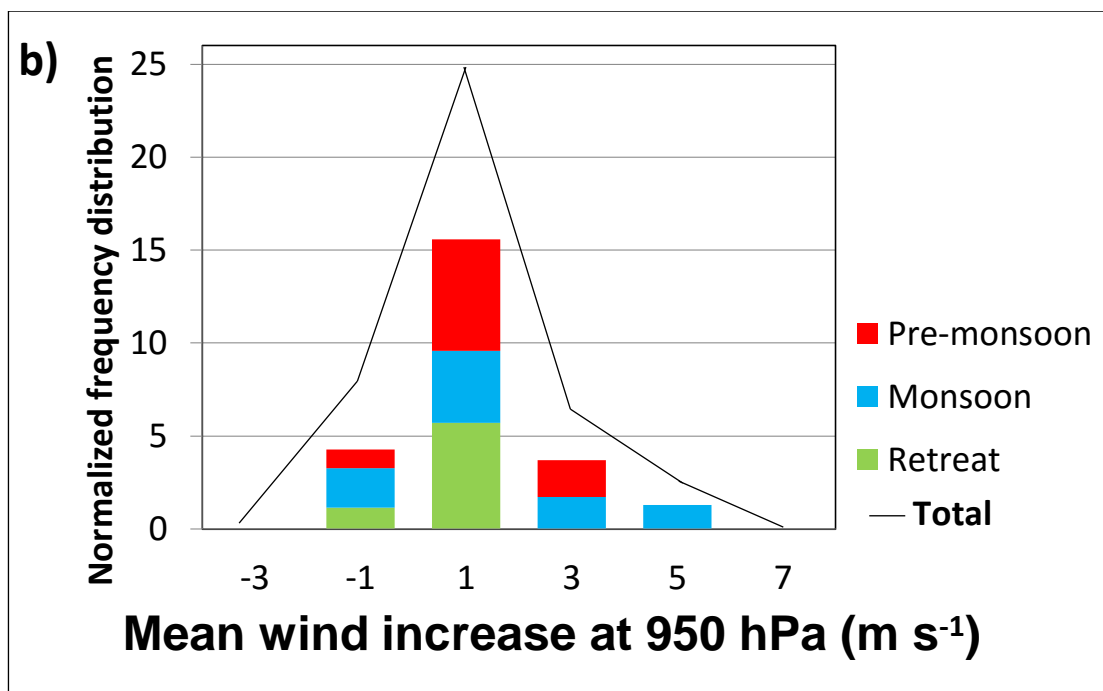
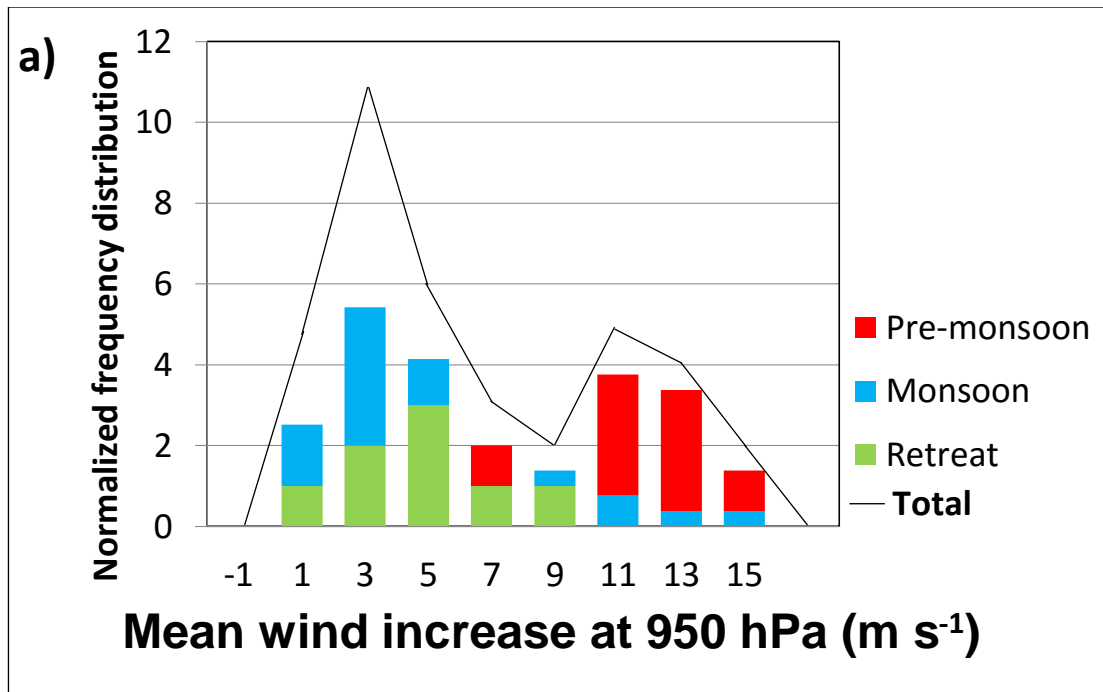


**Figure 3.20:** As Figure 3.18, but for a) observed and b) Cascade mean wind increase at 950 hPa. Observed winds obtained from wind-profiler data.

Figures 3.20 a) and 3.20 b) show that the population of observed mean wind changes at 950 hPa level has 2 peaks, the first having mean wind increases between  $\sim 1$ - $7 \text{ m s}^{-1}$  and the second between  $\sim 9$ - $15 \text{ m s}^{-1}$ . The smallest and largest values of mean wind increase being  $0.3 \text{ m s}^{-1}$  and  $15.8 \text{ m s}^{-1}$  respectively. The second peak is largely represented by pre-monsoon cold pools, which have a mean wind increase of  $11.3 \text{ m s}^{-1}$ , much larger than the mean wind increase of all cold pools, which is  $5.9 \text{ m s}^{-1}$ . At the surface, the observed mean wind increase in the pre-monsoon period is similar to that of the whole season. This shows that these stronger winds at 950 hPa in pre-monsoon do not get mixed to the surface, which is likely a

result of a strong nocturnal stable layer (7 out of 8 pre-monsoon cold pools crossed Niamey in the night-time (19-06 UTC) period). *Cascade* has only one peak with values of wind changes between  $\sim -1$  and  $+5 \text{ m s}^{-1}$ , with maximum value of  $4.7 \text{ m s}^{-1}$ . *Cascade* therefore still underestimates values of mean-wind changes at 950 hPa level by a factor of 4 to 5 compared with observations (and again produces too many decreasing mean winds).

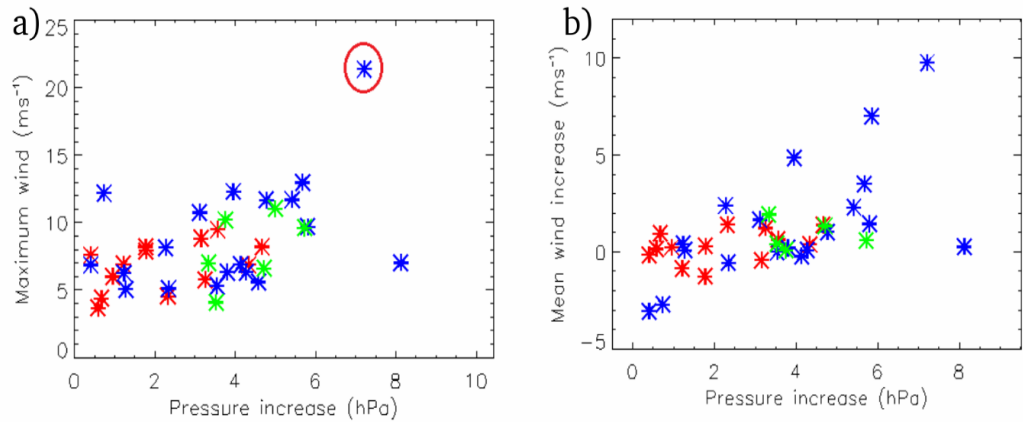


**Figure 3.21:** Observed cold-pool related maximum wind gusts at 3 m against pressure increases at 1.5 m a) and mean wind increases b). Colours represent different times of day (red: 8-17 UTC, blue: 19-6 UTC, green: 6-8 UTC and 17-19 UTC).

The relation between observed pressure changes and maximum wind gusts, which are partly driven by the pressure changes, is positive with a correlation of 0.46 ( $p < 0.1$  – statistically significant) (Figure 3.21 a)). In case of mean wind increase (Figure 3.21 b)), the relation is also positive with a correlation of 0.45 ( $p < 0.1$  – statistically significant). There was one outlier in Figure 3.21 a) – the 17<sup>th</sup> June event circled in Figure 3.21 a) – where additional features such as mixing of momentum from upper levels due to weak stable layer may have caused stronger winds than would be expected from the observed pressure increase alone. If this outlier (circled) is taken away from Figure 3.21 a), the correlation reduces to 0.42 ( $p < 0.01$ , statistically significant). The gradient of the best-fit lines is 0.84 and 0.66 for maximum wind and mean wind increase, respectively. The diurnal distribution of cold pool related wind gusts shows that the higher cold-pool related gusts (above  $\sim 10 \text{ m s}^{-1}$ ) weren't limited to the daytime. This does not contradict the fact that the stably stratified nocturnal boundary layer can inhibit cold-pool winds at night (Parker 2008; Marsham *et al.* 2011a); cold pools over Niamey from some of the mature nocturnal MCSs can clearly mix down through this night-time stable layer (see also temperature changes in section 3.3.2).

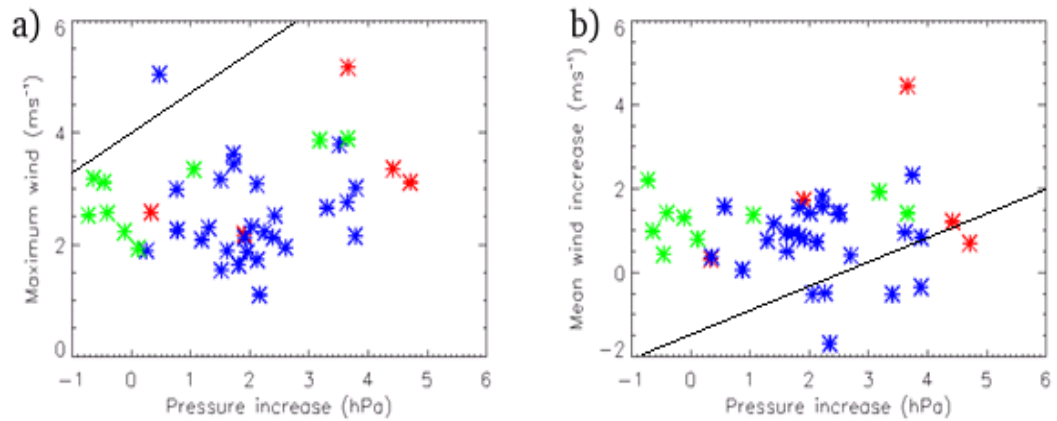


**Figure 3.22:** As Figure 3.21, but for Cascade. Black lines are best-fit lines for the corresponding observational relationships from Figure 3.21.

In *Cascade* (Figure 3.22) the relationship between pressure increase and wind is also positive with weak correlations of 0.33 and 0.34 for maximum wind and mean wind increase, respectively (these correlations are weaker than those for pressure increase vs maximum wind and mean wind increase in observations, with values of 0.46 and 0.45, respectively). Figure 3.22 shows lines of best fit corresponding to observations (obtained from Figure 3.21). Comparing these to the data in Figure 3.22, it can be seen that the relationship in *Cascade* has shallower gradient (slower increase of wind gusts and increases with increasing pressure changes), further confirming weaker surface winds in *Cascade* than in observations. As in observations, the greatest magnitudes of modelled cold-pool winds are not limited to daytime, showing that *Cascade* cold pools also routinely break through the near-surface stable layer.

### 3.4 Conclusions

MCSs are an important feature of the West African Monsoon, providing most of the rainfall over the Sahel. Cold pools contribute to the organisation of these MCSs, form a crucial component of the monsoon flow (Marshall *et al.* 2013) and ventilate the Saharan heat low (Garcia-Carreras *et al.* 2013). This study has quantified properties of cold pools from MCSs observed over Niamey in the Sahel during the 2006 AMMA field campaign, using a methodology similar to E2008. Properties were compared with those from a 4-km Unified Model simulation (run within the *Cascade* project) from the same 122-day period.

Every observed cold pool in this study was associated with a temperature decrease, ranging from 1.8 °C to 13.6 °C, and a pressure increase, ranging from 0.4 hPa to 8.1 hPa. These observed ranges generally agree with those observed by E2008 in the USA, but are missing E2008's largest values. Given the much smaller sample size of our study, it is not possible to say whether these more intense events are rarer in Niamey than the USA or whether our sample is too small to observe them.

Water vapour mixing ratio was found to decrease just after the cold pool passage in all but 10 cases. The magnitude of the decrease did not exceed  $3.5 \text{ g kg}^{-1}$ . This initial decrease was in many cases followed by an increase in the mixing ratio of around  $0.5 \text{ g kg}^{-1}$ , sometimes to values greater than before the cold pool passage, which appears to be generated by the MCS rainfall. The mean equivalent potential temperature was found to increase in 6 out of the 38 cases, but decrease in others. A maximum in observed winds has been identified with every passage of a MCS, ranging from  $3.4 \text{ m s}^{-1}$  to  $21.4 \text{ m s}^{-1}$ . The time-averaged 3-m mean wind from before to after the gust front was found to usually increase, although decreases were observed, with changes ranging from  $-2.3$  to  $+9.8 \text{ m s}^{-1}$ . At the 950 hPa pressure level, the mean wind increased in all cases (including when it decreased at 3 m) with magnitudes of the change being between  $0.3 \text{ m s}^{-1}$  and  $15.8 \text{ m s}^{-1}$ .

Cold pools in the pre-monsoon period gave larger pressure increases and temperature decreases, as well as larger maximum wind gusts and mean wind increases, when compared to the monsoon and retreat periods. These were, however, not statistically significant. At 950 hPa, pre-monsoon cold pools were associated with greater mean wind increases, which was statistically significant, further confirming stronger pre-monsoon cold-pools and showing that cold-pool winds are better represented at that level than at the surface. This is likely due to the fact that night-time cold pools often need to overcome the near-surface stable layer when momentum is being transported to the surface. Pre-monsoon cold pools increased rather than decreased WVMR. Pre-monsoon cases gave little overall change in equivalent potential temperature, which tended to be decreased by cold pools in the monsoon and retreat periods. These differences in changes in WVMR and  $\Theta_e$  between cold pools during the pre-monsoon and later periods were statistically significant at the 90% significance level. Furthermore, we define the Departure from Moist Adiabats (DMA) and Fractional Evaporational Energy Deficit (FEED) and use a simple 1D model to quantify how close the observed cold pools were near wet adiabatic (FEED=0%) or dry adiabatic (FEED=100%) descent. FEED varied from 17.6% to 64.5%, with drier descents for drier mid-levels and during the pre-monsoon period (with only a correlation of 0.5 between DMA and mid-level  $\Theta_w$  depression).

The results show that early season cold pools provide high equivalent potential temperature air at low levels, which especially if reheated could feed later convection, once the high CIN is overcome (see also Torri *et al.*, 2015). Later in the season, the cold pools reduce equivalent potential temperature but will still favour convection by lifting. The results are consistent with observations from Garcia-Carreras *et al.* (2013), who show that cold pools bring moist air towards the Saharan heat low early in the season. The results support the hypothesis that early in the monsoon season, when mid-levels are drier and there is therefore greater diabatic cooling, cold pools will make a greater contribution to the monsoon flow (Marshall *et al.*, 2013).

Cold pools in convection-permitting 4-km Unified Model simulations (*Cascade*) have been evaluated in this study. Cold pools in *Cascade* were always associated with cooling of magnitude up to  $10.1 \text{ }^\circ\text{C}$ , but generally in

the 2 to 6 °C range, which is consistent with observations, although *Cascade* lacks some of the larger magnitude events, which results in overall lower mean. 43% of *Cascade* cold pools were moister than environment (increase in WVMR) and 49% were associated with an increase in  $\Theta_e$ , showing that *Cascade* cold pools are moister than observed. Pressure increases were slightly lower than observed values with the largest *Cascade* pressure increases having magnitudes near 6 hPa, but most cold pools were associated with pressure increase below 2 hPa. Simulated cold-pool wind gusts at 4 m were underestimated by ~50% with mean wind increases being underestimated by ~20% with respect to observations. The relationship between 950 hPa and 3 m winds has shown that *Cascade* 3 m are in general underestimated by ~20%. A future study, on the lines of Stein *et al.* (2015) may investigate whether these weaker magnitudes in many variables associated with *Cascade* cold-pool changes are related to smaller mean MCS size when compared to observations.

*Cascade* simulations capture the seasonality of pressure increase and temperature decrease, as well as WVMR and equivalent potential temperature to some degree (mean values of these variables are higher in the pre-monsoon period). Regarding wind-speed, the seasonality can be seen in the cold-pool composite with pre-monsoon winds being stronger, but there is no clear signal in maximum winds and mean wind increases, which may be related to the overall underestimation of wind speeds.

The evaluation of the simulated cold pools reveals that *Cascade* is able to simulate cold pools that are relatively colder than their environment, with the magnitude of the difference only slightly lower than for observations. Pressure changes were lower than for observed cold pools, suggesting shallower cold pools as the expected pressure increase from the temperature decrease would have been larger if cold pools were of the same depth. Another reason could be differences in surface layers, where *Cascade* may have on average either greater afternoon super-adiabatic or weaker night time stable layers, enhancing the temperature contrast. Moisture content, shown by changes in WVMR and  $\Theta_e$  between the cold pool and its surroundings shows that *Cascade* cold pools are moister relative to their environment. Both of these differences could be due to misrepresentations of MCS microphysics or dynamics, such as errors in the levels from which cold-pool air is fed and into which rainfall evaporates in *Cascade*. Maximum winds and changes in wind speed were considerably lower in *Cascade* than in observations. This was not an artefact of the lower frequency of sampling from *Cascade* data as the 7min smoothing of observed data accounts for that. This was further investigated by comparison with winds at the 950 hPa level to see if surface roughness may play a role in *Cascade*. The results showed that *Cascade* underestimates wind-speeds at both levels with the underestimation being greater at 3 m

(interpolated from 4 m), suggesting that roughness errors may be important in *Cascade*.

It is anticipated that this climatology will be of use in evaluating future model versions. Marsham *et al.* (2011b) and Heinold *et al.* (2013) noted little Sahelian dust uplift and lower than expected cold-pool winds in the 4-km *Cascade* UM simulations. This study shows that the cold-pool winds in the model are weaker than observed (although this may be improved in higher-resolution runs). This suggests that in previous *Cascade*-based studies the contribution of cold pools to the monsoon (Marsham *et al.* 2013a) and in generating summertime dust uplift in the Sahel (Marsham *et al.* 2011b; Heinold *et al.* 2013) may have been underestimated. Future studies could investigate this further by performing a similar analysis using the Benin radar and investigating the entire *Cascade* domain to obtain a larger sample and perhaps spatial variations of cold-pool related wind changes and other properties within the domain.

## Chapter 4

# Case studies of two squall-line mesoscale convective systems

### 4.1. Introduction

This chapter presents two observational case studies of squall-line mesoscale convective systems (MCSs) that crossed an observational supersite in Niamey during the African Monsoon Multidisciplinary Analysis (AMMA) in 2006. Unlike Chapter 3, where cold-pool properties have been studied by looking at 38 cold pools together as a composite, this Chapter is studying two of these in detail. Together with the cold-pools, the focus of this Chapter is on the evolution of the internal structure of the parent MCSs, which ultimately produces the cold pool, as well as several thermodynamic and dynamic properties of the MCSs and their environment in space and time.

Most of previous squall-line case studies (both observational and simulated) have been performed in the USA on mid-latitude squall-line MCSs (e.g. Bryan and Parker, 2010). Many results of such studies conclude that the surface-based cold pool and its environmental wind shear are key in organizing the structure of the MCS and its future evolution. The most advanced of such theories is the RKW theory based on Rotunno *et al.* (1988) and Weisman *et al.* (1988), which has been reassessed by Weisman and Rotunno (2004). For more details about the RKW theory see section 1.1.2.

Research of tropical MCSs has been done largely by using numerical simulations, an example of which is Redelsperger *et al.* (2000), who used eight numerical models to analyse tropical squall-lines. Regarding observational tropical squall-line MCS case-studies, several have been performed on MCSs that passed over Niamey during the AMMA IOP in some detail. An extensive and detailed observational case study was presented by Chong, (2010), who analysed the squall-line MCS that crossed Niamey in the early hours of 11<sup>th</sup> August 2006. In their study, reflectivity and Doppler radar analysis was used in order to determine thermodynamic and kinematic processes within the squall line as well as some microphysical properties, which were obtained by the use of a simple 1D model and

soundings. The results of their work confirmed the front-to-rear flow, which opposes the rear-to-front flow (Rear Inflow Jet), which descends and converges with moist air, lifting it into the updraft. The updraft then diverges into forward and rearward anvils and feeds the stratiform region behind with ice particles formed in the convective region. In addition, an upper updraft and lower-level downdraught were identified in the stratiform region. In terms of microphysics, mixing-ratios of liquid water, ice water, graupel and water vapour were obtained and the importance of processes such as melting, evaporation, condensation and sublimation was analysed both within the convective and stratiform regions. An eastward deflection of the squall-line at its northern flank was identified and attributed to stronger rear-to-front and weaker front-to-rear flow, which was related to the overall wind shear. Also, the greater extent of stratiform precipitation at the northern flank was studied and attributed to weaker shear at that part of the MCS. Chong, (2010) suggested expanding similar work to other MCSs observed during AMMA SOP, which is done in this chapter.

Another case study was performed by Barthe, *et al.*, (2010) for the convective period of 25-29<sup>th</sup> July 2006. The study of Barthe *et al.*, (2010) concentrates on the multi-scale interactions between two successive convective systems and following local convection, as well as the internal thermodynamics of the MCSs and the interaction of the MCSs with synoptic features (particularly an African Easterly Wave). Both studies focused on two squall-line MCSs (in the mornings of 25<sup>th</sup> and 26<sup>th</sup> July), which were associated with a strong monsoon surge that penetrated up to 18° N and generated flooding near Tamanrasset on 26<sup>th</sup> July. These squall-line MCSs were associated with an African Easterly Wave. The first MCS was ahead of the African Easterly Wave trough and the second was in phase with the trough and there was isolated local convection in the afternoon of 26<sup>th</sup> July behind the trough in the region of the ridge. The first MCS was a well-organized convective line while the second MCS was less organized on its southern side, where it was associated with a meso-vortex. The conclusions of the study were that the low-level shear and moisture available to these systems were crucial in their organization and that these systems may have had a positive feedback on the actual African Easterly Wave. The local afternoon convection in the region of the ridge behind the African Easterly Wave, which followed on 26<sup>th</sup> July in the afternoon, was also studied in detail and the absence of low-level shear was contributed as being the most important factor (together with dry mid-levels and strong CIN) that prevented

that convection from organizing into a MCS. This was confirmed by the use of a simulation.

Taylor *et al.*, (2010) studied a MCS and conditions leading to its initiation on 31<sup>st</sup> July 2006 (note this was a different case to the one chosen for this study). They continued on their previous work, Taylor *et al.*, (2007), where they showed that horizontal gradients in soil moisture do create mesoscale atmospheric circulations. Here, they investigate the importance of these soil moisture boundary-induced circulations in determining where a MCS initiates. Their conclusions state that the boundary layer air above the wet soil had up to 4 g kg<sup>-1</sup> higher WVMR with 1-2 °C lower temperatures and increases in  $\Theta_e$  of magnitude between 10-15 °C. The MCS initiated near a soil-moisture gradient on the dry side above a dry soil patch, which was surrounded by moister soil. The initiation was coincident with the passage of an atmospheric wave feature – a bore or a wave-front, which had been emitted from a different storm further south (e.g. Bretherton and Smolarkiewicz, 1989; Parker and Burton, 2002, Birch, *et al.* 2014). The fact that this wave feature was associated with convective initiation only in the region of the soil-moisture gradient shows the importance of such land-surface variations. The overall results are in disagreement with most global models that initiate convection above a moist patch (Taylor, *et al.*, 2012). Later that afternoon, the studied MCS intensified and propagated westwards. Once new convective cells were triggered by the lifting mechanism of the cold pool (as opposed to circulations induced by the soil-moisture gradients), the most intense convective cells were no longer above pre-existing dry soil regions, but above the moist soils with higher  $\Theta_e$ .

Birch *et al.*, (2014) further studied this system by using several runs of the Met Office Unified Model, which could resolve the key aspect of this MCS. Two out of three runs succeeded in reproducing the initiation of the convective system with a reasonable precision as the analysis was very sensitive to initial conditions and differences in the representation of various convergence zones in the analyses. The control simulation captured the 30<sup>th</sup> July MCS (note this is the second case used in this study when it passed Niamey the following morning), which emitted the gravity wave, as well as the “daughter MCS” (the MCS studied in Taylor *et al.*, 2010) with reasonable precision. The only difference from observations was that the initial “daughter MCS” appeared to be tied more to the gravity wave, not the soil moisture gradient. There were actually two gravity waves in the model, the first initiated shallow convection and the second the deep convection

associated with the first initiation of the “daughter MCS”. Based on the simulation, Birch *et al.*, (2014) suggested that these gravity waves had wave-front patterns and were not bore-like as suggested in the observational study of Taylor *et al.*, 2010. This hints that they were caused by the updrafts of the “parent storm” as their wavelength was equal to the depth of the troposphere and caused displacement of air upwards in the lower half of troposphere and displacement of air downwards in the upper half. There were, however, other deep convective cells in the run, which initiated above soil moisture gradients and later merged with the “daughter storm”, which then propagated westwards as a MCS. In observations, there was only one region of initiation from which the storm grew upscale as opposed to the modelled merging of more storms. It was suggested that in order to produce the initiation of MCSs in a forecast precisely, the initial conditions including the distribution of land surface moisture need to be represented correctly. If secondary initiations are to be predicted with a great precision, gravity waves produced by other MCSs must be captured by the model.

The squall-line MCSs of 14<sup>th</sup> July and 8<sup>th</sup> September 2006 have been studied by Guy, *et al.*, (2011). MIT radar and radiosondes were used to determine microphysics and the structure of these two systems. The difference between them was the presence of an African Easterly Wave on 8<sup>th</sup> September unlike on the 14<sup>th</sup> July. The 8<sup>th</sup> September MCS was associated with larger CAPE and weaker wind shear, but the top of radar reflectivity was higher in the 14<sup>th</sup> July case. The 3D Goddard Cumulus Ensemble model (cloud resolving model with 1 km grid spacing) was used to simulate both MCSs and the output was evaluated. The issues with the simulation were underestimation of system size and height (values greater than 50dBz reached only up to 5km in the model, but based on radar observations such reflectivities were observed up to 10km high). The timing of system passage was also not accurately represented, as it was on average 5 hours sooner for both cases. The convective part of the system was generally better represented than the stratiform region. Features such as the bright band and evaporative signature of both systems were simulated reasonably well, but the underestimation of height affected the proportion of ice-particles, which were at lower elevations and their distribution was narrower. This may have in turn had an effect on storm dynamics. Regarding the stratiform region, there was significant underestimation of reflectivities below the bright band and overestimation of reflectivities above it. This was attributed to using a single-moment microphysics scheme and the use of a double-moment scheme was

suggested for future studies. It was also suggested for future studies that decreased grid size is used as microphysics of small spatial scales can vary considerably even on small length scales (Bryan and Morrison 2012). The author suggested increased focus on continental MCS cases (as opposed to previous abundance of maritime studies) as simulations are tuned to maritime cases, where kinematic properties are different and this could lead to biases.

Several other observational and modelling studies exist. Alonge *et al.* (2007) and Gantner and Kalthoff (2010) studied the relationship between soil moisture and the development of convection while Lauwaet *et al.* (2010) investigated the relationship between a modelled MCS and vegetation cover. Schwendike *et al.*, (2010) used several case studies during the pre-onset and monsoon periods to show the response of surface properties and related surface fluxes. Their conclusion was that the rainfall-related soil moisture increase resulted in significant decrease in surface temperature (up to 10 K) and evaporation. Lothon, *et al.* (2011) investigated a locally initiated MCS, its structure and complex interactions of outflows and related fluctuations in surface properties. Lothon, *et al.* (2011) concluded that there is likely a large number of such small and locally initiated MCSs during the pre-onset period when moisture and influence by African Easterly Waves is still low. As shown in Flamant, *et al.*, (2007), such systems can be the cause of significant dust plumes.

There were 26 cases considered for the detailed study performed in this chapter. The main criterion for choosing a case was that it has not been studied before by the use of observational data obtained in Niamey during AMMA in 2006. Furthermore, it was important for the studied squall-line to persist while being located at least partly in the radar domain (not dissipate within the radar domain) so that radar reflectivity cross-sections from both ahead and behind the convective region could be obtained. The squall-line MCS case studies, which have been selected for this study, are the cases of 22<sup>nd</sup> and 31<sup>st</sup> July 2006. The 22<sup>nd</sup> July 2006 case study was selected as a typical case, where a major organized MCS in the form of a squall-line crossed Niamey and persisted until leaving the radar domain to the west. In addition, as far as the author is aware, this 22<sup>nd</sup> July 2006 squall-line in Niamey has not been studied in a single case study before and there was good enough coverage of both directly and remotely sensed data to perform an analysis of its internal as well as environmental properties. The case of 31<sup>st</sup> July 2006 was the “parent storm” studied by Birch *et al.* 2014, as stated

above. The reason for choosing the 31<sup>st</sup> July 2006 case was the complexity of its double cold-pool (see section 4.3.1.) and a radiosounding, which sampled the cold-pool air in a region behind the outflow boundary, but ahead of the convective region of the MCS.

The aim of this chapter is to broaden the existing and rather limited literature (compared to US MCS case-study literature) describing West African squall-line MCS case studies by adding two cases that have not yet been investigated using observational datasets obtained in Niamey. Unlike Chapter 3, where a composite cold pool and data from 38 cold pools were analysed together, this chapter focuses on more details and visualises cold pools and the internal structure of their parent MCSs by maximising the use of observed data available. Cross-sections comprising of various data sources have been produced and studied. Features similar to those observed in other case studies have been identified and the role of various processes forming and maintaining these features is discussed. Section 4.2 describes the observational data and processes of the analysis. Section 4.3 provides detailed analyses of both observational case studies. Section 4.4 compares and summarizes the results and discusses their implications.

## **4.2. Methods**

### **4.2.1 Data**

Observational data used for the purpose of this chapter included the MIT C-band Doppler radar, radiosondes and surface station data. The MIT Doppler radar was deployed near Niamey airport, Niger, at 13.5° N, 2.2° E, during the AMMA field campaign. More details about the MIT Doppler Radar are given in section 2.1. For the purpose of this Chapter, both single elevation horizontal scans as well as zonal vertical cross sections through radar reflectivity were used.

In order to obtain vertical profiles of the troposphere, vertical soundings of temperature, dew-point temperature, relative humidity and wind were obtained from radiosondes. These radio-soundings provided detailed vertical data above the surface, often reaching beyond the tropopause, being the only thermodynamic data available for mid- and upper-levels, both in the pre-storm and post-MCS environment. More details about radiosondes are given in section 2.1. On 22<sup>nd</sup> July, two radiosondes were released at approximately equal time periods from the leading edge of the cold pool. The first being ~3 hours ahead of the gust front and the second ~3 hours behind

and well within the cold pool. This made them an ideal pair of soundings to compare the pre- and post-storm thermodynamic and wind environments throughout a deep layer. On 31<sup>st</sup> July, three radiosondes that were released have been used in the present study to investigate the properties of the MCS. The first radiosonde was released ahead of the first cold pool crossing, the second was within the first cold pool, but ahead of an additional cold pool, which crossed later in the day and the last radiosonde was released behind both cold-pool crossings. These soundings provided an opportunity to observe changes in the vertical tropospheric profile, which was affected by a squall-line MCS passage and two cold pools.

Because the frequency of radiosonde releases was too low to obtain a detailed picture of flows within the squall-line, data of zonal wind speed obtained from the Radar Wind Profiler (RWP) were used to complement radiosondes in order to increase the frequency of vertical wind profiles within the lowest ~5km. The RWP provides output in approximately 200-metre height steps. One-minute data are averaged to hourly data due to signal-to-noise ratio. For more information about the RWP, see section 2.1.

#### **4.2.2 Time-to-space conversion**

Because all the surface station data and the RWP scans have been recorded from one location and the radiosondes have been released from that same location, a time-to-space conversion had to be performed in order to create composites where these are overlaid on top of radar reflectivity provided by the MIT radar. In order to perform such conversion, it was necessary to assume that the surface variables ahead and behind the squall line changed negligibly in time (where this assumption fails is discussed in the results). The majority of squall-lines in Niamey propagate from an easterly direction (see e.g Figure 7 in Rickenbach *et al.*, 2009). Both of our cases were consistent with this general westward propagation. Therefore, all cross-sections are oriented east-west, which was approximately perpendicular to the leading edge of the squall lines and their direction of travel. This approach was chosen to enable the interpolation of radiosoundings and Radar Wind Profiler Data ahead of or behind the squall-line. The direction of propagation was approximated to be from east due west as changes in orientation and direction of propagation of the squall-line in radar data made it tricky to obtain the direction of propagation to the nearest degree.

Propagation speed was calculated by dividing a distance of 200 km in the radar domain by the time it took the front edge of squall-line related radar reflectivity of at least 35 dBz to cover that distance. The full 300 km wide radar domain (radar range for volumetric scans being 150 km) was not used in this calculation to avoid several instances of new cells merging with the squall-line, which would have considerably overestimated the speed of propagation, as discussed in section 4.2.4. below. The propagation speed was calculated to be  $45.0 \text{ kmh}^{-1}$  and  $54 \text{ kmh}^{-1}$  for the 22<sup>nd</sup> July and 31<sup>st</sup> July 2006 cases respectively.

The 31<sup>st</sup> July 2006 case was a combination of a primary squall-line with associated cold pool, which was later followed by a secondary convective cell that propagated on the edge of the cold pool of the squall-line, as discussed in section 4.3.4. The propagation speed of the primary squall line was estimated at  $54 \text{ kmh}^{-1}$  while that of the secondary cell at  $67 \text{ kmh}^{-1}$ . This estimation provided a propagation speed of nearly 25% faster for the secondary cell than the speed of propagation of the primary squall-line. Because the primary focus of this study is on the primary squall-line and its overall structure, with the secondary cell being only a part of, or substructure of, the primary squall-line, the propagation speed estimated for the primary squall-line was used in the time-to-space conversion.

### **4.2.3 Vertical profiles**

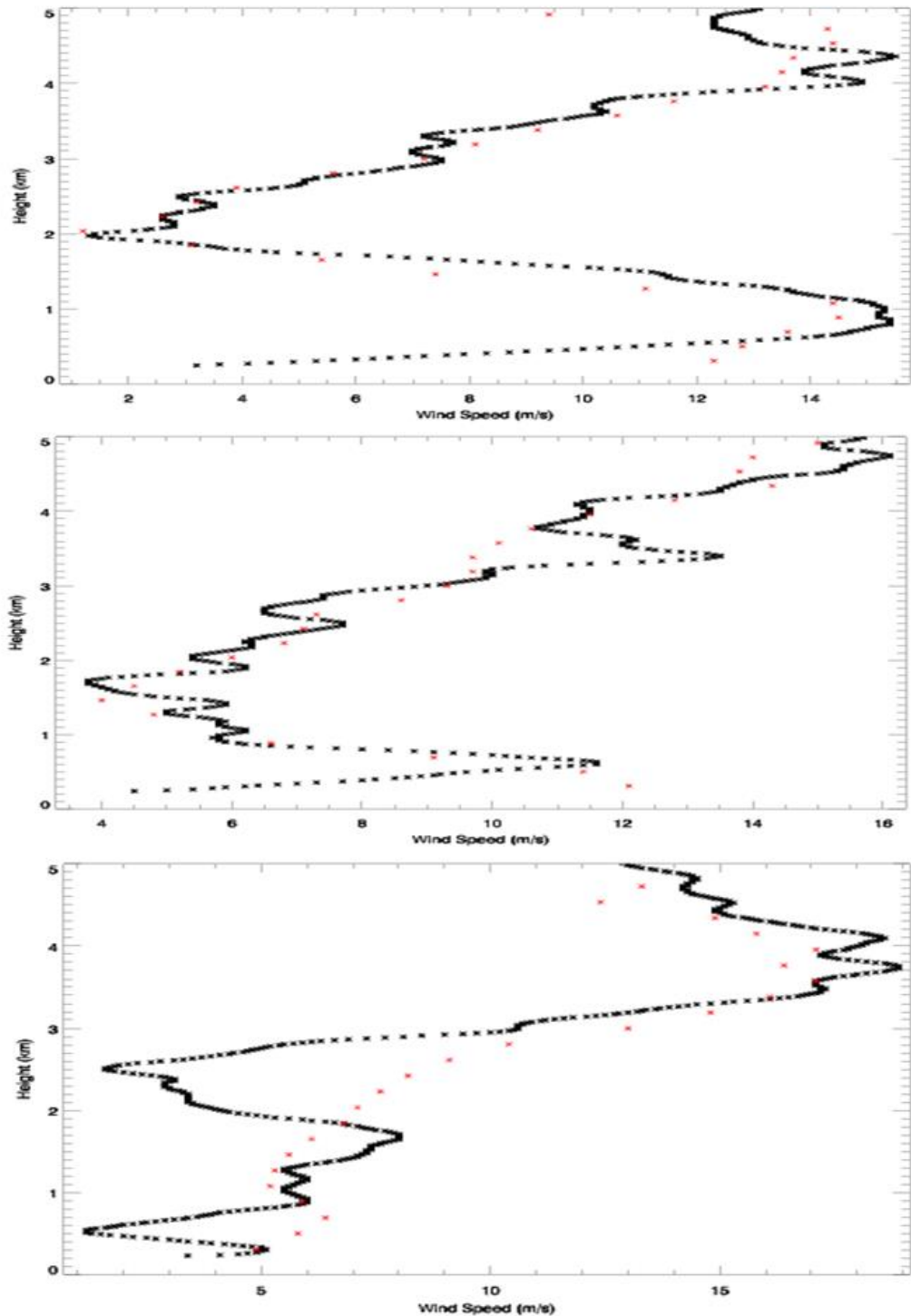


**Figure 4.1:** Vertical profiles of the magnitude of wind speed from radiosonde ascents (black) and RWP (red). Radiosondes were released at 05:38 UTC (top), 11:34 UTC (middle) and 17:32 UTC (bottom) with the RWP data being averaged for 05:30 – 06:30 UTC (top), 11:30 – 12:00 UTC (middle) and 17:30 – 18:30 UTC (bottom), all on 31. July 2006.

RWP data were used mainly as a complementary data source of zonal wind to fill-in the gaps between radiosondes. When a radiosonde was released, the RWP output averaged for the hour of release could be used to

compare and verify these two different data sources of the same variable obtained from the same location (Figure 4.1). The agreement between winds obtained by RWP and radiosondes is not expected to be perfect due to the different sampling methods of both instruments. While the RWP output was averaged from one-minute scans, centred at every hour, of the whole profile above the location of the instrument, radiosondes take measurements as they rise while drifting with the wind and hence the profile is not directly above the location of release. Also, it takes approximately 13-14 minutes for a radiosonde to rise throughout the depth of the 5km, which is being scanned instantaneously by RWP.

Figure 4.1 shows that the two datasets generally range within 20% of each other, but there are several smaller-scale features in the soundings, where the data differ. Figure 4.1 shows three such examples, one of a pre-storm sounding (Figure 4.1 top), one through a cold pool (Figure 4.1 middle) and one post-storm (Figure 4.1 bottom). While the instantaneous-reading radiosonde captures details, such as short-lasting eddies, RWP does not capture such details in the flow, which is a result of the hourly-mean and resultant smoothing of data as well as lower density of data-points in vertical. In all three cases, RWP has stronger-than-radiosonde winds in its lowest levels. In case of the noon sounding (Figure 4.1 middle) it needs to be highlighted that there was a second cold pool crossing approximately 36 minutes after the radiosonde was released (as discussed later in the chapter). Therefore, the hourly averaged RWP was measuring winds affected by this cold pool for approximately 30% of time, whereas the instantaneous wind measurement of the radiosonde ascent from that layer was still ahead of the cold pool.

The evening sounding (Figure 4.1 bottom) also shows good agreement, within 20%, between radiosondes and RWP. An exception is the minimum at ~2.5 km seen in the radiosonde output, but not in RWP (Figure 4.3 bottom). These differences in observed winds were likely again caused due to the RWP hourly averaging, which does not detect eddies like radiosondes.

## **4.3 Results**

### **4.3.1 Case study of 22<sup>nd</sup> July 2006 squall-line MCS**

## Overview

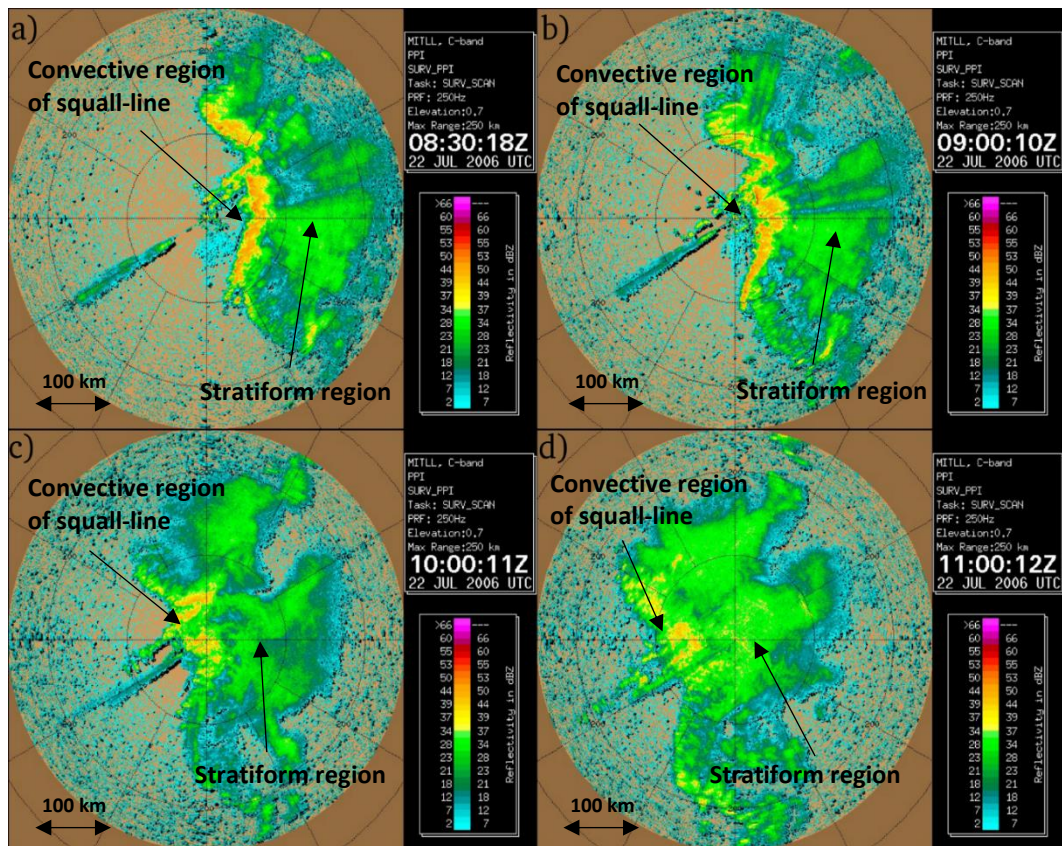


**Figure 4.2:** Single elevation (0.7°) MIT radar reflectivity images at: a) 08:30:18 UTC, b) 09:00:10 UTC, c) 10:00:11 UTC and d) 11:00:12 UTC on 22<sup>nd</sup> July 2006.

The case study of the 22<sup>nd</sup> July 2006 is a mature squall-line similar to other squall-line MCSs that have been observed elsewhere in the world (e.g. Bryan and Parker, 2010). One difference here, when compared to e.g. US or European squall-line MCSs, is that this squall-line, like the majority of other squall-lines observed in Niamey, propagated from east to west. Because of this, its structure resembled a mirror-image of most typical cases that are found in literature (e.g. Chang et al., 1980, Ogura and Liou, 1980). Radar images of the 22<sup>nd</sup> July case study can be seen in Figure 4.2. The cold pool shortly followed by the squall-line crossed Niamey at 09:04 UTC. The squall-line featured strong upright convection at the leading edge being followed by trailing stratiform rain (Figure 4.2 d)) and a clear cold pool signal in the surface data (see section below).

**Surface data and the cold pool**

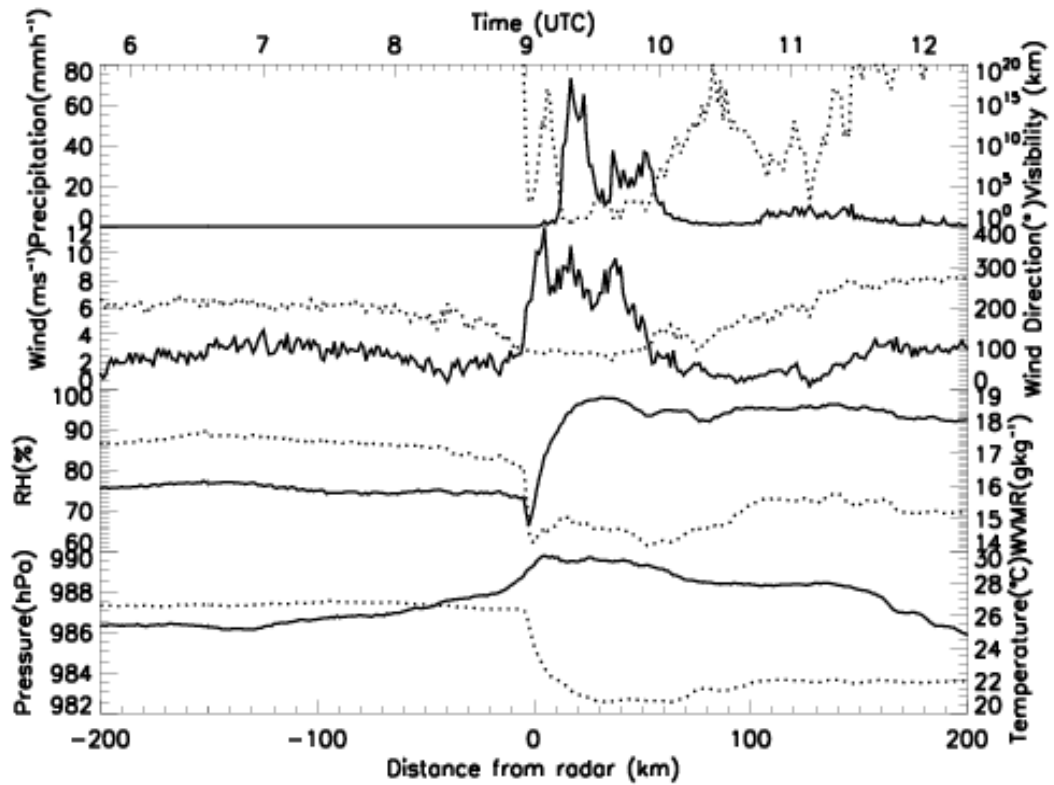


**Figure 4.3:** Observed surface time series of specified variables time-to-space converted into cross-section based on the east-west propagation of the squall-line on 22<sup>nd</sup> July 2006. Solid lines correspond to the left y-axis, dotted lines to the right y-axis. The cross section is centred at the cold pool edge and corresponds to approximately 5 minutes after the time of the 09:00 UTC radar scan in Figure 4.2 b). Top x-axis is time axis, bottom x-axis shows distance based on conversion.

The squall-line related cold pool crossed Niamey at ~09:05 UTC. Ahead, temperature and humidity were rather steady with temperature of ~26.5 °C, relative humidity (RH) of ~75% and WVMR of ~17.5 g kg<sup>-1</sup>. The outflow boundary can be identified at 0 km in Figure 4.3, when sharp and coincident drops in temperature, humidity and visibility occurred. Temperature decreased with the cold pool boundary passage down to ~20.5 °C, RH to ~65% and WVMR to ~15 g kg<sup>-1</sup>. The temperature decrease of ~6°C is a mid-range value of all cold-pool related coolings observed in Niamey in 2006 (see Chapter 3). Behind, WVMR continued to decrease down to 14.8 g kg<sup>-1</sup>, but the onset of precipitation, which was located ~8 km behind the gust front, and associated further cooling led to an increase in RH to nearly 100%. When compared to the average for the Monsoon sub-period (see Chapter 3), the drop in moisture is also in the mid-range of all

values. Associated with the temperature changes, surface pressure slowly rose ahead of the squall-line from ~986.5 hPa, having a maximum of 989.5 hPa just after the cold pool has passed, but before precipitation began. The increase of 3 hPa is in the lower third of all cold pools (see Chapter 3). Approximately 7.5 km after the cold-pool passage, rainfall was detected by the surface station (see Figure 4.3). WVMR then increased to a maximum of  $15.2 \text{ g kg}^{-1}$ , this being nearly coincident with the first and greatest peak in surface precipitation intensity. Temperature stayed at  $\sim 20 \text{ }^\circ\text{C}$  below the downdraft of the heavy convective precipitation and then slowly increased towards the rear side of the MCS. There was a broad but shallow pressure maximum 30-40km behind the gust-front, corresponding to a surface mesohigh (Rotunno *et al.* 1998). Further behind, pressure decreased down to 984 hPa, possibly due to the formation of a wake low 150-200km behind the gust front. The hydrostatic balance estimation gives a cold pool that is approximately 1300 metres deep, which would be a shallow cold pool when compared to the estimated average of 2100 metres for 38 identified cold pools. This estimate however assumes that the cold pool and the environment ahead is well-mixed.

Wind speed ahead of the cold pool was steady with the direction being approximately south-westerly, corresponding to the typical nocturnal monsoon flow. The cold pool passage was attended by a wind gust of  $11.9 \text{ m s}^{-1}$  magnitude. There were three peaks in wind speed linked to the cold pool passage. Wind changed direction to easterly ahead of the cold pool and stayed easterly until  $\sim 40\text{km}$  after the cold pool passage, consistent with easterly mid-level winds being brought to the surface by the convective downdraft. In general the wind speed pattern corresponds to the precipitation pattern as maxima in wind speed are generally located  $\sim 5\text{-}10 \text{ km}$  ahead of maxima in precipitation intensity. Following the end of precipitation occurrence, wind-speeds relaxed to nearly pre-storm values. This relationship shows that pulses of heavy rainfall were related to wind gusts in this case, likely as a result of both evaporative cooling or possibly momentum transport from higher levels by the downdraft. Approximately 40km after the gust front, wind started to turn westerly as a result of wind direction responding to the pressure distribution along the MCS.

Total accumulated precipitation in Niamey associated with this squall-line was 76.9 mm, with the heaviest precipitation being within the convective region, having intensities briefly exceeding  $70 \text{ mm hr}^{-1}$  (Figure 4.3). This convective region was associated with 2 precipitation intensity peaks, the

first having rainfall intensities over  $70\text{mmhr}^{-1}$  (at  $\sim 10$  km) with the intensities of the second peak approaching  $40\text{mmhr}^{-1}$  (at 30 km). Overall, it can be seen in Figure 4.3 that the convective rainfall intensity considerably varied with time unlike that of the stratiform region. The stratiform region brought much weaker precipitation intensity of only  $\sim 10\text{mmhr}^{-1}$  or less.

***Changes in atmospheric profile***

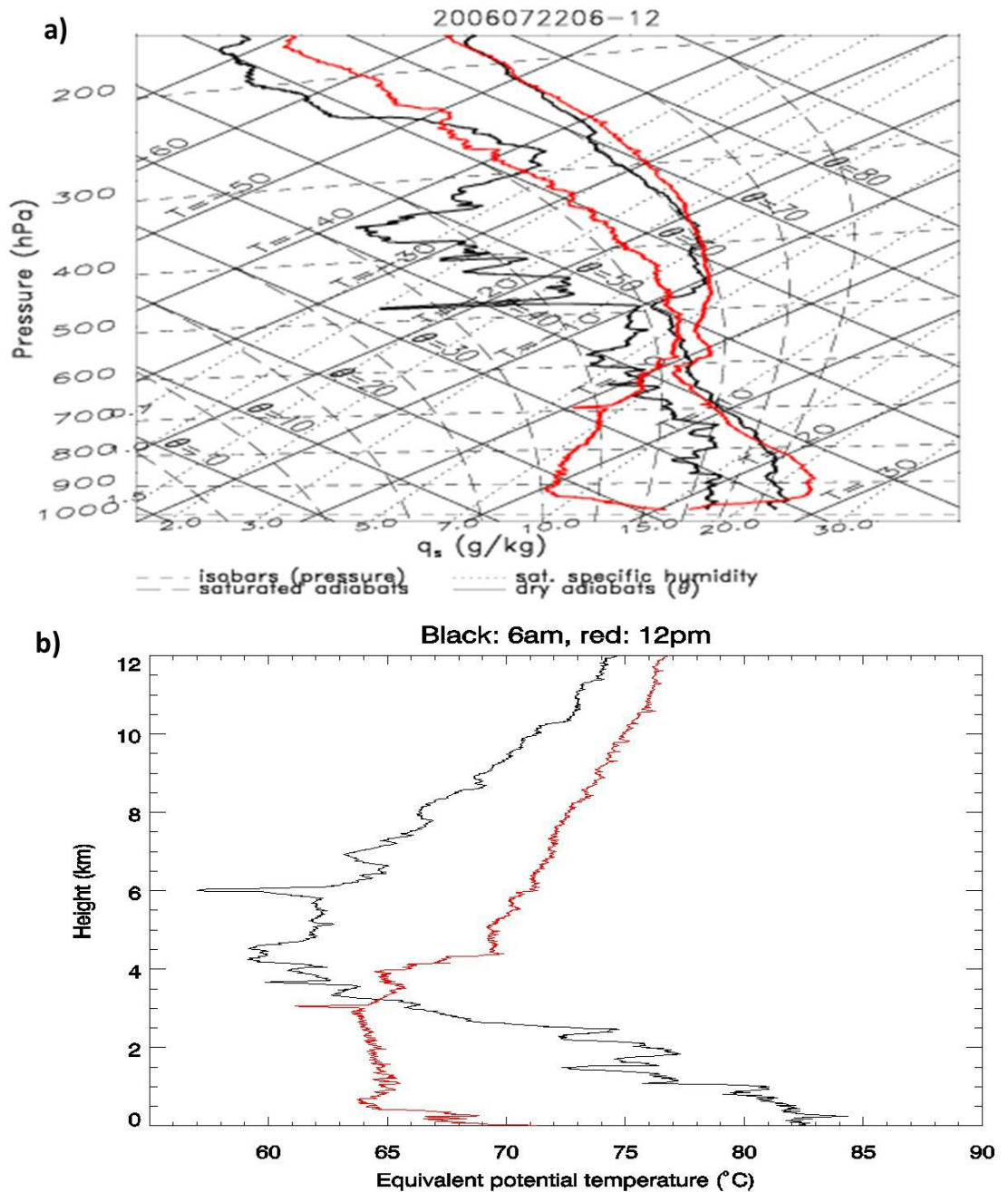


**Figure 4.4:** Comparison of morning (06:00 UTC, black line) and noon (12:00 UTC, red line) soundings on 22 July 2006 for a) T and Td tephigram, b)  $\theta_e$ .

The profiles in Figure 4.4 show and compare atmospheric stratification ahead and behind the MCS. The 06:00 sounding is well ahead of the MCS and the 12:00 UTC sounding is behind the stratiform precipitation (not shown). At 06:00 UTC a stable nocturnal near surface layer with a slight inversion at ~950 hPa was located ahead of the MCS (Figure 4.4 a)). Several regions of low temperature/dew-point depression show the likely presence of cloud, namely at ~500 hPa and possibly just above ~300 hPa. Overall, the atmosphere is moister below ~500 hPa in the monsoon

influenced airmass than above. This can be also seen in the 06:00 UTC equivalent potential temperature profile (Figure 4.4 b)) with highest values of ~70 – 85 °C below ~3 km, lowest values of ~55 – 70 °C in mid-levels between ~3 – 8 km and with values between 70 and 75 °C above ~8 km.

Such equivalent potential temperature profile is typical in the tropics.

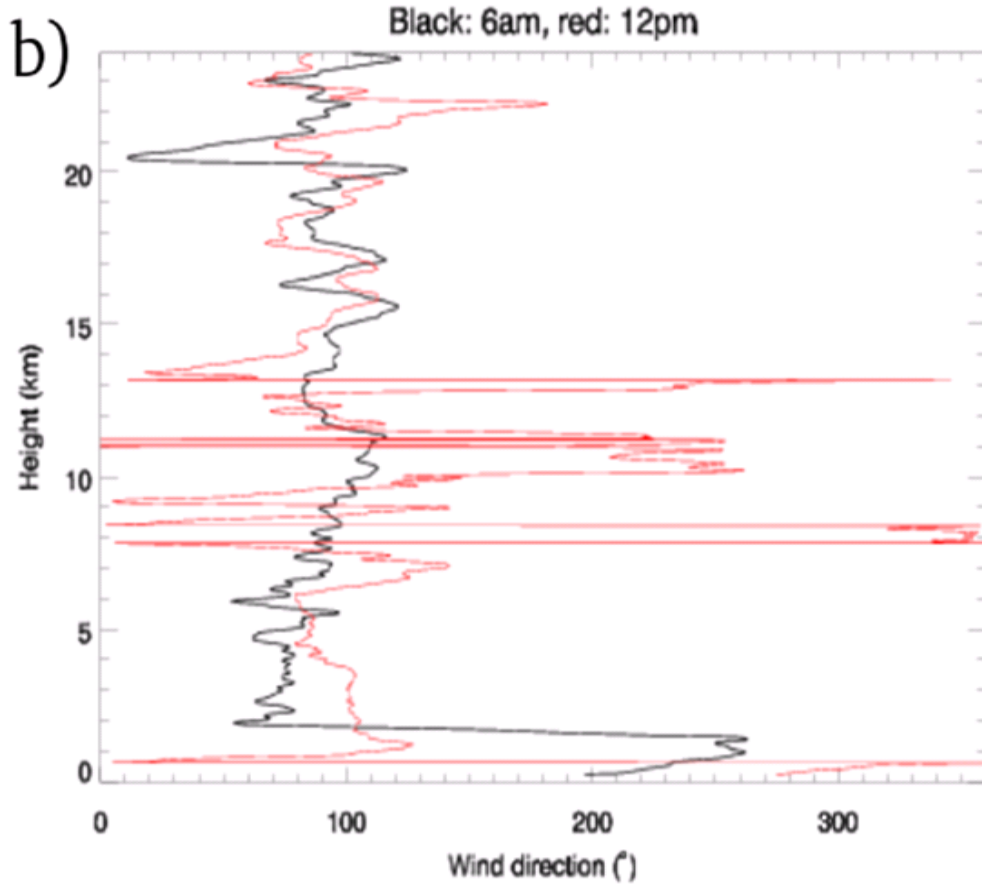
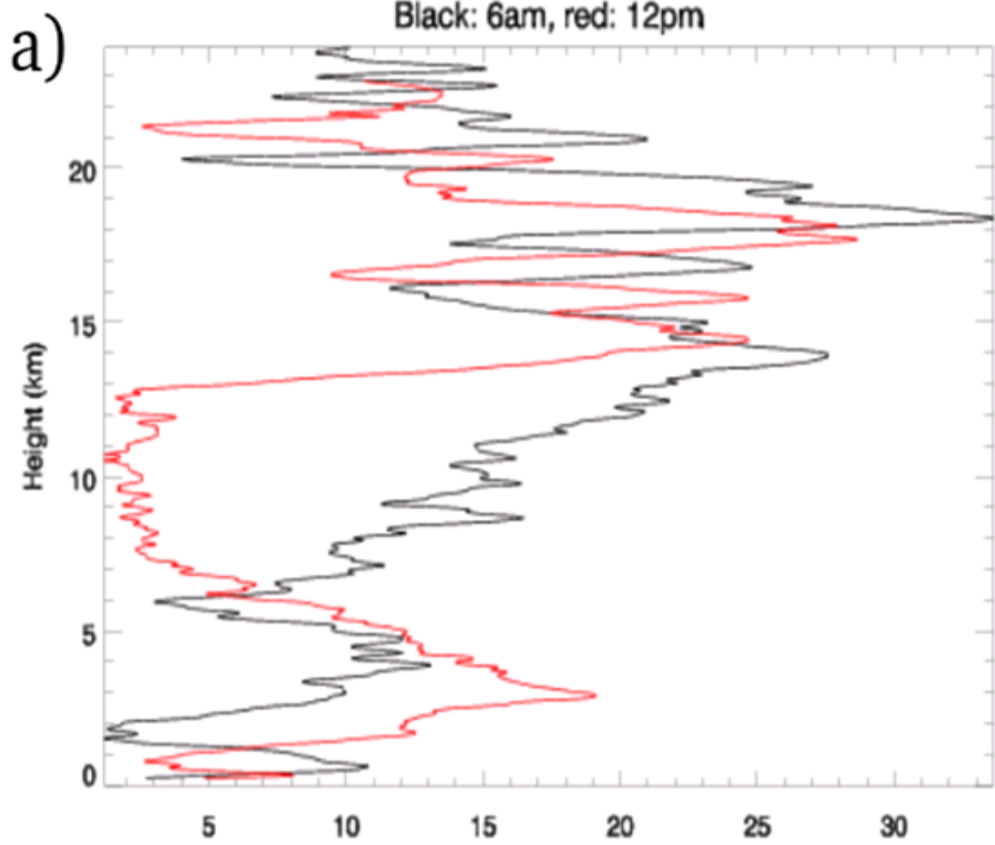


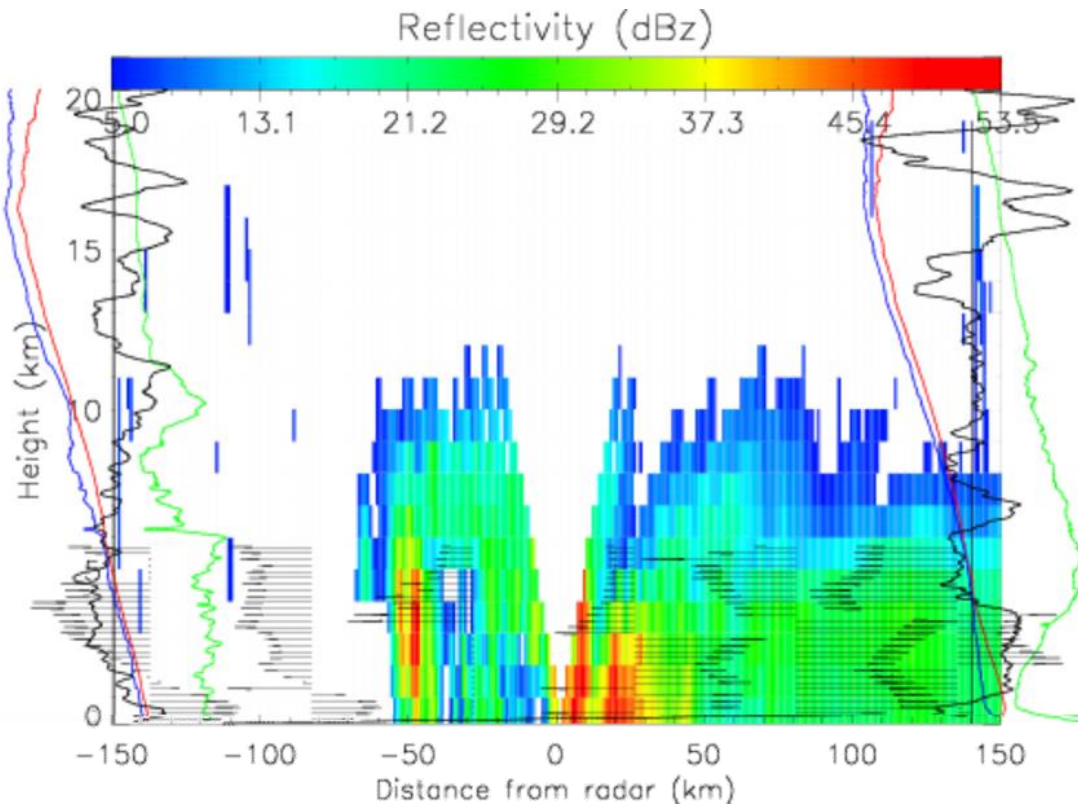
**Figure 4.5:** Differences in a) wind-speed and b) wind direction soundings between the morning (06:00 UTC, black line) and noon (12:00 UTC, red line) radiosonde releases on 22. July 2006.

The 06:00 UTC sounding (Figure 4.5 – black) shows a region of enhanced south-westerlies ~1.5 km deep located in the lowest levels, which agrees with surface data (see Figure 4.3), with a magnitude of  $8.6 \text{ m s}^{-1}$  at ~800 m above ground. This low-level flow represents the nocturnal low-level jet, which persisted from the night before and is above the low-level stable layer in Figure 4.4. Winds are nearly easterly at all levels above ~2 km, being enhanced between ~3-6 km with a maximum of  $\sim 13 \text{ m s}^{-1}$  at ~4 km.

Changes in atmospheric profile resulting from the MCS passage can be visualized by comparing the black (06:00 UTC) and red (12:00 UTC) profiles in Figures 4.4 and 4.5. The convective overturning has increased  $\theta_e$  aloft (above ~3.5 km) and decreased it below that level (Figure 4.4 b)). Winds are slightly stronger in the levels below ~6 km after the MCS, with much weaker/nearly zero winds above ~6 km. A region of warming with respect to the morning sounding can be seen between approximately 950 hPa and 800 hPa, this being due to descent of dry air from ~600 hPa (Figure 4.4 a)). A typical “onion type” sounding (Houze, 1977; Zipser, 1977) is evident below ~600 hPa as a shallow cool ( $\sim 6^\circ\text{C}$  temperature decrease, agreeing with surface station data) and nearly saturated surface layer with dry and well-mixed layer above, also seen as nearly constant  $\theta_e$  of  $\sim 65^\circ\text{C}$  below ~3 – 4 km with greater values in the lowest kilometre. The relative reduction of  $\theta_e$  due to the MCS was maximized at the bottom of the well-mixed layer at ~1 km, having a magnitude of  $17^\circ\text{C}$  and the decrease in dew-point temperature had a greatest magnitude of  $11.5^\circ\text{C}$  at ~990 hPa with respect to the morning sounding. This is related to the strong subsidence mentioned above and this region of subsidence is associated with strong easterlies (Figure 4.5 a)), with a maximum of  $\sim 18 \text{ m s}^{-1}$  located at ~3 km. This maximum is related to the morning wind maximum at ~4 km (Figure 4.5 – black) (the African Easterly Jet), which has been transported downwards by the subsidence and enhanced, creating a rear-inflow jet (seen in 12:00 UTC sounding). Winds above ~7 km are much weaker post-MCS, this most likely as a result of the upper-level outflow from the convective region of the storm, which balances the general easterly winds. The noon sounding (Figure 4.5 b) red) features sudden and temporary changes in wind direction. This is a result of very low wind speed (Figure 4.5 a)) on the rear side of the MCS leading to variable wind direction.

The “onion soundings” behind MCSs have been observed in other studies. They are caused by unsaturated descents of mid-level air, which are initially induced by evaporation and melting (Correia and Arritt, 2008). It was hypothesised by Zipser (1969) and Zipser (1977) that the near surface layer is a product of saturated downdrafts in the convective region of the squall-line. This is indeed confirmed in Figure 4.3., where RH remains near 100% from the convective region eastwards with 5-7 m s<sup>-1</sup> westerly 3 m winds transporting this cool saturated airmass rearwards through the MCS. The profiles show that these approximately westerly winds reach up to ~1 km and are likely related to the low-level outflow from the MCS, which had been located due west-southwest by noon. While near-surface airmass after the MCS is moister than the levels above (WVMR difference of ~7 g kg<sup>-1</sup> between the surface and the sounding report at 900hPa), its low temperature makes it stable with no CAPE left after the MCS passage.

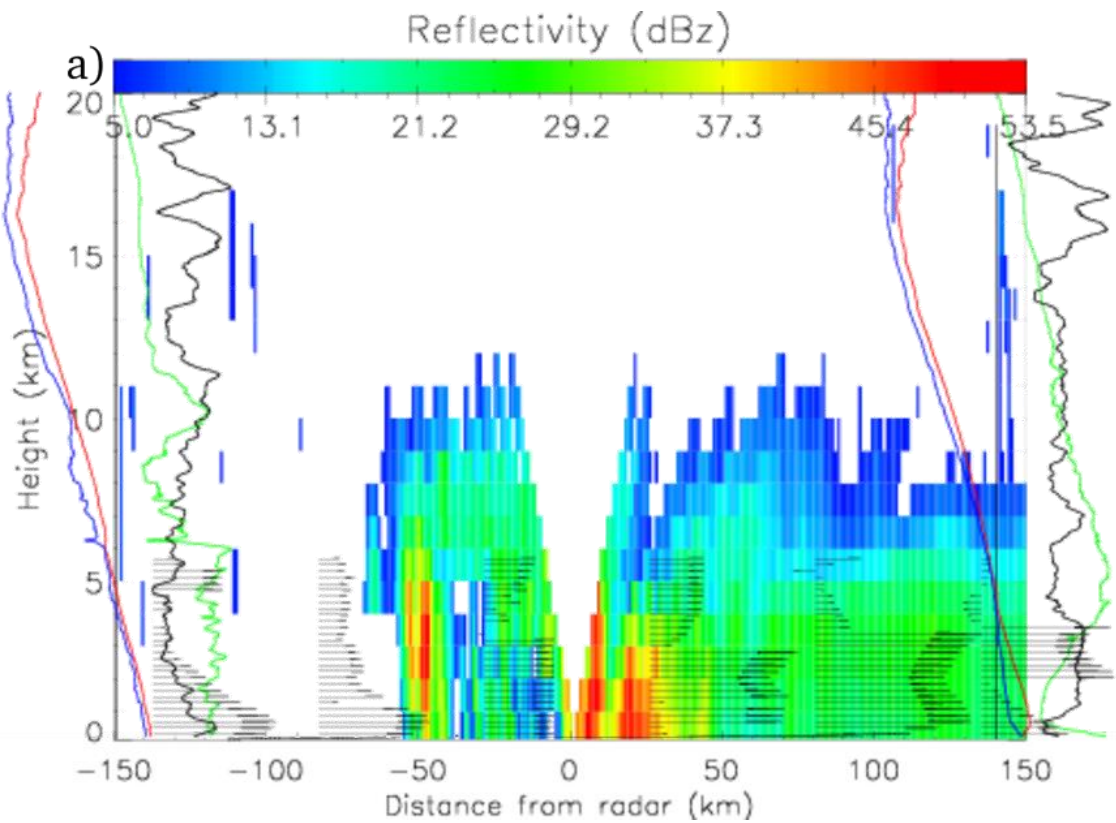
### ***Vertical structure***



**Figure 4.6:** Vertical west-east cross-sections through volumetric radar reflectivity at 09:31 UTC on 22<sup>nd</sup> July 2006, centered on Niamey. Overplotted are radiosonde ascents released from Niamey, their locations are specified by the vertical *y*-axes, where numbers represent height above ground level (km). The position of the ascents is time-to-space converted based on the mean east-west propagation of the squall-line, as discussed in the main text. The radiosonde variables are: Red=temperature (°C), Blue=dew-point (°C), Green=RH (%), Black=ground-relative zonal wind speed ( $m s^{-1}$ ). Values to the right of the *y*-axis are positive and to the left negative (for actual values see previous plots). Horizontal arrows represent the magnitude and direction of the zonal component of ground-relative wind as obtained from the Radar Wind Profiler (RWP). Note the V-shaped white area above 0km is a result of the radar scanning strategy missing the space directly above the radar. 0 km is centered approximately at the gust front crossing. Radiosonde at -150 km has been released at 05:36, radiosonde at +140 km at 12:17 UTC.

Figure 4.6 shows composites of several various variables that allow an easy overview of the squall-line MCS of 22<sup>nd</sup> July 2006 over Niamey and enables a qualitative and quantitative identification and description of several features associated with it. The squall-line was characterized by a region of convective cells organized into a more or less linear feature on its front side, being followed by a much broader but weaker radar reflectivity located on the rear (east) side of the MCS (see also Figure 4.2). Since radar reflectivity

is proportional to sixth power of particle size and hence precipitation intensity, rainfall intensity at different levels as well as the surface can be inferred from reflectivity. However, there are sometimes issues such as when snow is melting (see section 4.3.2 for the presence of brightband within the stratiform region). Indeed, radar reflectivity in Figure 4.6 relates well to the shape of the rainfall rate time series (Figure 4.3 d)), chiefly where radar reflectivity  $>40\text{dBz}$ , although a displacement of the surface rainfall of  $\sim 5\text{-}10\text{ km}$  to the east of the reflectivity is observed, which is explained by the use of RWP data below.



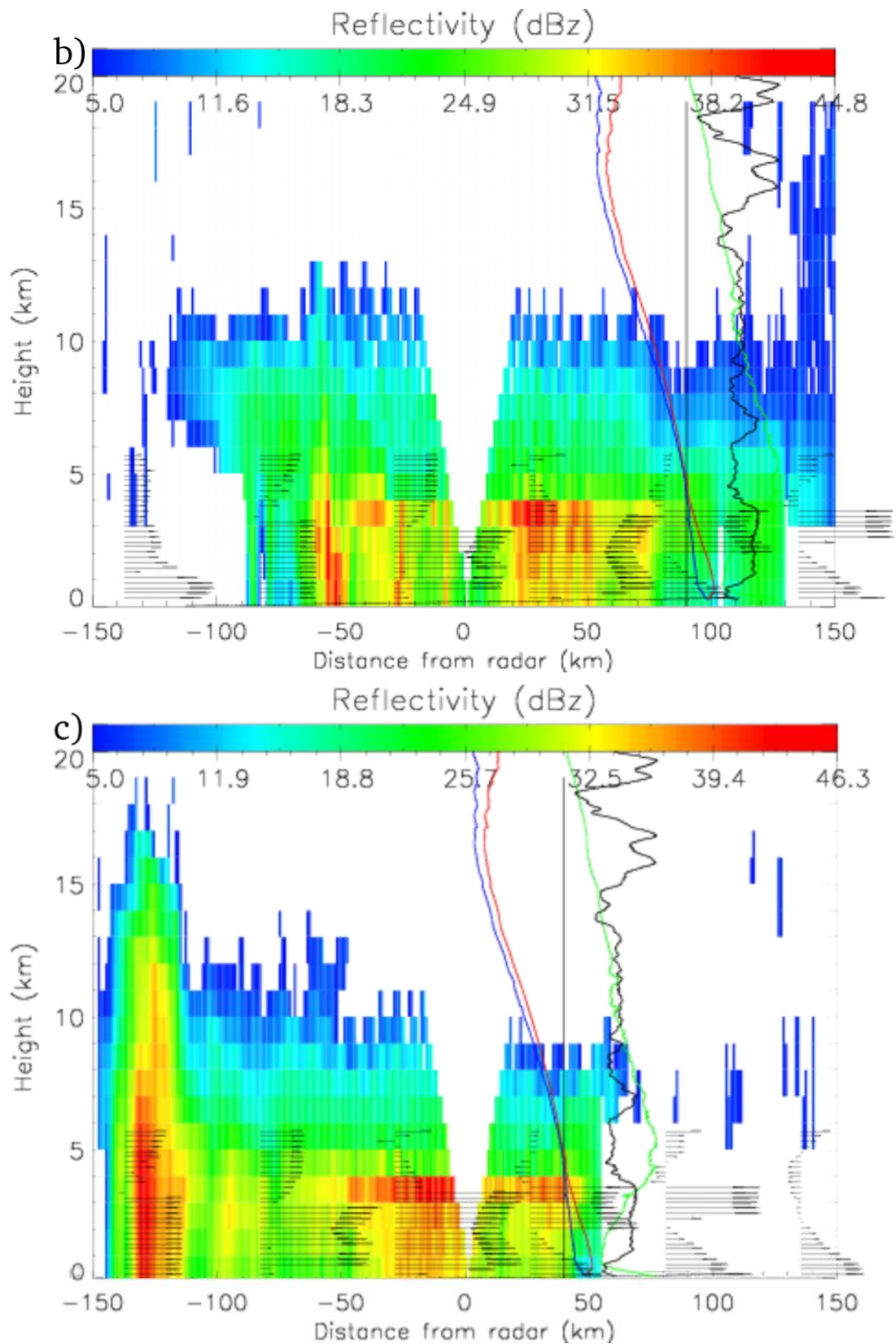


**Figure 4.7:** Same as Figure 4.6, but for storm-relative winds. Times of radar cross-sections are: a) 09:31 UTC, b) 10:31 UTC and c) 11:31 UTC on 22<sup>nd</sup> July 2006. Radiosonde at -150 km in a) released at 05:36 UTC, all other soundings are from radiosonde released at 12:17 UTC.

Wind-flow dynamics of the MCS can be seen in storm-relative wind data in Figure 4.7. Ahead of the squall-line, strong low-level westerly storm-relative winds are feeding the convective cells, these being related to the remaining low-level jet (seen in radiosonde and RWP in Figure 4.7 a) and b). Behind the gust front, this low-level inflow is lifted above the lowest levels, where the stable cold pool air is located near the surface, and forms the front-to-rear flow. The front-to-rear flow is responsible for the displacement of surface precipitation with respect to radar reflectivity discussed above, as it carried precipitation rearwards throughout the system. It also fed the stratiform precipitation on the rear side of the MCS with warm and moist air.

The first RWP profile within the squall line is located at  $\sim +27$  km (Figure 4.7 a) for storm relative winds, Fig 4.6 for ground relative). The lowest  $\sim 400$ m contain strong ground-relative easterlies associated with the low-level outflow from the convective region feeding the cold pool. Between  $\sim 400$ m and  $\sim 3$ km, the front-to-rear flow is present (as discussed above). At heights greater than  $\sim 3$ km, easterly ground-relative wind prevails. This easterly is stronger in the RWP scans further behind the gust front and is related to the rear-inflow-jet. The magnitude of storm-relative winds is greatly reduced above  $\sim 3$  km, approaching zero in places. These are the steering winds of the MCS (Figure 4.7).

Note that there is no rainfall measured by the surface station in association with the convective cell at  $\sim -50$  km (compare Figure 4.3 with 4.7). This is because this cell developed west of Niamey and never actually crossed Niamey. Such new cell formation ahead of squall-lines can often cause the propagation speed of squall-lines to be complex. According to Corfidi *et al.* (1996), the propagation of MCSs depends on the vector sum of the cell advection by the mean cloud-layer wind and a vector directed anti-parallel to the low-level jet as this is the direction where new cell development takes place due to convergence. In the Sahel, the general mean cloud layer wind is affected by the African Easterly Jet, hence being easterly, as observed in the case of 22<sup>nd</sup> July (Figure 4.5). Since the nocturnal low-level jet is generally from the southwesterly direction, the strongest convergence is expected to be on the southwest side of the MCS. The nocturnal low-level jet normally gradually dissipates through the morning hours, but is still evident in Figures 4.7 a) and b) as a region of strong storm-relative westerlies between  $\sim 0-2$  km above ground ahead of the MCS. This creates convergence in this region (note Figure 4.7 b), where strong low-

level jet is present at ~-85 km and nearly zero storm-relative wind at ~-35 km) and new cell formation occurs here as a result.

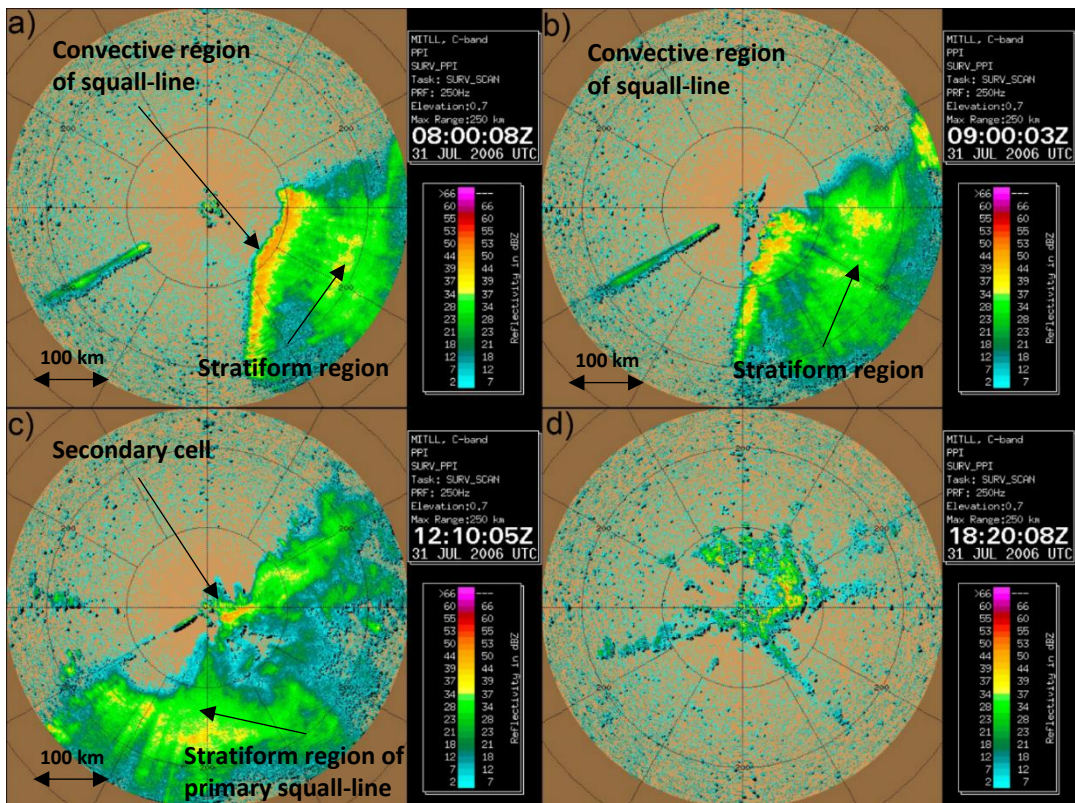
The process of new cell formation, merging with the squall-line, as well as cell dissipation can well be seen in Figure 4.7. At 09:31 UTC there is a region of developing cells that reach to mid-levels approximately 50 km west of Niamey, ahead of the main squall-line, which is just approaching Niamey at that time (Figure 4.7 a)). The maturing cells that are part of the convective region of the MCS are located at the front of the squall-line at ~-5km. The developing cells remained nearly stationary at ~-50km throughout the next hour and slightly intensified, while the squall-line propagated between approximately 0 and -50km in that hour, joining these cells. The originally maturing cells at 09:31 UTC are in their dissipating stage by 10:31 UTC (Figure 4.7 b)). These are located at ~-40 km and nearly dissipated, merging with the stratiform rainshield at ~-100 km at 11:31 UTC (Figure 4.7 c)). The newly developed cell is maturing at ~-120km at that time. This confirms that new cell development ahead of the main squall-line added to the overall speed of propagation. The convection ahead of the squall-line propagated at a different speed than the whole squall line. The isolated convection ahead propagated ~80km in the 2 hour period while the apparent edge of the system, which has by then merged with these cells, moved ~130km. This effect caused the apparent speed of the MCS to fluctuate over time, complicating the estimation of the mean speed of propagation. Because the isolated “pre-squall-line” convection to the west of Niamey did not affect the surface time series observed at Niamey by either rainfall or its cold pool, the propagation speed of the MCS was based only on images of the squall-line before the merging process. This provided an estimate of  $\sim 45.0 \text{ kmh}^{-1}$  for the speed of propagation for the 22<sup>nd</sup> July case.

Figure 4.7 c) presents an overview of properties and features in the stratiform rainfall region of the squall-line. The deep convective core on the leading edge of the MCS is now located at ~-120km, having reflectivities of ~45 dBz. In the stratiform region behind, reflectivities of ~30-40 dBz prevail between ~+50 and -50km. In-between these two regions at around -80 km , weaker reflectivity of ~15-30 dBz shows the presence of a “weak-echo” (e.g. Stolzenburg *et al.* 1994), which is associated with a mesoscale descent throughout a deep layer (Biggerstaff and Houze 1993). Braun and Houze (1994) argue that the appearance of this weak echo on radar is a microphysical effect caused by sorting near the melting level whereby large frozen particles are deposited near the convective line and small frozen

particles are transported upwards and rearwards away from the convective line. The weak echo is also evident in the surface rainfall cross-section (Figure 4.3), where convective rainfall rates exceeding  $55 \text{ mm hr}^{-1}$  in a region  $\sim 10 \text{ km}$  wide (at  $\sim +20 \text{ km}$ ) are followed by weak rainfall rates at  $\sim +20$ - $25 \text{ km}$ , which are then followed again by stronger rainfall to the east. A bright-band is evident in the stratiform region (Figure 4.7 c) between  $\sim -50$  and  $+50 \text{ km}$ ) at this time, which forms just below the melting layer and is a result of large snowflakes being wet on their surface and hence providing greater reflectivities (Sassen, 1975).

### 4.3.2 Case study of 31<sup>st</sup> July 2006 squall-line MCS

#### Overview



**Figure 4.8:** Single elevation (0.7°) MIT radar reflectivity images at: a) 08:00:08 UTC, b) 09:00:03 UTC, c) 12:10:05 UTC and d) 18:20:08Z on 31<sup>st</sup> July 2006.

On 31<sup>st</sup> July 2006 a mature squall-line MCS (Figure 4.8 a)), hereafter referred to as the “primary squall-line”, just missed Niamey to the southeast at approximately 09:00 UTC with its precipitation-free gust front crossing Niamey at 09:04 UTC (Figure 4.8 b)). This gust front is visible as a fine line of weak reflectivity on the radar in Figure 4.8 b) just east of Niamey, which is a result of dust and insects (Hajovsky *et al.*, 1966) being lifted at the gust front that is just approaching Niamey and later crossing the surface station. This was followed by a more isolated storm cell, hereafter referred to as the “secondary cell”, which crossed Niamey at 12:11 UTC on 31 July 2006 (Figure 4.8 c)). This was followed by large stratiform region of the MCS, seen in Figure 4.8 d) as a dissipating area of rainfall by 18:00 UTC. For the observation from Niamey this makes it a rather unusual case (for the monsoon season 2006 the only case) where two gust fronts produced by one MCS were detected.

#### ***Surface data and the cold pool***

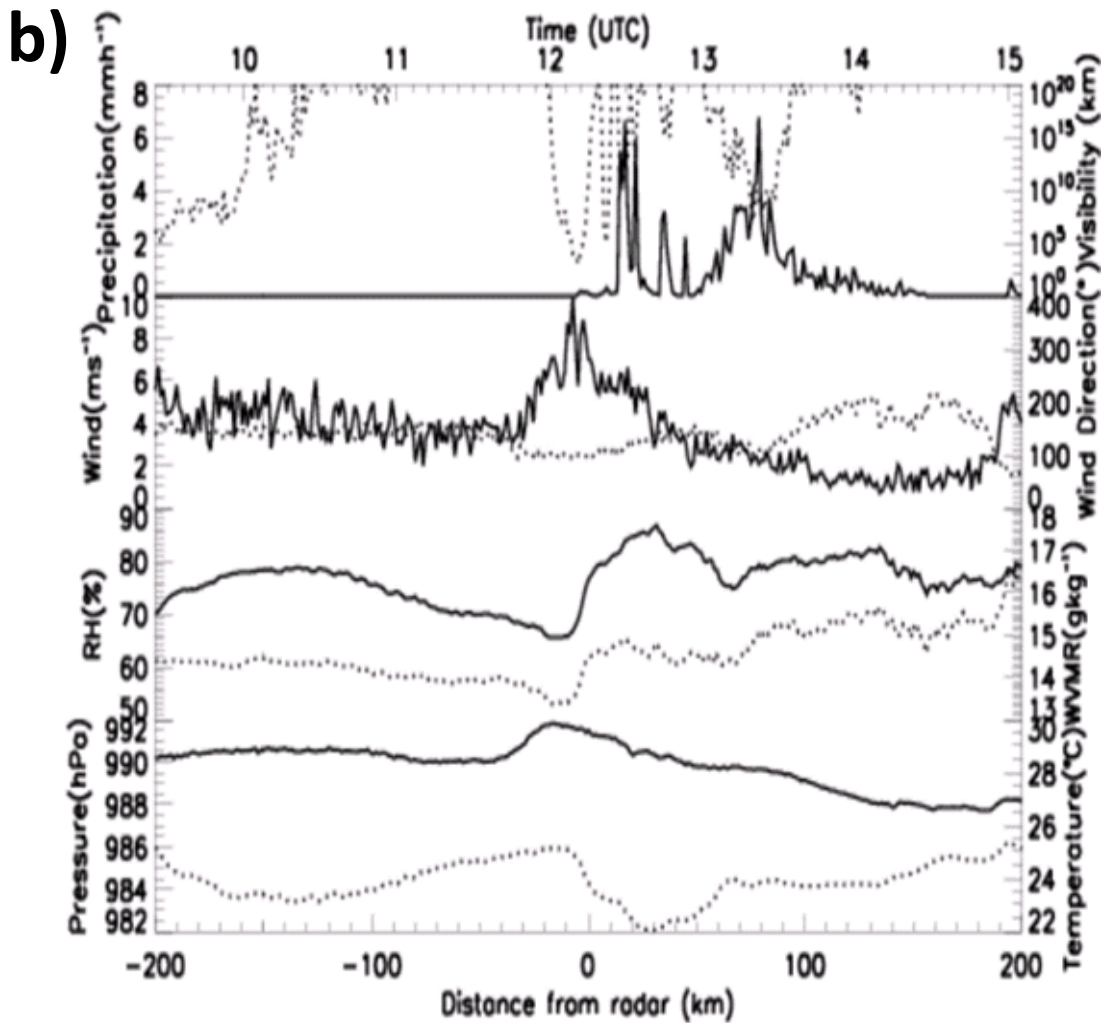
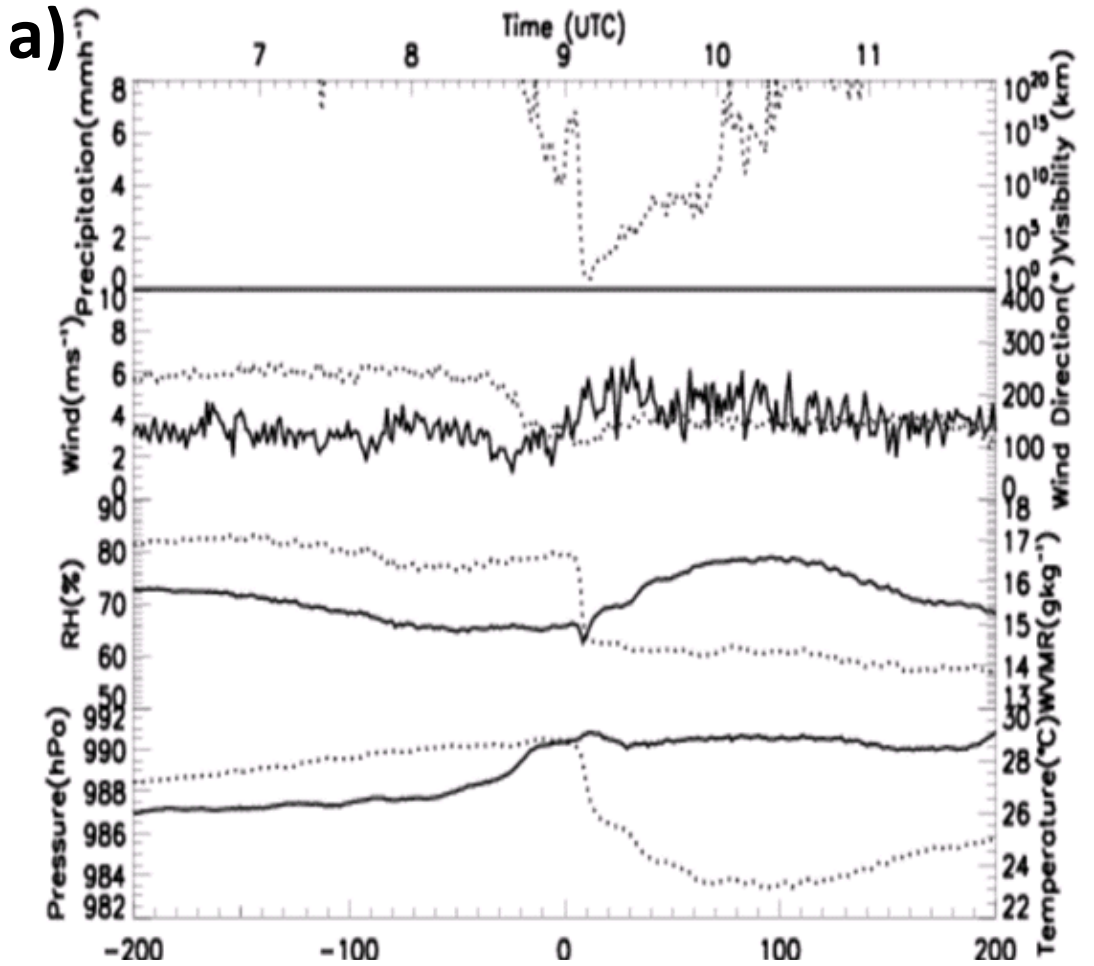


**Figure 4.9:** *Observed surface time series of specified variables time-to-space converted based on the east-west propagation of each squall-line. Solid lines correspond to the left y-axis, dotted lines to the right y-axis. a) is centred at the primary cold pool and approximately corresponds to radar in Figure 4.2 b). b) is centred at the secondary cold pool and approximately corresponds to radar in Figure 4.8 c). Top x-axis is time axis, bottom x-axis shows distance based on conversion.*

Cross-sections converted from time series for the two cold pools that crossed the surface station in Niamey can be seen in Figure 4.9. The first precipitation-free cold pool, hereafter referred to as the “primary cold pool” (see Figure 4.9 a)), was related to the squall-line. It remained in the vicinity of Niamey until the secondary cell approached. The secondary cell was then accompanied by its own cold pool (Figure 4.9 b)), hereafter referred to as the “secondary cold pool”, as well as both convective and stratiform precipitation at the Niamey surface station.

The environmental surface temperature had a maximum of 28.8 °C approximately 8.2km ahead of the primary gust front/cold pool with WVMR being 16.8 g kg<sup>-1</sup>. Before this maximum, surface temperature was steadily rising due to day-time BL warming (Figure 4.9. a)). On the passage of the primary cold pool both temperature and WVMR dropped to 23.3°C and 14.6 g kg<sup>-1</sup>, respectively, as would be expected with a cold pool passage due to change of airmass. Relative humidity initially dropped by ~3 %, but this was shortly followed by an increase due to decreasing temperature. Pressure rose by approximately 1 hPa, suggesting the cold pool was shallow (only ~550 metres based on the same hydrostatic equilibrium assumptions as stated in the previous case). The cold pool depth can also be seen as lower equivalent potential temperature in the lowest ~0.5 km in Figure 4.10 d) below, which agrees with the depth inferred from the assumption of hydrostatic equilibrium and a well mixed cold pool and environment. Pressure remained nearly constant after the first gust front until just before the arrival of the midday cold pool, when it started to rise. Temperature increased while WVMR steadily decreased in between the gust fronts down to 13.8 g kg<sup>-1</sup>, which was measured approximately 10 km ahead of the secondary gust front. Relative humidity followed the gradual decreasing trend of WVMR, further aided by rising temperature. This was contrary to most cold pools in Niamey, where a gradual increase in WVMR was observed after the initial decrease (see section 3.3.1.). This difference was possibly due to the rain-free nature of the primary cold pool at Niamey. Another reason could be that

air into which less rainfall previously evaporated or possibly air from higher (and drier) levels being located closer to the secondary gust front. A maximum in temperature of 25.1°C was measured ~5 km (approximately 5 minutes) before the secondary cold pool crossing. This increase was again very likely related to the diurnal cycle of temperature. Collocated with that was a local minimum in WVMR of ~13.3 g kg<sup>-1</sup> as well as a local pressure maximum and an increase of the wind speed to ~8 ms<sup>-1</sup>. This was ahead of the secondary cold pool and since this was not coincidental, it is consistent with a bore or gravity wave generated by the second cold pool interacting with the stable air of the first cold pool.

The passage of the second gust front/cold pool was more complex. Temperature further reduced, reaching a minimum of 22.1°C ~31.5km east of the secondary gust front while WVMR increased to 14.9 gkg<sup>-1</sup>. Relative humidity rose by ~20% both due to lowering temperature and increasing WVMR. The WVMR increase was related to the rainfall associated with the secondary convective cell, which moistened the secondary cold pool airmass to greater values than those of the dry primary cold pool. Interestingly, the cold-pool related pressure rise of the secondary cold pool was slightly out of phase with the surface temperature drop and the magnitude of the rise was 1.8 hPa. The width of this pressure maximum is similar to that of the secondary convective cell (~30 km – see also Figure 4.12 below). However, it is displaced slightly westwards (~7 km ahead of the cold pool/temperature drop and ~20 km ahead of the convective rain – see also Figure 4.3), which again hints at a presence of a gravity wave.

Ahead of the MCS, wind direction was generally from the southwest, slowly changing to southerly and south-southeasterly on the passage of the primary gust front. The gust front was accompanied by a 6.7 ms<sup>-1</sup> wind gust. Wind then remained gusty due to boundary layer turbulence and mixing with the direction changing back to southwesterly until the approach of the secondary gust front, when wind speed peaked at 9.8 ms<sup>-1</sup>. Wind then changed to southerly on the passage of the secondary gust front and remained so for the next ~20 km. The southerly component of surface wind direction was likely due to the general near-surface outflow from the now dissipating MCS, which was located due south (see radar in Figures 4.8 c) and d)). Approximately 100 km behind the secondary gust front, under the stratiform region, wind direction changed to nearly westerly, signifying again low-level outflow from the retreating and dissipating MCS now due west.

At Niamey no surface rainfall was detected during the passage of the primary cold pool. There was a drop in visibility, however, which was likely a result of dust being lifted by the gust front. The rainfall pattern of the secondary cell is characterised by two maxima of very similar magnitude, but different widths. The first rainfall maximum was located ~20 km behind the second cold pool edge and was collocated with the convective part of the secondary cell (Figure 4.9 c)), having a maximum magnitude of ~6 mm hr<sup>-1</sup>. There was a gap in the rainfall intensity between ~20 and ~40 km behind the gust front, with two minor peaks (~2mm hr<sup>-1</sup>) at ~30 km and ~40 km respectively. A second and much broader rainfall maximum associated with the stratiform part of the MCS (see Figure 4.9 d)) occurred between ~40 and ~100 km behind the gust front with a maximum of ~6 mm hr<sup>-1</sup> (almost identical to convective-rain associated maximum), but generally having rain-rates smaller than 4mm hr<sup>-1</sup>. The cumulative rainfall measured during the whole MCS event of 31<sup>st</sup> July 2006 was 22 mm, all accumulating in association with the secondary cell and stratiform precipitation on the rear side of the MCS.

### ***Changes in atmospheric profile***

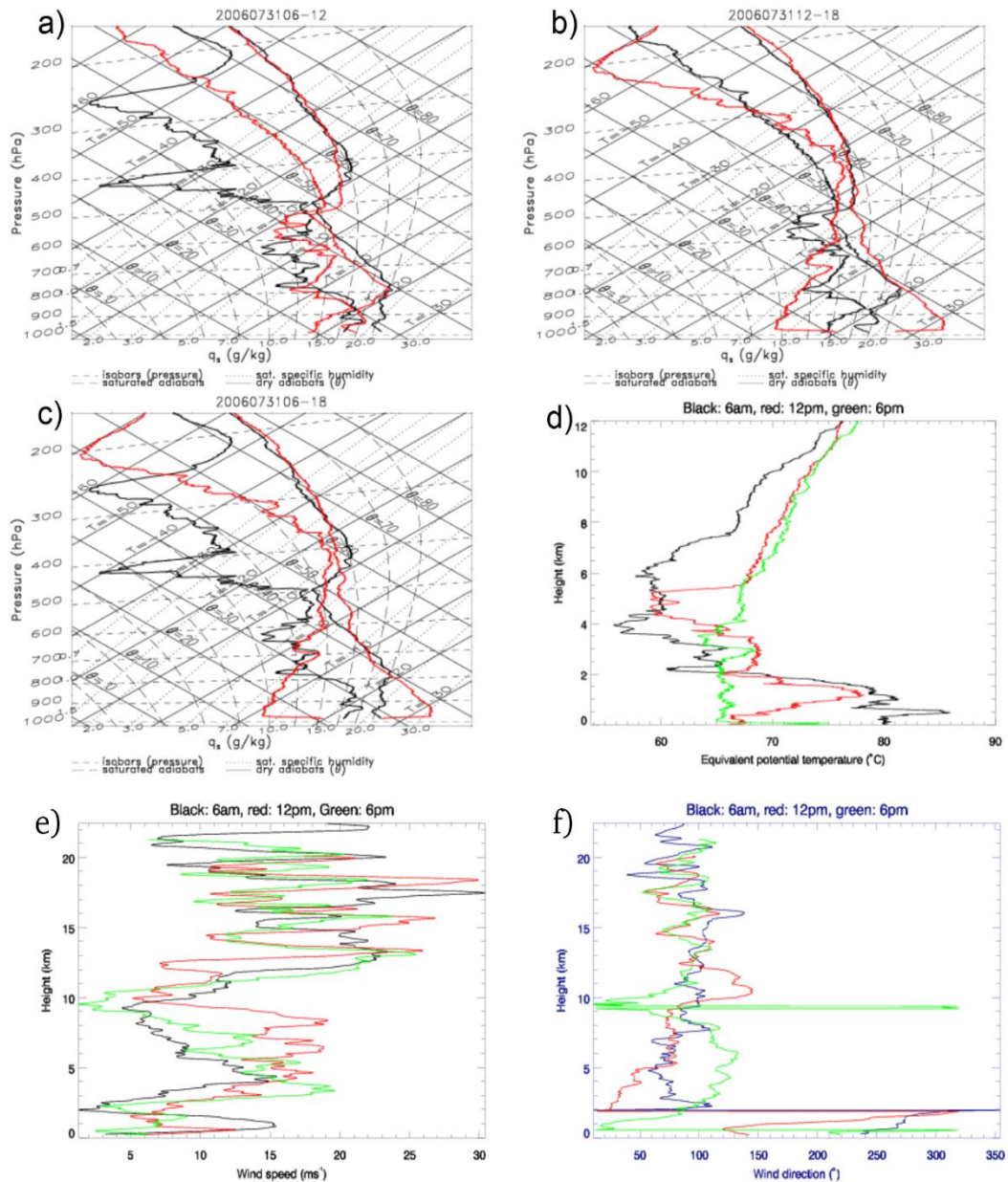


**Figure 4.10:** Comparison of soundings at a) 06:00 UTC and 12:00 UTC, b) 12:00 UTC and 18:00 UTC, c) 06:00 UTC and 18:00 UTC on 31. July 2006. Comparison of equivalent potential temperature profiles d), zonal wind speed profiles e), and wind-direction profiles f). In a), b) and c), the former time is black and the latter red. In d), e) and f), black is 06:00 UTC, red is 12:00 UTC and green is the 18:00 UTC profile.

At 06:00 UTC (Figure 4.10 a), black), the squall-line MCS had been far east of Niamey with no noticed influence on surface variables. A boundary between monsoon-air influenced layer and Saharan Aerosol Layer is evident near  $\sim 800$  hPa, with the top of the SAL being at  $\sim 500$  hPa. Concerning zonal wind-speed and wind direction (Figures 4.10 e) and f), black), the morning sounding has features similar to the 22<sup>nd</sup> July case (see Figure 4.5, black). There is a distinct west-southwesterly low-level jet with a

maximum of  $\sim 15 \text{ m s}^{-1}$  at  $\sim 1 \text{ km}$  at 06:00 UTC, nearly twice as strong as that of the 22<sup>nd</sup> July case (see Figure 4.5, black), transporting the moister airmass into the region. Above the low-level jet, winds of generally easterly direction of varying magnitudes are present in the drier Saharan Air Layer and above (Figure 4.10 e) and f), black). At  $\sim 4 \text{ km}$  a wind maximum of approximately  $15 \text{ m s}^{-1}$  corresponds to the African Easterly Jet.

A comparison between 06:00 UTC and 12:00 UTC soundings (Figure 4.10 a)) has been made in order to see changes in atmospheric profile associated with the primary cold pool. At noon (Figure 4.10 a), red), the outflow boundary of the primary cold pool had crossed Niamey and was located approximately 130 km to the west (see Figure 4.10 b)). At that time the cold-pool airmass reached to  $\sim 850 \text{ hPa}$ , which is indicated by the airmass being both drier and colder (up to  $\sim 6 \text{ }^\circ\text{C}$  at  $\sim 925 \text{ hPa}$ ) in the noon sounding than at 06:00 UTC (Figure 4.10 a), black). This is also evident in the equivalent potential temperature profile (Figure 4.10 d), red), where the primary cold pool led to a reduction of  $\theta_e$  everywhere below approximately 2 km, with the greatest reduction near the surface, having a magnitude of  $\sim 15 \text{ }^\circ\text{C}$ . However, the radiosonde likely encountered the secondary cold pool soon after its release at 11:56 UTC ( $\sim 10$  minutes later, see also Figure 4.10) and therefore this  $\theta_e$  reduction is likely a product of both the primary and the secondary cold pools. Winds in the 12:00 UTC sounding (Figure 4.10 e) and f), red) also suggest the encounter of the cold pool as they are different at the lowest levels with south-easterlies in the lowest 1km. Winds switch briefly back to westerlies between  $\sim 1\text{-}3 \text{ km}$  with a wind maximum of  $\sim 11 \text{ m s}^{-1}$  at  $\sim 1.5 \text{ km}$ . These westerlies just above the easterlies being likely related to the inflow into the approaching secondary cell, possibly being a residual of the LLJ, which had not broken down completely due to reduced mixing and boundary layer growth as a result of the primary cold pool, evident in reduced  $\theta_e$  below the jet (Figure 4.10 d), red). Winds at  $\sim 2\text{-}5 \text{ km}$  are weaker than in the morning, the difference being approximately  $5 \text{ m s}^{-1}$  throughout this layer (Figure 4.10 e) and f), compare black and red). The cause of this may be either damping of the African Easterly Jet by the nearing secondary cell or the approaching afternoon minimum in the diurnal cycle of the African Easterly Jet magnitude (Kalapureddy *et al.*, 2010).

Another difference between the 06:00 and 12:00 UTC soundings is the increase in dew-point temperature at all levels above  $\sim 500 \text{ hPa}$  (Figure 4.10 c)). This is due to the presence of cloud at these levels as the radiosonde entered the secondary cell at  $\sim 500 \text{ hPa}$  (clearly seen as an

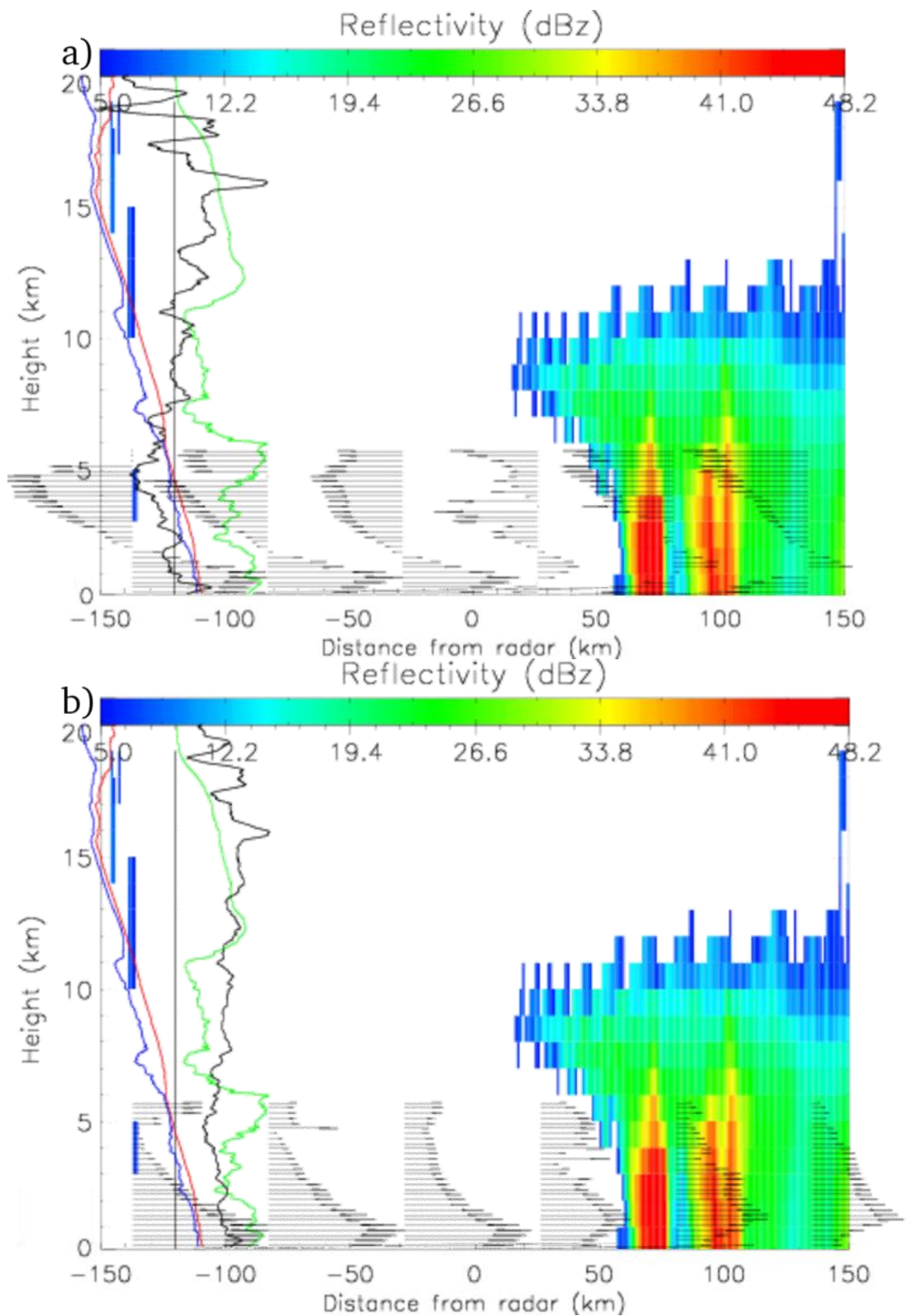
increase in both dry bulb and dew-point temperatures at ~520 hPa in Figures 4.10 a) (red colour) and b) (black colour)). The presence of cloud is further backed by relative humidity with respect to ice, which is above 99% at nearly all levels above ~520 hPa (not shown). Winds between ~6-9 km are stronger in the noon sounding (Figure e), red) and these stronger winds are likely a result of convective outflow from the secondary cell. There is no clear “onion-shaped” sounding behind the primary gust front (Figure 4.10 a), red) and both the dew-point and dry-bulb temperature sounding is not largely different above approximately 800 hPa, except above ~520 hPa due to the cloud. The reason for this is the fact that while the lowest approximately 200 hPa had been affected by the cold pool at 12:00 UTC the free troposphere above was still located ahead of the MCS.

The 18:00 UTC radiosonde was released on the rear side of the MCS, passing through stratiform rainfall area and related cloud (the radiosonde was located at 500 hPa at ~18:20 UTC, which corresponds to the radar in Figure 4.8 d). Comparing the 12:00 and 18:00 UTC soundings (Figure 4.10 b)), the main difference is located in the lowest ~500 hPa. This is because the 12:00 UTC radiosonde was ahead of the secondary convective cell below ~500 hPa and hence in a different airmass. The 18:00 UTC sounding features, like the 22<sup>nd</sup> July case (see Figure 4.4), an “onion shaped” feature below 600 hPa (both mixing ratio and  $\theta$  are nearly constant with cold and moist near-surface layer). This was caused by subsidence-related descent from ~700 hPa, where the airmass had been transported downwards by ~200 hPa. This is also evident between ~500 m and 3 km in  $\theta_e$  (Figure 4.10 d), green), where it is nearly constant and lowered compared to the 12:00 UTC sounding (Figure 4.10 d), red), due to this close-to dry-adiabatic descent of dry mid-level airmass that had been transported to this level. The result is a relative warming (up to 13.1 °C near ~960 hPa) and drying (up to 9.6 °C dew-point decrease near ~940 hPa) of the airmass relative to the 12:00 UTC sounding (Figure 4.10 c), black) below ~800 hPa caused by the MCS. At the lowest level (below ~985 hPa), the dew-point is ~1 °C higher than at noon, which is backed by higher mixing ratio behind the secondary cold pool (see Figure 4.10) and is again related to the rearward propagation of airmass through stratiform precipitation, which caused moistening. The fact that the near surface airmass originated from a different location than the airmass several hundred meters further above is also backed by surface  $\theta_e$  (Figure 4.10 d), green), the value of which is ~15 °C higher at the surface (based on lowest reading from the radiosonde) than at

~800m AGL (this agrees with other post-squall-line observations, e.g. Bryan and Parker, 2010).

When the 06:00 UTC and 18:00 UTC soundings are compared (Figure 4.10 c), the overall effect of the squall-line on the environment can be seen. Figure 4.10 e) shows that wind speed in the evening profile (green) was generally similar to that in the morning profile (black), except at the surface and in two other layers. At the surface, the magnitude of the westerly wind was roughly  $7.5 \text{ m s}^{-1}$  while at 222 m it was  $9.0 \text{ m s}^{-1}$ , with the surface value at 06:00 UTC being  $2.8 \text{ m s}^{-1}$ . The stronger post-MCS surface winds are likely related to the outflow from the MCS and the possible mesolow/mesohigh configuration created by the MCS (see Figure 4.9), as already discussed. Wind direction is generally similar in both soundings (12:00 and 18:00 UTC, see Figure 4.10 f)), except below ~2 km, where easterly winds in the 18:00 sounding prevail. This is due to the absence of the low-level jet and possibly residual easterly that had been mixed from higher levels. The close-to dry-adiabatic descent has warmed the atmosphere by  $6.9 \text{ }^\circ\text{C}$  and dried by  $9.7 \text{ }^\circ\text{C}$  at ~950 hPa with respect to the 06:00 UTC sounding. Based on surface data, 2 m temperature has been warmed by 0.4 degrees at 18:00 UTC when compared to 06:00 UTC, although this is more likely an effect of the diurnal cycle. Overall, the MCS has mixed away the lid/inversion at the top of the Saharan Aerosol Layer (Figure 4.10 c)), which had been present near 500 hPa in the 06:00 UTC sounding (Figure 4.10 c), black), slightly cooling and moistening the atmosphere above and warming below.  $\theta_e$  has been increased aloft (above ~4 km) and reduced at low-levels (below ~3 km), as expected (see Figure 4.10 d)). All three soundings feature a region of relatively strong easterlies with maxima in magnitude near  $15 \text{ ms}^{-1}$  at approximately 3-4 km (Figures 4.10 e) and f)). This maximum corresponds to the African Easterly Jet in the 06:00 UTC sounding (black), which gets stronger and is located at lower levels in the 12:00 and 18:00 UTC soundings (red and green, respectively) due to the descent.

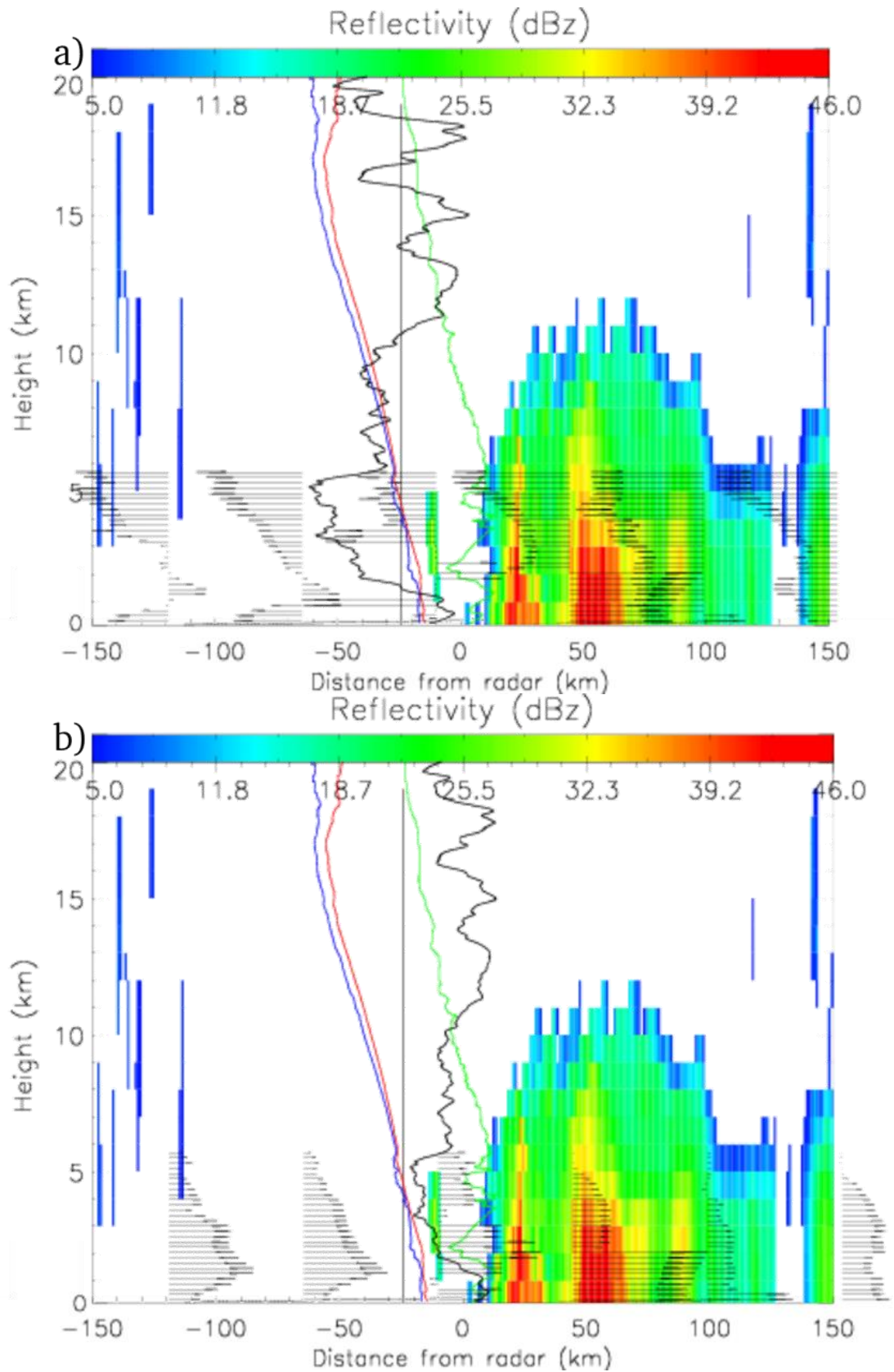
### ***Vertical structure***



**Figure 4.11:** As Figure 4.7, but for 08:30:08Z on 31<sup>st</sup> July 2006. a) are ground-relative winds, b) are storm-relative winds. Radiosonde has been released at 05:38 UTC.

The vertical structure in Figures 4.11 a) and b) shows that there was a convective region comprising of several convective cells (corresponding to the northernmost edge of the squall-line in Figure 4.8 a)). The cells were located at approximately 70 and 100 km east of Niamey at 08:30 UTC, reaching to a height of ~8 km, followed by the broad stratiform rainfall, the reflectivity of which reached up to ~13 – 14 km. Because this was the northernmost edge of the MCS, which was moving slightly south of west, none of this precipitation actually crossed Niamey (see Figure 4.9).

Data from the Radar Wind Profiler show a region of ground-relative westerlies in the lowest ~2 km ahead of the primary cold pool with an elevated wind maximum at ~1.5 km, which agrees with radiosonde data and confirms the presence of the remaining nocturnal low-level jet (Figure 4.10 e) and Figure 4.11). The RWP data also show the African Easterly Jet above ~3 km ahead of the MCS. When considering storm relative zonal winds (Figure 4.11 b)), wind direction at all levels is, like in the 22<sup>nd</sup> July case, into the squall-line, again a result of the relatively high speed of propagation. These storm-relative winds are strongest ahead of the primary cold pool in the Low-Level Jet, which then converges with the cold pool and is lifted above it. The fact that storm relative zonal wind is nearly zero at ~5 km above ground (Figure 4.11 b)) again shows that the steering flow of the squall-line is at that level.



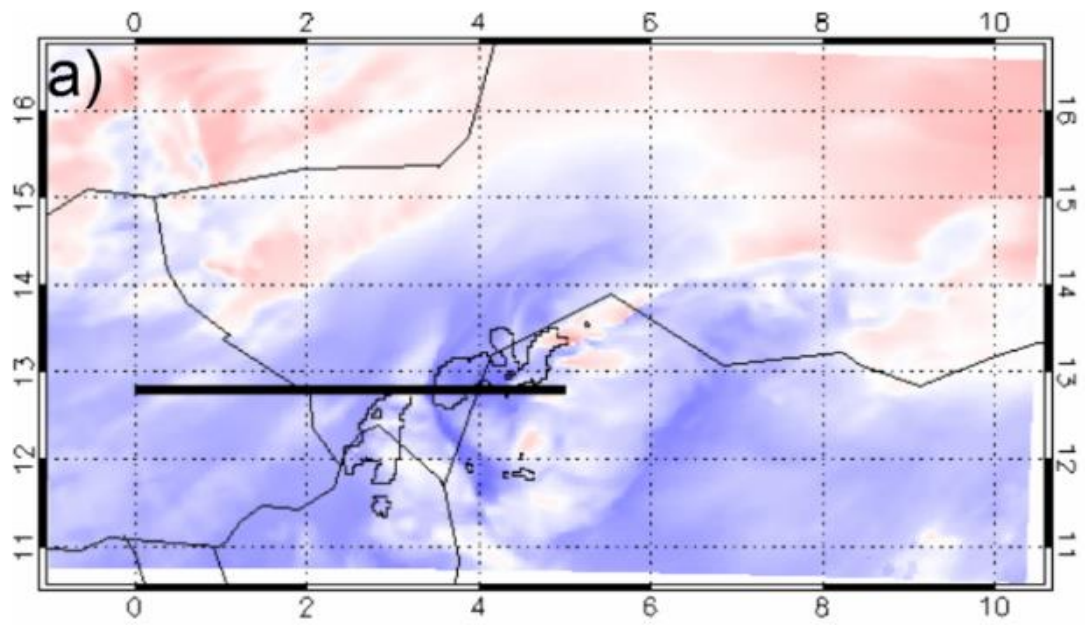
**Figure 4.12:** As Figure 4.11, but for 12:10:08Z on 31<sup>st</sup> July 2006. Winds in a) are ground-relative, in b) storm-relative. Radiosonde has been released at 11:54 UTC.

Figure 4.12 shows the secondary cell being located just east of Niamey at ~+20 km. Reflectivity of 40 dBz and greater reaches to ~4 km on the vertical radar cross-sections (Figures 4.12 a) and b)) in the secondary convective cell, which is approximately half of that in the primary convective region (Figure 4.12 a)). The reason for this is the fact that this cell was in a developing stage at the time. However, its height only ever reached ~3/4 of that of the primary squall-line (not shown), a result of overall weaker updraft. The reason for weaker updraft may have been reduced CAPE when compared to the primary squall-line, resulting from the primary cold pool under-cutting this convective cell. Another reason could be subsidence related to the primary MCS to the south and south-west.

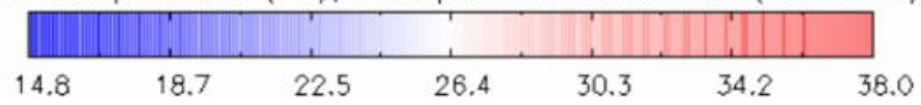
Unlike in case of the primary gust front, ground-relative winds ahead of the secondary gust front are easterly (this agrees with surface data in Figure 4.9 as well as with soundings in Figure 4.10 d). This is a result of the primary cold pool and outflow from the main MCS, which was located further south at this time (see Figure 4.8 c)). A narrow region of ground-relative westerly winds, however, remains above the cold pool (westerly winds above easterly winds ahead of the secondary cell in Figure 4.12 a)). These winds are coincident with enhanced dew-point and equivalent potential temperature (see Figure 4.10 b), black, and d), red) and form the residual of the low-level jet feeding the MCS with moist air, eventually becoming the front-to-rear jet.

### **4.3.3 Preliminary analysis of UM simulation of the 31<sup>st</sup> July 2006 squall-line MCS**

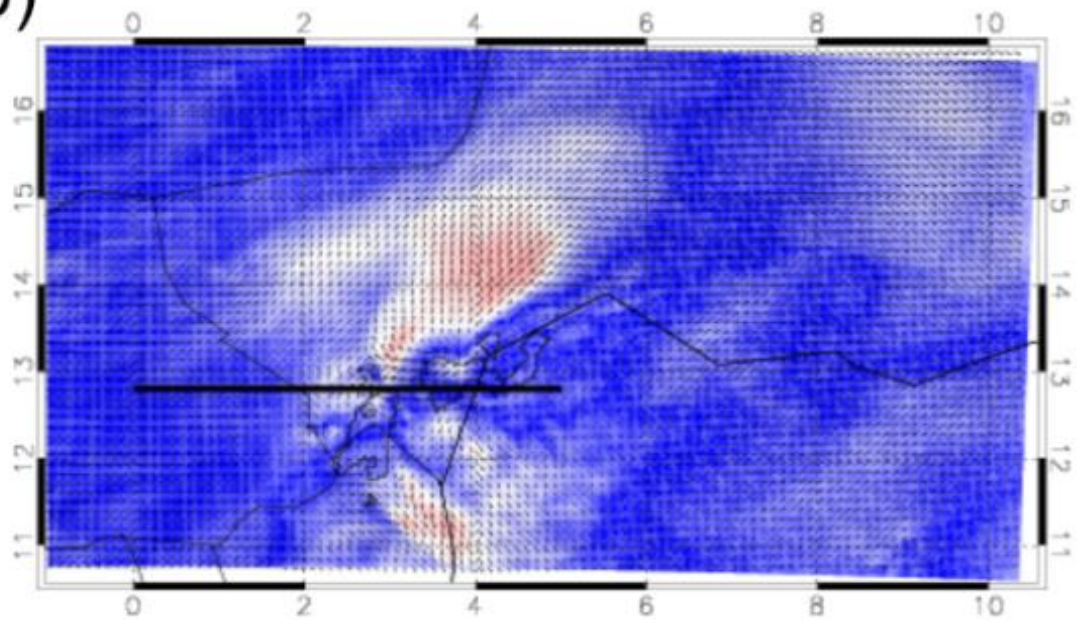
An insight into the dynamics of a Mesoscale Convective System simulated by the Unified model has been done, but further work is needed to evaluate the dynamics or microphysical properties in any details. The MCS was simulated by Unified Model 4-km convection-permitting simulation that had originally been run for the purpose of the study by Birch *et al.* (2014). The simulation captured the 31<sup>st</sup> July 2006 MCS with a reasonable precision to enable the use of simulated data for greater in-depth study of the case, which would have not been possible by using only existing observational datasets.



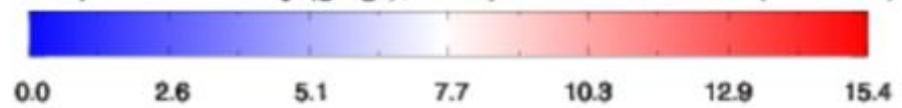
2m Temperature ( $^{\circ}\text{C}$ ); Precipitation occurrence (contours)



b)



4 m Specific humidity ( $\text{g kg}^{-1}$ ); Precipitation occurrence (contours)



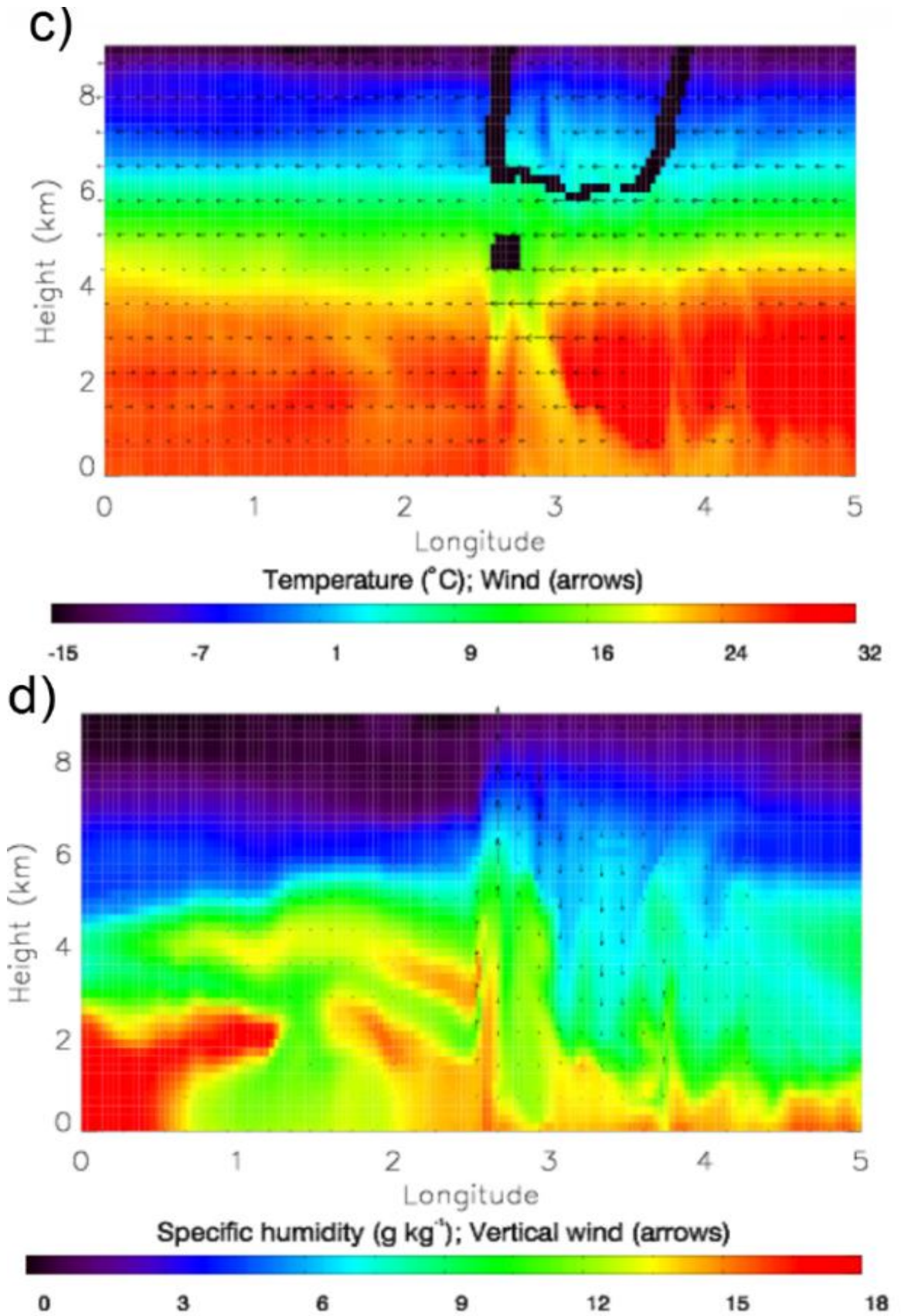


**Figure 4.13:** UM model simulation for 11:00 UTC on 31<sup>st</sup> July 2006 showing a) 1.5 m temperature, b) 4 m specific humidity c) zonal vertical cross-sections through the simulated squall-line at 12.8 °N (as denoted by thick

*black line in a) and b)) showing temperature and d) specific humidity. In a) and b) contours represent precipitation greater than 2 mm. Arrows in b) represent 4 m windspeed and wind direction. Arrows in c) indicate ground-relative zonal windspeed and direction. Arrows in d) indicate vertical windspeed and direction. Contours in c) enclose regions where the sum of cloud water and/or cloud ice densities is greater than  $0.01 \text{ kg m}^{-3}$ .*

The thermodynamic environment as well as flows and moisture transport within the simulated MCS are visualised in Figure 4.13. Several areas of precipitation located near  $3\text{-}5^\circ \text{E}$  and  $12\text{-}15^\circ \text{N}$  are producing a common surface cold pool, the 1.5 m temperature of which is  $\sim 7^\circ \text{C}$  colder than its environment. The cold pool is also drier than its environment at the surface (Figure 4.13 b)), spreading out in all directions and being characterized by a sharp temperature boundary on the western edge (Figure 4.13 a)). Ahead of the boundary, which is located near  $3^\circ \text{E}$ , westerly flow with wind maxima over  $10 \text{ m s}^{-1}$  at  $\sim 2 \text{ km}$  prevails below  $\sim 4 \text{ km}$ . This is the low-level jet. Moisture pooling due to converging winds is evident near  $2.5^\circ \text{E}$  with specific humidity of up to  $18 \text{ g kg}^{-1}$  (Figure 4.13 b) and d)), but this is reduced in the lowest approximately  $2 \text{ km}$  further west between  $\sim 0.75$  and  $2^\circ \text{E}$ , which is likely related to a previous cold pool that had affected that area (not shown). Positive moisture anomaly is present in the region of convective updrafts in Figure 4.13 d) near  $2.6^\circ \text{E}$ , representing vigorous convective updrafts, which are fed by moisture.

The convective updrafts are followed by broader downdrafts to the east (Figure 4.13 d)). Low-level wind direction changes to easterly on the passage of the MCS-related outflow boundary with easterlies of varying magnitudes at all levels behind the edge of the cold pool, representing the rear-inflow jet (Figure 4.13 c)). This Rear Inflow Jet has a wind maximum of  $\sim 15.5 \text{ m s}^{-1}$  at  $3.8 \text{ km}$ . On the rear side (between  $\sim 3$  and  $4^\circ \text{E}$ ), precipitation driven downdrafts are related to mixing of dry mid-level air towards the surface with the descent causing warming and drying (Figure 4.13 c) and d)). This descent, however, does not penetrate all the way to the surface. The lowest approximately  $1 \text{ km}$  east of  $3^\circ \text{E}$  features local maxima of specific humidity above  $\sim 15 \text{ g kg}^{-1}$  (Figures 4.13 d)) and temperature near  $22^\circ \text{C}$  (Figure 4.13 c)) while the air mass above features specific humidities nearly  $10 \text{ g kg}^{-1}$  lower (Figure 4.13 d)) and temperature nearly  $10^\circ \text{C}$  higher than near the surface (Figure 4.13 c)). This agrees with the observed “onion sounding” in Chapter 4, section 4.3.2., which was a result of descent both in the observations and the simulation. The cool and moist near-surface layer

also agrees with that observed in section 4.3.2. This layer is a result of evaporation of rainfall into the rearward spreading low-level airmass.

An interesting feature, which has not been detected in the observed case in section 4.3.2., is the relatively warmer patch on the rear side of the precipitation in Figure 4.13 a). Localised features associated with a sudden rise in temperature, which can also be associated with a drop in humidity and an increase in gustiness (see Figure 4.13 b)) have been described as “heat bursts” by Johnson (1983). The warm patch in Figure 4.13 a) was formed under a dissipating area of precipitation and Figure 4.13 b) confirms that reduced 4 m specific humidity is located, in addition to diverging 4 m winds, near/under the areas of precipitation.

The simulation produced the MCS of 31<sup>st</sup> July 2006 with a good precision, capturing all the main observed processes. These included convective updrafts followed by downdrafts, the low-level jet, the rear inflow jet and warming and drying due to descent (“onion shaped sounding”) on the rear side of the MCS. The cold pool of the simulated MCS was, like the observed case, colder and drier than its environment with similar magnitudes of changes.

#### **4.4 Discussion & Conclusions**

Two observed case studies of squall-line MCSs have been investigated using observational data from Niamey (obtained during AMMA). In general, both squall-line MCSs featured a region of convective updrafts on the front (western) side of the MCS with a trailing stratiform precipitation behind. Both MCSs were accompanied by a cold pool that crossed the surface station in Niamey, this being a single cold pool for the 22<sup>nd</sup> July 2006 case and a rain-free cold pool followed by a secondary cell with its own cold pool for the 31<sup>st</sup> July 2006 case. This study has investigated the structure of both MCS using radar, surface data, radiosonde data and Radar Wind Profiler.

The MCS of 22<sup>nd</sup> July 2006 and the primary squall-line of the MCS of 31<sup>st</sup> July 2006 passed Niamey in the morning hours as mature squall-lines that were beginning to enter the process of dissipation. A nocturnal low-level jet was present at a height between ~1-2 km in both cases, this being approximately twice as strong for the 31<sup>st</sup> July case, fuelling the MCSs with warm and moist air as a front-to-rear jet. In the 31<sup>st</sup> July 2006 case, the remainder of this nocturnal low-level jet persisted until noon above the

primary cold pool due to inhibited mixing in that cold pool or possibly due to greater magnitude of winds in the low-level jet. This remaining low-level jet fuelled the secondary cell with warm and moist air, providing convergence and enabling it to persist above the stable low-level cold pool. Both MCSs were driven westwards by mid-level (at ~4-5km) easterly winds that were associated with the African Easterly Jet. The African Easterly Jet related winds were enhanced by the MCS, where heating and evaporation/melting/sublimation normally results in a region of lower pressure at mid-levels on the rear side of the MCS. This led to the formation of rear-inflow jets, which fed the convective downdrafts and cold pools that were spreading ahead of the MCSs.

At the surface, cold pools played the major role in affecting near surface variables. Both cold pools were associated with a cooling and a temporary rise in pressure. The cold pool of the 22<sup>nd</sup> July 2006 case and the primary cold pool of the 31<sup>st</sup> July 2006 case were drier than the environment, which is typical for this time of the monsoon season (see section 3.3.2.). This was due to the transport of very dry mid-level airmass to the surface by convective downdrafts. The secondary cold pool of the 31<sup>st</sup> July 2006 case was moister than the primary cold pool, but drier than the environment, this being due to the precipitation accompanying the secondary cell. A possible gravity wave has been observed ahead of the secondary cold pool. This gravity wave would have been created by the interaction of the secondary cold pool with the primary cold pool, using the primary cold pool as a waveguide. All cold pools were associated with gusty winds, either due to transport of momentum to the surface by convective downdrafts or due to the ambient MCS-affected pressure field.

Wind direction ahead of both MCSs was from the westerly or south-westerly direction. This changed to easterly several kilometres ahead of the cold pools and then back to westerly behind the convective regions. This westerly low-level outflow on the rear sides of the MCSs transported the downdraft airmass through the stratiform region, where precipitation fell through it, cooling and moistening this near-surface airmass. Descents of African Easterly Jet winds in downdrafts on the rear sides of the MCSs generally penetrated to ~950 hPa, resulting in very dry and warm airmass above the cool and moist near surface post-MCS airmass. This led to "onion shaped profiles" on the rear side of both MCSs. Both squall-line MCSs were moving faster than the ambient wind at all levels above ~1 km, although the ambient wind was nearly zero at heights around 5 km. Therefore, the storm-

relative wind was always westerly, except in the cold pools. This agrees with many previous observational and modelling studies of squall-lines (e.g. Zipser, 1969; Miller and Betts, 1977; Houze 1977; Moncrieff and Miller, 1976).

The results of this chapter are an addition to the knowledge of West African squall-line MCSs. The details of internal structure of these MCSs that were possible to be obtained due to the availability of high density observations in both space and time provide a useful insight into many processes that govern the evolution of squall-line MCSs. The case of 31<sup>st</sup> July 2006 is an observational addition to the study of the primary MCS simulated by Birch *et al.* 2014. The visualisation of features in radar composites can be helpful for further exploration and evaluation of these in future studies as well as for model and convective parameterization developers.

#### **4.4.1 Future work**

The AMMA field campaign provided more observational data available for the two squall-line MCS case studies that future studies may utilize for further analysis. In addition to radar reflectivity, the MIT radar provided Doppler wind data, which would show the wind structure of both MCSs with a greater precision. The use of Doppler Radar wind data would give considerably greater resolution, both in space and time, of the internal MCS flows, such as the Rear Inflow Jet, the front-to-rear jet, anvil layer winds as well as the flow that feeds the cold pool. This would enable the identification of the level where the downdraft that feeds the cold pool originates as well as its trajectory through regions where processes such as evaporation of rainfall have an impact on the airmass.

For the 31<sup>st</sup> July case study, the inflow of moist air into the secondary cell could be further studied by the use of radiometer, which provides approximately six times more frequent data than radiosondes. The data is averaged for every hour, but assuming the inflow above the cold pool is nearly constant over the hour, a minimum of three radiometer scans could be utilized to envisage the temperature and moisture boundary between the dry cold pool and moist inflow above. In addition, further scans ahead of the primary cold pool could provide more data ahead, which would enable the verification that the moist inflow is a continuation of the low-level jet, which

does not break down due to reduced turbulence and mixing within the cold pool.

Section 4.3.3 of this study presents a preliminary and basic analysis of the UM simulated 31<sup>st</sup> July 2006 case (simulation provided by Birch *et al.* 2014). This simulated case may be further investigated with a large variety of UM data of high density in both space and time. More cross sections at different times and locations through the MCS would provide much more insight into the evolution of the MCS. While the MCS is already in progress at the beginning of this simulation, its dissipation is simulated and the details of processes, which led to weakening and dissipation of convective updrafts, can be explored. Since two areas of precipitation are present at the beginning of the simulation (not shown), the interaction of the two cold pools that were likely produced by evaporation of this precipitation may provide further insight into cold-pool collisions/combinations. Currently, there is no simulation for the 22<sup>nd</sup> July case. Future studies may attempt to capture the MCS observed on 22<sup>nd</sup> July 2006 in a UM simulation to enable further study of processes observed in that system, such as the initiation of isolated cells ahead of the main squall-line and their merging with the squall-line later on. The UM simulations may then be evaluated by comparing observed results with values provided by the simulation.

Future studies may also focus on a different case study from AMMA, which has not yet been published, or use a variety of case studies to characterize their properties. Current dataset holds similar amount of data for 38 squall-line MCSs, most of them not studied in a manner similar to this study, which may be enough to generalize conclusions about their structure and may even provide some insight into sub-seasonal changes in MCS internal structure. If future field campaigns similar to AMMA were to take place in West Africa, they may focus on different geographical area and provide local as well as remotely sensed data (such as radar) to enable comparison of the internal structure of MCSs in various West-African locations.

## Chapter 5

# Diurnal cycle of convective storms and their initiation in the Sahel

### 5.1 Introduction

The processes, which lead to convective initiation and organization of convection often follow a diurnal cycle (Janiga *et al.*, 2014). This is in the form of initiating convective storms in the afternoon, which are at first mainly isolated, then intensify and grow upscale overnight (Duvet, 1989) and persist even though there is no solar heating and surface temperature decreases (Davis *et al.* 2003), before dissipating the following morning. This chapter presents a study of the diurnal cycle of convective storms in the West African Sahel and various environmental properties that influence it. Both observational data and Unified Model *Cascade* simulations are used. The diurnal cycle in convective storms is an important aspect of the West African climate since deep moist convection brings a large majority of rainfall to the area and accounts for the largest changes in weather conditions. Current operational forecasting models fail to produce the diurnal cycle in deep moist convection correctly as they fail to produce some of the processes that are important in driving and maintaining deep moist convection with implications for the entire West African Monsoon (Marshall, 2013, Birch, 2014). Therefore, the aim of this chapter is to focus on and investigate processes in the environment that may be most important for the observed diurnal cycle. Deep moist convection brings a great majority of rainfall to most of the Sahel. Over 80% of rainfall on average is delivered by MCSs with nearly all of the remaining 20% being associated with other forms of more isolated convective rain during the monsoon season (D'Amato and Lebel, 1998; Dhonneur, 1973; Mathon *et al.* 2002; Redelsperger *et al.*, 2002).

There are previous studies, such as Carleton *et al.* (2001), or Taylor and Ellis, (2006), which investigate the role of individual properties, such as feedbacks between soil moisture and precipitation and the processes that control their relationship. Here, the focus is on the overall environmental state and the relative importance of the role of individual processes observed. This includes the thermodynamic profile, which controls the amounts of available CAPE and CIN, but also wind shear, the role of which

is important in organizing convection (Barnes and Sieckman, 1984). Focus is also given to the importance of surface properties as these can strongly influence convective initiations (e.g. Taylor *et al.*, 1997 and Koster *et al.*, 2004).

The diurnal cycle in deep moist convection is affected by a large number of factors, other than convective initiations. It depends on how favourable the environment is for deep moist convection and whether it could be sustained in this environment. The necessary ingredient for deep moist convection is atmospheric instability, which can be measured by Convective Available Potential Energy (CAPE) (Emanuel, 1994). It is very important at which layer this CAPE is present and whether convection is able to take profit from it and lift the unstable parcels. The important variable for sustaining existing convection is wind shear as unfavourable wind shear generally leads to unorganized short-lived convection even if CAPE is present (Barnes and Sieckman, 1984).

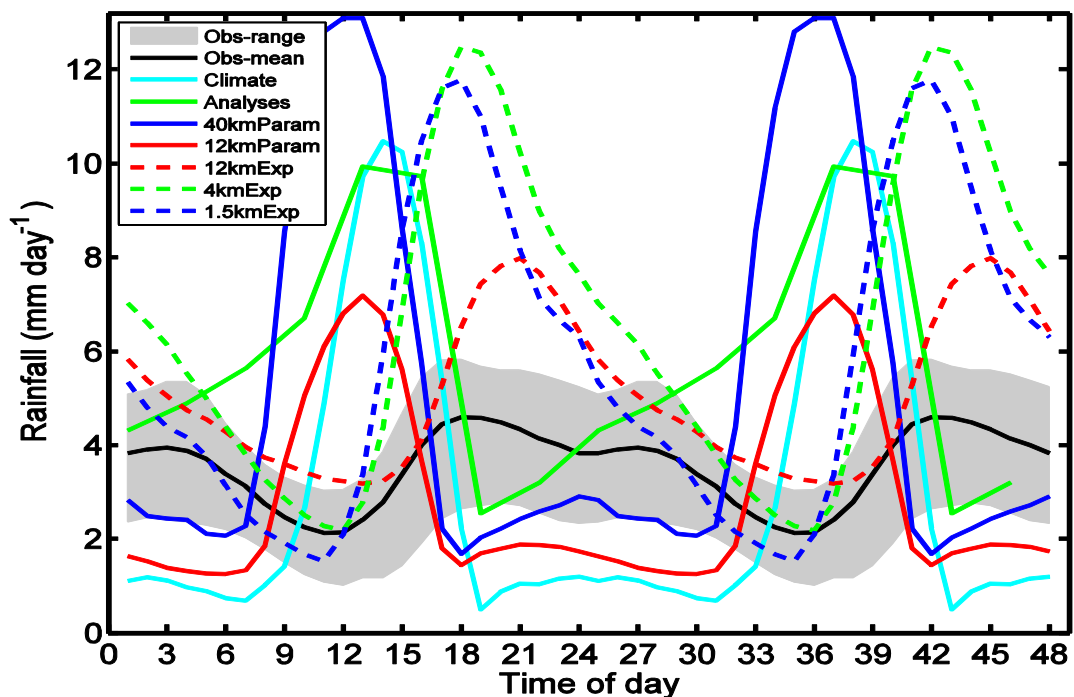


**Figure 5.1:** Mean observed and simulated diurnal cycle of rainfall. Output of various runs from Cascade is shown as specified. The grey area represents the range (minimum and maximum) of rainfall retrieved from satellite products. Figure obtained from Birch *et al.* (2014) – Figure 3.

Figure 5.1. shows an example of various runs of Unified Model (UM) simulations and compares them to observed values. The observed diurnal cycle in rainfall over the Sahel features a minimum at noon, followed by an increase in rainfall throughout the afternoon, which has a maximum around

6pm. Mean rainfall rate then decreases overnight, but has a secondary smaller peak at approximately 3am. This diurnal cycle is caused by convection initiating over orography the previous afternoon, then organizing into MCSs and propagating westwards over the Sahel while growing upscale (Duvel, 1989), remaining active long after daytime heating has ceased (Davis *et al.* 2003). The 4km *Cascade* simulation, which has been used in this study, largely overestimates rainfall, which is most pronounced in the late afternoon peak. The general timing of diurnal cycle is however simulated rather well, but the ~3am secondary peak in rainfall is smaller than in observations.

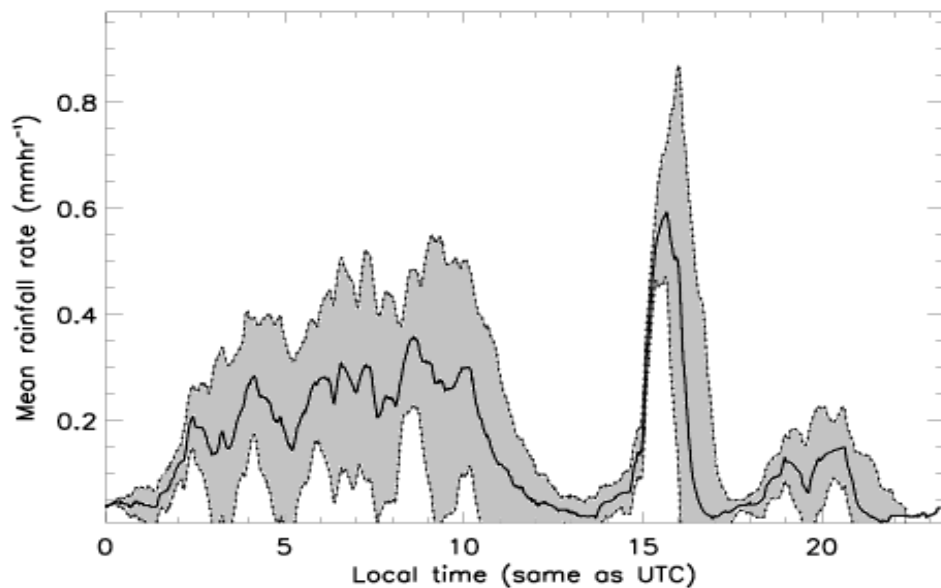


**Figure 5.2:** Mean rainfall rate ( $\text{mm hr}^{-1}$ ) by time of day between 1<sup>st</sup> June 2006 and 30<sup>th</sup> September 2006. Shaded area indicates the standard error. Data obtained from surface station in Niamey.

Because observational data used in this study have been obtained in Niamey, Niger, the diurnal cycle of rainfall over Niamey is considered. The difference between the observed mean rainfall rates over Niamey (Figure 5.2.) and over the whole of Sahel (Figure 5.1.) arises from the fact that convective storms in West Africa generally initiate over orography several hundred kilometres east of Niamey (such as the Air plateau) in late afternoon and then propagate westwards or south-westwards (see also section 1.1.1.). Therefore, many locations have a peak in rainfall activity that depends on the distance they are located from these orographic features.

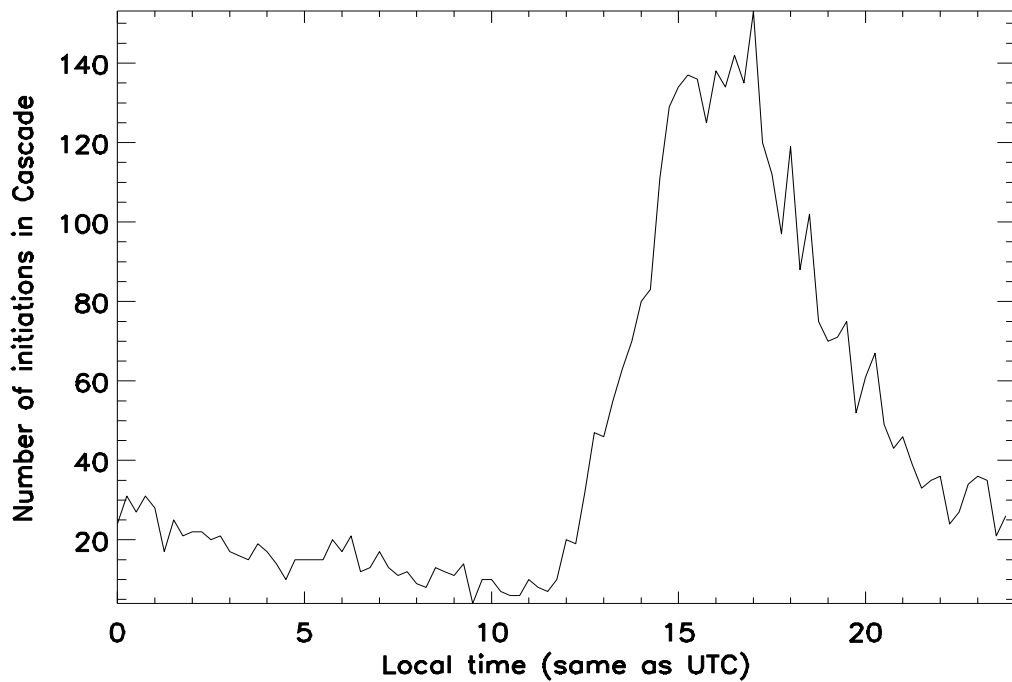


**Figure 5.3:** Number of convective initiations per 15 minutes in 4 km Cascade between 25<sup>th</sup> July 2006 and 2<sup>nd</sup> September 2006. Initiations from Taylor *et al.* 2013.

Figure 5.2. agrees with Rickenbach *et al.* (2009), who showed that the diurnal rainfall cycle in Niamey has two maxima. There is a broad rainfall maximum between ~02:00 UTC and approximately 10:00 – 11:00 UTC with several peaks, these being a result of individual heavy convective rain events (Figure 5.2.). The morning maximum in rainfall is a result of high nocturnal frequency of squall-line MCS passages in Niamey and if mean accumulated rainfall is taken into account (area under the curve), it shows that nearly 70% of rainfall is recorded in that time-frame. The broad maximum has a gradual reduction in intensity after 11:00 UTC, most likely due to the transition of intense convective rain into less intense but longer lasting stratiform rain. This is followed by a minimum in mean rainfall lasting from ~11:00 UTC until 15:00 UTC, which generally corresponds to the overall minimum in convective activity over the Sahel (see Figure 5.1.). An isolated sharp and high peak is observed between ~15:00 UTC and 16:00 UTC, which is when convective initiations sharply rise (see Figure 5.3.). This is a result of local isolated convective storms and smaller MCS initiated in the Air Mountains. While the afternoon convection may often be more intense than the nocturnal squall-lines, hence the strong magnitude of the mean rainfall rate, its localised characteristic means that its occurrence at Niamey is rare and hence the accumulated precipitation is much smaller

than for the overnight peak. These results agree with the diurnal cycle of convection as presented by Janiga *et al.* (2009), who also found a late-afternoon peak around 18:00 UTC (originating in Air Mountains) and a late-night/early morning peak around 05:00 UTC. The timing of these peaks is slightly different than those observed in this study, but this may be due to the use of satellite data rather than surface data by Janiga *et al.* (2009). Rickenbach *et al.* (2009) suggested that the secondary smaller peak in rainfall at 20:00 UTC is a result of delayed maximum in local afternoon convection early in the season. This is when convective inhibition is stronger, which is likely related to the absence of large-scale forcing from African Easterly Waves, the activity of which is not as great as during mid-season.

Convective triggering is one of the most important factors influencing diurnal cycle in deep moist convection. The diurnal cycle in initiations (Figure 5.3.) shows *Cascade* diurnal cycle in convective triggering/initiations and it can be seen that a distinct maximum occurs in the late afternoon and early evening. This is in agreement with observations from Janiga *et al.* (2009), who observed a maximum in convective initiations at 18:00 UTC, or Sultan *et al.* (2007), who also reported a maximum at 18:00 in the Intertropical Convergence Zone. Initiations sharply increase after midday with a maximum at 17:00 UTC. The drop is sharp until mid-evening (~20:00 UTC) and then the number of initiations gradually reduces overnight and in the morning until approximately noon when it reaches its diurnal minimum. The time when convective initiations rapidly increase between ~12:00 UTC and 18:00 UTC corresponds to the time of increase in mean rainfall rate (see also Figure 5.1.). The number of initiations then drops, but remains relatively high until ~21:00 UTC. It then sharply drops overnight, but rainfall intensity remains nearly unchanged until the morning hours. This further reflects that existing convective storms that had initiated in the preceding afternoon grow in intensity and size, producing more rainfall per storm overall.

Initiating convection is often forced by vertical motion, which requires convergence at the level from which convection initiates. The forcing can be produced by a range of mechanisms such as cold pools, soil-moisture boundary- or orography-induced circulations, gravity waves, potential vorticity anomalies or any other feature or mechanism, which can create surface forcing or a local circulation that can eventually force parcels through the convective inhibition and lead to initiation.

In the Sahel away from orography, initiations can be driven by various complex mechanisms, often driven by soil-moisture gradient-related thermally induced circulations in the afternoon hours. During the summer months in West Africa, soil moisture, associated with anomalies in  $\Theta_e$ , has strong influence on deep moist convection and precipitation (e.g. Taylor *et al.*, 1997 and Koster *et al.*, 2004). There is a feedback between precipitation and soil moisture, which could either be positive, as discussed in section 1.1.1., or negative (Taylor and Ellis, 2006). This is true in summertime West Africa as surface evaporation is limited by soil moisture rather than temperature, wind or radiation (Gash, *et al.*, 1997). For soil moisture and precipitation feedbacks to be sustained there has to be sensitivity of atmosphere to surface fluxes of heat and moisture as well as sensitivity of these fluxes to precipitation (Taylor, *et al.*, 2010).

When incoming solar radiation reaches the surface and is absorbed, it can be transformed either into latent heat, sensible heat, or re-emitted as long-wave radiation. How much is transformed into latent and sensible heat depends on the moisture content of the surface. Boundary layer air is cooler and moister over wetter ground and drier and warmer over dry ground (Kohler *et al.*, 2010). The lower sensible heat flux over wetter surfaces reduces mixing and associated entrainment and is more than offset by an increase in  $\Theta_e$ , resulting in larger amounts of CAPE (Adler *et al.*, 2011; Alonge *et al.*, 2007). According to Ek and Holtslag (2004), the increase in moisture at the top of the boundary layer is sensitive to the stability of the layer above the boundary layer. The resulting lower boundary layer over wetter surface, however, increases CIN (Garcia-Carreras *et al.*, 2011), which needs to be penetrated by initiating moist convection. Since fluxes of equivalent potential temperature are almost independent of Bowen ratio (Garcia-Carreras, 2011), there is no obvious direct preference for convection to form over wet ground than over dry ground. Recent observations however show that Sahelian convection tends to form over dry ground adjacent to a wet patch (Taylor *et al.* 2015). Taylor and Ellis, 2006). Differential heating of a surface with a soil-moisture gradient causes horizontal gradients in surface temperature, which can be the focus for the initiation of convection. This is supported by several modelling studies (Anthes, 1984; Chen and Avissar, 1994; Emori, 1998) and is based on the fact that the horizontal temperature gradients may induce circulations similar to land-sea-breezes (Segal and Arritt, 1992; Taylor *et al.*, 2007b). Therefore, convection has a preference to initiate over dry land that is adjacent to a wet patch several hours after maximum in incoming solar radiation (Taylor *et al.*, 2011; Emori, 1998).

Taylor *et al.* (2011) found that 37% of storm initiations over the Sahel occurred over the steepest 25% of soil-moisture gradients. When convective storms initiate, they often grow upscale and are then steered by the African Easterly Jet westwards throughout the evening, long after solar heating has subsided (see section 1.1.1. for more details). These storms then normally persist overnight, but dissipate in the morning when solar heating commences again.

The main aim of this chapter is to investigate the relative role of thermodynamic as well as dynamical processes that play an important role in this behaviour of convection throughout the diurnal cycle. Here, the diurnal cycle of several parameters that influence atmospheric instability and the organization of convection are studied to infer their influence on the observed diurnal cycle of convection. Section 5.2. describes the observational and model analysis methods. Section 5.3.1. focuses initially on the observed thermodynamic environment of convective storms and then on various dynamical processes that can influence the diurnal cycle. The role of moisture flux convergence as well as other mechanisms that may influence the intensity of convective rainfall are investigated. Section 5.3.2. focuses on convective initiations and the processes that control the diurnal cycle of these. Section 5.4. summarizes the results and discusses their implications.

## **5.2 Methods**

### **5.2.1 Observational data**

In this Chapter data obtained during the AMMA SOP have been used for the purpose of obtaining profiles of thermodynamic and wind-related environmental variables. Profiles of temperature, potential temperature, CIN and wind speed have been obtained from radiosondes. Moisture-related profiles, such as WVMR, equivalent potential temperature and CAPE have been obtained from a radiometer.

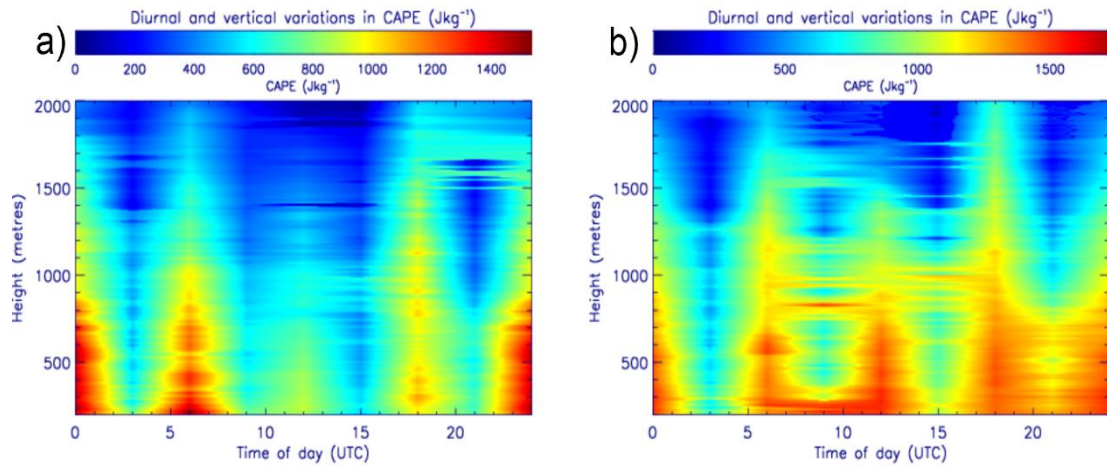


**Figure 5.4:** Diurnal variations in vertical CAPE ( $\text{J Kg}^{-1}$ ) distributions. Data obtained between 1<sup>st</sup> June 2006 and 30<sup>th</sup> September 2006 in Niamey from raw radiosonde data a) and moisture-bias corrected radiosonde data b).

The reason for using data from a radiometer rather than from radiosondes for the variables related to moisture was a moisture bias, which has been identified in the original radiosonde data obtained during AMMA SOP in Niamey (Agusti-Panareda *et al.*, 2009). This bias is pronounced more in the 03:00, 09:00, 15:00 and 21:00 (all UTC) soundings (further described as the intermittent soundings) than in the 06:00, 12:00, 18:00 and 00:00 (all UTC) soundings (further described as the main soundings) (see Figure 5.4. a)). This is because two radiosonde types have been used – the Vaisala RS80A and the Vaisala RS92. The bias is either an underestimation or overestimation of moisture that has been evident to a varying degree dependant on height, time of day and type of radiosonde used. The time of day dependent systematic bias has been caused by variations in solar radiation and its effect on the dew point sensor of the radiosonde. A correction to this bias has been suggested and performed by Agusti-Panareda *et al.* (2009) and the bias-corrected radiosonde data have been considered for this study (Figure 5.4. b)). The corrected dataset nevertheless featured significant differences in moisture (dew-point temperature) between the main and intermittent soundings giving spurious 3-hourly variations in CAPE. Because data provided by the radiometer included profiles of pressure, temperature and dew-point temperature, which are sufficient for the calculation of CAPE, the CAPE profiles have been calculated from radiometer data instead of radiosondes. Radiometer scanned at 1-minute intervals, was available as hourly averages and spanned the vertical profile between 200 metres and 4 km above ground.

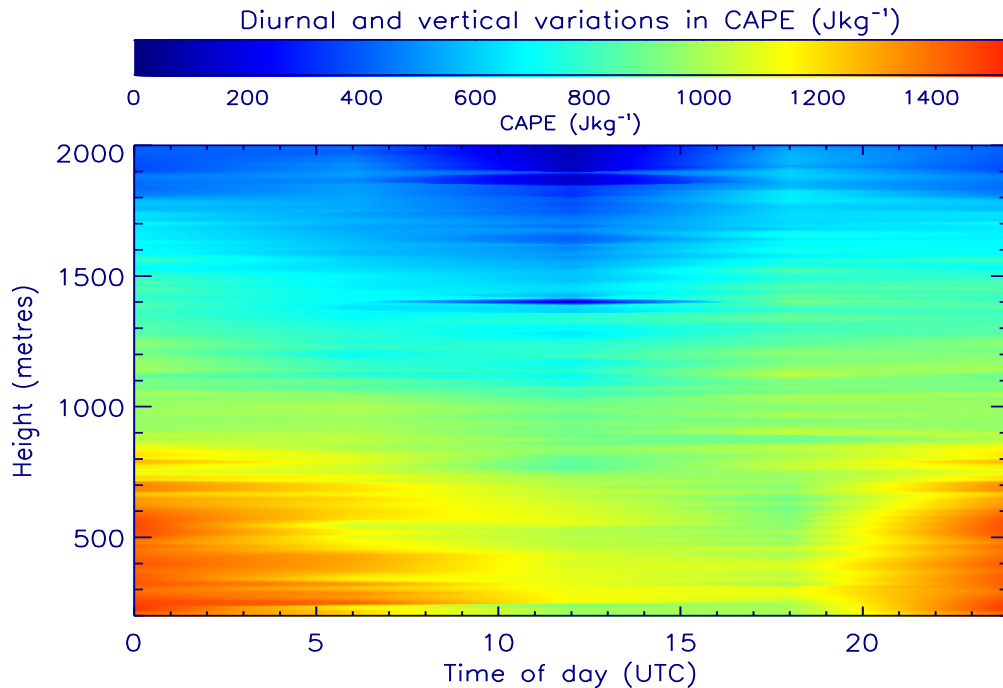


**Figure 5.5:** As Figure 5.4. a), but using 00, 06, 12 and 18 UTC radiosondes only.

When only the main (00, 06, 12 and 18 UTC) soundings have been considered (Figure 5.5), the spurious diurnal cycle seen in Figure 5.4 is not apparent. However, since CAPE depends strongly on moisture of the source parcel, and both the main and intermittent soundings featured a moisture bias (Agusti-Panareda *et al.*, 2009), profiles of properties that depend on moisture were not taken from radiosondes. While a residual bias of only 1-2  $\text{g kg}^{-1}$  in WVMR may appear minor, if that change affects a source parcel ascending through the troposphere, the effect can be very significant. This is because CAPE is integrated throughout the troposphere and every decrease in WVMR and associated dew-point temperature lowers the equilibrium level of the parcel and the latent heat released. Therefore, it is vital for a correct calculation of CAPE to have minimal error or bias in the data to be used for the source parcel. Replacing only the source parcel data by radiometer whilst keeping mean profile from radiosondes produced nearly an identical profile of CAPE to the one when both the source parcel and atmospheric profile above have been replaced by data from radiometer (Figure 5.19). However, note that radiometer provides data only to ~4 km and in both cases, profile data above the highest radiometer point were provided by radiosondes. Both of these profiles have been averaged at the same 3 hourly intervals. The only differences between these two profiles are slightly lower magnitudes of CAPE in the afternoon when radiometer only is used

and more stable low-levels (below ~500 m) in the early morning when radiometer is used only for the source parcel.

In addition, sub-sampled profiles of environmental variables in situations within 12 hours prior to a time of MCS passage have been produced. This was done to differentiate environmental conditions that may be specifically conducive to or typical of a situation prior to an MCS occurrence. Also, this excluded post-MCS soundings, where the environment is contaminated by convection. For this reason, where an MCS passage was identified within 12 hours prior to a sounding, this sounding was not used for the purpose of this sub-sample. Also, where a radiosonde was released less than 30 minutes before the MCS, it was not counted as it takes ~30 minutes to ascend through the atmosphere and hence the radiosonde may then encounter the MCS mid-air. The time of MCS passage was defined as being identical to the time of cold pool crossings. This is nearly identical to the front edge of the MCS and the cold pool is generally the first part of the MCS that begins to affect the profile.

### 5.2.2 Initiations in *Cascade*

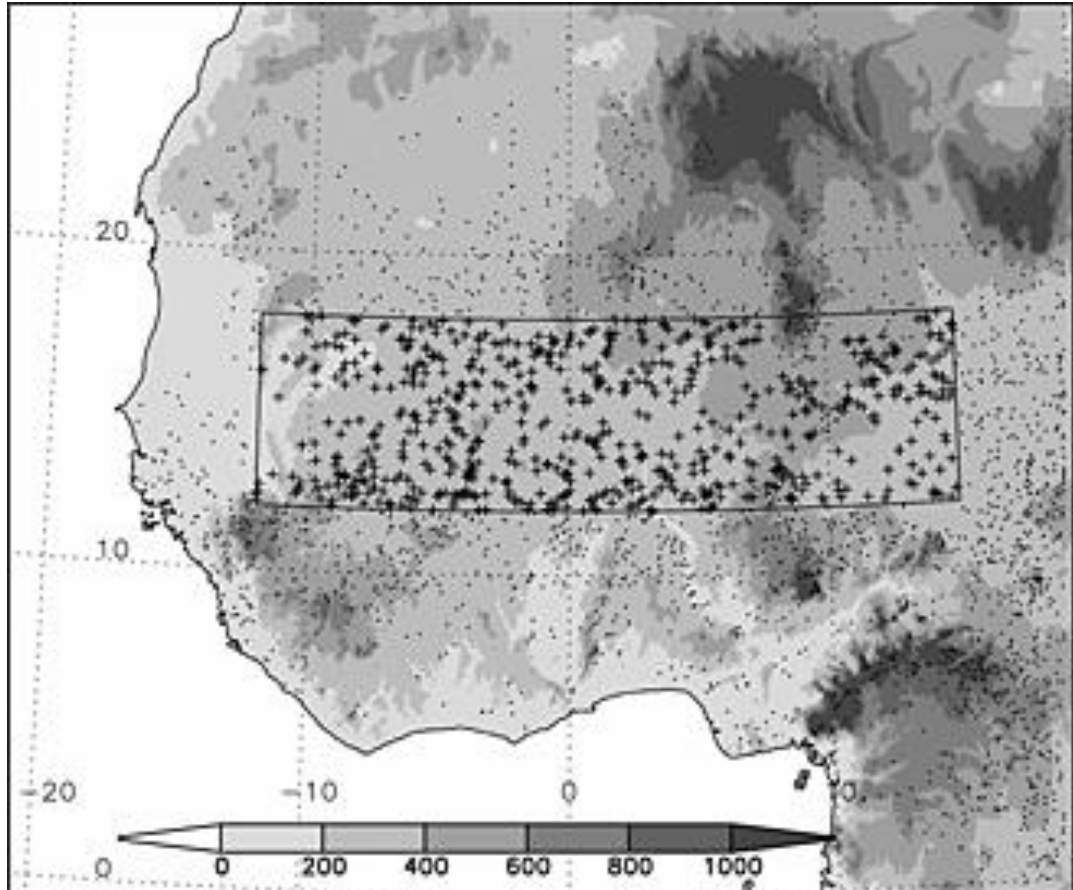


**Figure 5.6:** Topographic height (m) across the Cascade domain. Dots denote convective initiations (see text) and “plus” symbols indicate initiations within the Sahel subdomain (12–18°N, 12°W–15°E) analysed later. Figure obtained from Taylor *et al.* (2013) – Figure 1.

Data for convective initiations over the Sahel was obtained from 4-km Met Office UM *Cascade* simulations. These, being a source of high spatial and temporal data, enabled the calculation of composites of various surface and mid-level variables around initiation-locations at a resolution of 4 km. The locations and times of convective initiations were obtained from Taylor *et al.* (2013), who used a tracking algorithm applied to 15 min model output. Their algorithm identified initiating convective storms from contiguous rainy areas exceeding 1000 km<sup>2</sup>, which were tracked back in time and space to the appearance of the first rainy grid cell, which defined the initiation point and time. Taylor *et al.* (2013) identified only rainy areas between 1000 and 2100 UTC to be tracked back to initiation, but initiation times spanned the whole diurnal cycle. This means that if a rain area exceeded the threshold 1000 km<sup>2</sup> after 2100 and reduced below 1000 km<sup>2</sup> before 1000 UTC, it was not counted. However, if a rain area exceeded the threshold after 1000 UTC, but initiated between 1000 and 2100 UTC, the initiation time was recorded and counted. Taylor *et al.* (2013) calculated the times and locations of 2504 cases over 36 days of the 40-day *Cascade* period (Figure 5.6.). This provided 84, 175, 94, 79, 359, 644, 732 and 337 initiations between 00-03, 03-06, 06-09, 09-12, 12-15, 15-18, 18-21 and 21-24 UTC, respectively.

### 5.2.3 Identification of *Cascade* cold pools

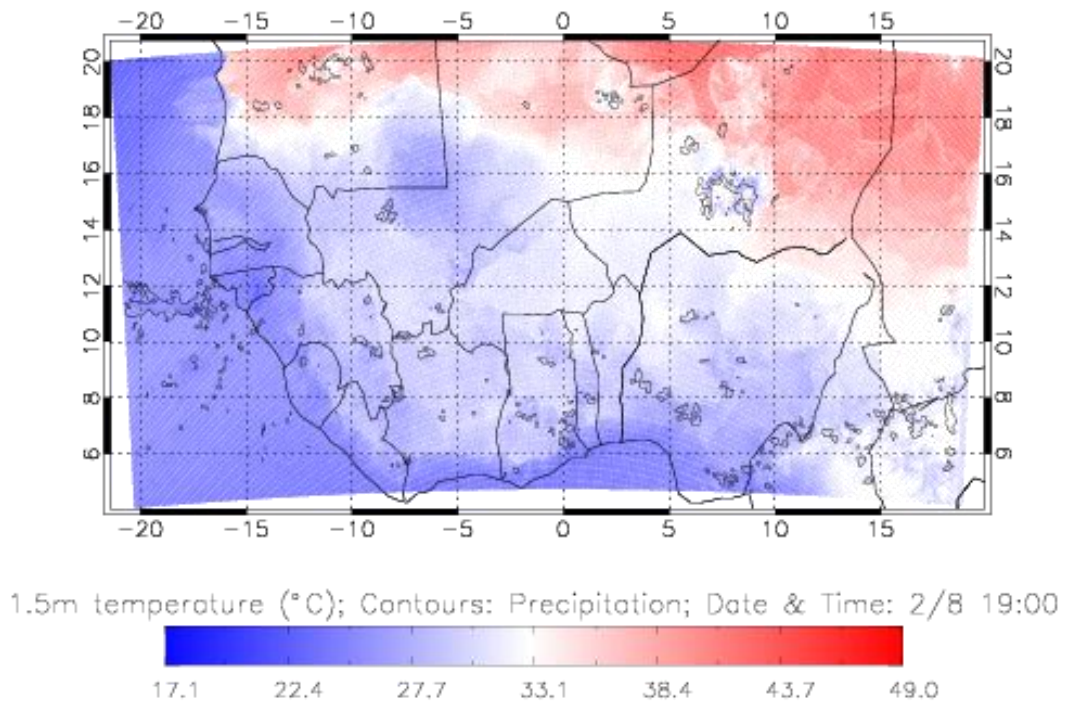


**Figure 5.7:** An example showing *Cascade* simulated 1.5 m temperature ( $^{\circ}\text{C}$ ) (shaded) and precipitation  $> 0.5 \text{ mmh}^{-1}$  (contours) for simulation time equivalent to 19:00 (UTC) on 2<sup>nd</sup> August 2006.

Due to the hourly output from *Cascade* (Figure 5.7.) it was possible to track areas of precipitation/modelled convective storms and MCSs. 1.5 m temperature evolution enables a recognition of the cold pools, which spread out as density currents away from the precipitation and sometimes persist for many hours afterwards. Plots like Figure 5.7. also enabled the identification of overnight monsoon surges, which are visible as northward propagating areas of colder than average temperature. In addition, sea-breezes could very clearly be identified, but these were not specifically analysed in this study as they directly affect only a very small fraction of the Sahel.

Cold pools are generally not distinguishable in temperature the next day as diurnal warming occurring the following morning cancels out the temperature deficit in the 1.5 m layer. While precipitation and temperature images were sufficient to see same-day initiations on the gust front, it was rather complicated to find a case where a cold-pool was responsible for an initiation the following day. For the purpose of determining whether an initiation had been caused by convergence on the edge of previous days/nights cold-pool, it is necessary to know the location of the cold-pool airmass and boundary the following day with a reasonable precision.

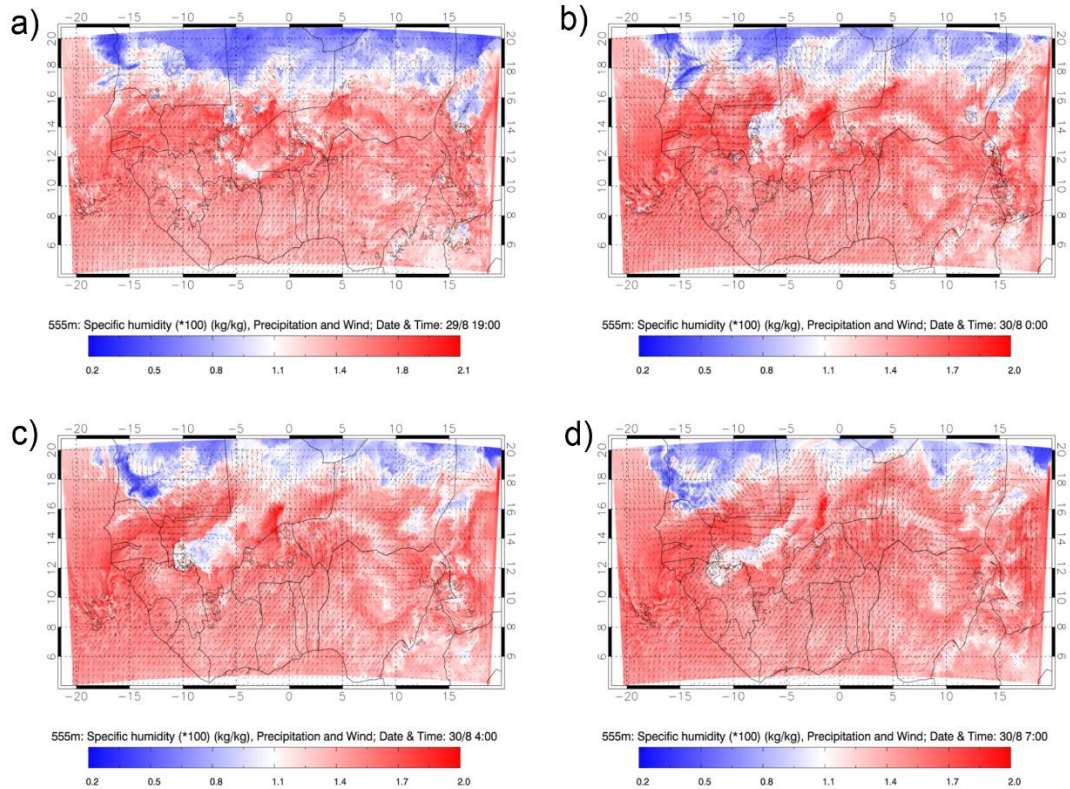


**Figure 5.8:** As Figure 5.7., but for precipitation  $> 0.5 \text{ mm h}^{-1}$  (contours), specific humidity ( $\text{kg kg}^{-1}$ ) (shaded) and wind (arrows), the latter two at the 10m level. Times are a) 19:00 UTC on 29<sup>th</sup> August 2006, b), c) and d) is for 00:00, 04:00 and 07:00 UTC, respectively.

Figure 5.8. is an example showing the propagation of a MCS – propagating across Mali and entering northern Guinea and southern Senegal – and its effect on specific humidity. In the majority of cases, such as in this case, there was a negative anomaly in the cold-pool when compared to its environment. The long track in specific humidity reduction behind the MCS shows that the humidity anomaly, being a result of the cold pool, persists for up to ~18 hours and the 10 m specific humidity has been found as the longest lasting “tracer” of cold-pool airmass. Cold pools also tend to be more clearly defined in the specific humidity field, but nonetheless, they tend to mix with surrounding air the next day. The example in Figure 5.8. shows this strong and moist south-westerly monsoon flow converging with the cold pool and feeding the MCS over Guinea.

#### 5.2.4 Identification of PV anomalies leading to new initiations in *Cascade*

Bookend vortices are a frequent feature that accompanies the northern and southern limits of squall-lines and many have been documented and studied over the USA (e.g. Fujita, 1978). Cases of bookend vortices have been observed to persist after MCS dissipation and reinforce or initiate convection the next day (e.g. Raymond and Jiang, 1990). There are no observational studies known to the author of cases of bookend vortices in West Africa as observational data is sparse. Therefore, as in the case of cold-pool induced initiations, *Cascade* data have been studied to identify anomalies of Potential Vorticity (PV). These have been investigated whether there are any cases, where a large PV anomaly persisted after dissipation of precipitation and where it may have contributed to cause new storm initiation (Russel *et al.* 2008).

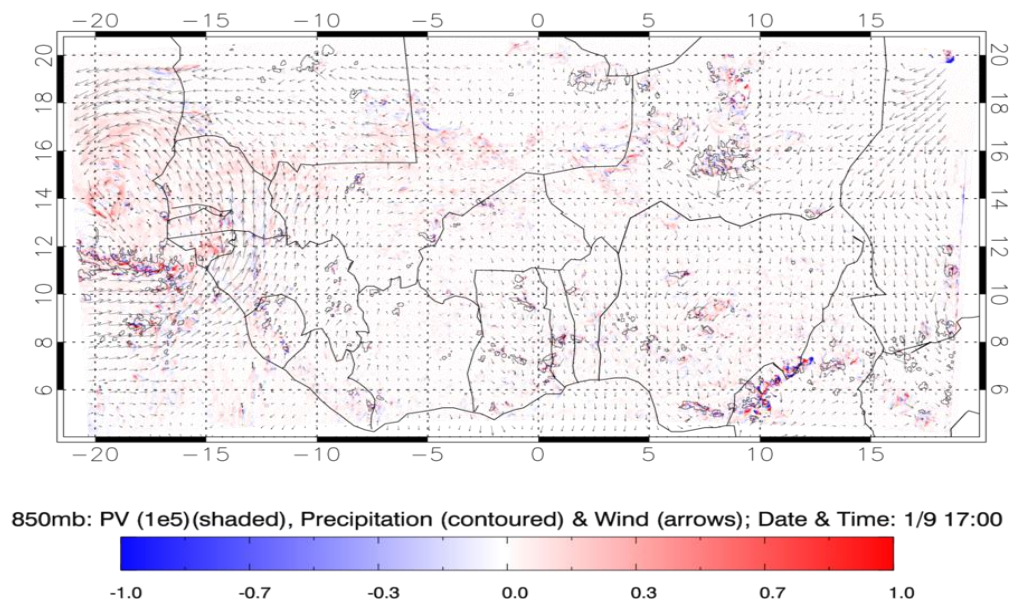


**Figure 5.9:** An example showing surface precipitation  $> 0.5 \text{ mm h}^{-1}$  (contours), PV anomalies  $10^{-5} (\text{m}^2\text{s}^{-1}\text{Kkg}^{-1})$  (shaded) and wind (arrows), the latter two at the 850hPa level.

Figure 5.9 is an example of typical afternoon convective activity over West Africa and the PV anomalies associated with that activity. Nearly every initiating convective activity is accompanied by a production of a potential vorticity couplet. In such a scenario, it would prove to be very time consuming to identify every individual couplet, determine its origin and search for a case associated with bookend vortices. Therefore, a different approach has been created.

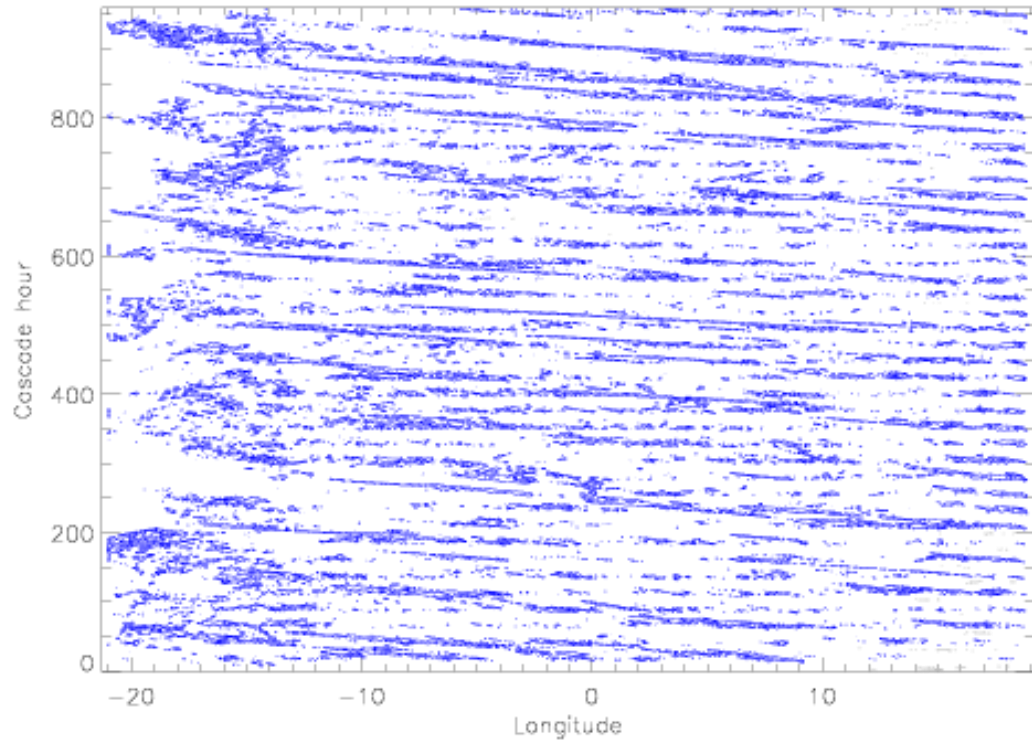
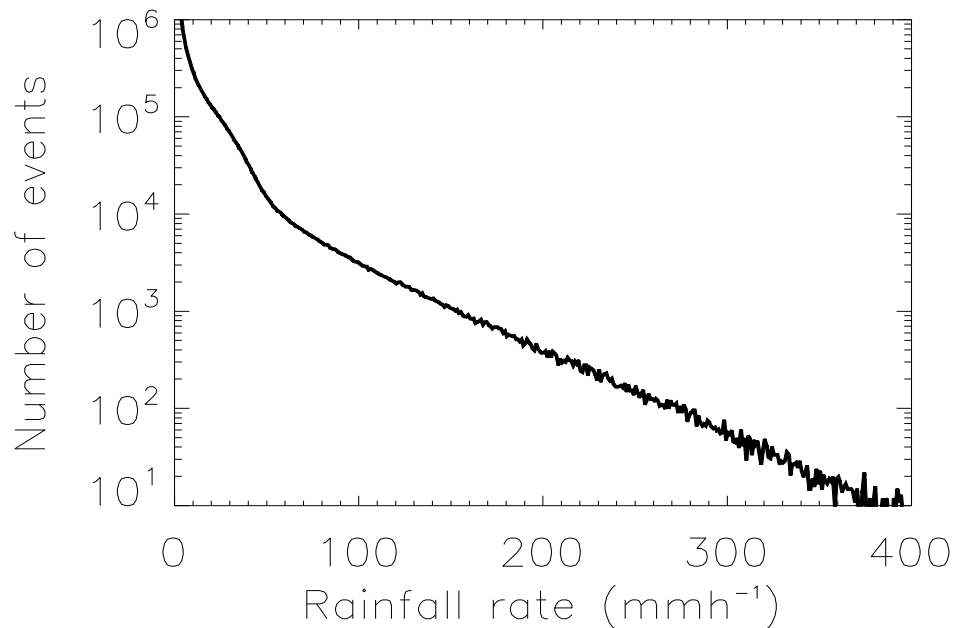


**Figure 5.10:** Hovmuller diagram of surface rainfall between  $10^{\circ}\text{N}$  and  $20^{\circ}\text{N}$  for the 40day Cascade period.

The Hovmuller diagram in Figure 5.10. shows longitudinal propagations of surface precipitation. Most of the longer track cases were associated with MCSs. Any track that has an interruption shows that precipitation associated with the MCS has dissipated, but some mechanism has been sustained, propagated in the same direction at similar speed as its parent MCS and later caused re-initiation of the MCS or initiation of a new MCS. Such breaks in rainfall activity are potential cases where a PV anomaly may have been the mechanism for the re-initiation. Since there were other features such as cold pools and gravity waves responsible for such re-initiations, the longitudes and times of all  $\text{PV} > 10\text{e}^{-5} \text{ m}^{-2} \text{ s}^{-1} \text{ K Kg}^{-1}$  have been identified at pressure levels between 850 and 700 hPa. Where the location of PV of such a magnitude coincided with the location of a break in the precipitation trace in the Hovmuller, a potential case of PV anomaly persisting and causing new initiation has been identified. This was then verified by studying the actual PV that remained after dissipation of precipitation and determining whether there was a cold pool or another obvious factor that could have led to the initiation. By using this method, only 2 such cases have been identified.

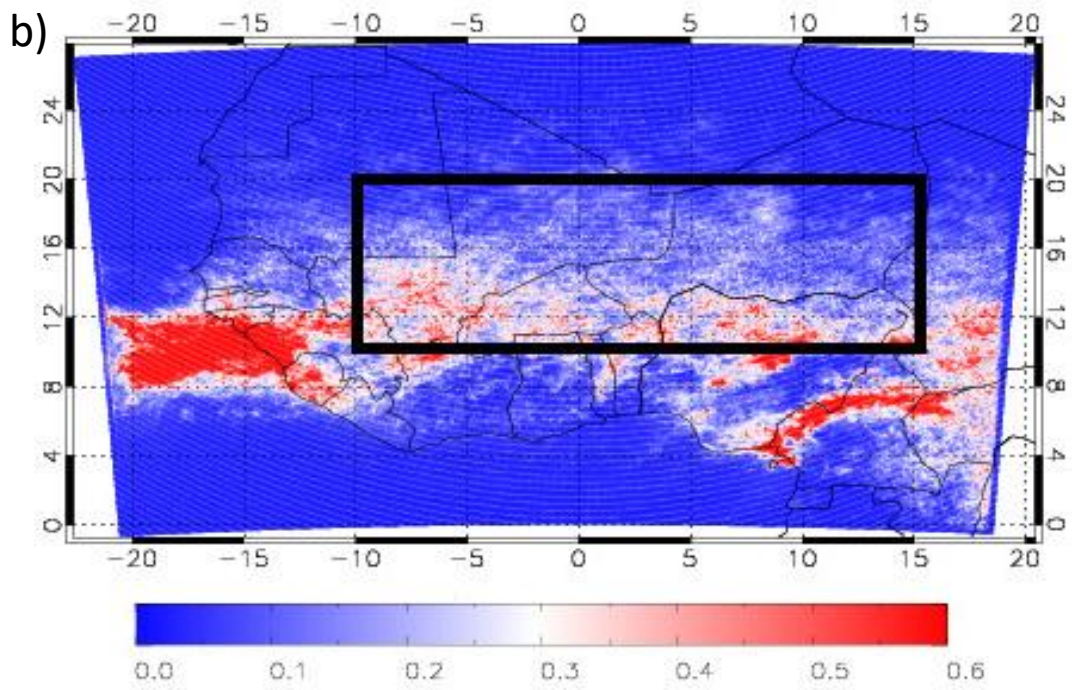
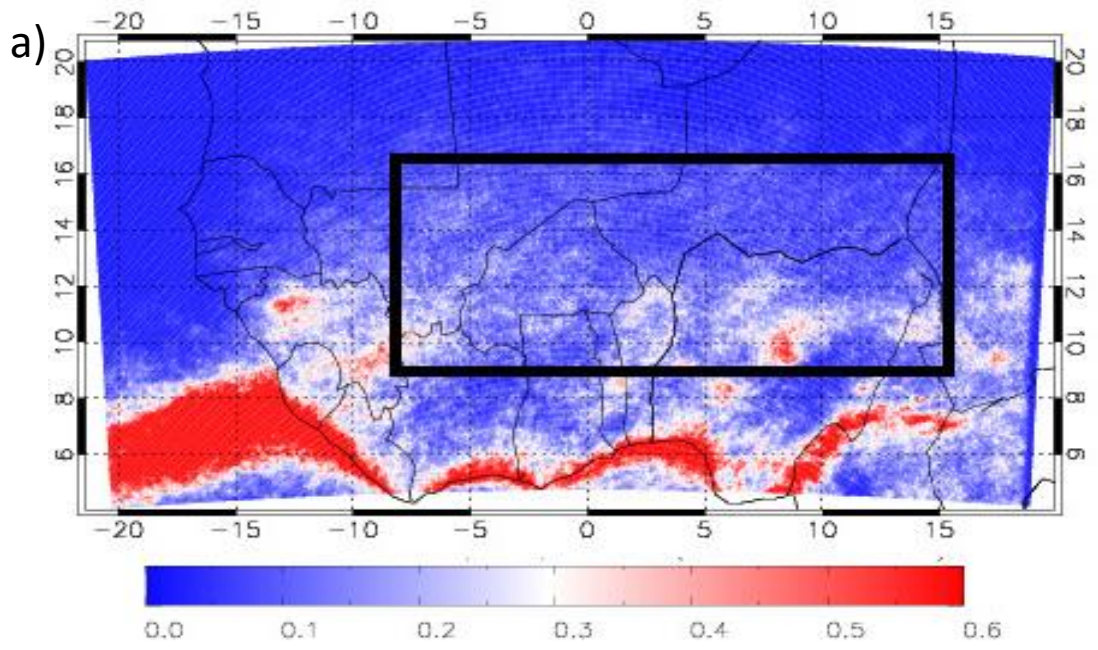
### 5.2.5 2D composites of environmental variables around locations of initiations and rainfall

While investigation of case studies is vital for detailed understanding of various processes leading to initiation (e.g. initiation occurred in a location within previous days cold-pool or near a location where an edge of a cold-pool had been present), case studies could not determine the mean relative contribution of different mechanisms leading to convective initiations. Also, the mean state of the atmosphere prior to convective initiations or during convective events and how this varies throughout the diurnal cycle could not be investigated by looking at case studies only. A compositing method has therefore been used for investigating the relative role of processes in *Cascade* simulations, such as whether new storms are more likely to initiate over pre-existing cold pools or on its edges and possibly how this varies throughout the day.



**Figure 5.11:** Frequency distribution of rainfall rate (mm hr<sup>-1</sup>) across all grid boxes in the whole *Cascade* period.

There is a variety of processes, examples of which have been discussed in section 5.1., which can lead to convective initiations and reinforcing/sustaining of rainfall in the Sahel. Often, a combination of more than one process can play an important part and hence the relative role of processes has been investigated by obtaining composites of the state of the atmosphere. For initiations, locations were taken in the model domain where isolated precipitation pixel appeared for the first time. These locations were obtained from Chris Taylor (Taylor *et al.* 2013) and were available for the 40-day period only, hence all initiation composites were calculated for the period between 25<sup>th</sup> July and 2<sup>nd</sup> September (see section 5.2.2.). Composites have also been investigated around grid-boxes with the heaviest rainfall. For the purpose of this investigation, points with rainfall greater than  $180 \text{ mm h}^{-1}$  (approximately top 0.05% of rainfall, see Figure 5.11.) have been used to calculate the composites. This is unrealistic rainfall rate caused by the 4 km grid spacing, but still allows the study of most intense modelled storms.



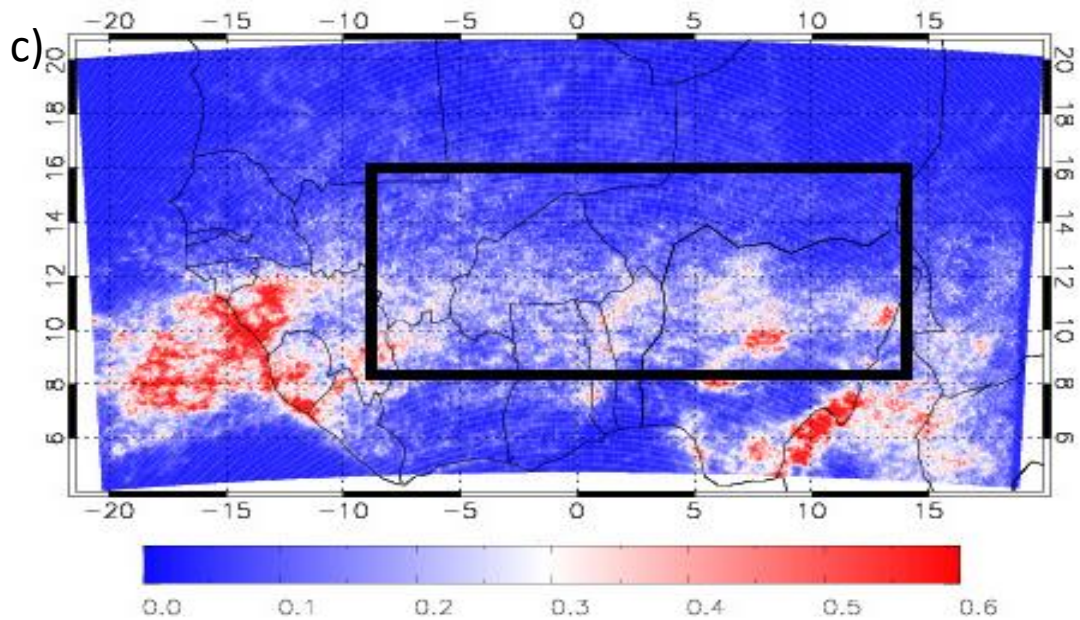


**Figure 5.12:** Cascade accumulated precipitation (m) during the three simulation runs between 1<sup>st</sup> June – 30<sup>th</sup> July a), 25<sup>th</sup> July and 2<sup>nd</sup> September b) and 3<sup>rd</sup> September -30<sup>th</sup> September c).

Because this present study is interested primarily in rainfall associated with MCSs in the West-African Sahel, not all points of initiation or heavy precipitation in the simulations were included in the composites. Instead, a sub-domain was chosen (see Figure 5.12.) and if an initiation or heavy precipitation grid-box was located within that sub-domain, it was included in the calculation of the composite. This sub-domain was used in order to exclude convection over the ocean, as well as grid-boxes too close to the edge of the model domain where it would not be possible to create a full 600x600 box around the grid-box of interest. The size and location of the box was slightly varied between the model runs as locations of initiation and MCS tracks vary throughout the monsoon season. The southern boundary was placed so that no point of the averaging box lies above the ocean and the northern boundary was placed 1 grid box to the north of either the northernmost point of initiation or rain  $> 180 \text{ mmh}^{-1}$ , whichever was greater. Since many variables, such as temperature, feature a mean gradient present within this box (e.g. greater mean temperature in the north than in the south), this would also be present in the composites, potentially masking any anomalies related to MCSs or their initiations. Therefore, the mean of every variable across 5000 randomly selected points in this box has been

subtracted from the composites so that anomalies truly related to the MCS can be identified.

### **5.2.6 Calculating moisture budget around rainfall**

The moisture budget has been calculated around all points in *Cascade* where rainfall rate exceeded  $180 \text{ mm h}^{-1}$ . Because the moisture budget around the whole MCSs rather than the individual points was considered, a box of  $200 \times 200 \text{ km}$  (or  $50 \times 50$  grid boxes) has been used for the calculation of moisture budget around grid-boxes with rain greater than  $180 \text{ mm h}^{-1}$  in order to investigate the relationship between precipitation, evaporation and moisture flux convergence. The size of the box was obtained based on the mean area covered by precipitation (see 5.21. in section 5.3.6.).

The moisture flux convergence varies with the velocity of propagation of precipitation/MCS. This is because for a moving MCS, the velocity of the storm-relative winds depends on the velocity of propagation of the MCS. Since the majority of West-African MCSs propagate westwards and the inflow winds are normally south-westerly, the greater the speed of propagation the greater the storm-relative inflow. Because south-westerly inflow winds in West-African MCSs are generally moister than the westerly outflow winds at upper levels, an increase in westerly storm propagation and related storm-relative wind speed increases the moisture flux convergence into the MCS. Because of this effect, two scenarios have been investigated for the purpose of MCS moisture budget. The first being a stationary precipitation and the second being precipitation moving due west at  $11 \text{ m s}^{-1}$ , which has been estimated in *Cascade* to the nearest  $1 \text{ m s}^{-1}$  to be the average velocity of propagation of MCSs based on 50 randomly selected cases and the distance they covered in one hour. This velocity of propagation broadly agrees with previous observational studies (e.g. Laing *et al.*, 2008; Rickenbach *et al.*, 2009).

## 5.3 Results

### 5.3.1 Diurnal cycle of deep moist convection

#### *The environment of deep moist convection*

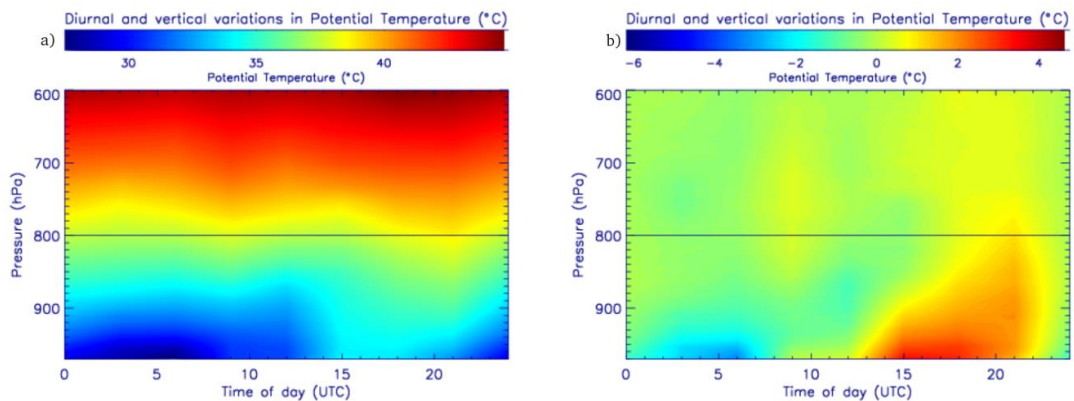


**Figure 5.13:** (a) Diurnal variations in potential temperature ( $^{\circ}$  C). (b) as a), but with pressure-level mean subtracted (b). Estimated maximum boundary layer height shown by thin horizontal line. Data obtained from Niamey radiosondes between 1<sup>st</sup> June 2006 and 30<sup>th</sup> September 2006.

The boundary layer is an important part of the troposphere in terms of its effect on diurnal cycle of deep moist convection as it is the region of energy (latent and sensible) transfer between the surface and the troposphere. In many cases, it is also the source for air-parcels that feed updrafts of deep moist convection. There are a large number of definitions of the boundary layer, the height of which is strongly influenced by mixing and can vary considerably throughout the diurnal cycle. Generally, the boundary layer is thought of as a layer where the effects of turbulence, mainly influenced by mixing, are significant and where diurnal variations in potential temperature are greatest. Figure 5.13 a) shows mean potential temperature

by time of day while Figure 5.13 b) highlights the greatest diurnal changes in potential temperature. It can be seen that a stable low-level layer is present between approximately midnight and 07:00 UTC (Figure 5.13. a)), a result of outgoing long wave radiation and negative sensible heat flux from the surface. There is generally an increase of potential temperature with height with the exception being the afternoon (~15:00 -18:00 UTC) when the lowest ~100-150 hPa are well mixed with nearly constant potential temperature. The greatest diurnal changes in potential temperature are observed near the surface with a minimum centred at 05:00 UTC before sunrise and a maximum at 17:00 UTC before sunset. The strong surface minimum in diurnal perturbation reaches up to ~950 hPa while the maximum reaches up to ~800 hPa, a result of mixing and boundary layer growth in the afternoon. The maximum in diurnal perturbation shifts to later times with height (it has a maximum at ~21:00 UTC at 800 hPa) due to diurnal development of the boundary layer. Above ~800 hPa, the diurnal changes are very weak or non-existent and therefore, for the purpose of this study, the mean maximum boundary layer height is taken as 800 hPa as denoted by the horizontal line in Figure 5.13.

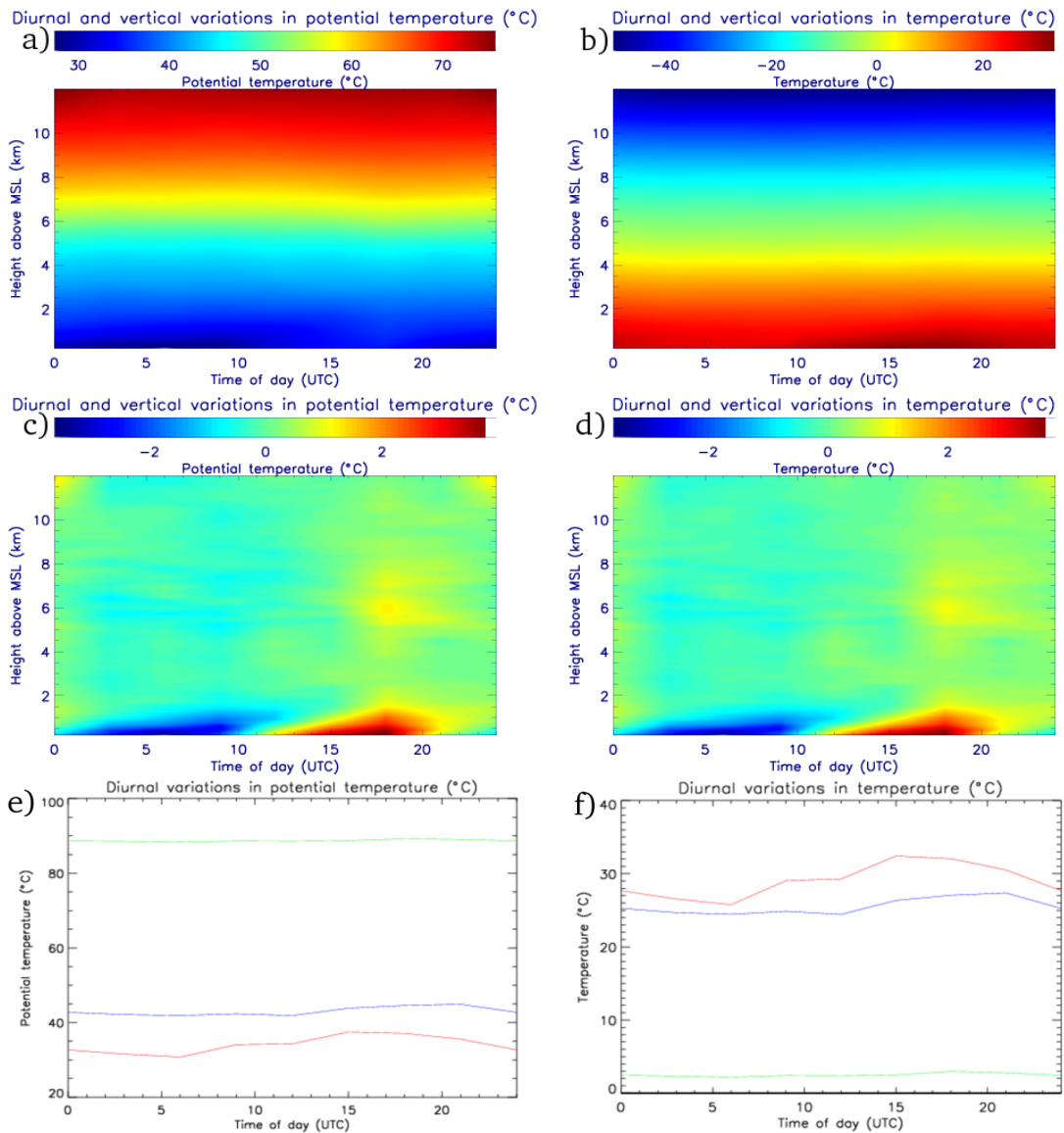


**Figure 5.14:** a) as Figure 5.13. a), but with respect to height and for greater depth of the troposphere between surface and 12km. b) same as a), but for dry-bulb temperature. c) and d) are same as a) and b) respectively, but with the mean at any given height subtracted from the diurnal cycle. Potential temperature (e) and dry-bulb temperature (f) at 200 m (red), 1 km (blue) and 4 km (green). All data obtained from Niamey radiosondes.

Figure 5.14. shows that the lowest ~3 km, which have the greatest diurnal variation, have a diurnal cycle in potential temperature that is approximately 6 hours delayed with respect to the maximum in incoming solar radiation, which peaks approximately at 12:00 UTC. The lowest 1 km features a maximum in dry-bulb temperature in the late afternoon and early evening, with the highest mean of 33 °C being observed at 15:00 UTC. This results in steepest low-level lapse rates (see the closest location of 200 m and 1 km potential temperature curves in Figure 5.14. e) at 15:00 UTC) and

hence creates conditions favourable for low-level mixing. Low-level mixing can erode convective inhibition and therefore is related to the increase in convective initiations and rainfall at this time of day (Figures 5.1. and 5.3.). This warm low-level layer is distinguishable until midnight. It can be seen in Figure 5.14 c) that near-surface cooling starts to take place after 18:00 UTC, at sunset. The cooling propagates upwards through the boundary layer with time and slowly erodes the warm low-level layer during the night, creating a cold stable layer. A minimum in 200 m dry-bulb temperature of 25.5 °C occurs at 06:00 UTC (see Figure 5.14. f)). This coincides with the minimum in the distribution of 200 m potential temperature. Figure 5.14. f) also shows that 1 km and 200 m temperatures are very similar between approximately midnight and 06:00 UTC, indicating a stable nocturnal low-level layer at that time. Mean advection of cool low-level air, which takes place at night, contributes to this minimum along with nocturnal radiative cooling of the land surface. After ~06:00 UTC, diurnal heating begins near the surface and propagates upwards, eroding the low-level stable layer by approximately noon. At heights above ~3 km both dry-bulb and potential temperatures (which are directly related) feature little diurnal variations. The only exception is a localised maximum at mid-levels (~4-8 km above MSL) at 18:00 UTC. This could be a result of convective heating and would correspond to occasional but intense afternoon convection, which is suggested by the localised and high peaks in mean rainfall rate in Figure 5.2.

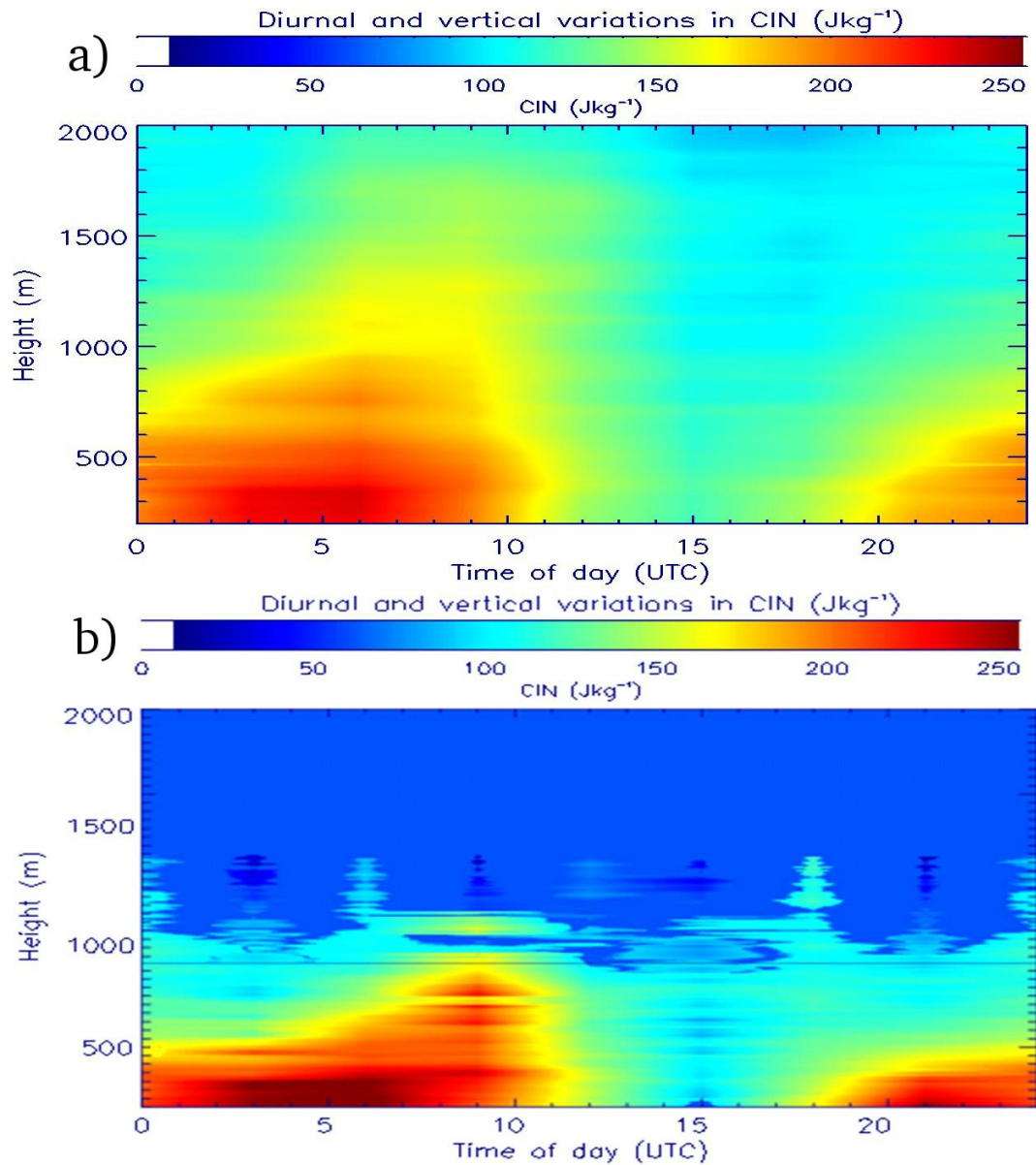


**Figure 5.15:** As Figure 5.14. a), but for CIN. Data obtained between 1<sup>st</sup> June 2006 and 30<sup>th</sup> September 2006 from Niamey from radiometer. a) is for all soundings available, b) only for soundings within 12 hours prior to an MCS passage, and excluding soundings when an MCS passed within the 12 hours prior to their release.

The diurnal cycle in Convective Inhibition (CIN) (Figure 5.15 a)) depends on the diurnal cycles of temperature (Figure 5.14) and equivalent potential temperature (see Figure 5.18 b) below). In general, the lower the temperature of the source parcel the higher the CIN it has to penetrate to reach the Level of Free Convection. Low-level CIN is maximized overnight when temperature is the lowest, with greatest values of CIN peaking at nearly  $250 \text{ J Kg}^{-1}$  generally below 300 metres around 06:00 UTC. During the

forenoon hours, mean low-level CIN rapidly decreases due to the onset of heating (Figure 5.15.) and related mixing. Interestingly, CIN between approximately 1000 - 2000 metres also increases overnight, but it peaks later at approximately 09:00 UTC, being coincident with the delay in temperature diurnal cycle at that level (Figure 5.15.). A sharp decrease in mid-level CIN follows in the afternoon hours with a minimum of approximately  $50 \text{ J Kg}^{-1}$  at  $\sim 15:00$  UTC, which is when afternoon heating (Figure 5.14.) erodes the CIN. CIN at all levels starts to increase after sunset, the increase beginning at the lowest levels, coincident with cooling below 500 metres (see also Figure 5.14.). In order to examine whether the diurnal cycle is significantly different from the mean diurnal cycle on the days with storms, Figure 5.15 b) shows the mean environmental state prior to observed MCSs, demonstrating that the diurnal cycle in CIN on storm days is very similar to the mean. One difference is that afternoon CIN goes nearly to zero even near the surface, making it very easy for convective cells to initiate. The overnight stable layer is slightly stronger, but shallower, presumably because it is not perturbed by cold pools.

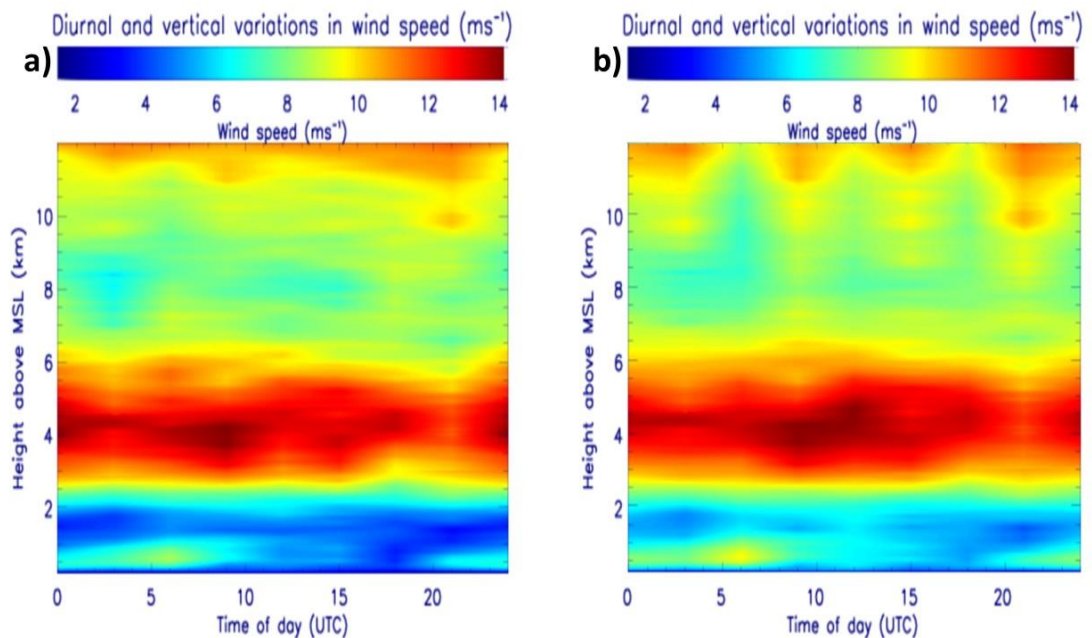


**Figure 5.16:** As Figure 5.15, but for wind-speed. b) as a), but considering only soundings within 12 hours prior to an MCS passage, excluding soundings when an MCS passed within the 12 hours prior to their release. Data obtained from Niamey radiosondes between 1<sup>st</sup> June 2006 and 30<sup>th</sup> September 2006.

Figure 5.16. displays the mean profile of wind-speed and its mean diurnal evolution. The mean sounding can be divided into four main regions:

- 1) A region of generally weak winds of  $5 \text{ m s}^{-1}$  or less below  $\sim 2 \text{ km}$  with an

embedded nocturnal low-level jet. 2) A region of strong winds of  $\sim 10\text{-}14\text{ m s}^{-1}$  at heights of  $\sim 2\text{-}6\text{ km}$  with maximum winds centred at 4 km. This region corresponds to the level of African Easterly Jet. 3) A region of moderately strong winds of  $\sim 6\text{-}10\text{ m s}^{-1}$  magnitude at heights of  $\sim 6\text{-}11\text{ km}$ . 4) A region of very strong winds of  $10\text{ m s}^{-1}$  and more at heights above 11km, corresponding to the height of the Tropical Easterly Jet. Again, restricting the analysis to only soundings from the 12 hours before an MCS shows a very similar diurnal cycle with the nocturnal low-level jet being  $\sim 2\text{ m s}^{-1}$  stronger. This is again likely due to the fact that no cold pools were included in Figure 5.16 b), unlike in a), where they contributed to disruption of the low-level jet on some days, hence reducing the mean wind-speed at the height of the jet.

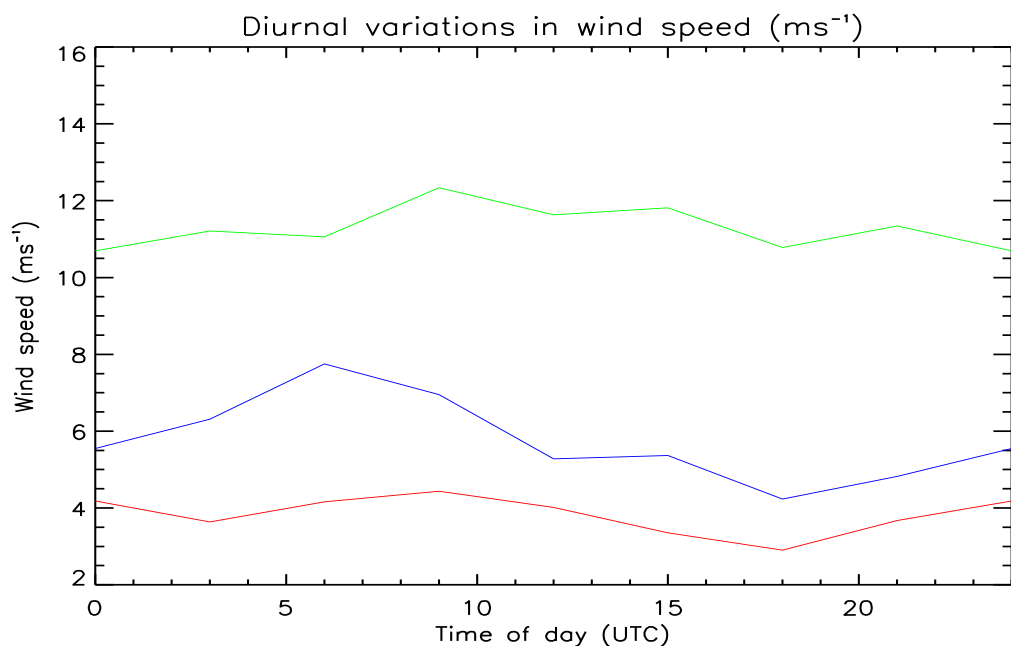


**Figure 5.17:** Mean wind-speed at 200 m (red), 800 m (blue) and 3000 m (green) between 1<sup>st</sup> June 2006 and 30<sup>th</sup> September 2006 in Niamey. Data obtained from radiosondes.

The mean diurnal profile shows features that are typical of a west-African wind profile. This is best visualised by the wind-speed curves in Figure 5.17. as well as by magnitudes of diurnal changes (Figure 5.16. b)). From  $\sim 20:00$  UTC until  $\sim 10:00$  UTC and between  $\sim 500\text{-}1500\text{ m}$ , a concentrated layer of stronger winds of varying magnitude and depth is visible in Figure 5.16. a). This corresponds to the low-level jet and its diurnal cycle and is best seen in fluctuations of the 800 m curve in Figure 5.17. The low-level jet is non-existent in the afternoon, which is a result of strong mixing in the deep boundary layer at that time (see 5.13.), which effectively

disrupts any winds in the lowest ~2 km layer. After sunset, low-level stabilization and cessation of turbulent mixing again gives way to the formation of the low-level jet. It then strengthens and deepens throughout the night with a maximum in strength and depth in the 06:00 UTC profile, having strongest maximum mean wind-speeds of approximately  $8 \text{ m s}^{-1}$  at 800 m. This early morning maximum in LLJ agrees with Lothon *et al.* (2008). After sunrise, turbulent mixing and boundary layer growth (see Figure 5.13.) disrupts the low-level jet and causes its breakdown, which on average happens at approximately 06:00 UTC.

The African Easterly Jet is present throughout the whole diurnal cycle on average. However, it features diurnal fluctuations (see the 3000 m curve in Figure 5.17. and variations in Figure 5.16.). Several maxima and minima in its strength appear throughout the diurnal cycle with the most pronounced maximum in depth and strength being at 09:00 UTC. A distinct minimum is present between ~19:00 - 21:00 UTC. This agrees with Kalapureddy *et al.* (2010), who found a minimum at approximately 18:00 UTC and attributed this to daytime dry convection that weakens the lower-tropospheric flow.

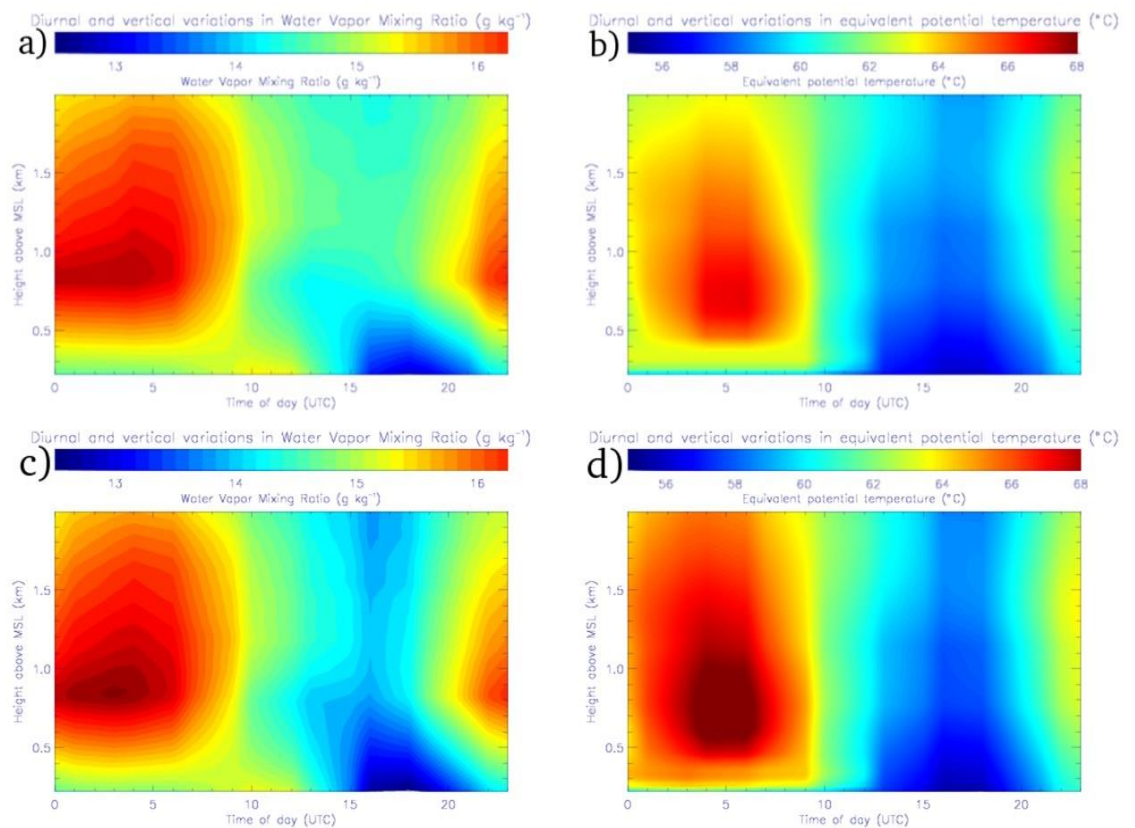


**Figure 5.18:** As Figure 5.16 a), but for water vapour mixing ratio ( $\text{g kg}^{-1}$ ) (a) and equivalent potential temperature ( $^{\circ}\text{C}$ ) (b). c) and d) are as a) and b),

respectively, but only considering soundings within 12 hours prior to an MCS passage, excluding soundings when an MCS passed within the 12 hours prior to their release. Data obtained from Niamey Radiometer between 1<sup>st</sup> June 2006 and 30<sup>th</sup> September 2006.

The mean diurnal cycle in tropospheric moisture profile is shown in Figure 5.18 as profiles of WVMR a) and  $\theta_e$  b). While WVMR is a measure of the actual water vapour content in the atmosphere,  $\theta_e$  depends both on potential temperature and water vapour. The highest moisture content, as well as highest  $\theta_e$ , across a diurnal cycle is on average present at approximately 900 m in the early morning hours with a minimum in late afternoon. Again, there is very little difference when only pre-storm soundings are considered, with slightly greater nocturnal WVMR (on the order of  $0.5 \text{ g kg}^{-1}$ ) and  $\theta_e$  (on the order of  $1^\circ \text{ C}$ ) on pre-storm days.

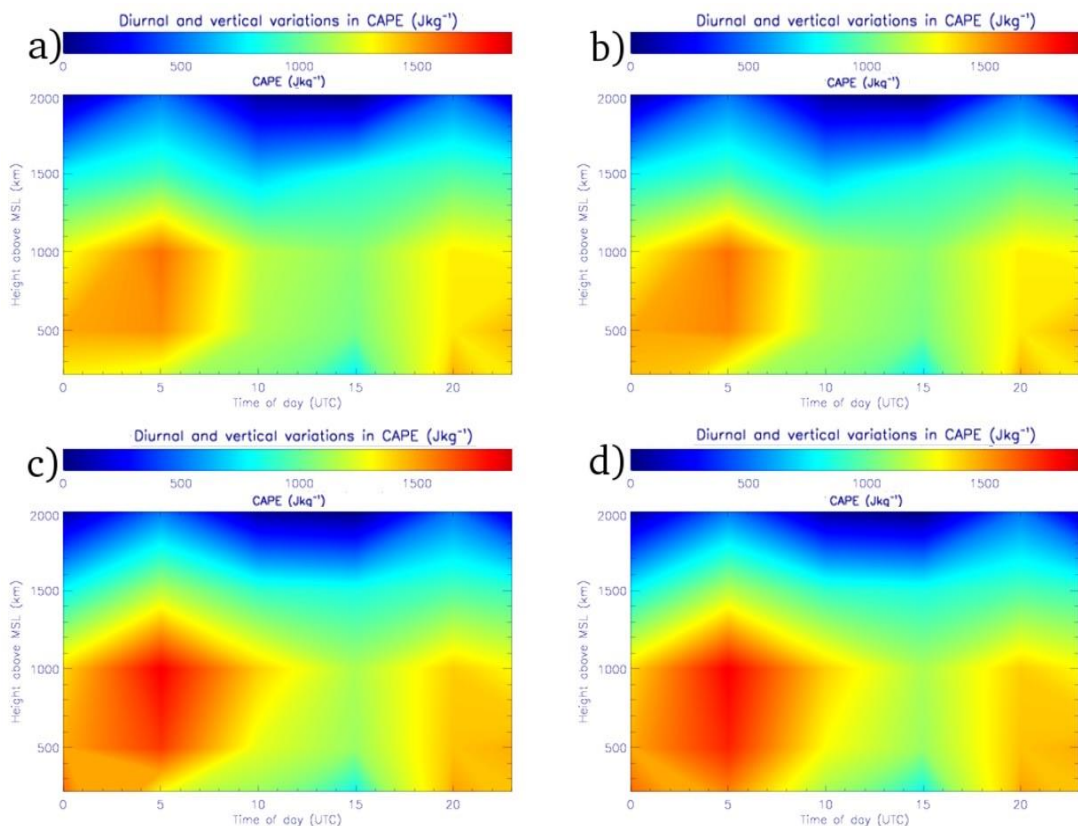


**Figure 5.19:** As 5.4. a), but data obtained from radiometer a). In b), data for temperature and dew-point of the source parcel were taken from radiometer, but data for the environmental profile of temperature were taken from radiosondes. c) and d) are as a) and b), respectively, but only considering soundings within 12 hours prior to an MCS passage, excluding soundings when an MCS passed within the 12 hours prior to their release. Data

*provided hourly (averages of 1min data), but averaged to 3-hourly, centred at 00, 03, 06, 09, 12, 15, 18 and 21 UTC.*

Consistent with equivalent potential temperature (Figure 5.18.), the diurnal cycle in CAPE between the surface and 2 km has a minimum between ~10:00 UTC and ~18:00 UTC with lowest values being in the late afternoon and a maximum at most levels overnight and in the early morning (see Figure 5.19). CAPE generally increases between midnight and 07:00 UTC both in terms of depth and magnitude with slightly higher magnitudes being located above ~600 m in the nocturnal low-level jet (see Figure 5.16). There is, however, a decrease in both WVMR and equivalent potential temperature, which have a minimum at ~18:00 UTC (see Figure 5.18.) and are the reason for these relatively lower values of CAPE in the afternoon. CAPE begins to increase after 18:00 UTC. A secondary maximum in CAPE, which has a greater magnitude than the morning maximum in low-levels (below ~500 m), occurs after 20:00 UTC. The overnight maximum is by approximately  $300 \text{ J Kg}^{-1}$  stronger when only soundings within 12 hours prior to an MCS are considered (Figure 5.19 c) and d)), consistent with the greater water vapour and  $\theta_e$  in 5.18 c) and d) compared with 5.18 a) and b).

Several features of the diurnal cycle in CAPE (Figure 5.19.) and CIN (Figure 15) such as the increase in low-level CIN overnight and decrease during the day are well known and would be expected. However, there are other features that require more consideration. An interesting aspect is the elevated low-level maximum in CAPE in the early morning hours, which is evident above ~600 m in Figure 5.19. This occurs at a time when solar heating is absent, boundary layer cooled and hence no increase in CAPE might be expected. The timing, location and magnitude of both equivalent potential temperature (Figure 5.18.) and CAPE (Figure 5.16.) increases correspond well to those of the low-level jet (Figure 5.16.). This is strong evidence that the low-level jet transports moisture into the region overnight. This CAPE maximum is located above a shallow cool and stable layer in the lowest ~200 m (see Figure 5.19.). This layer contains moist air (Figure 5.18. b)), which however does not contain much CAPE due to lower equivalent potential temperature (Figure 5.18. a)) as it is cold as a result of nocturnal cooling (Figure 5.13.).

The weakening in low-level CAPE during the forenoon hours, which is at a time when solar heating of the boundary layer increases in intensity leading to increased sensible and latent heat fluxes from the surface, which might be expected to result in increasing CAPE (low-level potential

temperature increases). However, the minimum in CAPE is a result of decreasing equivalent potential temperature (see Figure 5.18. a)), which is related to the low-level jet weakening in the morning due to its breakdown (Figure 5.16.) as well as decreasing WVMR (Figure 5.18. b)), which is affected by boundary layer growth (Figure 5.13.) and entrainment of dry air as discussed above. Another effect that might affect morning CAPE is convective overturning created by MCSs from previous night and subsidence behind these. However, minimum in CAPE occurs in the afternoon (Figure 5.19) and shows that the entrainment of dry air into the boundary layer is key in reducing CAPE.

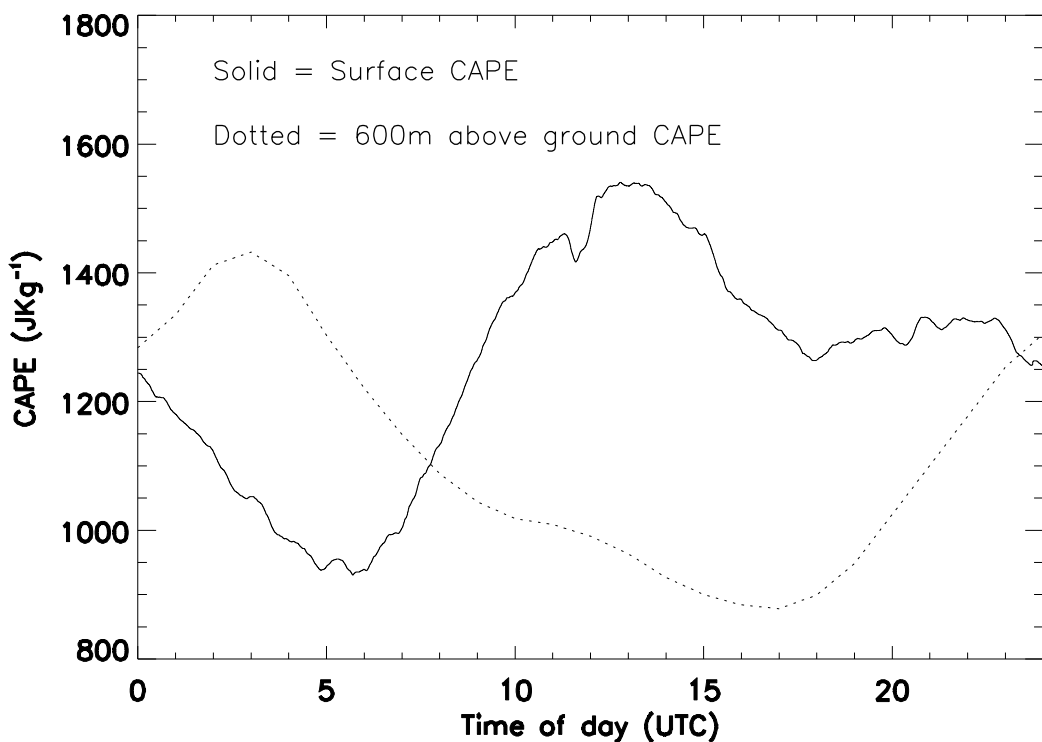


**Figure 5.20:** Surface-based (solid) and 600 m above ground (dotted) CAPE by time of day, using all profiles. Data for surface-based parcel obtained from surface station at Niamey airport, data for 600 m parcel and atmospheric profile obtained from radiometer.

Surface-based CAPE is known to differ from boundary layer and elevated CAPE (Zawadzki *et al.*, 1981). Because the radiometer does not provide data in the lowest tens of metres above ground and radiosonde data were biased (see section 5.2.1.), surface-based CAPE was calculated by the use of data from the surface station for the source parcel together with profile data obtained from the radiometer. It can be seen that diurnal cycle in surface CAPE is different, nearly opposite, to the diurnal cycle of CAPE at

600 m. A minimum of  $\sim 900 \text{ J Kg}^{-1}$  in surface-based CAPE is observed between 05:00 – 06:00 UTC corresponding to the minimum in surface temperature before sunrise (see Figure 5.20.). This minimum is still more than sufficient for convection, if lifted, but the parcel needs to penetrate the inhibition of  $>200 \text{ J Kg}^{-1}$  of CIN (see Figure 5.15.) and therefore this CAPE is generally not released in the form of convection unless strong forcing is provided by a cold pool of pre-existing convection. Surface CAPE then increases throughout the morning due to sensible heat flux and a maximum in CAPE is observed between noon and 13:00 UTC having a magnitude of over  $1500 \text{ J Kg}^{-1}$ . CAPE then decreases throughout the afternoon with a local minimum of  $\sim 1250 \text{ J Kg}^{-1}$  centred near 18:00 UTC, which is now due to decreasing sensible heat fluxes. Surface based CAPE slightly increases throughout the evening, up to a value of  $\sim 1300 \text{ J Kg}^{-1}$  at  $\sim 22:00$  UTC. This small increase occurs well after sunset and must be caused by increasing equivalent potential temperature due to advection (Figure 5.18. a)) more than outweighing nocturnal cooling (Figure 5.14.). At the same time, cessation of turbulent mixing after 18:00 UTC, which is responsible for entraining dry air into the boundary layer, results in no entraining of dry air from above while latent heat fluxes from the surface may still be present, leading to remaining or even slightly increasing CAPE. After approximately 23:00 UTC, surface-based CAPE begins to drop until its 06:00 UTC minimum.

Unlike surface based CAPE, 600 m CAPE increases in the evening hours (Figure 5.20.). This is caused by increasing equivalent potential temperature (Figure 5.18.) due to advection of moist air by the low-level jet (Figure 5.16.) as already discussed. This higher equivalent potential temperature air may be mixed down to the surface and hence be at least partly responsible for the slight increase of mean surface-based CAPE between 18:00 and 23:00 UTC.

***Moisture budget around deep moist convection***

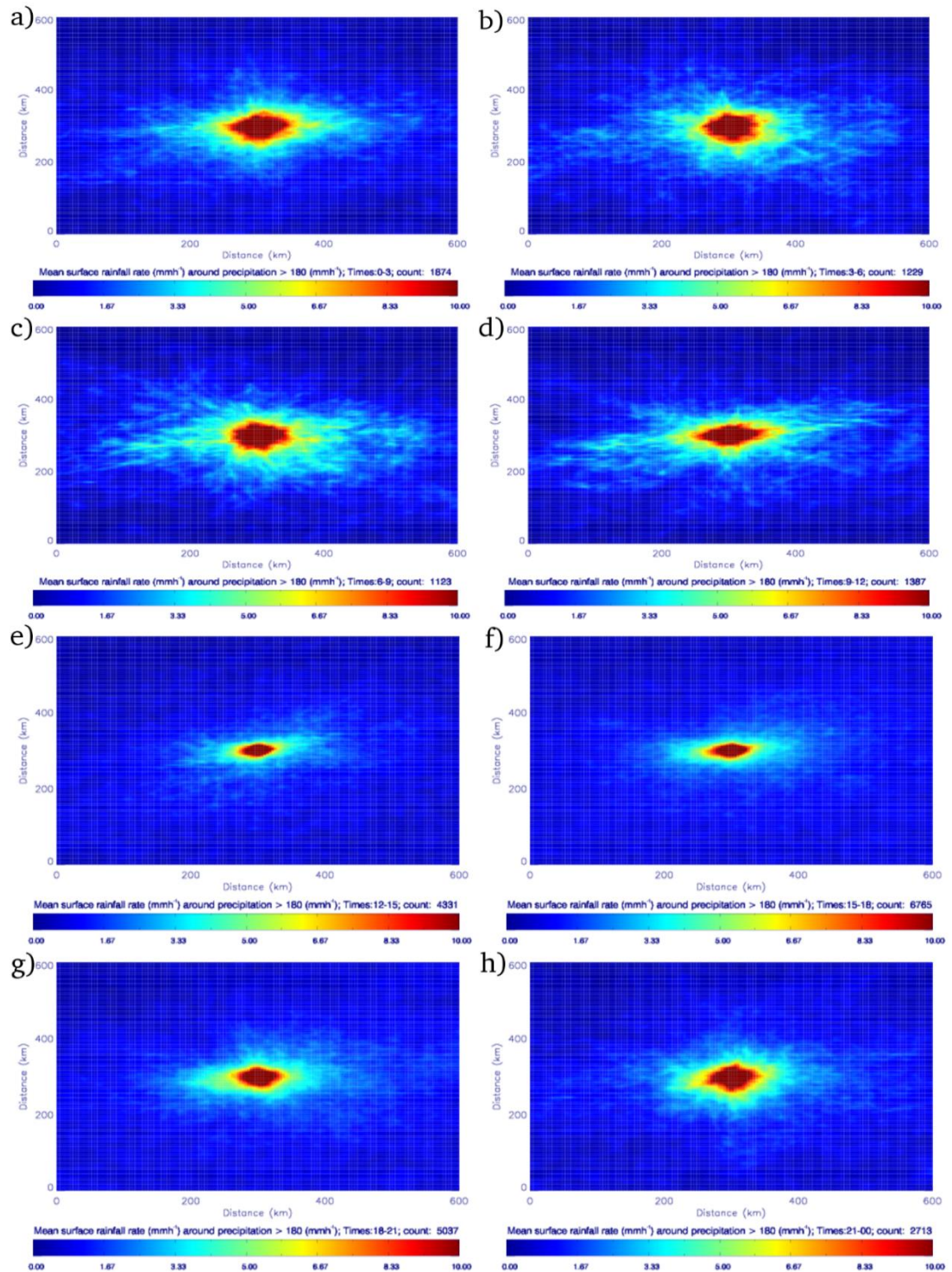


**Figure 5.21:** Surface rainfall rate ( $\text{mm h}^{-1}$ ) by time of day around Cascade points where rainfall exceeds  $180 \text{ mm h}^{-1}$ . Times are as follows: a) 00-03 UTC, b) 03-06 UTC, c) 06-09 UTC, d) 09-12 UTC, e) 12-15 UTC, f) 15-18 UTC, g) 18-21 UTC, h) 21-00 UTC. The number of points used to create the composite is 1874, 1229, 1123, 1367, 4331, 6765, 3037 and 2713 respectively. The colour-scale has been “cut-off” at  $10 \text{ mm h}^{-1}$  in order to be able to see the extent of the rainfall more clearly.

The mean rainfall rate in Figure 5.21 shows how the size of precipitation changes throughout the diurnal cycle. Mean area of all rainfall greater than approximately  $2 \text{ mm h}^{-1}$  is relatively small and localised in the afternoon and its size gradually increases between 12:00 – 15:00 UTC and 00:00 – 03:00 UTC. This is due to the fact that the initial isolated convective storms in the afternoon, which could produce rainfall greater than  $180 \text{ mm h}^{-1}$  in *Cascade*, occupy relatively small area. Later in the evening, these storms organize and grow upscale and hence the mean area covered by rainfall increases. Between 00:00 – 03:00 UTC and 09:00 – 12:00 UTC time-periods, the area covered by mean rainfall greater than  $\sim 2 \text{ mm h}^{-1}$  does not change considerably, but rainfall smaller than  $\sim 2 \text{ mm h}^{-1}$  spreads-out with time. This indicates the dissipation of MCSs in the morning hours as their weakening rainfall increasingly becomes stratiform-like and spreads out to cover greater area.

In terms of rainfall intensity, the diurnal variations are not very large. Several pixels in the centre of Figure 5.21. always feature rainfall of over  $200 \text{ mm h}^{-1}$ . This is not seen in Figure 5.21. as the scale is cut off at  $10 \text{ mm h}^{-1}$  in order for the rainfall at intensities smaller than  $5 \text{ mm h}^{-1}$  to be distinguishable. The mean maximum rainfall rate ranges between  $222.8 \text{ mm h}^{-1}$  in the 12:00 – 15:00 UTC time frame and  $228.7 \text{ mm h}^{-1}$  in the 03:00 – 06:00 UTC time frame, but the area covered by the heaviest rainfall changes with it being largest in the 03:00 – 06:00 UTC time frame and smallest in the 12:00 – 15:00 UTC time frame. However, the changes in area covered by rainfall rate greater than  $180 \text{ mmh}^{-1}$  are small, the difference being only 2-3 pixels.

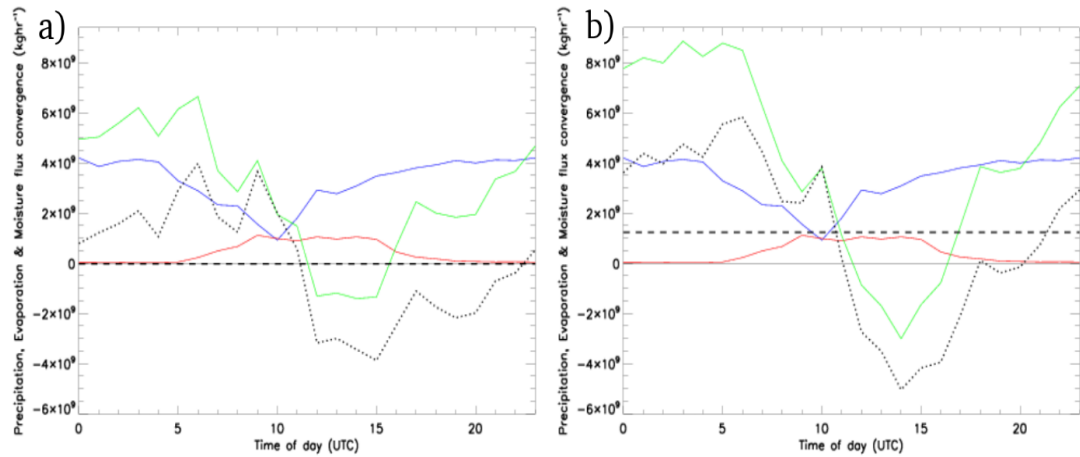
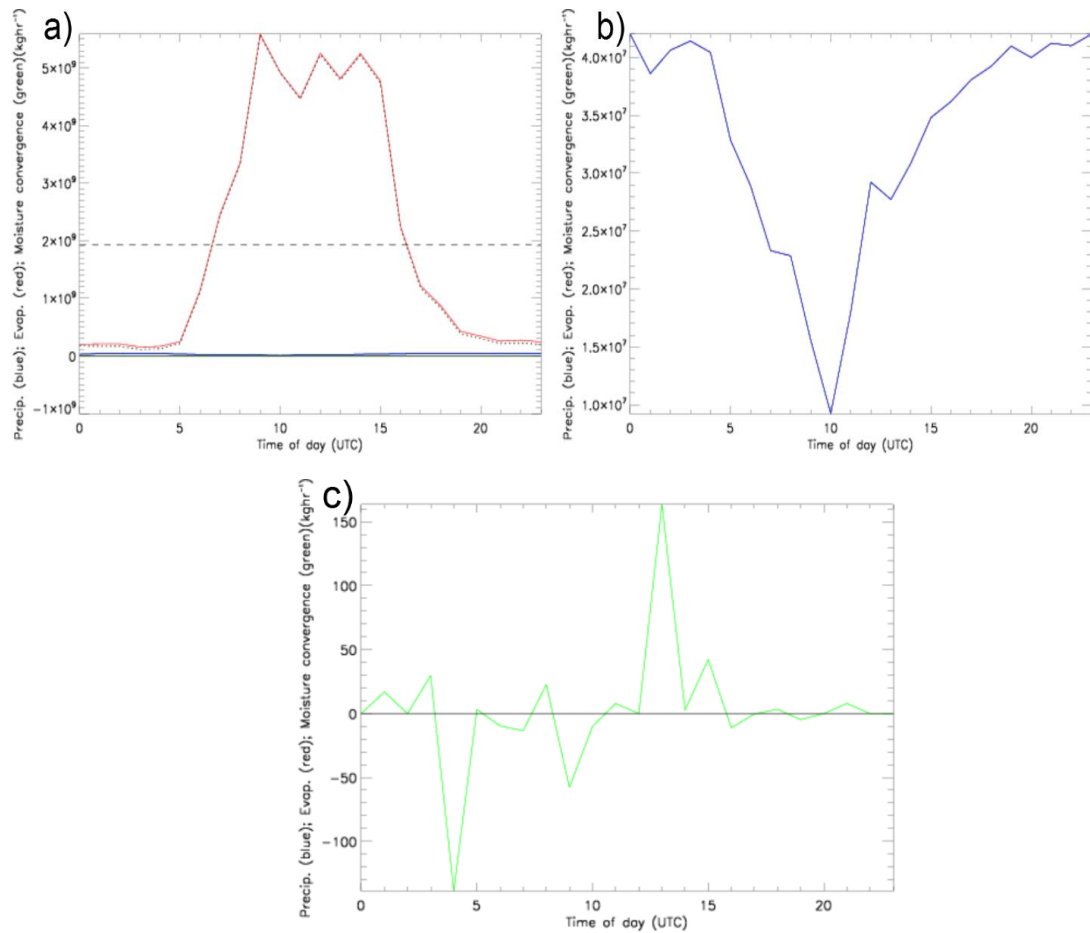


**Figure 5.22:** Diurnal cycle of total mean precipitation (blue), mean evaporated water from surface (red) and mean moisture flux convergence (green) in a 200\*200 km box around every grid-box with precipitation greater than 180 mm h<sup>-1</sup> assuming stationary rainfall (a), assuming that the area of rainfall is propagating at a speed of 11 m s<sup>-1</sup> from east to west (b). Dotted line is mean difference between moisture input and output by time of day and dashed line is the same, but averaged for the whole day.

Moisture budget around rainfall rate greater than 180 mm h<sup>-1</sup> has been investigated in *Cascade* in order to study the mean diurnal cycle in rainfall, evaporation and moisture flux convergence as can be seen in Figure 5.22. The mean diurnal cycle of rainfall features a maximum in the early morning hours and a minimum centred at 10:00 UTC (Figure 5.22.). This is related both to the size of the precipitation areas (MCSs) within the box considered (Figure 5.21.) as well as to the mean intensity of rain. The area of precipitation greater than ~2 mm h<sup>-1</sup> remains nearly constant between midnight and noon (Figures 5.21. a) – d)) and reduces thereafter with a minimum between noon and 15:00 UTC (see Figure 5.21. e)). Therefore, the decrease in mean precipitation between 03:00 UTC and 10:00 UTC (Figure 5.22.) is attributed to weakening mean intensity of rainfall within MCSs. Since the mean area covered by rainfall rate greater than ~4 mm h<sup>-1</sup> does not increase considerably between 09:00 and 12:00 UTC, the increase in precipitated water in that time period is related to an increase in rainfall intensity. The area covered by rainfall decreases in the afternoon (Figure 5.21. e) and f)), but mean precipitation intensity gradually increases (Figure 5.22.), which again shows that mean rainfall rate is increasing. In the evening hours the area covered by rainfall increases (Figure 5.21. g) and h)), which is the most important factor in the increase in rainfall throughout the evening hours (Figure 5.22.). This diurnal cycle in rainfall generally

agrees with observations (Figure 5.1.) if slight discrepancies in timing are taken into account.

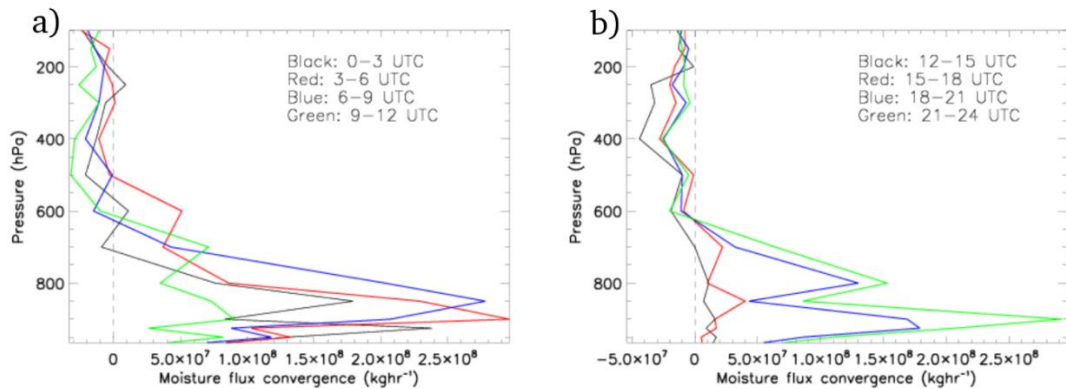
Mean evaporation from the surface gradually increases from approximately 06:00 UTC (sunrise), has a maximum at 13:00 UTC and then gradually decreases until 18:00 UTC (sunset). Evaporation is nearly zero when solar radiation is absent. In the morning, evaporation increases less sharply than it decreases in the afternoon. The explanation for this is presumably a larger fraction of the box covered by cloudiness associated with the larger area covered by rainfall (Figure 5.21.) in the morning. In the afternoon, rainfall is more localised and isolated, hence leaving a greater fraction of the box cloud free and enabling mean evaporation to respond to changes in solar radiation more rapidly. Mean moisture flux convergence has a very similar diurnal cycle for the stationary rainfall (Figure 5.22. a)) and propagating rainfall (Figure 5.22. b)) with magnitude being the greatest difference. For the propagating rainfall, the magnitude of moisture flux convergence is generally stronger by 30-50%. Regarding diurnal cycle, maximum in moisture flux convergence occurs approximately between midnight and 06:00 UTC. After that time it plummets during the morning, but remains positive until 11:00 UTC. This behaviour generally follows the diurnal cycle of the low-level jet (Figure 5.16.) and confirms that it plays an important role in advecting moist air mass to the region. There is negative moisture flux convergence in the afternoon and rainfall during that time instead takes profit from the afternoon locally-sourced moisture that entered the box through evaporation. The dotted lines in Figure 5.22. represent variations in total tendency (difference between input and output) of moisture in the 200x200 km<sup>2</sup> box considered. Sources (surface evaporation and moisture flux convergence) and sinks (precipitated water and moisture flux divergence, which is the negative moisture flux convergence) in moisture do not always equal as air is able to store moisture to some degree. In addition, the mean is taken around several hundreds of rain pixels/surrounding boxes and only at times when there is rainfall intensity of at least 180 mm hr<sup>-1</sup>.



**Figure 5.23:** a) as Figure 5.22., but for 5000 randomly selected points. For clarity, mean precipitation in b) and moisture flux convergence in c) is shown again.

Diurnal changes in moisture budget in the general environment not necessarily containing deep moist convective storms have been studied (Figure 5.23.) to investigate whether the moisture budget is independent of the presence of MCSs. This primarily question was whether MCSs drive the moisture flux convergence or whether they are driven by it. Figure 5.23. shows that environmental moisture budget is largely driven by surface evaporation, which has the greatest magnitude and dominates over precipitation and moisture flux convergence. Mean surface evaporation features a broad daily maximum with sharp increase in the morning and a sharp decrease in the evening. There is rainfall present (Figure 5.23. b)) as the figure has been calculated from data taken over 5000 random points, the boxes around which are likely to contain rainfall. When averaged, this rainfall is weaker and covers a smaller fraction of the box than that averaged over boxes containing rainfall greater than 180 mm h<sup>-1</sup> in the centre, which results in weaker precipitation magnitudes (~100 times lower). The diurnal cycle of rainfall is, however, very similar. The moisture flux convergence is negligible

in this case (Figure 5.23. c)), which is a result of moisture entering and leaving the box being generally equal away from precipitation.



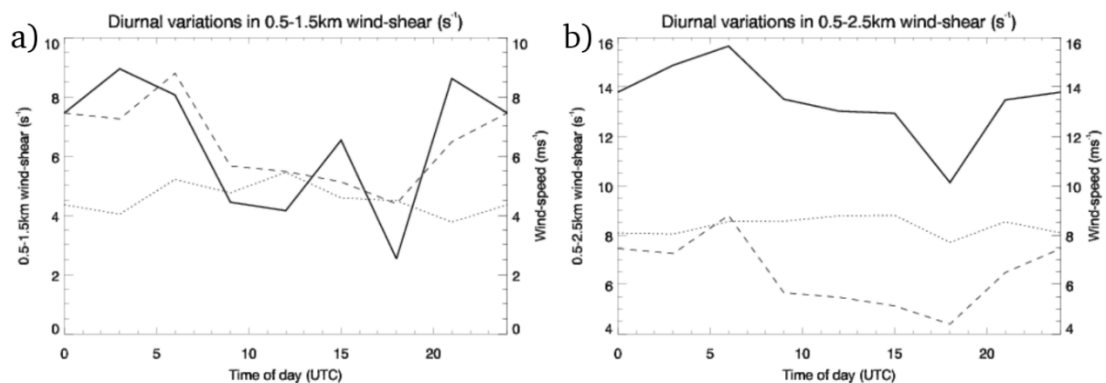
**Figure 5.24:** Mean moisture flux convergence in a 200\*200 km<sup>2</sup> box around every grid-box with precipitation greater than 180 mm h<sup>-1</sup> by height and averaged over 3-hourly time periods by time day, assuming a MCS is propagating at a speed of 11 m s<sup>-1</sup> from east to west.

Figure 5.24. shows variations in moisture flux convergence and divergence at different levels by time of day. It can be seen that there are distinct diurnal variations in the magnitude of moisture flux convergence. Overnight and in the early morning, maximum moisture flux convergence is concentrated in the lowest levels below ~600 hPa. At these times there is a sharp maximum located between ~800-900 hPa, the magnitude of which peaks near 3\*10<sup>8</sup> kg hr<sup>-1</sup> between 03:00 UTC and 06:00 UTC and is a result of moisture advected into the region by the LLJ (see also Figure 5.16.). This further emphasizes the importance of the low-level jet in maintaining MCSs overnight.

Between 11:00 UTC and approximately 16:00 UTC mean moisture flux convergence is negative, being a divergence (see Figure 5.23). Since low-level flow is weakest at this time due to maximised turbulence in the boundary layer (see Figure 5.13.), no strong convergence in the low-levels is expected. Figure 5.24. b) shows that these negative moisture flux convergence values are due to very low positive values at low-levels and negative values at upper levels, which are probably related to outflow from the MCSs at upper levels in the anvil layer. Moisture flux divergence might also be expected at the lowest levels due to cold pool outflows. This is not the case in Figure 5.23. and is likely due to the large spatial size of the box around precipitation, which is too large for cold pools to leave it and cause moisture divergence.

### ***The implications of changing shear according to RKW theory***

As discussed in section 1.1.2., the ratio between the strength of the environmental low-level shear and cold pool intensity influences the tilt of the convective updrafts in MCSs, which can affect their intensity. While environmental data are very well documented in Niamey, there is sparse data from within the cold-pools to obtain their average depth. Only several MCSs had a radiosonde released within one hour of a cold pool passage and severe disruption of radiometer data occurred during heavy precipitation events, which nearly always accompany cold-pools in Niamey. Therefore, the mean cold-pool depth was estimated from the handful of soundings available, as well as from hydrostatic balance using surface data (surface pressure increases hydrostatically as a function of temperature and the depth of the cold pool, Wakimoto, 1982). This method however assumes well mixed environment and cold pool. This suggested cold-pool depths ranging from only 300 m up to 3.2 km. However, care needs to be taken when estimating cold-pool depth from surface data by hydrostatic balance as there are many processes that can disrupt the hydrostatic increase in surface pressure due to the cold-pool and the environment ahead of the cold pool is often not well mixed (see Figure 5.13.). Therefore, the most extreme values were not considered and the mean cold-pool depth was estimated to be in the 1-2.5 km range, consistent with USA studies (e.g. Weisman and Rotunno, 2005). As a result, two layers were considered for the calculation of low-level wind shear. The former between 0.5-1.5km, which is a layer affected mainly by variations in the low-level jet. The latter between 0.5-2.5km, which is a layer partly affected by the lower regions of the African Easterly Jet.



**Figure 5.25:** Mean diurnal variations in a) 0.5 - 1.5 km and b) 0.5 - 2.5 km wind-shear ( $s^{-1}$ ) between 1<sup>st</sup> June 2006 and 30<sup>th</sup> September 2006 in Niamey. Dotted line is wind-speed at the upper level (1.5 km in a) and 2.5 km in b)) and dashed line is wind-speed at 0.5 km.

Overall, the 0.5-1.5 km wind shear is weaker than the 0.5-2.5 km wind shear (Figure 5.25.). The difference between these two sets of levels is that in the former, the mean wind at 0.5 km is either stronger or of similar magnitude as wind at 1.5 km. The reason for the stronger 0.5 km wind is the presence of the low-level jet in the overnight hours and in the first part of the morning (Figure 5.16.). Around noon and in the afternoon, winds at both levels are of similar magnitude. The latter region is characterized by generally stronger wind at the 2.5 km level, which is due to the presence of stronger winds associated with the African Easterly Jet (Figure 5.16.).

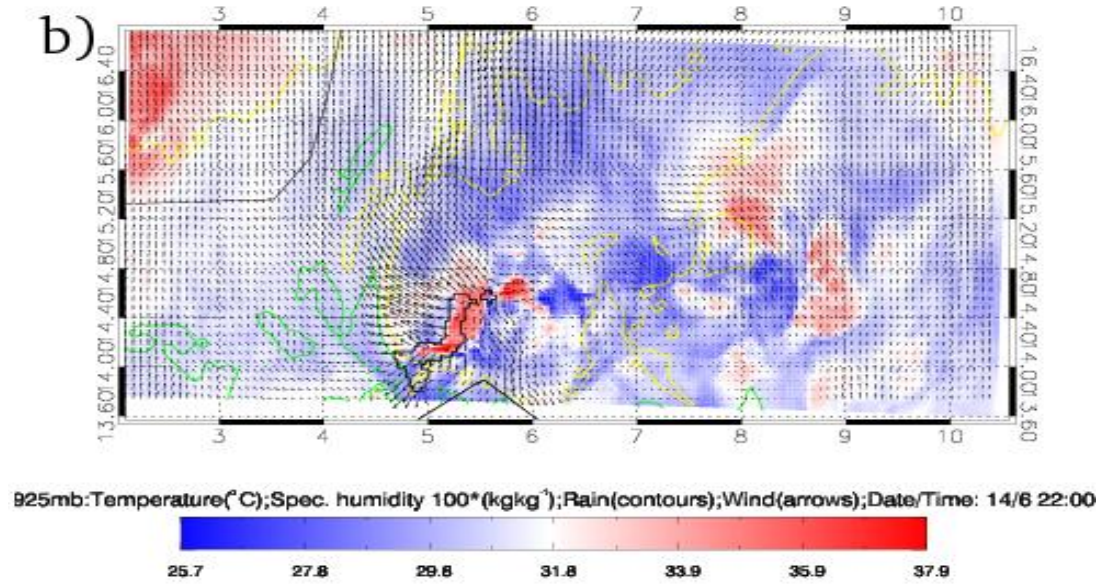
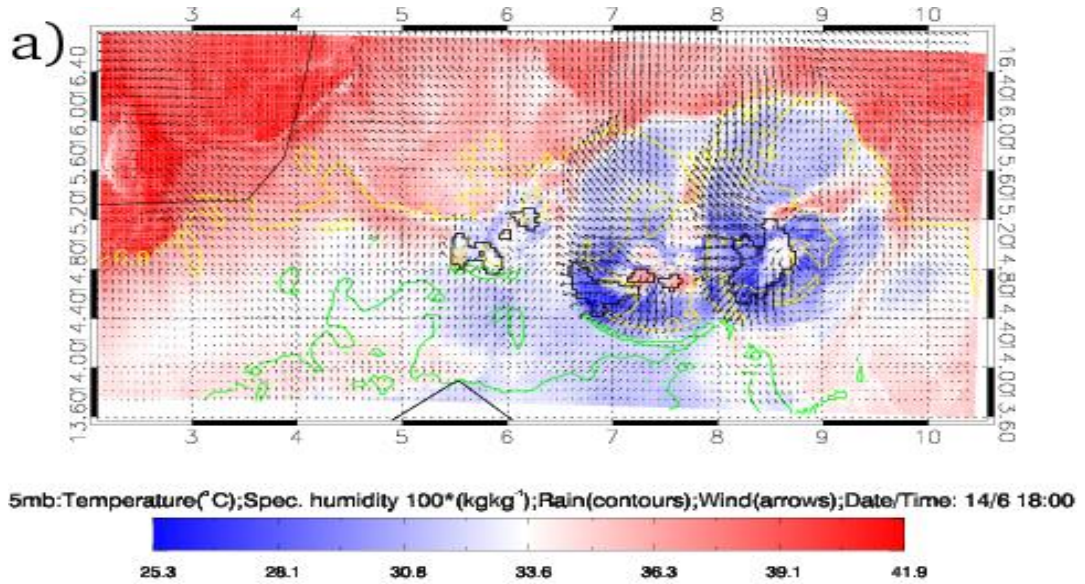
The diurnal cycle of the wind-shear generally features a maximum in the early morning (~03:00 – 06:00 UTC) and a minimum in the afternoon. It can be seen that these changes are affected by the diurnal cycle of the low-level jet as the 0.5 km wind speed is responsible for a majority of the diurnal variation (Figure 5.25.). The decrease in wind-shear is slightly steeper in the 0.5-1.5 km layer as that layer is more affected by diurnal turbulent mixing of the boundary layer. Both layers, however, feature a distinct minimum at 18:00 UTC, which coincides with the time of highest low-level temperature (Figure 5.13.), still relatively weak CAPE (Figure 5.19.), local minimum in rainfall (Figure 5.2.) and weakest winds below 2.5 km (Figure 5.16. a)). These conditions are conducive to the presence of dry convection, which would cause a minimum in 2.5 km winds due to turbulent mixing in the deep boundary layer, which can reach higher than 2.5 km at that time. After 18:00 UTC, wind-shear across both layers increases in response to the development of the low-level jet.

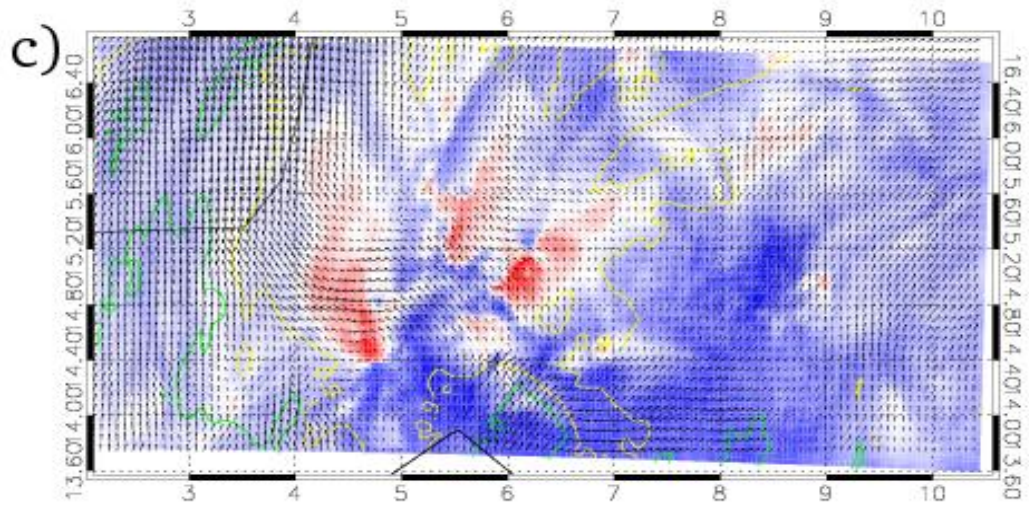
Due to the lack of observational data through Niamey cold-pools, as discussed above, examples from literature (e.g. Weisman and Rotunno, 2004; Bryan and Parker *et al.* 2010) have been used as a rough estimate of typical values of cold pool depth and strength,  $C$ , over the US plains. Since US cold pools are generally of similar magnitude to West African cold pools (regarding surface cold-pool properties, see Section 3.4), the values of  $C$  given in literature for cold pools produced by USA MCSs of approximately  $17\text{-}25\text{ m s}^{-1}$  are assumed to be similar to values of  $C$  for West African cold pools. Using this assumption, the values of  $C$  would be close to the environmental wind shear (this is called the “optimal state” for squall-lines by RKW, see section 1.1.2) overnight and greater than the environmental wind shear for most of the rest of the day. If  $C$  is greater than wind shear, this results, according to RKW, in the squall-line to lean up-shear as shear would be generally weaker than the cold-pool. The closeness of  $C$  to environmental

wind shear overnight would be another favourable state of the environment for intensification and maintenance of MCSs. The weakening of the wind shear in the morning, being a result of the low-level jet breakdown, would then cause the value of  $C$  to be greater than the wind shear. The state then becomes less favourable for strong convective updrafts and would lead to the general dissipation of MCSs and attendant reduction in mean rainfall intensity in the morning hours (as seen in Figures 5.1. and 5.2.).

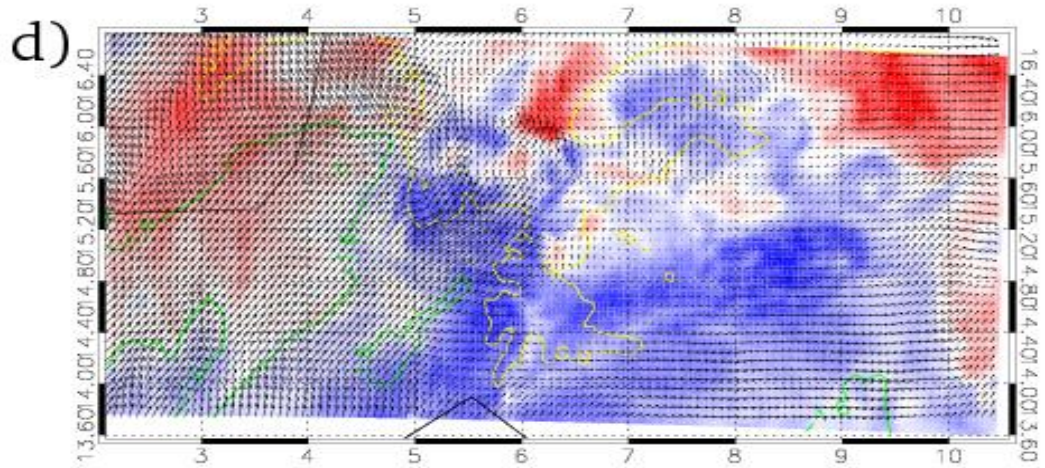
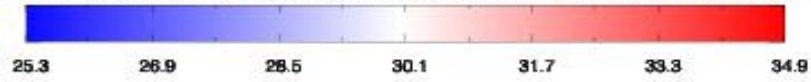
### 5.3.2 Diurnal cycle in convective initiations

#### *The role of cold pools and surface forcing*

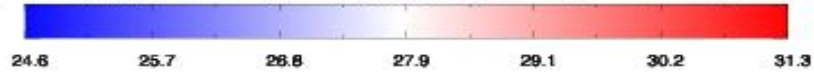


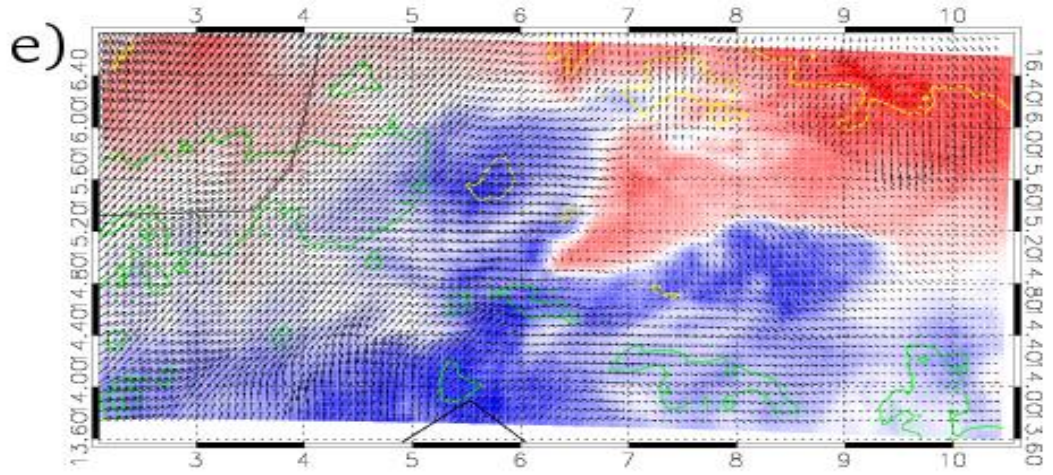


925mb:Temperature(°C);Spec. humidity 100\*(kgkg<sup>-1</sup>);Rain(contours);Wind(arrows);Date/Time: 15/6 2:00

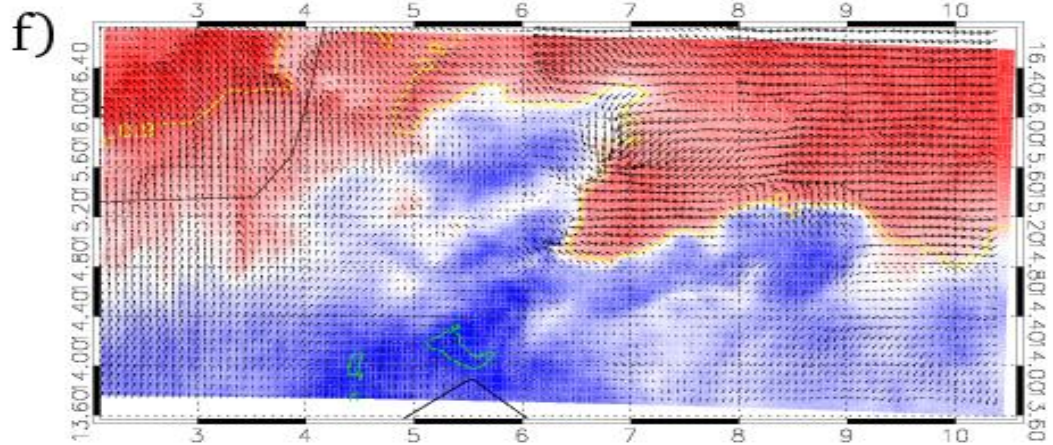


925mb:Temperature(°C);Spec. humidity 100\*(kgkg<sup>-1</sup>);Rain(contours);Wind(arrows);Date/Time: 15/6 6:00





925mb:Temperature( $^{\circ}$ C);Spec. humidity  $100*(\text{kgkg}^{-1})$ ;Rain(contours);Wind(arrows);Date/Time: 15/6 9:00



925mb:Temperature( $^{\circ}$ C);Spec. humidity  $100*(\text{kgkg}^{-1})$ ;Rain(contours);Wind(arrows);Date/Time: 15/6 12:00

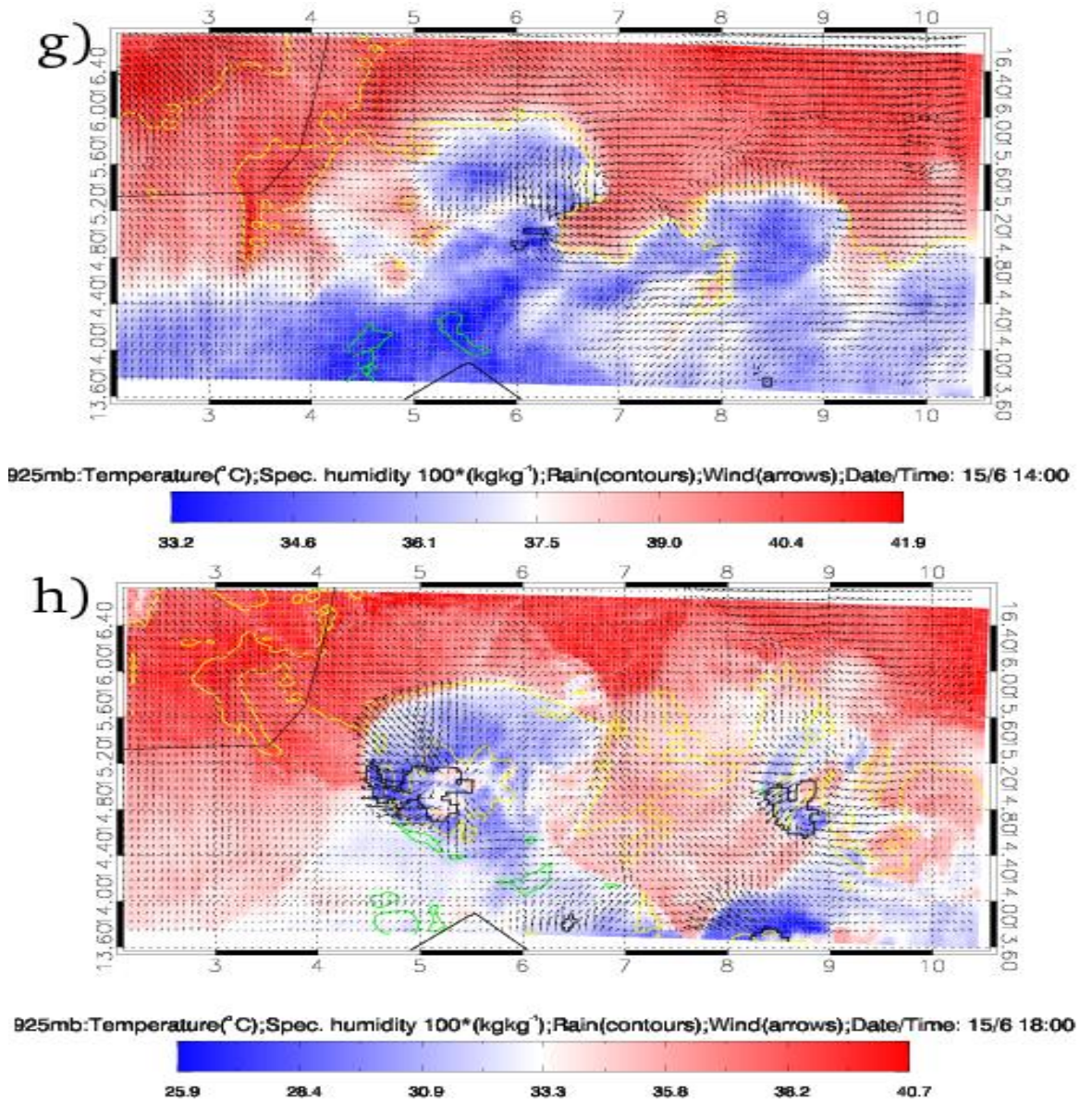


**Figure 5.26:** An example case in Cascade simulation: 1.5m temperature (shaded), 10m specific humidity (coloured contours), 10m wind (arrows) and surface precipitation (black contours). Two contours have been used for specific humidity – yellow shows  $9 \text{ g kg}^{-1}$  and green shows  $16 \text{ g kg}^{-1}$ . Precipitation contour denotes areas where instantaneous precipitation at the hour given is greater than  $0.5 \text{ mmh}^{-1}$ . Times of simulation: a) 18:00 and b) 22:00 on 14<sup>th</sup> June 2006. c) 02:00, d) 06:00, e) 9:00, f) 12:00, g) 14:00 and h) 18:00 on 15<sup>th</sup> June 2006. All times are UTC.

Cold pools have known influence on the location of convective initiations (e.g. Tompkins, 2000; Moncrieff and Liu, 1998) and Figure 5.26 is an example of new initiation occurring on the boundary of a previous cold pool. On 14<sup>th</sup> June 2006 at 18:00 UTC, a mature MCS is moving west-southwest across the domain (Figure 5.26 a)). It is producing a cold pool,

which is noticeably colder and drier than its environment. The cold pool spreads into the warmer and moister airmass and lifts surrounding unstable air-parcels, forming new cells at its edge as it propagates, sustaining the parent MCS (Figure 5.26 a)). By 22:00 UTC, the cold pool starts to outrun the parent MCS and no new initiation takes place on its edge (Figure 5.26 b)). By 02:00 UTC, the parent MCS has dissipated (Figure 5.26 c)). Overnight, strong south-westerly low-level jet winds (west of  $\sim 5^\circ$  E in Figure 5.26 d)) develop west of the remaining cold pool (now best visible as the colder and drier air running approximately north-south between  $\sim 5$ - $6.5^\circ$  E) in Figure 5.26 d)) at this level and push the cold pool to the northeast while advecting moist air into the Sahel west of the cold pool. By 09:00 UTC (Figure 5.26 e)), the nocturnal low-level jet has weakened considerably, but the moisture boundary associated with the now old cold pool (located between  $\sim 6.5$  and  $7^\circ$  E to the north of  $\sim 14.8^\circ$  N in Figure 5.26 e)) remains with the cold-pool airmass now being warmer than surroundings, presumably due to reduced cloud cover in the drier airmass (not shown). By noon (Figure 5.26 f)), larger mixing of low-level moisture and entrainment of dry air from the Saharan Air Layer into the boundary layer in the warmer more turbulent airmass due to enhanced dry convection (see enhanced winds in cold-pool airmass in Figure 2.26 f)) further reinforces the moisture boundary (still present between  $\sim 6.5$  and  $7^\circ$  E). By this time, the low-level jet winds have ceased and larger wind speeds can now be observed over the cold-pool region than elsewhere, a result of enhanced mixing in the warm and dry airmass. The direction of these winds is generally easterly, which is possibly a result of easterly winds from higher levels (e.g. the African Easterly Jet – see Figure 5.16) being transported to the 925 hPa layer due to momentum transport by the dry convection. On the old cold pool boundary (still present between  $\sim 6.5$  and  $7^\circ$  E by 12:00 UTC, Figure 5.26 f)), local circulation begins to develop, creating a region of convergence (near  $\sim 15.2^\circ$  N and  $6.5^\circ$  E). This convergence results in convective initiation by 14:00 UTC (near  $\sim 15.2^\circ$  N and  $7^\circ$  E in Figure 5.26 g)). It would generally be expected for convective initiation to occur on the dry side of the boundary (Taylor, 2015). In this case, first convective precipitation appears over the moist side. The convective cell may have however initiated over the dry region and propagated westwards to be over the moist region by the time of the saved hourly model output, which would agree with the mean propagation speed of MCSs of  $\sim 11 \text{ m s}^{-1}$  or  $\sim 0.3^\circ$  in one hour. At 18:00 UTC (Figure 5.26 h)), new MCS has organized and is propagating westwards. It is producing a drier than environment cold pool, which spreads out in all

directions. There is a region of enhanced moisture on the south-western edge of the cold pool (~14.5° N and 5° E in Figure 5.26 h)), a result of moisture pooling. On the rear side of the area of precipitation, warm anomalies are visible (near 14.8° N and 5.2° E). These are likely a result of subsidence under the stratiform rain area, which causes air to descend and warm as a result of compression (the same mechanism as observed in Figure 4.13 c) in section 4.3.3).

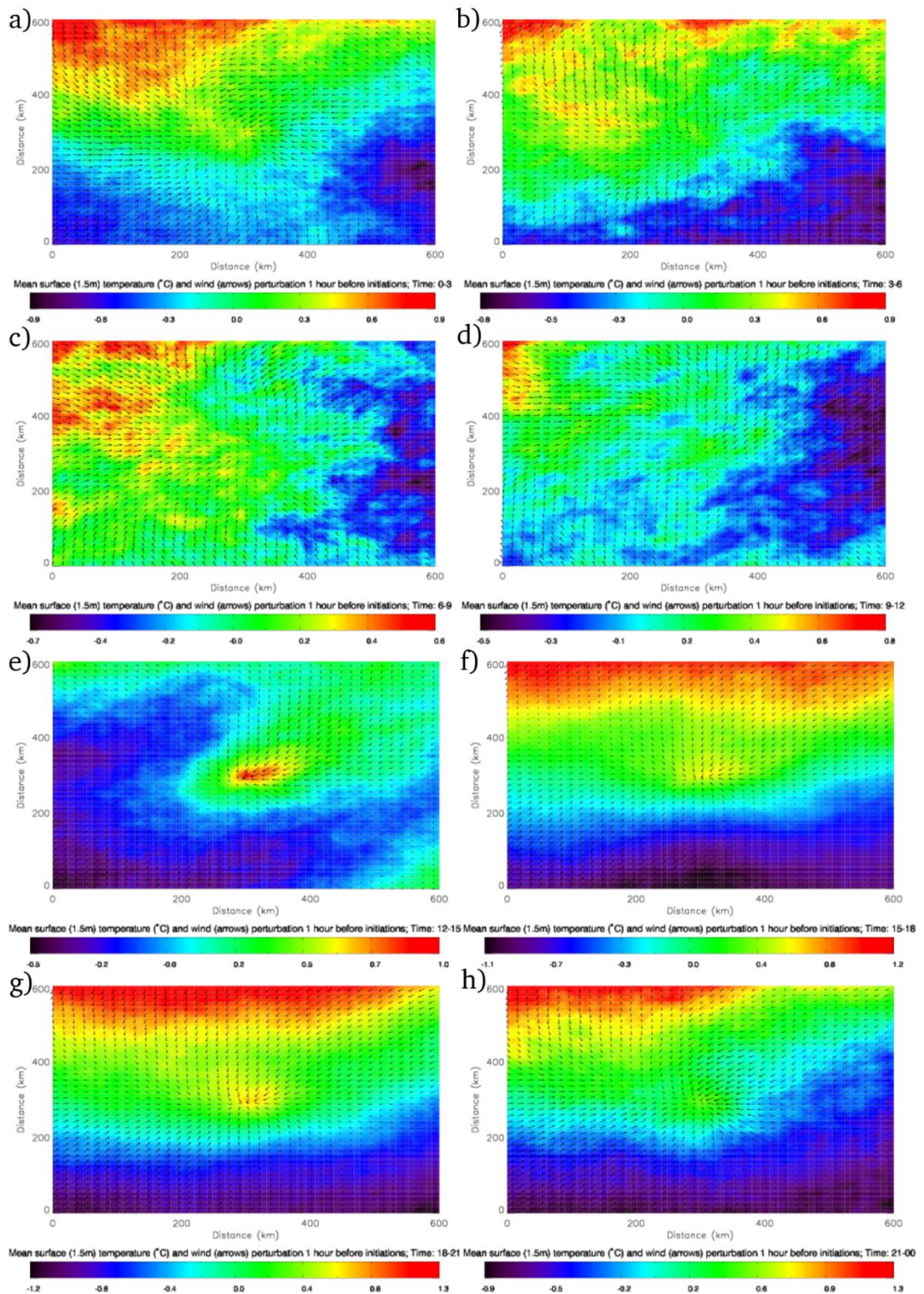


**Figure 5.27:** Composite of 1.5 m temperature (shaded) and 10 m wind (vectors) perturbations centred on points 1 hour before initiations by time of day. The composite is for 00-03, 03-06, 06-09, 09-12, 12-15, 15-18, 18-21 and 21-00 for a), b), c), d), e), f), g) and h), respectively. All times are UTC. Data obtained from Cascade 4km convection-permitting model simulation.

Composites of temperature (Figure 5.27) show that convective storms generally initiate over a warm patch between midday and midnight (Figures 5.27 e) – h)). The presence of this hot spot, driver by solar heating, causes rising motions and results in low-level convergence, which leads to convective initiations. Figure 5.27 e) highlights that north-easterly wind anomaly is present NE of the warm patch, presumably due to the circulation associated with the warmer patch blocking the mean south-westerlies. The hot-spot at one hour before initiation is nearly 2 degrees warmer than locations being ~200 km south or west of the initiation. The wind anomalies converge in the region of initiation, as would be expected. Although still present, the role of the hot spot becomes less significant between 15:00 and 21:00 UTC (Figures 5.27 f) and g) respectively). In this time-frame, wind perturbations from the north-easterly quadrant still prevail, but their magnitude is weaker than between 12:00 and 15:00 UTC, this most likely being a result of the weaker temperature gradient associated with the hot spot and hence weaker circulation. Between 18:00 and 21:00 UTC (Figure 5.27 g)), when boundary layer mixing has subsided and stabilization is preventing stronger winds to mix into the boundary layer from above, the perturbation due to convergence into the hot spot is more clearly apparent.

Except in the 12:00 – 15:00 UTC time frame (Figure 5.27 e)), the initiating storm is located on a temperature gradient rather than a completely isolated hot-spot, the magnitude and orientation of which changes throughout the diurnal cycle. Generally, colder temperatures are present east of or south of the location of initiation. This tends to be to the south before midnight (Figures 5.27 f), g) and h)) and to the east after midnight (Figures 5.27 a), b), c) and d)). The boundary is clearest and strongest between 15:00 UTC and midnight (Figures 5.27 f), g) and h)). Starting in the 21:00 – 00:00 UTC time-frame (Figure 5.27 h)), a mean east-west temperature gradient being accompanied by strong north-easterly wind anomalies from the cool side becomes apparent. Westerly wind anomalies are also present, these being even more pronounced between 00:00 and 03:00 UTC (Figure 5.27 a)). Since cold pools in West Africa generally propagate from the easterly direction westwards and are known to produce

forcing for convective initiations on their leading edge when elevated CAPE is present (see section 5.3.3.), they are the most likely explanation for this gradient. While the converging winds weaken between 03:00 and noon (Figures 5.27 b), c) and d)), the east-west temperature gradient becomes more dominant. This suggests that the convergence on the cold-pool edge weakens in the morning as both nocturnal low-level jet and cold-pool related flow weaken due to mixing/turbulence, but cold pools tend to be strongest and deepest, dominating the overall temperature gradient. The cold boundary in the east becomes more diffuse between 09:00 UTC and noon (Figure 5.27 d)).

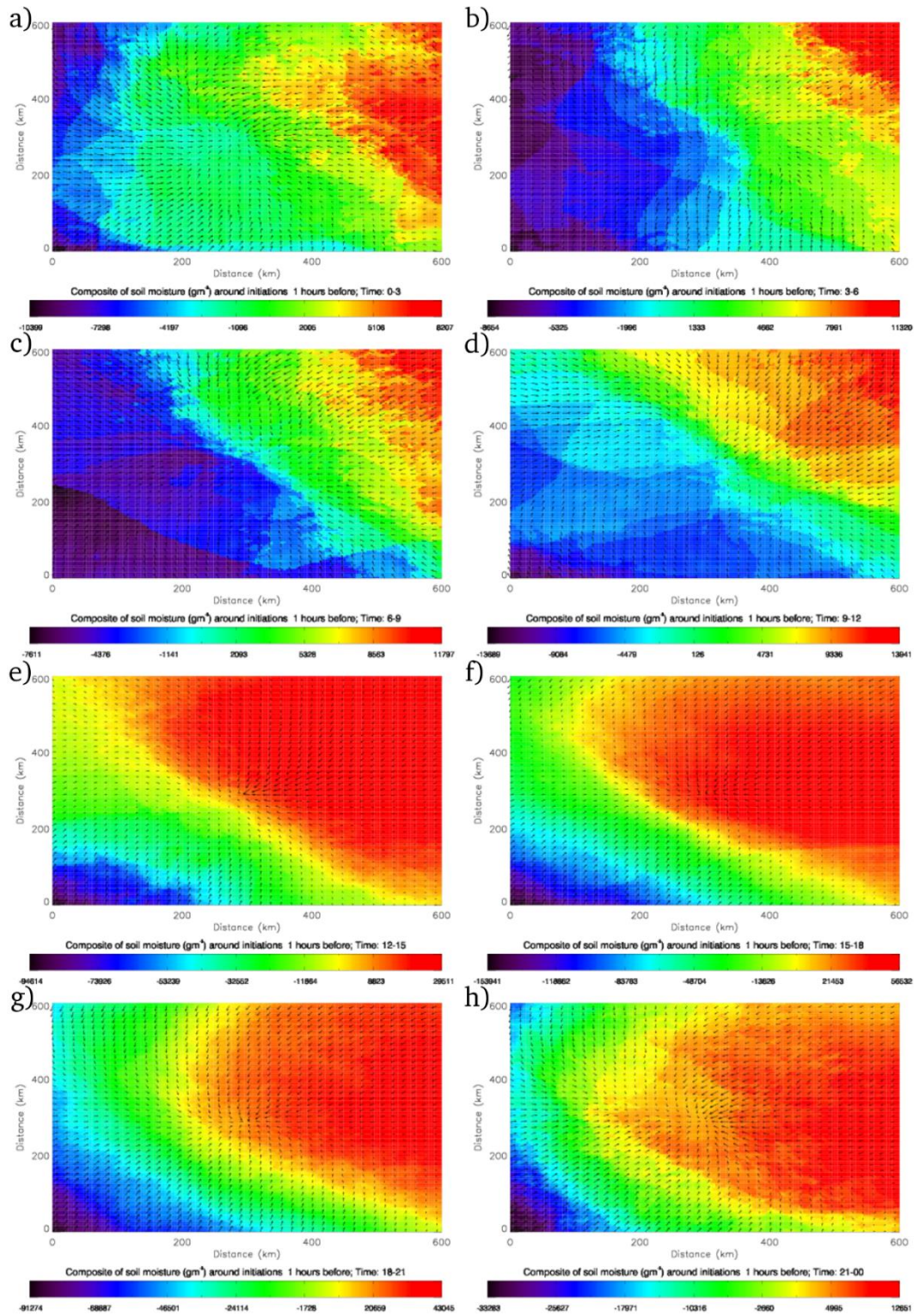


**Figure 5.28:** As Figure 5.27, but for Cascade soil moisture.

Soil moisture is often responsible for variations in low-level air temperature as it has significant influence on the percentage of incoming solar radiation being split between sensible and latent heat (i.e. Bowen ratio). Taylor *et al.* (2011) concluded that variations in soil moisture on length

scales of 10-40 km control storm initiations and 37% of storm initiations in their study occurred over 25% of steepest soil-moisture gradients. Here, the role of soil moisture in triggering convective initiations has been investigated by compositing it around the locations of initiations (Figure 5.28). A majority of convective initiations at all times of day are located close to a soil moisture boundary or a gradient of varying magnitude. In the 12:00 – 15:00 UTC time frame (Figure 5.28 e)), convective initiations are focused along a mean soil-moisture boundary with the wind anomalies into the developing updraft being from above the moist soil to the northeast. This wind anomaly is however likely a result of blocking the mean wind, which is southwesterly (not shown) by the convective circulations, as discussed above. At the same time, a localised mean patch of warm air is present at the boundary (see Figure 5.28 e)) where the initiation is to occur and the 1.5 m temperature hot spot is located at the downstream (northeast, since low-level mean winds are from southwest) side of the drier soil. This agrees with Taylor *et al.* (2011), where they state that soil-moisture induced circulations produce low-level wind flow from the moister to the drier soil and where this flow opposes the general synoptic scale flow, convergence occurs. Between 15:00 UTC and midnight (Figures 5.28 f), g) and h)), the focus of initiations shifts more over the moist soil with time. Since, in general, isolated afternoon initiations tend to occur near a boundary over the dry side and overnight cold-pool driven initiations tend to occur over the moist surface (Taylor *et al.* 2011), this further supports the increasing importance of existing cold-pools in driving convective initiations. The increasing gradient in soil moisture in the late afternoon and evening hours also supports the fact that rainfall (and related cold-pool) is located to the east or north-east of the new initiation, moistening the ground. Between 21:00 UTC and noon (Figures 5.28 a), b), c), d) and h)), the moisture gradient is approximately five times weaker and less coherent than in the late afternoon, showing that it has little effect on the location of convective initiations. Generally, moister surface is present to the east and northeast, but at these times the convergence between the southwesterly flow and the cold pool is presumably the major driving process.

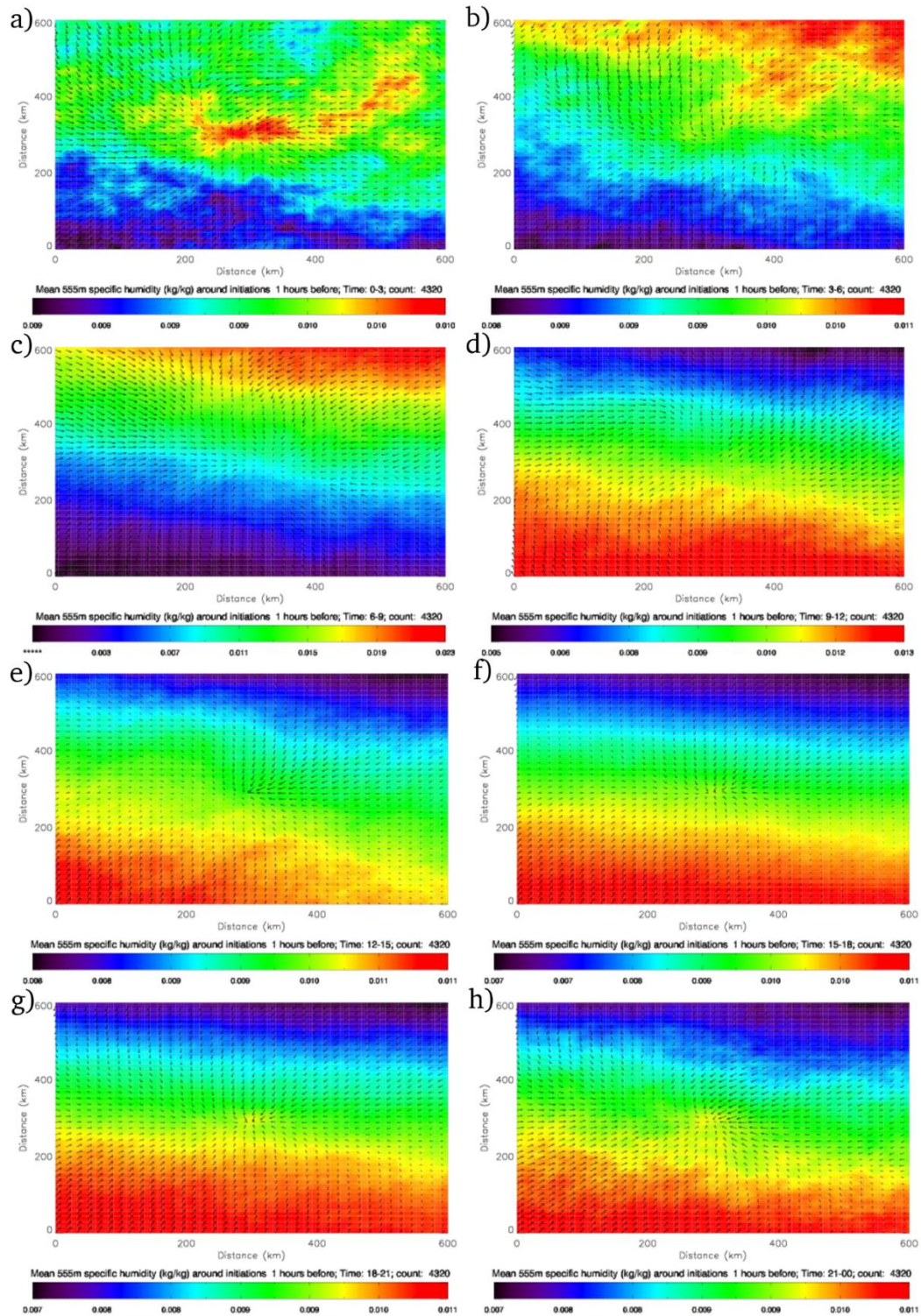


**Figure 5.29:** As Figure 5.28, but for Cascade 10 m specific humidity anomaly (composite around convective initiations with mean around 5000 random points subtracted). The composite domain size is 150x150 grid points, or 600x600km.

Overnight, convective initiations are located in a zone of mean moisture convergence, which is most pronounced between midnight and

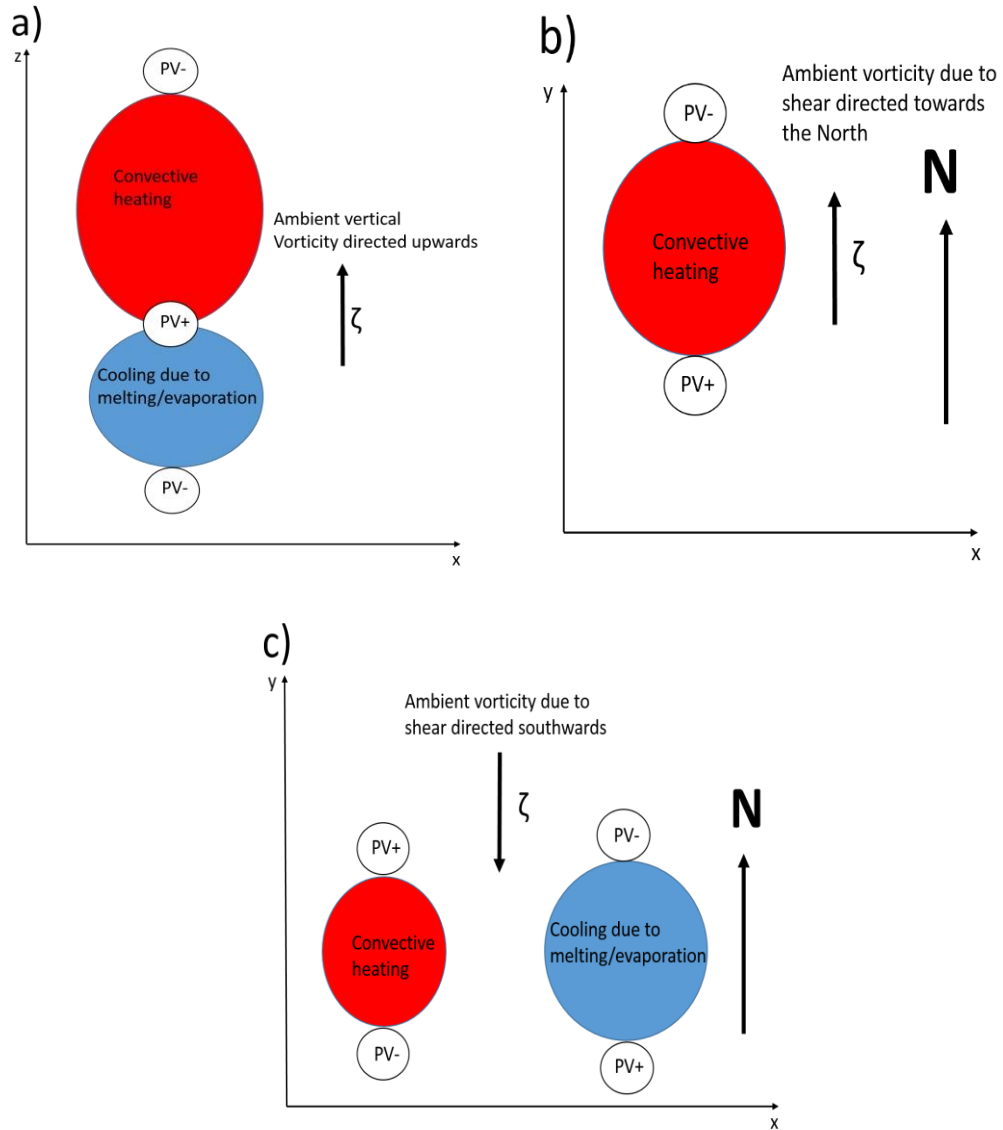
03:00 UTC (Figure 5.29 a)) when a mean elongated patch of moister air is located close to the initiation locations. If Figures 5.29 a) and b) are compared to Figures 5.27 a) and b), it can be seen that mean positive moisture anomaly to the northeast of the convective initiation is located to the northwest of the negative temperature anomaly. This positive moisture anomaly is less evident between 06:00 and 15:00 UTC (Figures 5.29 c) – e)), when temperature anomalies are also less pronounced (see Figures 5.27 c) – e)). This may be related to cold pools and moisture convergence ahead, but further work would be needed to confirm this. Between 15:00 and midnight, convective storms again initiate over a mean moist patch, which is much localised in this time frame.

### ***The role of PV anomalies***

Potential Vorticity (PV) is a scalar product of vorticity with potential temperature gradient. Following a parcel of air, it can only be changed by diabatic processes or friction. The evolution of PV can be expressed using Ertel's form of potential vorticity given by equation (Haynes and McIntyre, 1987):

$$\frac{D}{Dt} PV = \frac{1}{\rho} \zeta^a \cdot \nabla \left( \frac{d\theta}{dt} \right) \quad (4)$$

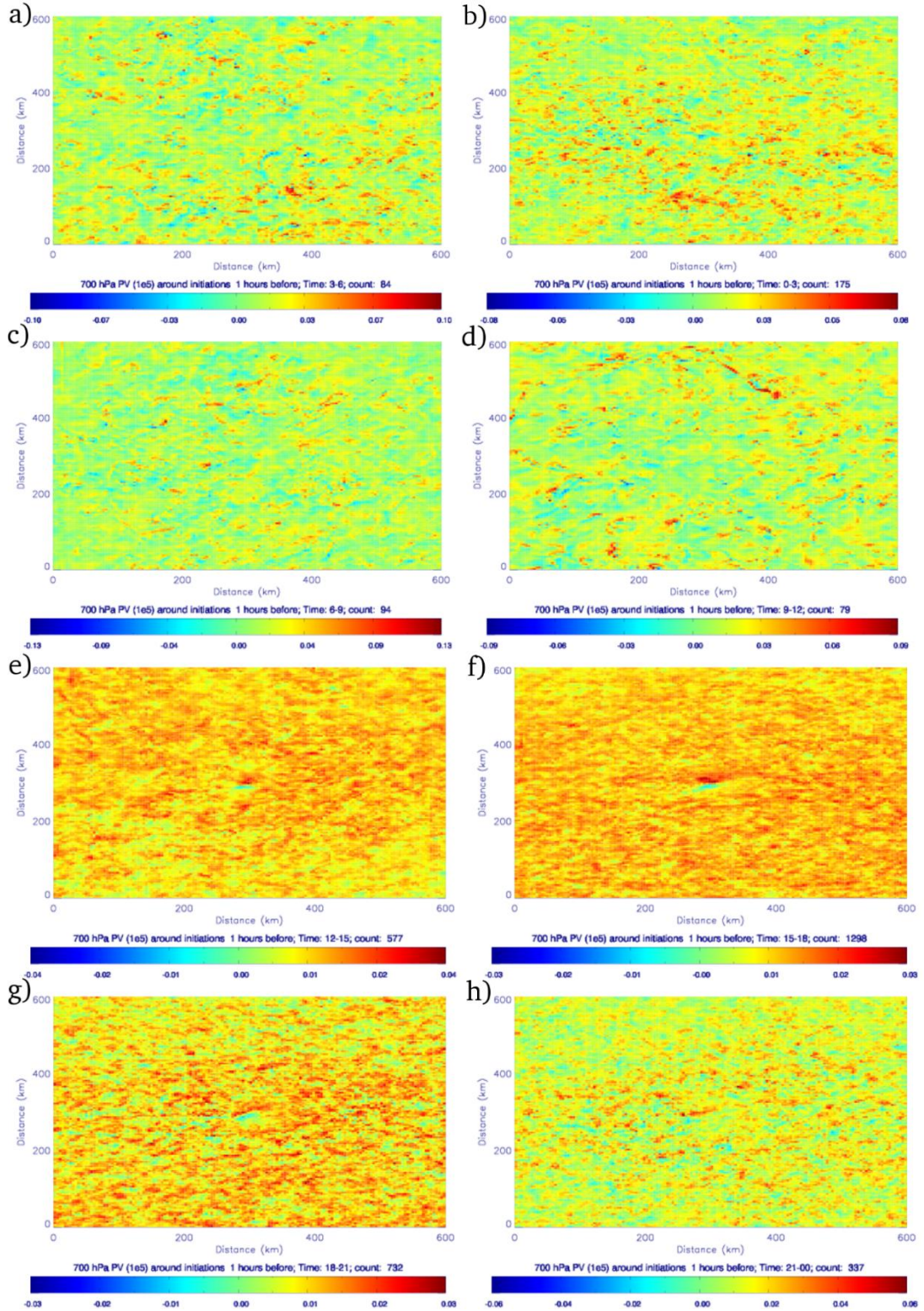
In equation (4), PV stands for potential vorticity,  $\rho$  for density of the fluid/air,  $\zeta^a$  is the absolute 3D vorticity and  $\nabla \theta$  is potential temperature gradient.



**Figure 5.30:** Schematics showing a) a vertical plane through a convective storm and the production of increases and decreases in Potential Vorticity (PV+ and PV-, respectively) due to convective heating and cooling (due to evaporation of rainfall). In b) and c), a horizontal plane shows the modification of PV if the convective heating is b) above the AEJ (vorticity therefore northwards) and c) below the AEJ (vorticity therefore southwards).

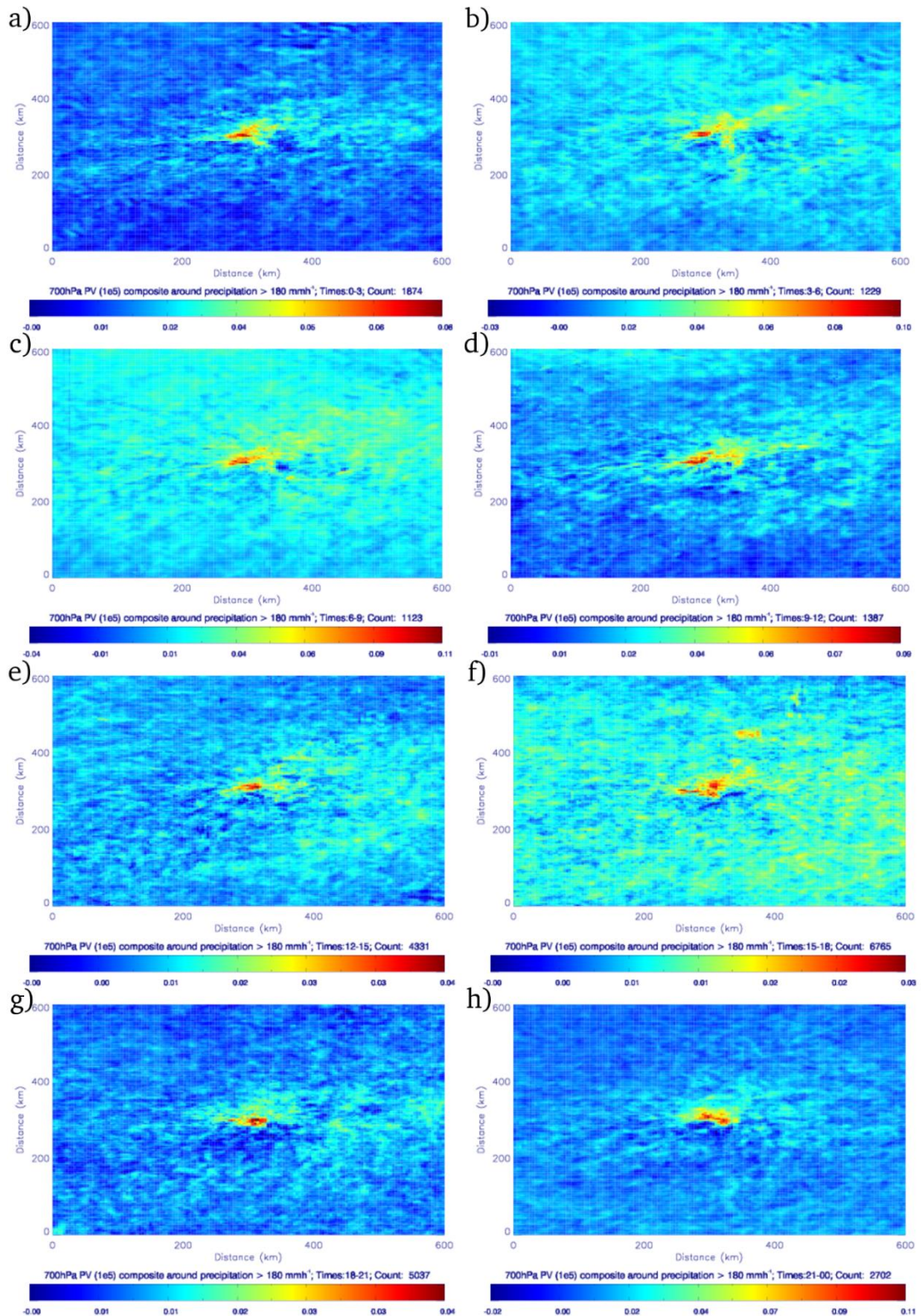
Figure 5.30 shows a schematic PV changes as a result of convective heating or cooling (due to evaporation). Figure 5.30 a) is a vertical plane showing the tendencies due to the vertical component of vorticity. In this case, the horizontal vorticity due to shear doesn't affect the tendency, and the PV is always increased in between the heating and cooling, and decreased above the heating and below the cooling. Figures 5.30 b) and c) show PV in the horizontal plane with the north at the top. In b), the vorticity vector due to the AEJ shear is towards the north above the AEJ. In this case, there is an increase in PV to the south of the heating and a decrease in PV to the north of the heating. It is assumed that there is no cooling at these levels above the AEJ. In c) the plane is located towards the south,

below the AEJ. In this case the PV depends on whether there is heating or cooling. If there is convective heating, an increase in PV is located to the south with decrease in PV to the north. For cooling, it is the opposite (positive to the north and negative to the south) than for warming.



**Figure 5.31:** As Figure 5.29., but for Cascade potential vorticity anomalies  $10^{-5}$  ( $m^2 s^{-1} K Kg^{-1}$ ) at the 700 hPa level.

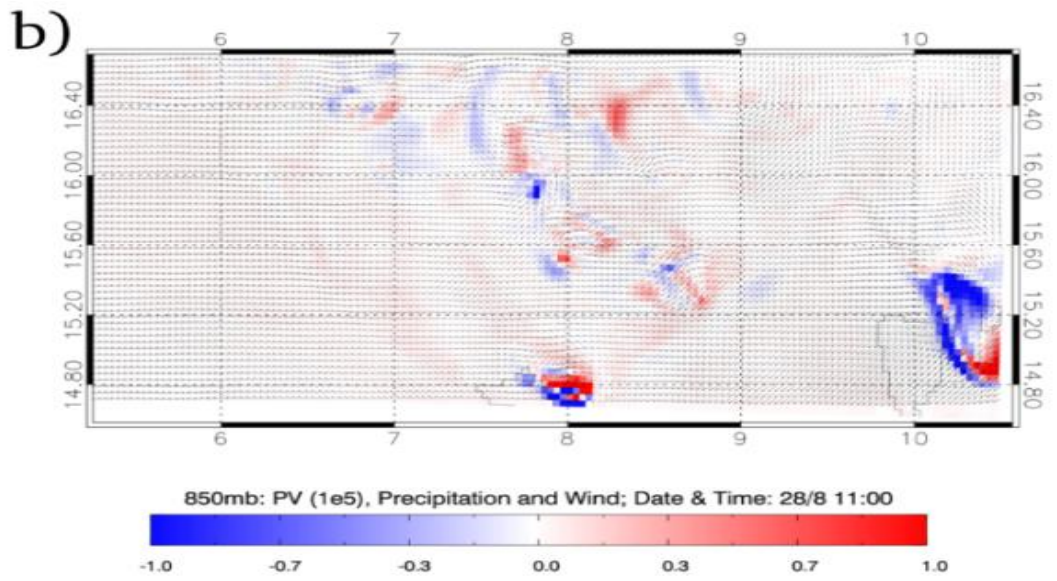
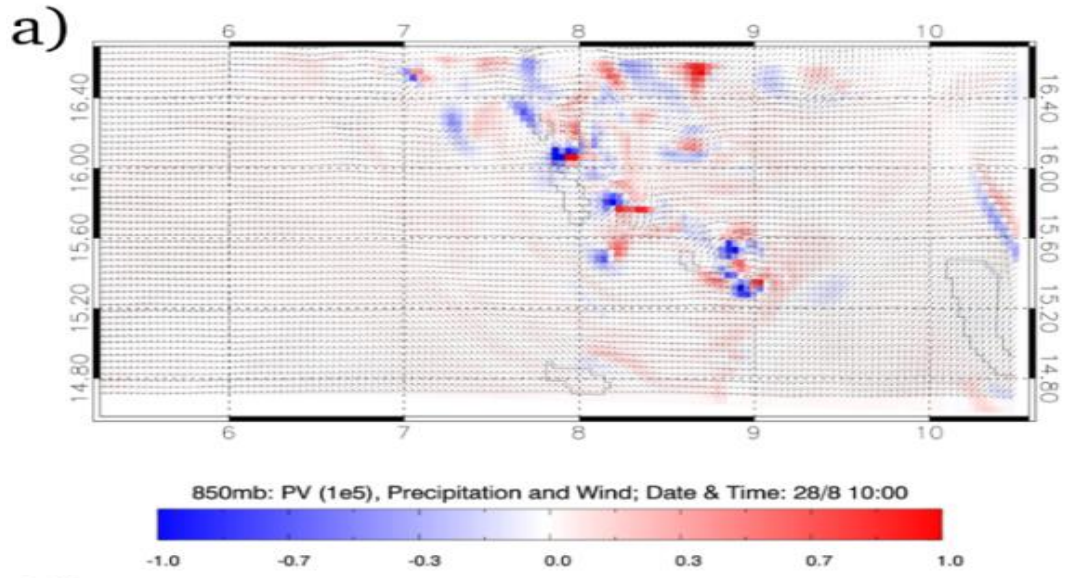
Convective initiations can be affected by PV anomalies (Russel *et al.* 2008) produced by pre-existing convective storms (e.g. bookend vortices). These bookend vortices are regions with high values of PV, which is a source of lift and can therefore lead to, or aid in, convective initiation. The state of the composite Potential Vorticity (PV) anomaly shows no clear signal between midnight and midday (Figures 5.31 a), b), c) and d)). Between noon and 18:00 UTC (Figures 5.31 e) and f)), a PV anomaly couplet centred at initiation location with a positive value to the north and negative to the south, which would agree with the convective heating below the AEJ on average (see Figure 5.30). This couplet is less clear in the 18:00 – 21:00 UTC time frame (Figure 5.31 g)) and not present anymore in the 21:00 UTC to midnight time frame (Figure 5.31 h)). The PV couplet has not been present at two hours before initiations. The presence of this couplet one hour before the initiation at times hints at the fact that convective initiations may tend to occur in the vicinity of PV anomalies, which may have been initially caused by pre-existing convection. These composites were, however, produced as mean anomalies at one hour before the presence of first rainfall. There may have been developing convective cloud already present at the time of the composite, which may have actually caused the anomaly. Therefore, further research would need to confirm that no such cloud is already developing at the time of these composites.

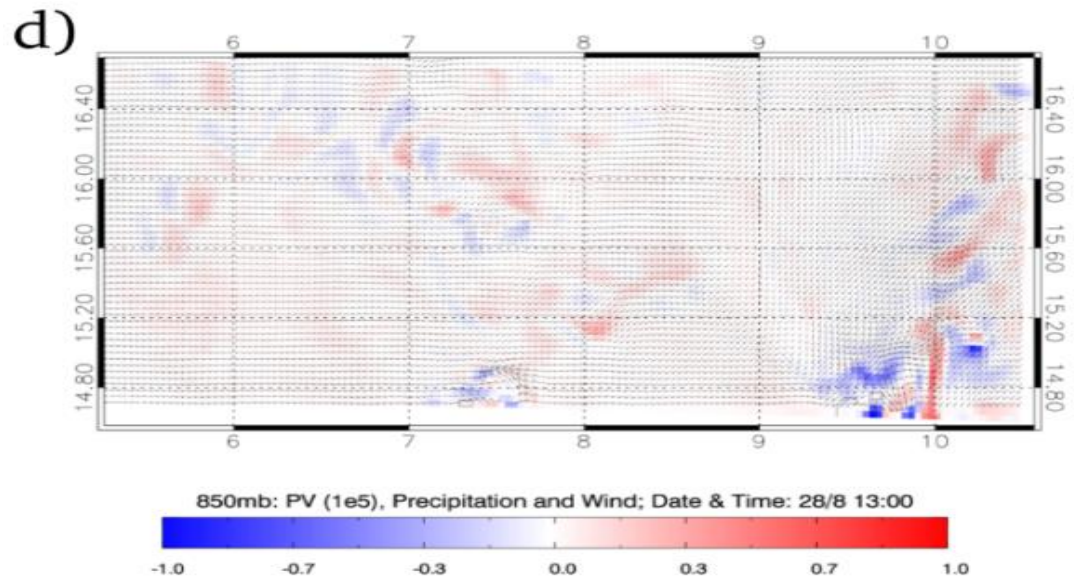
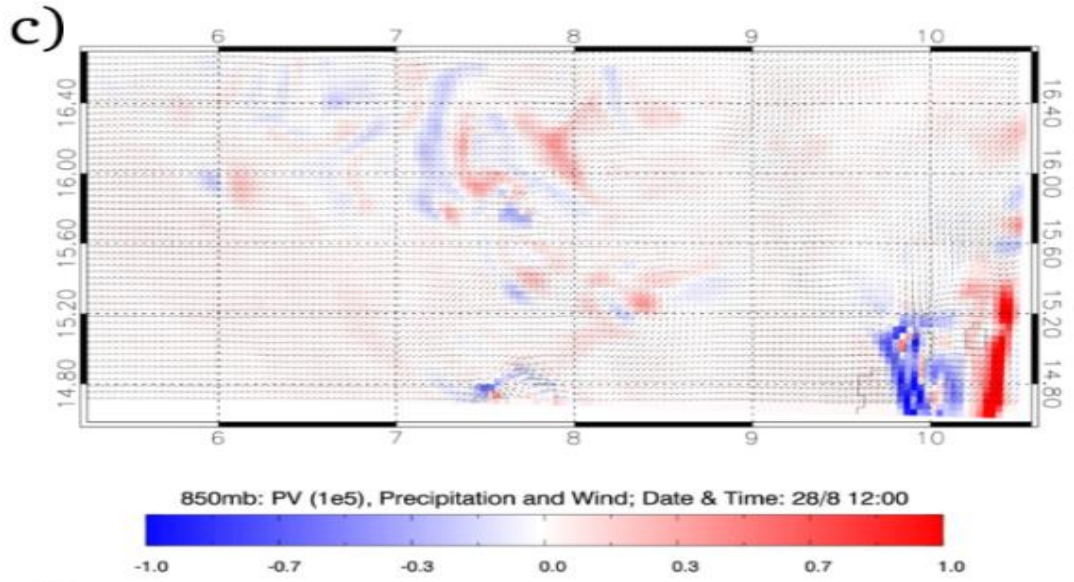


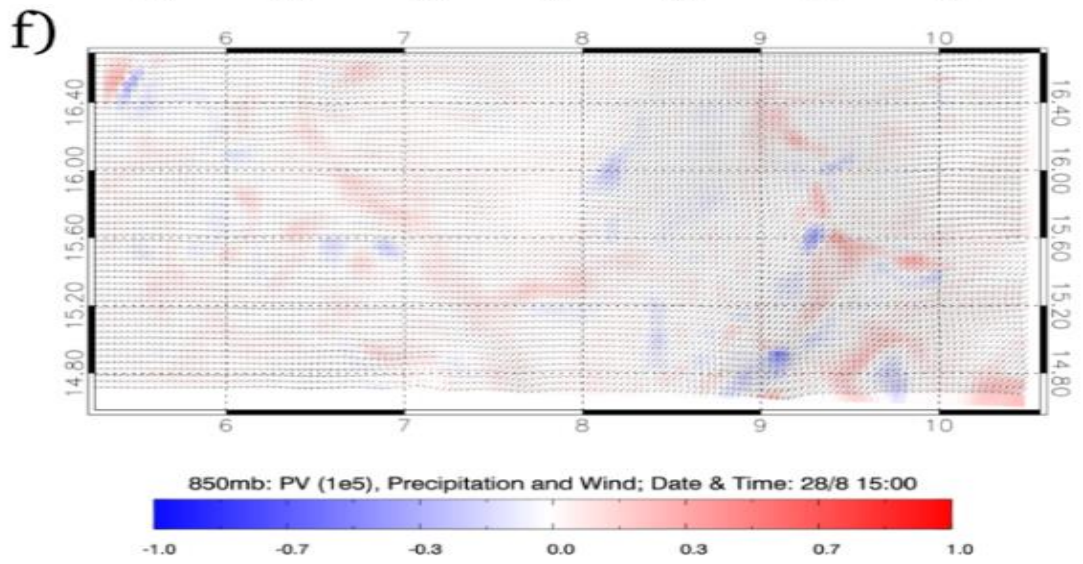
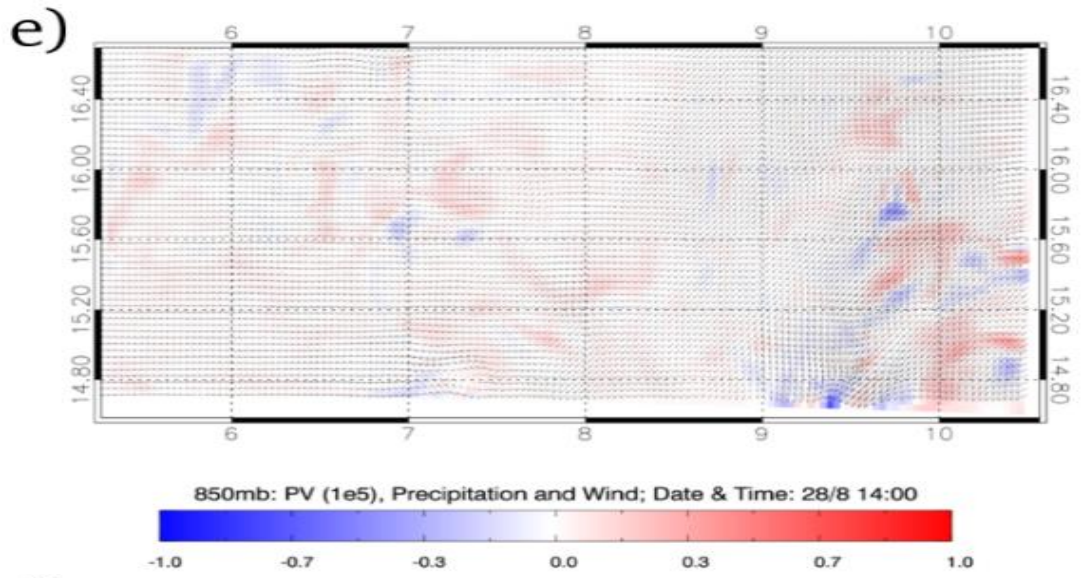
**Figure 5.32:** As Figure 5.31, but for Cascade potential vorticity anomalies  $10^{-5} (m^2 s^{-1} K Kg^{-1})$  at the 700 hPa level around points where rainfall rate is greater than  $180 mm h^{-1}$ .

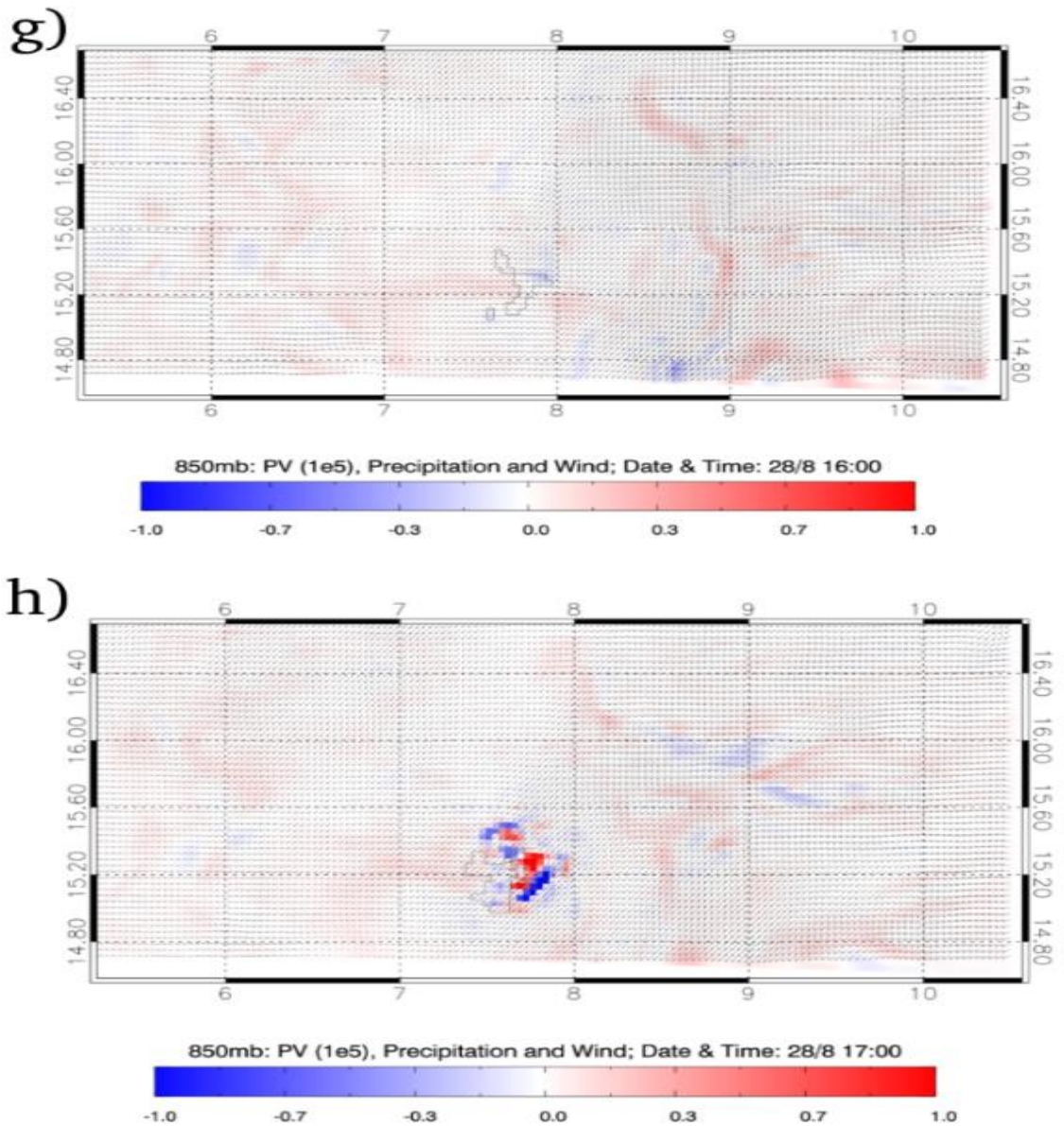
The structure of PV around rainfall has been investigated by composites (Figure 5.32), which show that PV (note these are actual values, not anomalies as in e.g. Figure 5.29) around strongest rainfall generally

features a dipole structure at all times of day. This structure is also apparent at 850 hPa, although less clear, showing that it extends through a depth of 100-200 hPa. It was initially hypothesised that these potential vorticity anomalies may be related to bookend vortices produced by squall-lines. The sign of the PV, however, is opposite to what would be expected regarding PV of bookend vortices in westward propagating MCSs. In addition, bookend vortices were identified only in a handful of organized simulated squall-lines and they would unlikely dominate the composites. The PV structure seen in the composites is therefore presumably a result of convective heating being below the AEJ, on average (see Figure 5.30), although air is advected both during and after the convective heating or cooling that modifies PV, which complicates interpretation.





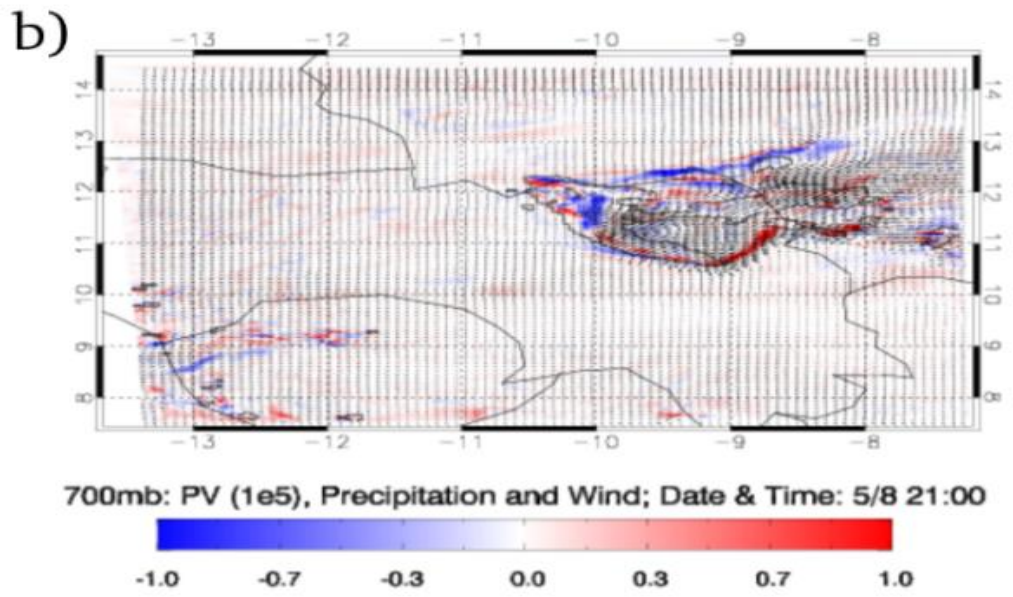
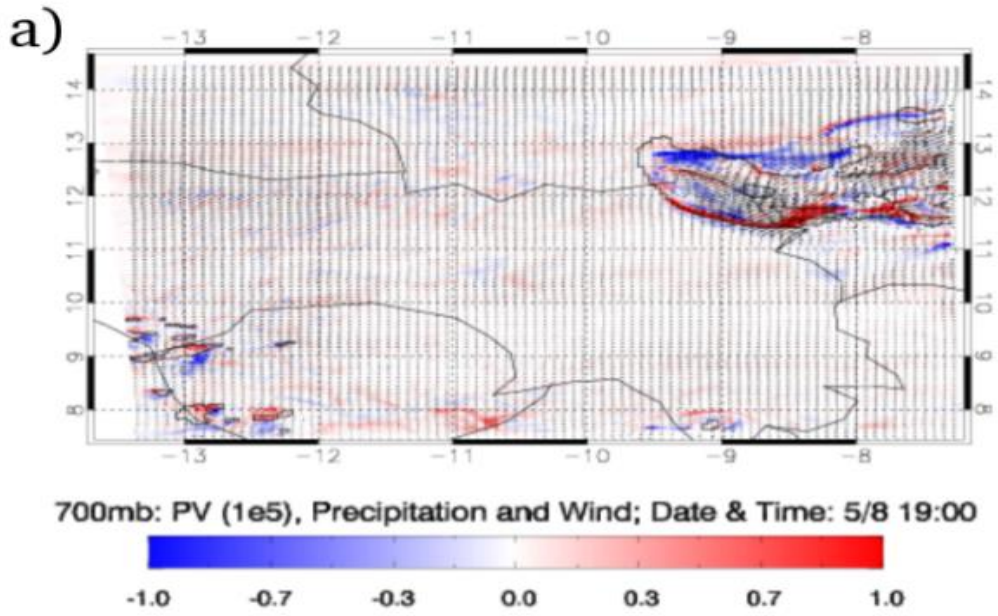


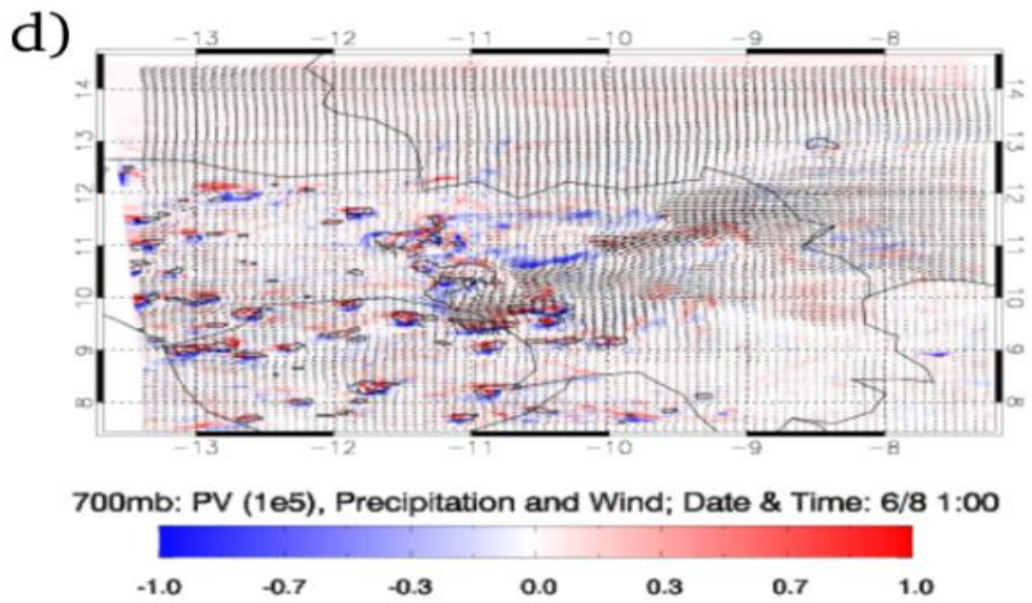
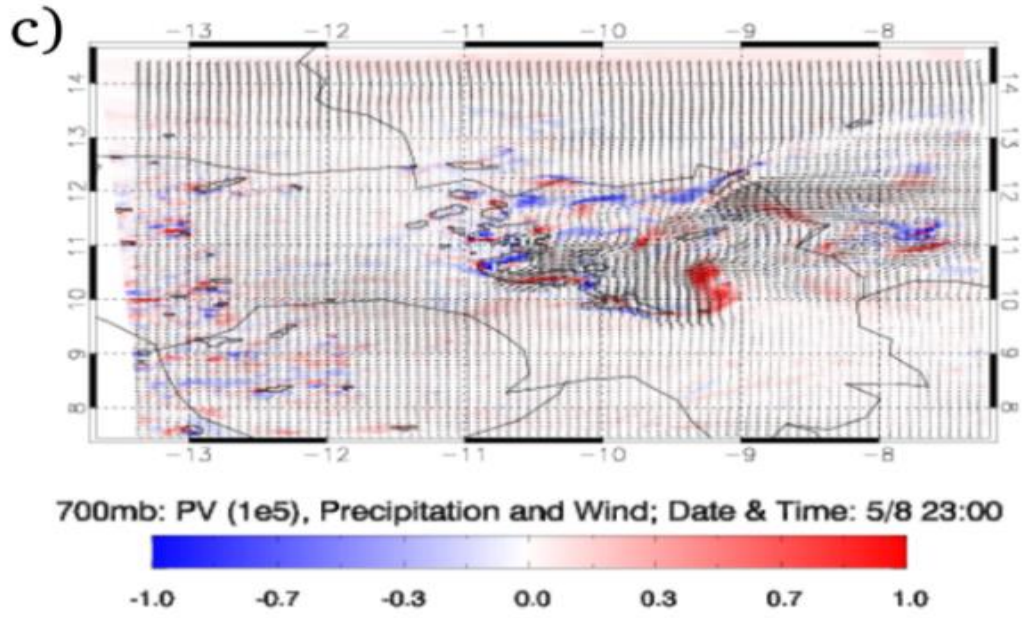


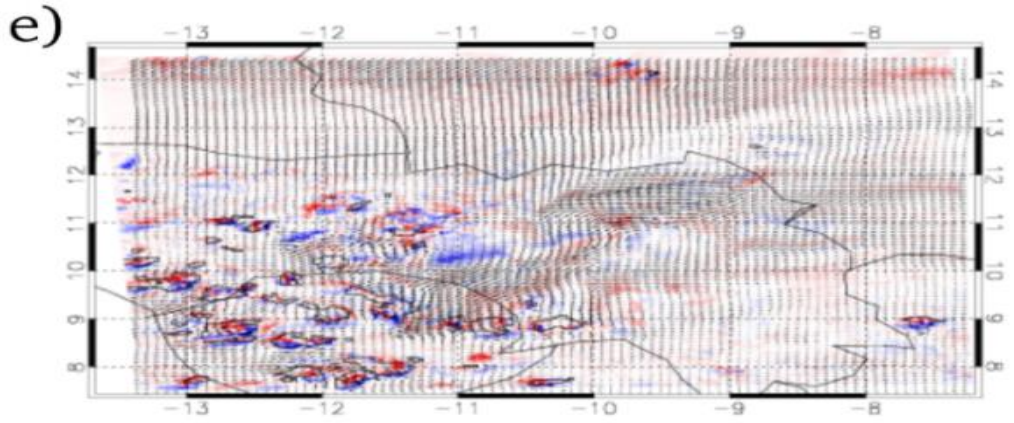
**Figure 5.33:** Cascade 850 hPa PV  $10^{-5}$  ( $m^2 s^{-1} K Kg^{-1}$ ) (shaded), precipitation (contours) and 10m wind (arrows). a)-h) are for 10:00-17:00 UTC respectively.

Individual cases, where PV has persisted and led to the initiation of a new convective storm, have been identified using methods described in section 5.3.4. This led to the identification of two such cases. The first example can be seen in Figure 5.33 of a PV anomaly persisting after dissipation of a convective storm in the morning hours (Figure 5.33. a) and b) at  $\sim 8.8^\circ E$  and  $\sim 15.4^\circ N$ ). This anomaly then slowly propagated with the mean flow through the afternoon (located at  $\sim 8.3^\circ E$  and  $\sim 15.2^\circ N$  in Figure 5.33 c) and persisting near  $8^\circ E$  and  $15.2^\circ N$  in Figures d), – f)) and being located nearly over an initiating storm in the evening hours (Figure 5.33 g) at  $\sim 7.9^\circ E$ ,  $\sim 15.2^\circ N$ ). In this example, the PV anomaly was not a true bookend

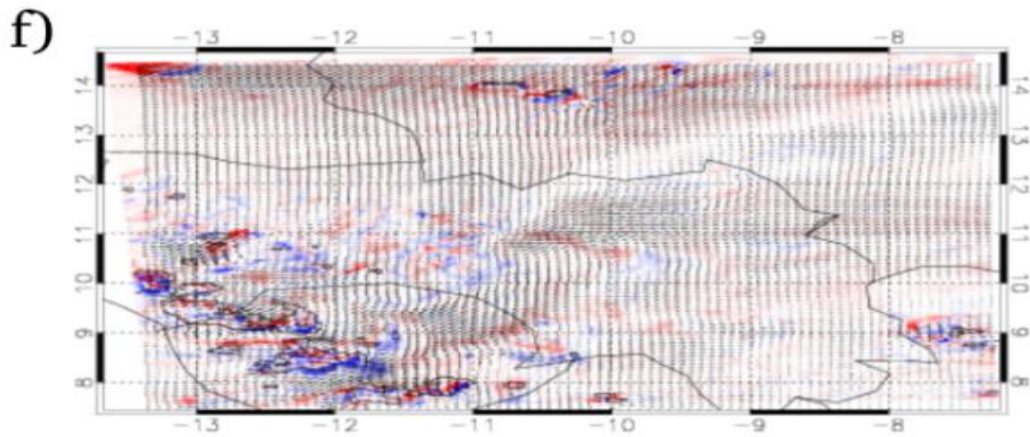
vortex located at the end of a squall-line, but a region of PV created by convective heating in the updraft (Figure 5.33 a) at  $\sim 8.8^\circ \text{E}$  and  $\sim 15.4^\circ \text{N}$ . No obvious mechanism, other than the PV anomaly, was found to be responsible for the secondary initiation. The secondary storm initiated far west of the cold pool of the primary storm and the cold pool was not recognizable by the time of initiation in neither temperature nor specific humidity. The initiation occurred in a region of convective inhibition of  $\sim 80 \text{ J Kg}^{-1}$ . There is no soil-moisture boundary or any obvious orographic feature in the location of the initiation and hence the PV couplet that could be traced from the dissipation of the primary storm until the initiation of the secondary storm is a probable cause of the new initiation.







700mb: PV (1e5), Precipitation and Wind; Date & Time: 6/8 3:00



700mb: PV (1e5), Precipitation and Wind; Date & Time: 6/8 5:00



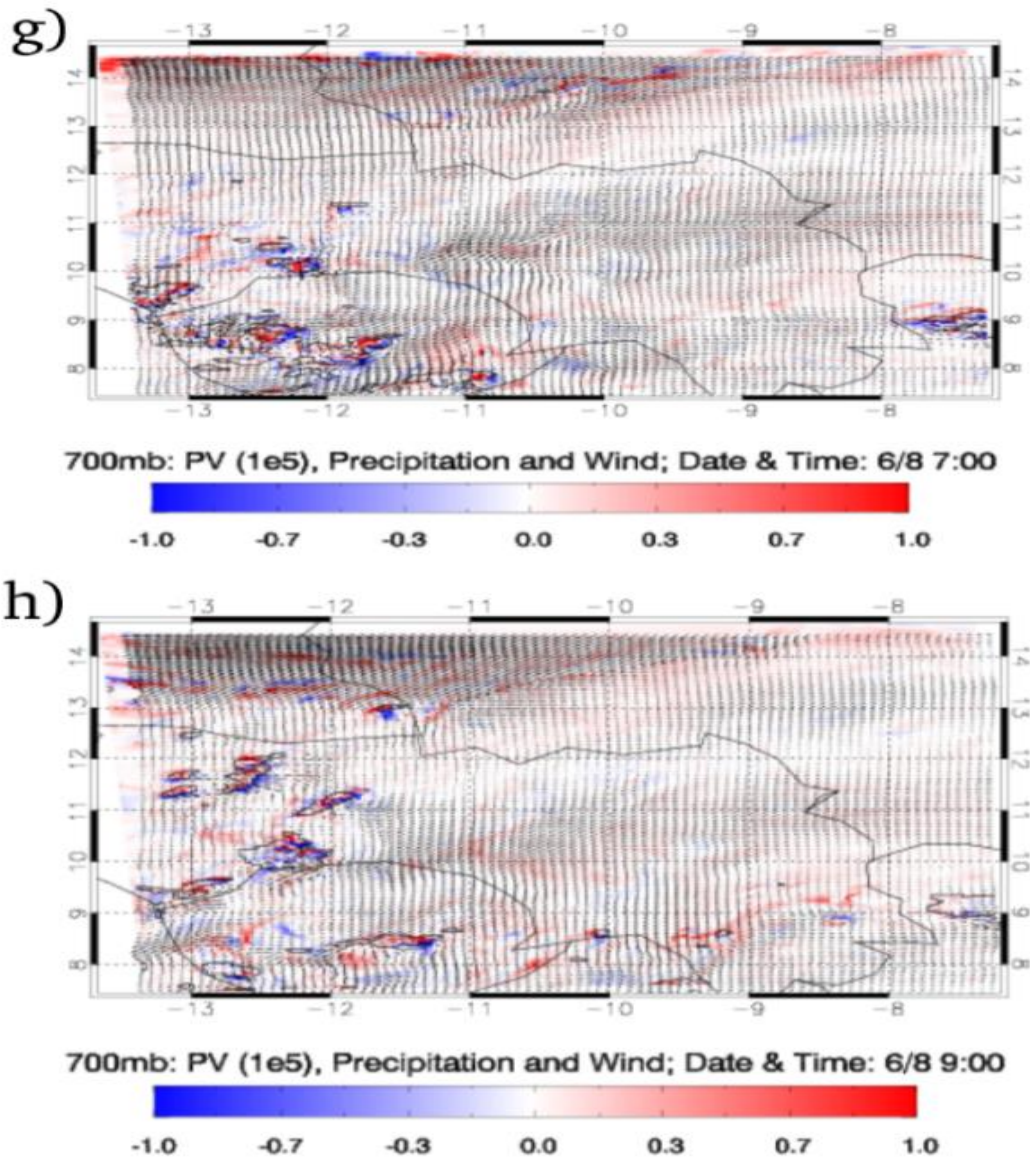


**Figure 5.34:** Cascade 700 hPa PV  $10^{-5}$  ( $m^2 s^{-1} K Kg^{-1}$ ) (shaded), precipitation (contours) and 10m wind (arrows). Times of simulation: a) 19:00 and b) 21:00, c) 23:00, d) 01:00, e) 03:00, f) 05:00, g) 07:00 and h) 09:00, all in UTC, on 5<sup>th</sup> (before midnight) and 6<sup>th</sup> (after midnight) August 2006.

Two bookend vortices associated with a mature squall-line, one of which later forces convective initiation, are shown in Figure 5.34. Initially, a squall-line propagates into the domain, having two PV anomalies in Figure 5.34 b), a negative (10W, 12N) at its northern end and a positive (9W, 11N) at its southern end. After dissipation/disorganization of the squall-line around midnight (Figure 5.34. c-d)), the positive PV anomaly propagates further southwestwards, detached from any new convective precipitation, which at that time forms on the edge of the cold pool further southwest (-12W, 10N). The positive anomaly can be seen near -9.5 E, 10 N at 14:00 (Figure 5.34

d)), near -10 E, 9.5 N at 16:00 (Figure 5.34 e)), near -10.5 E, 9.5 N at 18:00 UTC (Figure 5.34 f)), near -11 E, 8.5 N at 20:00 (Figure 5.34 g)) and new initiation forms in the region of the PV anomaly near -11.5 E, 8.5 N at 22:00 UTC (Figure 5.34 h)). There is again no other typical forcing that could be responsible for this new initiation. Moreover, the new initiation occurs over the cold pool of the primary MCS, which is colder and dryer than environment and hence new initiation would not be expected in this region.

## 5.4. Conclusions

The diurnal cycle in deep convective storms and MCSs over the Sahel has been investigated using observational data from Niamey (obtained during AMMA) and 4 km *Cascade* simulations. Past studies have shown that, in general, a maximum in convective initiations in the afternoon hours leads to many isolated storms forming, with upscale growth and intensification overnight. In the morning after sunrise storms then weaken and nearly always dissipate before noon. This study has investigated the role of various environmental properties that may affect these diurnal variations and the organization of convective storms.

The role of convective initiations is very important for the diurnal cycle of convective storms as initiations dictate when and where convective storms form. *Cascade* simulations support the fact that convective initiations can often be forced either by a cold pool or by local circulations associated with gradients in soil moisture content. The role of these varies by time of day. In the afternoon, initiations tend to preferably occur due to locally produced forcing mechanisms such as over a “hot spot” and on a soil moisture boundary. In the evening and overnight, the local effects become less pronounced. The composites in section 5.3.2 suggest that cold-pool forced initiations may dominate, but further research would be needed to find the dominant process leading to the overnight initiations. Potential Vorticity (PV) anomalies have been found to play some role for convective initiations in the afternoon hours. These PV anomalies are caused by pre-existing convective storms, persist after the dissipation of the storms and can force new initiations later.

Thermodynamic profile of the environment surrounding convective storms plays an important role in the observed diurnal cycle of convection and results were largely independent of whether all observed profiles were analysed, or only those profiles in the 12 hours before deep convection.

Afternoon heating results in boundary layer growth and a decrease in convective inhibition. Strong mixing in the boundary layer results in entrainment of dry mid-level low equivalent potential temperature air into the boundary layer, reducing mean equivalent potential temperature and CAPE in the afternoon. The relatively low CAPE still has a mean value of  $\sim 600 - 800 \text{ J Kg}^{-1}$ , which is sufficient to support convective storms. The low convective inhibition in the afternoon makes it easy to be overcome and a large number of convective initiations occurs. After sunset, low levels stabilize and surface based CAPE decreases while convective inhibition increases, making new initiations less likely.

Elevated CAPE increases in the evening hours and overnight, being a result of an increase in equivalent potential temperature at levels greater than  $\sim 600$  metres above ground. This increase was slightly stronger in profiles within 12 hours before deep convection. While potential temperature decreases overnight, increasing Water Vapour Mixing Ratio outweighs that decrease and results in the equivalent potential temperature increase. Existing storms can then take profit from the elevated CAPE if they can lift it using their cold pools. The increase in Water Vapour Mixing Ratio is a result of the nocturnal low-level jet, which advects moist tropical air mass into the Sahel. After sunrise, the low-level jet breaks down, disrupting the advection of moist air, which results, together with the onset of mixing in a decrease of CAPE, making conditions less favourable for sustaining convective storms.

The role of the low-level jet is not, however, limited to providing high equivalent potential temperature air to convective storms. In the lowest  $\sim 2\text{km}$  of the atmosphere in the Sahel the diurnal variations in the low-level jet provide the largest variations in wind speed and wind shear, with a maximum in the early morning and a sharp minimum in the afternoon. Wind shear over the Sahel calculated over the typical cold-pool depths between  $0.5-1.5\text{km}$  and  $0.5-2.5\text{km}$  has been compared to typical cold-pool strengths of mid-latitude squall-line MCSs (Weisman and Rotunno, 2004). Based on the RKW theory, the optimal state between the wind-shear and cold-pool strength occurs in the early morning hours with the decrease in wind shear after sunrise creating weaker wind shear and hence conditions less optimal for the sustaining of the MCSs.

Mean moisture budget has been calculated for  $200 \times 200 \text{ km}^2$  boxes around the most intense storms in *Cascade* simulations. The mean diurnal cycle of rainfall in the Sahel in *Cascade* is similar to the observed diurnal cycle with both the intensity and areal coverage of rainfall being important.

Overnight, a maximum in moisture flux convergence occurs in the lowest ~200 hPa. This is located at the same level as the low-level jet and confirms yet another important role of the low-level jet, being the provision of moisture flux convergence. After sunrise, the moisture flux convergence in the lowest levels plummets due to low-level jet breakdown, contributing to a minimum of rainfall at 11am. In the early afternoon surface evaporation is maximised. At this time, storms also use moisture that had been stored in the air of the box. There is a mean moisture flux divergence in the early afternoon, but this may be due to the smaller size of the storms at this time and there may still be a mean convergence if a smaller box was used. In the evening, with diurnal reduction of sunlight surface evaporation plummets, but the increase in moisture flux convergence provided by the low-level jet outweighs this, allowing further increase in rainfall. Away from rainfall, moisture flux convergence is negligible. Evaporation then dominates, storing moisture in the atmosphere that would later be advected by the low-level jet and possibly be part of the moisture flux convergence supporting convective storms.

Investigation of the diurnal cycle in convective storms and their environment in the Sahel has concluded that the interaction between MCSs and the low-level jet is very important for storm organization and their mean diurnal lifecycle. The results support that the low-level jet supplies water vapour to existing convective storms and provides wind shear to create environmental conditions optimal for the MCSs to be sustained (due to vorticity interaction as stated by RKW theory). Furthermore, it advects high equivalent potential temperature airmass above the stable nocturnal boundary layer, resulting in increased elevated CAPE overnight. This all explains the 03:00 UTC maximum present both in the simulations and in observations. During the day, the breakdown/absence of the low-level jet together with dry air entraining into the boundary layer reduces CAPE, leading to a minimum in convective activity in the late morning.

It is anticipated that the results of this chapter would be of interest to developers of future forecasting models and would improve convective parametrizations. The main implications of the results show that models need to be able to resolve and correctly simulate the nocturnal low-level jet and resulting large-scale convergence in order to get the organisation and persistence of convection overnight. In addition, convective parametrizations need to be able to consider convergence and trigger convection from above the surface layer if the nocturnal rainfall is to be captured. Future studies

may focus on a different geographical area that is characterised by a nocturnal maximum in convective rainfall and use results of this study to find similarities or differences in mechanisms supporting that diurnal cycle in convection.

## Chapter 6

### Conclusions

This thesis has deepened our knowledge of processes controlling the organization and diurnal cycle of convection in the West-African Sahel. Observed data obtained during the West African Monsoon of 2006 by the AMMA field campaign were used. Because the monsoon season of 2006 can be taken as representative of the long term average (Janicot *et al.*, 2006), the results can be generalised to other monsoon seasons as well. Observational data and results were supplemented by convection-permitting simulations where observations were not available or representative enough, for the purpose of investigating environmental and convection-related processes, which control the evolution of deep moist convection. This was performed by studying properties of cold pools and the dynamics of Mesoscale Convective Systems both on a case-study base as well as by compositing around many events. Some of the results have been used to evaluate existing simulations, which has been done in Chapter 3 for cold pools or partly in Chapter 4 for a structure of a MCS and its environment. Evaluating simulations and describing issues in simulations helps to identify areas of bias and leads to improvement in simulating deep moist convection. This may lead to improved understanding of errors in forecasts, and so ultimately improvements in forecasts in the future.

Before this study it was known that cold pools were an important component of Sahelian MCSs, but there existed no systematic survey of their properties. In Chapter 3 data obtained at Niamey during AMMA were used to present an observational characterization of cold-pool properties in the West African Sahel using an approach based on Engerer *et al.* (2008). Observed cold pools are associated with temperature drops and pressure increases, which are shown to be similar to those observed in the USA with some stronger events in the USA (compared to Engerer *et al.*, 2008), but this was not found to be statistically significant due to small sample size. Cold pool airmasses are normally drier than the environment at the surface, which is because cold pools originate in the drier mid-levels, except in the pre-monsoon sub-period when they are often moister than the environment. A novel technique using Fractional Evaporation Energy Deficit (FEED) and Departure from Moist Adiabats (DMA) in a simple 1D model has shown that drier mid-levels tend to lead to drier descents of air feeding the cold pool. In

the pre-monsoon period, mid-levels were drier than later in the season. This resulted in driest pre-monsoon cold pools, but relative to the environment, pre-monsoon cold pools were actually moister. This was attributed to a much drier and deeper boundary layer in the pre-monsoon period, which appeared to provide the source airmass for cold pools, since cold pools in this sub-period had the same equivalent potential temperature as the pre-cold-pool environment. The difference between the environmental and cold-pool airmass was hence only the fact that precipitation had evaporated into the cold-pool airmass. Cold pools were often associated with strong wind gusts. These were attributed to both mixing of momentum from strong easterly winds at mid-levels in the African Easterly Jet to the surface by the convective downdrafts as well as to the pressure perturbation associated with the cold pool. Cold-pool related surface wind gusts were stronger during the pre-monsoon period, although this was not statistically significant, except above the surface at 950 hPa. In addition, magnitudes of cold-pool related changes in temperature and pressure were also greater in the pre-monsoon period. This was attributed to the drier mid-levels early in the season. It was concluded that the role of cold pools changes throughout the season and this has implications on the overall role of deep moist convection on the Monsoon. Cold pools bring moisture northwards into the Sahel early in the season and are hence an important part of the West African Monsoon flow, ventilating the Saharan Heat Low: the cold-pool airmass, being moister, may get recycled by convection on subsequent days. Cold pools are however also important later in the season when they force convection mechanically at their boundaries. Overall, cold pools are integral for the organization of MCSs, which themselves are an important part of the West African monsoon.

The objective to evaluate convection-permitting simulations was addressed in Chapter 3, where cold pools simulated by convection-permitting Unified Model simulations performed as part of the *Cascade* project were evaluated and weaknesses in simulated cold pools and resulting errors were identified. The main conclusions are that *Cascade* is able to simulate cold pools that are colder than environment and associated with the properties as observed cold pools (e.g. pressure increase). The magnitudes of these properties in *Cascade* are, however, generally weaker than those observed. Simulated cold pools are associated with lower magnitudes of surface pressure, temperature and moisture changes as well as weaker near-surface wind gusts and wind increases than observed cold pools with the underestimation of winds being the most severe. The

underestimation is much reduced at the 950 hPa level, suggesting too much surface friction in *Cascade*. These weaker simulated cold-pool related winds at the surface are expected to lead to an underestimation of dust uplift (e.g. in Marsham et al. 2011 and Heinold et al. 2013). *Cascade* captures the seasonality of cold pools to some degree.

The structure of Sahelian MCSs and the processes controlling them was further investigated in Chapter 4. Here, two case studies of squall-line MCSs associated with cold pool passages at Niamey are studied in detail in Chapter 4. This has expanded the existing case-study oriented literature of squall-line MCS studies in West Africa (e.g. Barthe, *et al.*, 2010; Chong, 2010; Schwendike *et al.*, 2010; Taylor *et al.*, 2010; Guy, *et al.*, 2011; Lothon, *et al.* 2011). The first of the case studies here was a classic mature squall-line crossing Niamey while the second was a squall-line just missing Niamey but with its cold pool crossing Niamey and being followed by a more isolated complex of convective cells related to the main squall-line MCS. Both MCSs propagated at a similar speed or faster than the environmental wind, a result of initiation of new cells ahead and their subsequent merging with the squall-line. This was more prominent in the first case. The structure of these squall-line MCSs revealed the presence of a low-level jet ahead of both systems, which was lifted above the first cold pool in the second case study, where it persisted until midday, which is approximately four hours longer than usual, and fed the second complex of convective cells. The low-level jet was then feeding the convective parts on the front side of the MCSs, continuing into the rear parts as a front-to-rear jet. Both MCSs were driven westwards by easterly winds related to the African Easterly Jet, which were transported downwards (and intensified in the first case) as a Rear Inflow Jet. The cold pool airmass was drier than the environment in both cases with the driest parts being ahead of precipitation with precipitation eventually moistening the cold-pool airmass, which was spreading rearwards relative to the system. A bore or a wave was likely present ahead of the midday cold pool of the second case, a result of the midday cold pool exciting the wave on the persisting morning cold pool, which then acted as a waveguide. Regions of descent were observed with both MCSs, resulting in classic “onion shaped” profiles (Zipser, 1977) behind. The system-relative rearward spreading cold-pool airmass was getting moister under the areas of precipitation, forming a shallow (<50 hPa) cool and moist layer near the surface. The observational results obtained in Chapter 4 could be used for future model evaluation. This has been started in section 4.3.3.

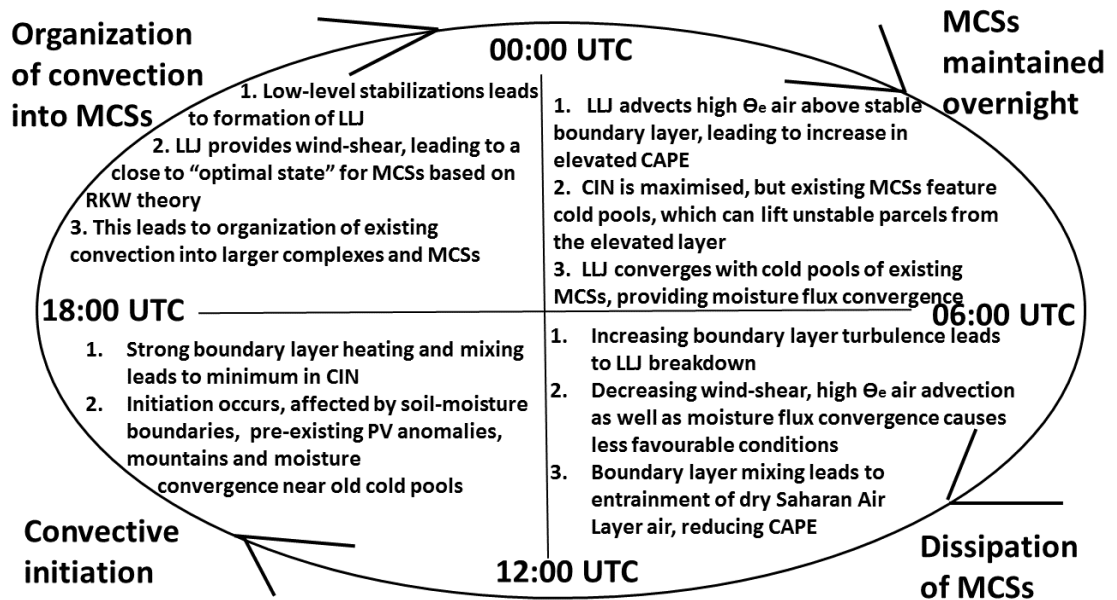


**Figure 6.1:** A conceptual model of the identified processes and their importance for the observed diurnal cycle of deep moist convection in the West African Sahel.

The objective to improve our understanding of the interaction of deep moist convection with its environment and how it changes during a diurnal cycle was addressed in Chapter 5, where processes responsible for the observed diurnal cycle of convection (e.g. Janiga *et al.*, 2009) are investigated. Figure 6.1 shows the processes, which have been identified as controlling the diurnal cycle of deep moist convection, which features a maximum in convective activity overnight with a minimum between late morning and early afternoon. A maximum in convective initiations occurs in the late afternoon as a result of the diurnal minimum in CIN at this time, which makes it easier for parcels to reach the level of free convection, resulting in an increase in convective activity. This is despite the diurnal minimum in CAPE, which is, however, still sufficient for convection. Overnight, CIN increases due to low-level cooling. Increasing CIN is not favorable for new convective initiations, but existing convection, the majority of which has organized into MCSs by this time, features cold pools that provide forcing to lift parcels to their level of free convection through the inhibition, maintaining existing convection. Conditions for these existing MCSs become more favorable overnight as elevated CAPE increases due to advection of moister high equivalent potential temperature air by the nocturnal low-level jet. The low-level jet also provides wind-shear in the

lowest ~2 km, which according to the RKW theory results in a near “optimal state” for cold-pool driven squall-line MCSs. The most optimal state in the Sahel occurs in the early morning based on RKW criteria. The importance of the low-level jet is not limited to advection of high equivalent potential temperature air and wind shear as it also creates moisture flux convergence with existing cold pools. This moisture convergence is maximized overnight at the jet-level, showing that the low-level jet is the dominant factor in providing moisture to MCSs overnight. The breakdown of the low-level jet in the morning hours results in less favorable conditions for maintenance of MCSs. This is because wind shear weakens, resulting in less optimal state for MCSs according to RKW theory. In addition, advection of high equivalent potential temperature monsoon air vanishes resulting in weakening elevated CAPE and moisture flux convergence decreases rapidly. The MCSs, which have persisted overnight now weaken or eventually dissipate as a result. The results of Chapter 5 show that the low-level jet and its interaction with existing cold pools and MCSs is important for the sustaining of MCSs overnight. This meets the aim to identify difficulties that prevent us from predicting convection successfully. Forecasting models generally miss this overnight maximum in convective activity, which is at least partly a result of their struggle with simulating processes such as the nocturnal low-level jet and the stable layer correctly, or their interaction with moist convection. Therefore, forecasting models need to capture the low-level jet and resulting elevated convergence correctly if they are to simulate the sustaining MCSs overnight.

Afternoon convective initiations were found to be forced mainly by local circulations resulting from soil-moisture boundaries or sometimes old cold-pool boundaries. Overnight, when the number of convective initiations is significantly lower, the role of soil-moisture or old boundaries become less pronounced and the dominant process leading to convective initiations is less clear. Dynamically forced initiations due to convergence of the cold pool with the low-level jet may be far more important overnight. The role of pre-existing PV anomalies, created by previous convection, may also play an important role and the results suggest that the role of PV anomalies would be more dominant in the afternoon. Only two cases, where the PV anomaly was likely responsible for secondary initiation, were found and these demonstrate that PV anomalies can, at least partly, influence future convective initiations over West Africa, but their relative importance when compared with other factors may be low. Further research is, however, needed to make any more definite conclusions regarding these.

Overall, the results of this thesis show that a large variety of processes controls the evolution of deep moist convection in West African Sahel. The diurnal cycle of convection observed can be explained using existing observations, but there are still features that require future study. The environment in West Africa is similar to environments observed in other parts of the world, where squall-line MCSs are a frequent occurrence. There are, however, certain features that are unique to West Africa (e.g. African Easterly Jet, Saharan Air Layer, the Saharan Heat Low and related low-level jet as well as local topography, which is unique in all regions). These show the importance to focus on this region separately and compare similarities and difference between convective features observed here and elsewhere. Feedbacks of convection on the environment are important in the Sahel, for example early in the season, when cold pools help to transport moisture northwards and form hence part of the monsoon. The observations obtained and presented here highlight the areas where current forecasting models and simulations struggle. An example is that observed cold pools are stronger than those simulated and this may have further effects in the simulation, such as reduced progression of the monsoon or lower dust uplift. The results of this thesis may be used as a guidance for future model developers to improve parametrizations. Regarding improvements of the diurnal cycle of precipitation, the features to focus on are the ability of models to simulate the nocturnal low-level jet correctly, its related convergence with existing cold pools as well as correct simulation of convective initiations from the jet level.

## 6.1 Future work

This study has utilized a vast amount of data that has been obtained during the AMMA field campaign in Niamey in 2006 to study processes controlling the evolution of deep moist convection in West-African Sahel. Further work may be done by using existing *Cascade* simulations to understand processes that are missed by observational data due to their small size or short duration. Also, discrepancies such as the generally weaker cold pools in *Cascade* can be further explored. The cause can be related to issues with model microphysics, dynamics of MCSs or even smaller MCS size in *Cascade*. This can be done by studying the origin of air feeding the cold pool in greater detail as an extension of the 1D model used in section 3.1.3 for observations to compare FEED, mid-level dryness and decrease of temperature associated with a cold pool. Existing *Cascade*

simulations or some other high-resolution simulation may be used to do this. Instead of using a pre-storm sounding and an assumption that the airmass does not change considerably ahead of the MCS (as was done in section 3.1.3), the use of tracers in the simulation sourced from the evaporation/melting/sublimation layer could identify the source airmass for cold pools, the nature and location of which could hint at processes that lead to cold-pool formation. Rather than averaging values of mid-level dryness (wet-bulb potential temperature depression) in a specified layer (like in section 3.1.3), exact values of mid-level dryness of the source parcel could be compared with the temperature decrease resulting from the cold pool formed by that source parcel. This method would provide more precise values and would better reveal the relationship between the dryness of the source parcel and the strength of the cold pool (decrease of temperature with respect to the environment).

The size of MCSs in simulations can be compared to observed cases, but some criteria would be needed to specify the exact method of determining the MCS size. For the purpose of cold-pool intensity, the evaporation of precipitation is the important factor and hence the size of precipitation can be compared both in simulations and in observations. This may be done on a case-by-case study (to compare given cold pools and MCSs both in observations and simulations) or as an overall relationship (to see if there is a relationship between MCS size and cold pool intensity and if this differs between observations and simulations). Since radar coverage in West Africa is sparse, some other method for obtaining MCS-related precipitation would be needed, such as retrievals from satellite data.

Further research on these lines could also be done for observations. Data from radiosondes or the radiometer (which provides data up to 4 km above ground) could be used to explore the role of the boundary layer, free troposphere and wind shear in cold pool intensity. A starting point would be looking at mean mid-level wet-bulb potential temperature depressions for the three sub-periods of the monsoon season of 2006 (Pre-monsoon, Monsoon and Retreat). This may be done as an average for all soundings by sub-periods (to see the mean mid-level dryness sub-seasonally), or additionally an average of all pre-storm soundings (see if mid-level dryness is different in the vicinity of MCSs – e.g. related to large scale subsidence). Radiometer data could be used to explore the role of boundary layer stratification and cold-pool related cooling. Boundary layer tends to be super-adiabatic in the late afternoon and features a stable near-surface layer at night. Therefore,

cold-pool related cooling would be overestimated during the afternoon and underestimated at night. A better approach for calculating cold-pool related cooling would be taking either the average potential temperature of the whole boundary layer, or the potential temperature of the top of the boundary layer, which is least likely to be affected by surface sensible heat fluxes, and comparing it with the potential temperature of the cold pool. The role of wind-shear can be explored as well, either by the use of radiosondes or the radar wind profiler. This may be done either as mean wind-shear sub-seasonally (to see e.g. if stronger wind gust in the Pre-monsoon period might be due to stronger wind-shear), or for every event as a comparison with other cold-pool characteristics. Every cold pool with unusual anomalies (such as mean wind decrease, rather than increase, which is expected) could also be explored in more detail using Radar Wind Profiler and Radiometer to find a cause of that anomaly (e.g. stable layer that inhibited cold-pool related winds). Alternatively, idealized simulations could be used to test the role of shear and its interactions with the moist convection.

The AMMA field campaign provided a high density, high frequency data in the location of the supersite at Niamey. While this was sufficient for observations of details in the general West African monsoon circulation on the synoptic scale, higher density data would be needed to explore the dynamical features of the observed MCSs on meso-beta scale in great detail and with precision. An example would be more radiosondes through a squall-line MCS with a frequency similar to that of the study by Bryan and Parker, (2010). Such radiosonde releases would have to be concentrated around a squall-line MCS passage, having hourly frequency or greater and starting 3-4 hours before the expected passage and ending 1-2 hours after the passage. These would enable obtaining a much greater amount of details of the MCS structure and its environment. If no field campaigns that would provide such data occur in the near future, there is still a great amount of data that has been collected during AMMA and which includes squall-line MCSs that have not been used as case studies. A study on the lines of Chapter 4 of this thesis, but using a composite squall-line of all 38 squall-line MCSs detected, could highlight more features that would not be possible to obtain by studying two cases only. In addition, the use of data from Doppler radar would provide more information about the internal dynamics of MCSs.

Future research may also perform a similar study of cases, such as those presented in Chapter 4, using more of the existing data that is available on the 38 squall-line MCSs observed in Niamey. In addition, data

from more geographical locations than that of Niamey can be utilized. High frequency data obtained by surface stations in various regions could be used to characterize cold pool properties and make a more representative sample from the Sahel by using more locations than Niamey. If radar data could be provided in the other locations, this would enable comparison of the vertical MCS structure across the locations.

Regarding future work using UM (*Cascade*) data, more can be done regarding the environmental state of convective initiations. The composite rainfall rate around locations of initiation would provide more information about where new storms initiate with respect to previous convection, which could further hint on the processes that lead to initiations. The study of the importance of pre-existing PV anomalies can also be significantly broadened using the existing *Cascade* data if the PV anomalies could be traced. A much greater in-depth study of the Birch *et al.* (2014) case can be performed using existing data by comparing cross-sections at various latitudes and times, similar to the preliminary study in section 4.3.3. More such cases can be simulated to be compared with existing studies, or simply more cases can be identified in the existing *Cascade* simulation and these may be studied more in-depth either on a case-by-case basis or using a *Cascade* composite MCS.

## References

- Adams, D.K.; Souza, E.P. CAPE and Convective Events in the Southwest during the North American Monsoon. *Mon Weather Rev.* 137:83-98; 2009
- Addis, R.P. A Numerical-Model of Surface Outflows from Convective Storms. *Bound-Lay Meteorol.* 28:121-160; 1984
- Adler, B.; Kalthoff, N.; Gantner, L. The impact of soil moisture inhomogeneities on the modification of a mesoscale convective system: An idealised model study. *Atmos Res.* 101:354-372; 2011
- Agusti-Panareda, A.; Beljaars, A.; Cardinali, C.; Genkova, I.; Thorncroft, C. Impacts of Assimilating AMMA Soundings on ECMWF Analyses and Forecasts. *Weather Forecast.* 25:1142-1160; 2010
- Alonge, C.J.; Mohr, K.I.; Tao, W.K. Numerical studies of wet versus dry soil regimes in the West African Sahel. *J Hydrometeorol.* 8:102-116; 2007
- Anabor, V. Serial Upstream-Propagating Mesoscale Convective System Events over Southeastern South America (vol 136, pg 3087, 2008). *Mon Weather Rev.* 137:2408-2409; 2009
- Anthes, R.A. Enhancement of Convective Precipitation by Mesoscale Variations in Vegetative Covering in Semiarid Regions. *J Clim Appl Meteorol.* 23:541-554; 1984
- Arakawa, A.; Schubert, W.H. Interaction of a Cumulus Cloud Ensemble with Large-Scale Environment .1. *J Atmos Sci.* 31:674-701; 1974
- Aspliden, C.I.; Tourre, Y.; Sabine, J.B. Some Climatological Aspects of West-African Disturbance Lines during Gate. *Mon Weather Rev.* 104:1029-1035; 1976
- Bain, C.L.; Parker, D.J.; Dixon, N.; Fink, A.H.; Taylor, C.M.; Brooks, B.; Milton, S.F. Anatomy of an observed African easterly wave in July 2006. *Q J Roy Meteor Soc.* 137:923-933; 2011
- Barnes, G.M.; Sieckman, K. The Environment of Fast-Moving and Slow-Moving Tropical Mesoscale Convective Cloud Lines. *Mon Weather Rev.* 112:1782-1794; 1984
- Barthe, C.; Asencio, N.; Lafore, J.P.; Chong, M.; Campistron, B.; Cazenave, F. Multi-scale analysis of the 25-27 July 2006 convective period over Niamey: Comparison between Doppler radar observations and simulations. *Q J Roy Meteor Soc.* 136:190-208; 2010
- Barthe, C.; Deierling, W.; Barth, M.C. Estimation of total lightning from various storm parameters: A cloud-resolving model study. *J Geophys Res-Atmos.* 115; 2010
- Barthlott, C.; Corsmeier, U.; Meissner, C.; Braun, F.; Kottmeier, C. The influence of mesoscale circulation systems on triggering convective cells over complex terrain. *Atmos Res.* 81:150-175; 2006
- Bechtold, P.; Chaboureaud, J.P.; Beljaars, A.; Betts, A.K.; Kohler, M.; Miller, M.; Redelsperger, J.L. The simulation of the diurnal cycle of convective precipitation over land in a global model. *Q J Roy Meteor Soc.* 130:3119-3137; 2004
- Benjamin, T.B. Gravity Currents and Related Phenomena. *J Fluid Mech.* 31:209-&; 1968
- Berry, G.J.; Thorncroft, C. Case study of an intense African easterly wave.

- Mon Weather Rev. 133:752-766; 2005
- Berthier, S.; Chazette, P.; Couvert, P.; Pelon, J.; Dulac, F.; Thieuleux, F.; Moulin, C.; Pain, T. Desert dust aerosol columnar properties over ocean and continental Africa from Lidar in-Space Technology Experiment (LITE) and Meteosat synergy. *J Geophys Res-Atmos.* 111; 2006
- Biggerstaff, M.I.; Houze, R.A. Kinematics and Microphysics of the Transition Zone of the 10-11 June 1985 Squall Line. *J Atmos Sci.* 50:3091-3110; 1993
- Birch, C.E.; Parker, D.J.; Marsham, J.H.; Copsey, D.; Garcia-Carreras, L. A seamless assessment of the role of convection in the water cycle of the West African Monsoon. *J Geophys Res-Atmos.* 119:2890-2912; 2014
- Birch, C.E.; Parker, D.J.; O'Leary, A.; Marsham, J.H.; Taylor, C.M.; Harris, P.P.; Lister, G.M.S. Impact of soil moisture and convectively generated waves on the initiation of a West African mesoscale convective system. *Q J Roy Meteor Soc.* 139:1712-1730; 2013
- Bounoua, L.; Krishnamurti, T.N. Thermodynamic Budget of the 5 Day Wave over the Saharan Desert during Summer. *Meteorol Atmos Phys.* 47:1-25; 1991
- Braun, S.A.; Houze, R.A. The heat and potential vorticity budgets of a midlatitude squall line. *Sixth Conference on Mesoscale Processes*:335-338; 1994
- Braun, S.A.; Houze, R.A. The Transition Zone and Secondary Maximum of Radar Reflectivity Behind a Midlatitude Squall Line - Results Retrieved from Doppler Radar Data. *J Atmos Sci.* 51:2733-2755; 1994
- Bretherton, C.S.; Smolarkiewicz, P.K. Gravity-Waves, Compensating Subsidence and Detrainment around Cumulus Clouds. *J Atmos Sci.* 46:740-759; 1989
- Brown, R.G.; Zhang, C.D. Variability of midtropospheric moisture and its effect on cloud-top height distribution during TOGA COARE. *J Atmos Sci.* 54:2760-2774; 1997
- Bryan, G.H.; Fritsch, J.M. Discrete propagation of surface fronts in a convective environment: Observations and theory. *J Atmos Sci.* 57:2041-2060; 2000
- Bryan, G.H.; Knievel, J.C.; Parker, M.D. A multimodel assessment of RKW theory's relevance to squall-line characteristics. *Mon Weather Rev.* 134:2772-2792; 2006
- Bryan, G.H.; Morrison, H. Sensitivity of a Simulated Squall Line to Horizontal Resolution and Parameterization of Microphysics. *Mon Weather Rev.* 140:202-225; 2012
- Bryan, G.H.; Parker, M.D. Observations of a Squall Line and Its Near Environment Using High-Frequency Rawinsonde Launches during VORTEX2. *Mon Weather Rev.* 138:4076-4097; 2010
- Burpee, R.W. Origin and Structure of Easterly Waves in Lower Troposphere of North Africa. *J Atmos Sci.* 29:77-&; 1972
- Byers, H.R. Structure and Dynamics of the Thunderstorm. *Science.* 109:437-437; 1949
- Carleton, A.M.; Adegoke, J.; Allard, J.; Arnold, D.L.; Travis, D.J. Summer season land cover - convective cloud associations for the Midwest US

- "Corn Belt". *Geophys Res Lett.* 28:1679-1682; 2001
- Charba, J. Application of Gravity Current Model to Analysis of Squall-Line Gust Front. *Mon Weather Rev.* 102:140-156; 1974
- Charney, J.; Stone, P.H.; Quirk, W.J. Drought in Sahara - Biogeophysical Feedback Mechanism. *Science.* 187:434-435; 1975
- Chen, F.; Avissar, R. Impact of Land-Surface Moisture Variability on Local Shallow Convective Cumulus and Precipitation in Large-Scale Models. *J Appl Meteorol.* 33:1382-1401; 1994
- Chen, T.C.; Wang, S.Y.; Clark, A.J. North Atlantic Hurricanes Contributed by African Easterly Waves North and South of the African Easterly Jet. *J Climate.* 21:6767-6776; 2008
- Chong, M. The 11 August 2006 squall-line system as observed from MIT Doppler radar during the AMMA SOP. *Q J Roy Meteor Soc.* 136:209-226; 2010
- Chronis, T.G.; Williams, E.; Anagnostou, E.N. Evidence of tropical forcing of the 6.5-day wave from lightning observations over Africa. *J Atmos Sci.* 64:3717-3721; 2007
- Clark, D.B.; Taylor, C.M.; Thorpe, A.J. Feedback between the land surface and rainfall at convective length scales. *J Hydrometeorol.* 5:625-639; 2004
- Clark, D.B.; Taylor, C.M.; Thorpe, A.J.; Harding, R.J.; Nicholls, M.E. The influence of spatial variability of boundary-layer moisture on tropical continental squall lines. *Q J Roy Meteor Soc.* 129:1101-1121; 2003
- Comer, R.E.; Slingo, A.; Allan, R.P. Observations of the diurnal cycle of outgoing longwave radiation from the Geostationary Earth Radiation Budget instrument. *Geophys Res Lett.* 34; 2007
- Coniglio, M.C.; Hwang, J.Y.; Stensrud, D.J. Environmental Factors in the Upscale Growth and Longevity of MCSs Derived from Rapid Update Cycle Analyses. *Mon Weather Rev.* 138:3514-3539; 2010
- Cook, K.H. Generation of the African easterly jet and its role in determining West African precipitation. *J Climate.* 12:1165-1184; 1999
- Cooper, H.J.; Garstang, M.; Simpson, J. The Diurnal Interaction between Convection and Peninsular-Scale Forcing over South Florida. *Mon Weather Rev.* 110:486-503; 1982
- Cornforth, R.J.; Hoskins, B.J.; Thorncroft, C.D. The impact of moist processes on the African Easterly Jet-African Easterly Wave system. *Q J Roy Meteor Soc.* 135:894-913; 2009
- Correia, J.; Arritt, R.W. Thermodynamic Properties of Mesoscale Convective Systems Observed during BAMEX. *Mon Weather Rev.* 136:4242-4271; 2008
- Couvreux, F.; Guichard, F.; Austin, P.H.; Chen, F. Nature of the Mesoscale Boundary Layer Height and Water Vapor Variability Observed 14 June 2002 during the IHOP\_2002 Campaign. *Mon Weather Rev.* 137:414-432; 2009
- Cram, J.M.; Pielke, R.A.; Cotton, W.R. Numerical-Simulation and Analysis of a Prefrontal Squall Line .2. Propagation of the Squall Line as an Internal Gravity-Wave. *J Atmos Sci.* 49:209-225; 1992
- Crook, N.A.; Miller, M.J. A Numerical and Analytical Study of Atmospheric Undular Bores. *Q J Roy Meteor Soc.* 111:225-242; 1985
- Dai, A. Precipitation characteristics in eighteen coupled climate models. *J Climate.* 19:4605-4630; 2006

- Dai, A.; Trenberth, K.E. The diurnal cycle and its depiction in the Community Climate System Model. *J Climate*. 17:930-951; 2004
- D'Amato, N.; Lebel, T. On the characteristics of the rainfall events in the Sahel with a view to the analysis of climatic variability. *Int J Climatol*. 18:955-974; 1998
- Davies, T.; Cullen, M.J.P.; Malcolm, A.J.; Mawson, M.H.; Staniforth, A.; White, A.A.; Wood, N. A new dynamical core for the Met Office's global and regional modelling of the atmosphere. *Q J Roy Meteor Soc*. 131:1759-1782; 2005
- Davis, C.A.; Manning, K.W.; Carbone, R.E.; Trier, S.B.; Tuttle, J.D. Coherence of warm-season continental rainfall in numerical weather prediction models. *Mon Weather Rev*. 131:2667-2679; 2003
- Derbyshire, S.H.; Beau, I.; Bechtold, P.; Grandpeix, J.Y.; Piriou, J.M.; Redelsperger, J.L.; Soares, P.M.M. Sensitivity of moist convection to environmental humidity. *Q J Roy Meteor Soc*. 130:3055-3079; 2004
- Dhonneur, G. Study of a Line Squall in Niger Bend. *B Am Meteorol Soc*. 54:1075-1075; 1973
- Diatta, S.; Hourdin, F.; Gaye, A.T.; Viltard, N. Comparison of Rainfall Profiles in the West African Monsoon as Depicted by TRMM PR and the LMDZ Climate Model. *Mon Weather Rev*. 138:1767-1777; 2010
- Diedhiou, A.; Janicot, S.; Viltard, A.; de Felice, P.; Laurent, H. Easterly wave regimes and associated convection over West Africa and tropical Atlantic: results from the NCEP/NCAR and ECMWF reanalyses. *Clim Dynam*. 15:795-822; 1999
- Dione, C.; Lothon, M.; Badiane, D.; Campistron, B.; Couvreur, F.; Guichard, F.; Sall, S.M. Phenomenology of Sahelian convection observed in Niamey during the early monsoon. *Q J Roy Meteor Soc*. 140:500-516; 2014
- Diongue, A.; Lafore, J.P.; Redelsperger, J.L.; Roca, R. Numerical study of a Sahelian synoptic weather system: Initiation and mature stages of convection and its interactions with the large-scale dynamics. *Q J Roy Meteor Soc*. 128:1899-1927; 2002
- Dirmeyer, P.A.; Cash, B.A.; Kinter, J.L.; Jung, T.; Marx, L.; Satoh, M.; Stan, C.; Tomita, H.; Towers, P.; Wedi, N.; Achuthavarier, D.; Adams, J.M.; Altshuler, E.L.; Huang, B.H.; Jin, E.K.; Manganello, J. Simulating the diurnal cycle of rainfall in global climate models: resolution versus parameterization. *Clim Dynam*. 39:399-418; 2012
- Dixon, N.S.; Parker, D.J.; Taylor, C.M.; Garcia-Carreras, L.; Harris, P.P.; Marsham, J.H.; Polcher, J.; Woolley, A. The effect of background wind on mesoscale circulations above variable soil moisture in the Sahel. *Q J Roy Meteor Soc*. 139:1009-1024; 2013
- Drobinski, P.; Sultan, B.; Janicot, S. Role of the Hoggar massif in the West African monsoon onset. *Geophys Res Lett*. 32; 2005
- Droegemeier, K.K.; Wilhelmson, R.B. 3-Dimensional Numerical Modeling of Convection Produced by Interacting Thunderstorm Outflows .1. Control Simulation and Low-Level Moisture Variations. *J Atmos Sci*. 42:2381-2403; 1985
- Droegemeier, K.K.; Wilhelmson, R.B. 3-Dimensional Numerical Modeling of Convection Produced by Interacting Thunderstorm Outflows .2. Variations in Vertical Wind Shear. *J Atmos Sci*. 42:2404-2414; 1985
- Druyan, L.M.; Hastenrath, S. Modeling the Differential Impact of 1984 and

- 1950 Sea-Surface Temperatures on Sahel Rainfall. *Int J Climatol.* 11:367-380; 1991
- Ducrocq, V.; Lafore, J.P.; Redelsperger, J.L. An attempt of initialization of a cloud resolving model for the prediction of convective systems. 19th Conference on Severe Local Storms:352-355; 1998
- Duvel, J.P. Convection over Tropical Africa and the Atlantic-Ocean during Northern Summer .1. Interannual and Diurnal-Variations. *Mon Weather Rev.* 117:2782-2799; 1989
- Duvel, J.P. Convection over Tropical Africa and the Atlantic-Ocean during Northern Summer .2. Modulation by Easterly Waves. *Mon Weather Rev.* 118:1855-1868; 1990
- Ek, M.B.; Holtslag, A.A.M. Influence of soil moisture on boundary layer cloud development. *J Hydrometeorol.* 5:86-99; 2004
- Eldridge, R.H. A Synoptic Study of West African Disturbance Lines. *Q J Roy Meteor Soc.* 83:303-314; 1957
- Emori, S. The interaction of cumulus convection with soil moisture distribution: An idealized simulation. *J Geophys Res-Atmos.* 103:8873-8884; 1998
- Engerer, N.A.; Stensrud, D.J.; Coniglio, M.C. Surface Characteristics of Observed Cold Pools. *Mon Weather Rev.* 136:4839-4849; 2008
- Essery, R.; Pomeroy, J. Sublimation of snow intercepted by coniferous forest canopies in a climate model. *Int J Climatol.* 21:343-347; 2001
- Faccani, C.; Rabier, F.; Fourrie, N.; Agusti-Panareda, A.; Karbou, F.; Moll, P.; Lafore, J.P.; Nuret, M.; Hdidou, F.; Bock, O. The Impacts of AMMA Radiosonde Data on the French Global Assimilation and Forecast System. *Weather Forecast.* 24:1268-1286; 2009
- Ferreira, R.N.; Rickenbach, T.; Guy, N.; Williams, E. Radar Observations of Convective System Variability in Relationship to African Easterly Waves during the 2006 AMMA Special Observing Period. *Mon Weather Rev.* 137:4136-4150; 2009
- Fink, A.H.; Reiner, A. Spatiotemporal variability of the relation between African Easterly Waves and West African Squall Lines in 1998 and 1999. *J Geophys Res-Atmos.* 108; 2003
- Fink, A.H.; Vincent, D.G.; Ermert, V. Rainfall types in the West African Sudanian zone during the summer monsoon 2002. *Mon Weather Rev.* 134:2143-2164; 2006
- Flamant, C.; Chaboureaud, J.P.; Parker, D.J.; Taylor, C.A.; Cammas, J.P.; Bock, O.; Timouk, F.; Pelon, J. Airborne observations of the impact of a convective system on the planetary boundary layer thermodynamics and aerosol distribution in the inter-tropical discontinuity region of the West African Monsoon. *Q J Roy Meteor Soc.* 133:1175-1189; 2007
- Folkens, I.; Mitovski, T.; Pierce, J.R. A simple way to improve the diurnal cycle in convective rainfall over land in climate models. *J Geophys Res-Atmos.* 119:2113-2130; 2014
- Fortune, M. Properties of African Squall Lines Inferred from Time-Lapse Satellite Imagery. *Mon Weather Rev.* 108:153-168; 1980
- Fovell, R.G.; Ogura, Y. Effect of Vertical Wind Shear on Numerically Simulated Multicell Storm Structure. *J Atmos Sci.* 46:3144-3176; 1989
- Fovell, R.G.; Tan, P.H. The temporal behavior of numerically simulated multicell-type storms. Part II: The convective cell life cycle and cell regeneration. *Mon Weather Rev.* 126:551-577; 1998

- Gantner, L.; Kalthoff, N. Sensitivity of a modelled life cycle of a mesoscale convective system to soil conditions over West Africa. *Q J Roy Meteor Soc.* 136:471-482; 2010
- Garcia-Carreras, L.; Marsham, J.H.; Parker, D.J.; Bain, C.L.; Milton, S.; Saci, A.; Salah-Ferroudj, M.; Ouchene, B.; Washington, R. The impact of convective cold pool outflows on model biases in the Sahara. *Geophys Res Lett.* 40:1647-1652; 2013
- Garcia-Carreras, L.; Parker, D.J.; Marsham, J.H. What is the Mechanism for the Modification of Convective Cloud Distributions by Land Surface-Induced Flows? *J Atmos Sci.* 68:619-634; 2011
- Gash, J.H.C.; Kabat, P.; Monteny, B.A.; Amadou, M.; Bessemoulin, P.; Billing, H.; Blyth, E.M.; deBruin, H.A.R.; Elbers, J.A.; Friborg, T.; Harrison, G.; Holwill, C.J.; Lloyd, C.R.; Lhomme, J.P.; Moncrieff, J.B.; Puech, D.; Soegaard, H.; Taupin, J.D.; Tuzet, A.; Verhoef, A. The variability of evaporation during the HAPEX-Sahel intensive observation period. *J Hydrol.* 189:385-399; 1997
- Geotis, S.G. Comparison of Reflectivity Measurements by Radar and by Disdrometer. *J Appl Meteorol.* 17:1403-1405; 1978
- Giangrande, S.E.; Luke, E.P.; Kollias, P. Characterization of Vertical Velocity and Drop Size Distribution Parameters in Widespread Precipitation at ARM Facilities. *J Appl Meteorol Clim.* 51:380-391; 2012
- Giannini, A.; Saravanan, R.; Chang, P. Oceanic forcing of Sahel rainfall on interannual to interdecadal time scales. *Science.* 302:1027-1030; 2003
- Gilmore, M.S.; Wicker, L.J. The Influence of midtropospheric dryness on supercell morphology and evolution. *Mon Weather Rev.* 126:943-958; 1998
- Grandpeix, J.Y.; Lafore, J.P. A Density Current Parameterization Coupled with Emanuel's Convection Scheme. Part I: The Models. *J Atmos Sci.* 67:881-897; 2010
- Grandpeix, J.Y.; Lafore, J.P.; Cheruy, F. A Density Current Parameterization Coupled with Emanuel's Convection Scheme. Part II: 1D Simulations. *J Atmos Sci.* 67:898-922; 2010
- Gray, W.M.; Jacobson, R.W. Diurnal-Variation of Deep Cumulus Convection. *Mon Weather Rev.* 105:1171-1188; 1977
- Gregory, D.; Rowntree, P.R. A Mass Flux Convection Scheme with Representation of Cloud Ensemble Characteristics and Stability-Dependent Closure. *Mon Weather Rev.* 118:1483-1506; 1990
- Guichard, F.; Asencio, N.; Peugeot, C.; Bock, O.; Redelsperger, J.L.; Cui, X.F.; Garvert, M.; Lamptey, B.; Orlandi, E.; Sander, J.; Fierli, F.; Gaertner, M.A.; Jones, S.C.; Lafore, J.P.; Morse, A.; Nuret, M.; Boone, A.; Balsamo, G.; de Rosnay, P.; Decharme, B.; Harris, P.P.; Berges, J.C. An Intercomparison of Simulated Rainfall and Evapotranspiration Associated with a Mesoscale Convective System over West Africa. *Weather Forecast.* 25:37-60; 2010
- Guy, N.; Rutledge, S.A.; Cifelli, R. Radar characteristics of continental, coastal, and maritime convection observed during AMMA/NAMMA. *Q J Roy Meteor Soc.* 137:1241-1256; 2011
- Haase, S.P.; Smith, R.K. The Numerical-Simulation of Atmospheric Gravity Currents .1. Neutrally-Stable Environments. *Geophys Astro Fluid.* 46:1-33; 1989

- Haase, S.P.; Smith, R.K. The Numerical-Simulation of Atmospheric Gravity Currents .2. Environments with Stable Layers. *Geophys Astro Fluid.* 46:35-51; 1989
- Hajovsky, R.G.; Deam, A.P.; Lagrone, A.H. Radar Reflections from Insects in Lower Atmosphere. *Ieee T Antenn Propag.* Ap14:224-&; 1966
- Hamilton, R.A.; Archbold, J.W. Meteorology of Nigeria and Adjacent Territory. *Q J Roy Meteor Soc.* 71:231-&; 1945
- Hastenrath, S.; Lamb, P. Some Aspects of Circulation and Climate over Eastern Equatorial Atlantic. *Mon Weather Rev.* 105:1019-1023; 1977
- Heinold, B.; Knippertz, P.; Marsham, J.H.; Fiedler, S.; Dixon, N.S.; Schepanski, K.; Laurent, B.; Tegen, I. The role of deep convection and nocturnal low-level jets for dust emission in summertime West Africa: Estimates from convection-permitting simulations. *J Geophys Res-Atmos.* 118:4385-4400; 2013
- Hodges, K.I.; Thorncroft, C.D. Distribution and statistics of African mesoscale convective weather systems based on the ISCCP Meteosat imagery. *Mon Weather Rev.* 125:2821-2837; 1997
- Hohenegger, C.; Stevens, B. Preconditioning Deep Convection with Cumulus Congestus. *J Atmos Sci.* 70:448-464; 2013
- Hourdin, F.; Musat, I.; Guichard, F.; Ruti, P.M.; Favot, F.; Filiberti, M.A.; Pham, M.; Grandpeix, J.Y.; Polcher, J.; Marquet, P.; Boone, A.; Lafore, J.P.; Redelsperger, J.L.; Dell'aquila, A.; Doval, T.L.; Traore, A.K.; Gallee, H. Amma-Model Intercomparison Project. *B Am Meteorol Soc.* 91:95-+; 2010
- Houze, R.A. Gate Radar Observations of a Tropical Squall Line. *B Am Meteorol Soc.* 57:870-870; 1976
- Houze, R.A. Structure and Dynamics of a Tropical Squall-Line System. *Mon Weather Rev.* 105:1540-1567; 1977
- Houze, R.A. Observed Structure of Mesoscale Convective Systems and Implications for Large-Scale Heating. *Q J Roy Meteor Soc.* 115:425-461; 1989
- Houze, R.A. Mesoscale convective systems. *Rev Geophys.* 42; 2004
- Houze, R.A.; Betts, A.K. Convection in Gate. *Rev Geophys.* 19:541-576; 1981
- Houze, R.A.; Geotis, S.G.; Marks, F.D.; West, A.K. Winter Monsoon Convection in the Vicinity of North Borneo .1. Structure and Time-Variation of the Clouds and Precipitation. *Mon Weather Rev.* 109:1595-1614; 1981
- Hsieh, J.S.; Cook, K.H. Generation of African easterly wave disturbances: Relationship to the African easterly jet. *Mon Weather Rev.* 133:1311-1327; 2005
- Hsieh, J.S.; Cook, K.H. On the instability of the African easterly jet and the generation of African waves: Reversals of the potential vorticity gradient. *J Atmos Sci.* 65:2130-2151; 2008
- Janicot, S.; Thorncroft, C.D.; Ali, A.; Asencio, N.; Berry, G.; Bock, O.; Bourles, B.; Caniaux, G.; Chauvin, F.; Deme, A.; Kergoat, L.; Lafore, J.P.; Lavaysse, C.; Lebel, T.; Marticorena, B.; Mounier, F.; Nedelec, P.; Redelsperger, J.L.; Ravegnani, F.; Reeves, C.E.; Roca, R.; de Rosnay, P.; Schlager, H.; Sultan, B.; Tomasini, M.; Ulanovsky, A.; Team, A.F. Large-scale overview of the summer monsoon over West Africa during the AMMA field experiment in 2006. *Ann Geophys-*

- Germany. 26:2569-2595; 2008
- Janiga, M.A.; Thorncroft, C.D. Convection over Tropical Africa and the East Atlantic during the West African Monsoon: Regional and Diurnal Variability. *J Climate*. 27:4159-4188; 2014
- Johnson, B.C. The Heat Burst of 29 May 1976. *Mon Weather Rev*. 111:1776-1792; 1983
- Kalapureddy, M.C.R.; Lothon, M.; Campistron, B.; Lohou, F.; Said, F. Wind profiler analysis of the African Easterly Jet in relation with the boundary layer and the Saharan heat-low. *Q J Roy Meteor Soc*. 136:77-91; 2010
- Kalthoff, N.; Adler, B.; Barthlott, C.; Corsmeier, U.; Mobbs, S.; Crewell, S.; Traumner, K.; Kottmeier, C.; Wieser, A.; Smith, V.; Di Girolamo, P. The impact of convergence zones on the initiation of deep convection: A case study from COPS. *Atmos Res*. 93:680-694; 2009
- Karyampudi, V.M.; Palm, S.P.; Reagen, J.A.; Fang, H.; Grant, W.B.; Hoff, R.M.; Moulin, C.; Pierce, H.F.; Torres, O.; Browell, E.V.; Melfi, S.H. Validation of the Saharan dust plume conceptual model using lidar, Meteosat, and ECMWF data. *B Am Meteorol Soc*. 80:1045-1075; 1999
- Kiladis, G.N.; Thorncroft, C.D.; Hall, N.M.J. Three-dimensional structure and dynamics of African easterly waves. Part I: Observations. *J Atmos Sci*. 63:2212-2230; 2006
- Klemp, J.B. Dynamics of Tornadoic Thunderstorms. *Annu Rev Fluid Mech*. 19:369-402; 1987
- Knippertz, P.; Deutscher, C.; Kandler, K.; Muller, T.; Schulz, O.; Schutz, L. Dust mobilization due to density currents in the Atlas region: Observations from the Saharan Mineral Dust Experiment 2006 field campaign. *J Geophys Res-Atmos*. 112; 2007
- Knippertz, P.; Todd, M.C. Mineral Dust Aerosols over the Sahara: Meteorological Controls on Emission and Transport and Implications for Modeling. *Rev Geophys*. 50; 2012
- Knupp, K.R. Observational analysis of a gust front to bore to solitary wave transition within an evolving nocturnal boundary layer. *J Atmos Sci*. 63:2016-2035; 2006
- Knupp, K.R.; Cotton, W.R. An Intense, Quasi-Steady Thunderstorm over Mountainous Terrain .3. Doppler Radar Observations of the Turbulent Structure. *J Atmos Sci*. 39:359-368; 1982
- Kohler, M.; Kalthoff, N.; Kottmeier, C. The impact of soil moisture modifications on CBL characteristics in West Africa: A case-study from the AMMA campaign. *Q J Roy Meteor Soc*. 136:442-455; 2010
- Kollias, P.; Miller, M.A.; Johnson, K.L.; Jensen, M.P.; Troyan, D.T. Cloud, thermodynamic, and precipitation observations in West Africa during 2006. *J Geophys Res-Atmos*. 114; 2009
- Koster, R.D.; Dirmeyer, P.A.; Guo, Z.C.; Bonan, G.; Chan, E.; Cox, P.; Gordon, C.T.; Kanae, S.; Kowalczyk, E.; Lawrence, D.; Liu, P.; Lu, C.H.; Malyshev, S.; McAvaney, B.; Mitchell, K.; Mocko, D.; Oki, T.; Oleson, K.; Pitman, A.; Sud, Y.C.; Taylor, C.M.; Versegny, D.; Vasic, R.; Xue, Y.K.; Yamada, T.; Team, G. Regions of strong coupling between soil moisture and precipitation. *Science*. 305:1138-1140; 2004
- Koster, R.D.; Suarez, M.J.; Liu, P.; Jambor, U.; Berg, A.; Kistler, M.; Reichle,

- R.; Rodell, M.; Famiglietti, J. Realistic initialization of land surface states: Impacts on subseasonal forecast skill. *J Hydrometeorol.* 5:1049-1063; 2004
- Lafore, J.P.; Moncrieff, M.W. A Numerical Investigation of the Organization and Interaction of the Convective and Stratiform Regions of Tropical Squall Lines - Reply. *J Atmos Sci.* 47:1034-1035; 1990
- Laing, A.G.; Carbone, R.; Levizzani, V.; Tuttle, J. The propagation and diurnal cycles of deep convection in northern tropical Africa. *Q J Roy Meteor Soc.* 134:93-109; 2008
- Laing, A.G.; Fritsch, J.M. Mesoscale Convective Complexes in Africa. *Mon Weather Rev.* 121:2254-2263; 1993
- Lauwaet, D.; van Lipzig, N.P.M.; Kalthoff, N.; De Ridder, K. Impact of vegetation changes on a mesoscale convective system in West Africa. *Meteorol Atmos Phys.* 107:109-122; 2010
- Lavaysse, C.; Diedhiou, A.; Laurent, H.; Lebel, T. African Easterly Waves and convective activity in wet and dry sequences of the West African Monsoon. *Clim Dynam.* 27:319-332; 2006
- Lean, H.W.; Clark, P.A.; Dixon, M.; Roberts, N.M.; Fitch, A.; Forbes, R.; Halliwell, C. Characteristics of high-resolution versions of the Met Office Unified Model for forecasting convection over the United Kingdom. *Mon Weather Rev.* 136:3408-3424; 2008
- Lebel, T.; Cappelaere, B.; Galle, S.; Hanan, N.; Kergoat, L.; Levis, S.; Vieux, B.; Descroix, L.; Gosset, M.; Mougou, E.; Peugeot, C.; Seguis, L. AMMA-CATCH studies in the Sahelian region of West-Africa: An overview. *J Hydrol.* 375:3-13; 2009
- Lebel, T.; Parker, D.J.; Flamant, C.; Bourles, B.; Marticorena, B.; Mougou, E.; Peugeot, C.; Diedhiou, A.; Haywood, J.M.; Ngamini, J.B.; Polcher, J.; Redelsperger, J.L.; Thorncroft, C.D. The AMMA field campaigns: Multiscale and multidisciplinary observations in the West African region. *Q J Roy Meteor Soc.* 136:8-33; 2010
- Lele, M.I.; Lamb, P.J. Variability of the Intertropical Front (ITF) and Rainfall over the West African Sudan-Sahel Zone. *J Climate.* 23:3984-4004; 2010
- Liu, C.H.; Moncrieff, M.W. Effects of convectively generated gravity waves and rotation on the organization of convection. *J Atmos Sci.* 61:2218-2227; 2004
- Lock, A.P.; Brown, A.R.; Bush, M.R.; Martin, G.M.; Smith, R.N.B. A new boundary layer mixing scheme. Part I: Scheme description and single-column model tests. *Mon Weather Rev.* 128:3187-3199; 2000
- Lothon, M.; Campistron, B.; Chong, M.; Couvreur, F.; Guichard, F.; Rio, C.; Williams, E. Life Cycle of a Mesoscale Circular Gust Front Observed by a C-Band Doppler Radar in West Africa. *Mon Weather Rev.* 139:1370-1388; 2011
- Lothon, M.; Said, F.; Lohou, F.; Campistron, B. Observation of the diurnal cycle in the low troposphere of West Africa. *Mon Weather Rev.* 136:3477-3500; 2008
- Machado, L.A.T.; Rossow, W.B.; Guedes, R.L.; Walker, A.W. Life cycle variations of mesoscale convective systems over the Americas. *Mon Weather Rev.* 126:1630-1654; 1998
- Maddox, R.A. Mesoscale Convective Complexes. *B Am Meteorol Soc.* 61:1374-1387; 1980

- Mapes, B.E. Gregarious Tropical Convection. *J Atmos Sci.* 50:2026-2037; 1993
- Marsham, J.H.; Dixon, N.S.; Garcia-Carreras, L.; Lister, G.M.S.; Parker, D.J.; Knippertz, P.; Birch, C.E. The role of moist convection in the West African monsoon system: Insights from continental-scale convection-permitting simulations. *Geophys Res Lett.* 40:1843-1849; 2013
- Marsham, J.H.; Knippertz, P.; Dixon, N.S.; Parker, D.J.; Lister, G.M.S. The importance of the representation of deep convection for modeled dust-generating winds over West Africa during summer. *Geophys Res Lett.* 38; 2011
- Marsham, J.H.; Parker, D.J.; Grams, C.M.; Johnson, B.T.; Grey, W.M.F.; Ross, A.N. Observations of mesoscale and boundary-layer scale circulations affecting dust transport and uplift over the Sahara. *Atmos Chem Phys.* 8:6979-6993; 2008
- Marsham, J.H.; Parker, D.J.; Grams, C.M.; Taylor, C.M.; Haywood, J.M. Uplift of Saharan dust south of the intertropical discontinuity. *J Geophys Res-Atmos.* 113; 2008
- Mathon, V.; Laurent, H. Life cycle of Sahelian mesoscale convective cloud systems. *Q J Roy Meteor Soc.* 127:377-406; 2001
- Mathon, V.; Laurent, H.; Lebel, T. Mesoscale convective system rainfall in the Sahel. *J Appl Meteorol.* 41:1081-1092; 2002
- McBride, J.L.; Frank, W.M. Relationships between stability and monsoon convection. *J Atmos Sci.* 56:24-36; 1999
- Mertz, O.; D'haen, S.; Maiga, A.; Moussa, I.B.; Barbier, B.; Diouf, A.; Diallo, D.; Da, E.D.; Dabi, D. Climate Variability and Environmental Stress in the Sudan-Sahel Zone of West Africa. *Ambio.* 41:380-392; 2012
- Miller, M.J.; Betts, A.K. Traveling Convective Storms over Venezuela. *Mon Weather Rev.* 105:833-848; 1977
- Mohino, E.; Rodriguez-Fonseca, B.; Losada, T.; Gervois, S.; Janicot, S.; Bader, J.; Ruti, P.; Chauvin, F. Changes in the interannual SST-forced signals on West African rainfall. AGCM intercomparison. *Clim Dynam.* 37:1707-1725; 2011
- Mohr, K.I.; Thorncroft, C.D. Intense convective systems in West Africa and their relationship to the African easterly jet. *Q J Roy Meteor Soc.* 132:163-176; 2006
- Moncrieff, M.W. A Theory of Organized Steady Convection and Its Transport-Properties. *Q J Roy Meteor Soc.* 107:29-50; 1981
- Moncrieff, M.W. Organized Convective Systems - Archetypal Dynamic-Models, Mass and Momentum Flux Theory, and Parametrization. *Q J Roy Meteor Soc.* 118:819-850; 1992
- Moncrieff, M.W.; Liu, C.H. Convection initiation by density currents: Role of convergence, shear, and dynamical organization. *Mon Weather Rev.* 127:2455-2464; 1999
- Moncrieff, M.W.; Miller, M.J. Dynamics and Simulation of Tropical Cumulonimbus and Squall Lines. *Q J Roy Meteor Soc.* 102:373-394; 1976
- Monkam, D. Convective available potential energy (CAPE) in northern Africa and tropical Atlantic and study of its connections with rainfall in Central and West Africa during Summer 1985. *Atmos Res.* 62:125-147; 2002
- Mounier, F.; Janicot, S.; Kiladis, G.N. The west African monsoon dynamics.

- Part III: The quasi-biweekly zonal dipole. *J Climate*. 21:1911-1928; 2008
- Mueller, C.K.; Carbone, R.E. Dynamics of a Thunderstorm Outflow. *J Atmos Sci*. 44:1879-1898; 1987
- Neale, R.; Slingo, J. The maritime continent and its role in the global climate: A GCM study. *J Climate*. 16:834-848; 2003
- Nesbitt, S.W.; Zipser, E.J. The diurnal cycle of rainfall and convective intensity according to three years of TRMM measurements. *J Climate*. 16:1456-1475; 2003
- Newell, R.E.; Kidson, J.W. African Mean Wind Changes between Sahelian Wet and Dry Periods. *J Climatol*. 4:27-33; 1984
- Newman, J.F.; Heinselman, P.L. Evolution of a Quasi-Linear Convective System Sampled by Phased Array Radar. *Mon Weather Rev*. 140:3467-3486; 2012
- Nicholls, S.; Lemone, M.A. The Fair Weather Boundary-Layer in Gate - the Relationship of Sub-Cloud Fluxes and Structure to the Distribution and Enhancement of Cumulus Clouds. *J Atmos Sci*. 37:2051-2067; 1980
- Nicholson, S.E. The Nature of Rainfall Fluctuations in Sub-Tropical West-Africa. *Mon Weather Rev*. 108:473-487; 1980
- Nicholson, S.E.; Some, B.; Kone, B. An analysis of recent rainfall conditions in West Africa, including the rainy seasons of the 1997 El Nino and the 1998 La Nina years. *J Climate*. 13:2628-2640; 2000
- Ogura, Y.; Liou, M.T. The Structure of a Mid-Latitude Squall Line - a Case-Study. *J Atmos Sci*. 37:553-567; 1980
- Ohsawa, T.; Ueda, H.; Hayashi, T.; Watanabe, A.; Matsumoto, J. Diurnal variations of convective activity and rainfall in tropical Asia. *J Meteorol Soc Jpn*. 79:333-352; 2001
- Omotosho, J.B. The Separate Contributions of Line Squalls, Thunderstorms and the Monsoon to the Total Rainfall in Nigeria. *J Climatol*. 5:543-552; 1985
- Parker, D.J.; Burton, R.R. The two-dimensional response of a tropical jet to propagating lines of convection. *J Atmos Sci*. 59:1263-1273; 2002
- Parker, D.J.; Burton, R.R.; Diongue-Niang, A.; Ellis, R.J.; Felton, M.; Taylor, C.M.; Thorncroft, C.D.; Bessemoulin, P.; Tompkins, A.M. The diurnal cycle of the West African monsoon circulation. *Q J Roy Meteor Soc*. 131:2839-2860; 2005
- Parker, D.J.; Fink, A.; Janicot, S.; Ngamini, J.B.; Douglas, M.; Afiesimama, E.; Agusti-Panareda, A.; Beljaars, A.; Dide, F.; Diedhiou, A.; Lebel, T.; Polcher, J.; Redelsperger, J.L.; Thorncroft, C.; Wilson, G.A. The Amma Radiosonde Program and Its Implications for the Future of Atmospheric Monitoring over Africa. *B Am Meteorol Soc*. 89:1015-1027; 2008
- Parker, D.J.; Thorncroft, C.D.; Burton, R.R.; Diongue-Niang, A. Analysis of the African easterly jet, using aircraft observations from the JET2000 experiment. *Q J Roy Meteor Soc*. 131:1461-1482; 2005
- Parker, M.D.; Johnson, R.H. Organizational modes of midlatitude mesoscale convective systems. *Mon Weather Rev*. 128:3413-3436; 2000
- Parker, M.D.; Johnson, R.H. Structures and dynamics of quasi-2D mesoscale convective systems. *J Atmos Sci*. 61:545-567; 2004
- Payne, S.W.; Mcgarry, M.M. Relationship of Satellite Inferred Convective

- Activity to Easterly Waves over West-Africa and Adjacent Ocean during Phase 3 of Gate. *Mon Weather Rev.* 105:413-420; 1977
- Pearson, K.J.; Hogan, R.J.; Allan, R.P.; Lister, G.M.S.; Holloway, C.E. Evaluation of the model representation of the evolution of convective systems using satellite observations of outgoing longwave radiation. *J Geophys Res-Atmos.* 115; 2010
- Peters, M.; Tetzlaff, G. The Structure of West-African Squall Lines and Their Environmental Moisture Budget. *Meteorol Atmos Phys.* 39:74-84; 1988
- Petersen, W.A.; Cifelli, R.; Boccippio, D.J.; Rutledge, S.A.; Fairall, C. Convection and easterly wave structures observed in the eastern Pacific warm pool during EPIC-2001. *J Atmos Sci.* 60:1754-1773; 2003
- Peyrille, P.; Lafore, J.P. An idealized two-dimensional framework to study the West African monsoon. Part II: Large-scale advection and the diurnal cycle. *J Atmos Sci.* 64:2783-2803; 2007
- Pytharoulis, I.; Thorncroft, C. The low-level structure of African easterly waves in 1995. *Mon Weather Rev.* 127:2266-2280; 1999
- Ramel, R.; Gallee, H.; Messenger, C. On the northward shift of the West African monsoon. *Clim Dynam.* 26:429-440; 2006
- Randall, D.A.; Huffman, G.J. A Stochastic-Model of Cumulus Clumping. *J Atmos Sci.* 37:2068-2078; 1980
- Redelsperger, J.L.; Brown, P.R.A.; Guichard, F.; Hoff, C.; Kawasima, M.; Lang, S.; Montmerle, T.; Nakamura, K.; Saito, K.; Seman, C.; Tao, W.K.; Donner, L.J. A GCSS model intercomparison for a tropical squall line observed during TOGA-COARE. I: Cloud-resolving models. *Q J Roy Meteor Soc.* 126:823-863; 2000
- Redelsperger, J.L.; Diongue, A.; Diedhiou, A.; Ceron, J.P.; Diop, M.; Gueremy, J.F.; Lafore, J.P. Multi-scale description of a Sahelian synoptic weather system representative of the West African monsoon. *Q J Roy Meteor Soc.* 128:1229-1257; 2002
- Redelsperger, J.L.; Lafore, J.P. A 3-Dimensional Simulation of a Tropical Squall Line - Convective Organization and Thermodynamic Vertical Transport. *J Atmos Sci.* 45:1334-1356; 1988
- Redelsperger, J.L.; Thorncroft, C.D.; Diedhiou, A.; Lebel, T.; Parker, D.J.; Polcher, J. African monsoon multidisciplinary analysis - An international research project and field campaign. *B Am Meteorol Soc.* 87:1739-+; 2006
- Reed, R.J.; Norquist, D.C.; Recker, E.E. Structure and Properties of African Wave Disturbances as Observed during Phase Iii of Gate. *Mon Weather Rev.* 105:317-333; 1977
- Rickenbach, T.; Ferreira, R.N.; Guy, N.; Williams, E. Radar-observed squall line propagation and the diurnal cycle of convection in Niamey, Niger, during the 2006 African Monsoon and Multidisciplinary Analyses Intensive Observing Period. *J Geophys Res-Atmos.* 114; 2009
- Rickenbach, T.M.; Rutledge, S.A. Convection in TOGA COARE: Horizontal scale, morphology, and rainfall production. *J Atmos Sci.* 55:2715-2729; 1998
- Roca, R.; Louvet, S.; Picon, L.; Desbois, M. A study of convective systems, water vapor and top of the atmosphere cloud radiative forcing over the Indian Ocean using INSAT-1B and ERBE data. *Meteorol Atmos*

- Phys. 90:49-65; 2005
- Roehrig, R.; Bouniol, D.; Guichard, F.; Hourdin, F.; Redelsperger, J.L. The Present and Future of the West African Monsoon: A Process-Oriented Assessment of CMIP5 Simulations along the AMMA Transect. *J Climate*. 26:6471-6505; 2013
- Rottman, J.W.; Simpson, J.E. The Formation of Internal Bores in the Atmosphere - a Laboratory Model. *Q J Roy Meteor Soc*. 115:941-963; 1989
- Rotunno, R.; Klemp, J. On the Rotation and Propagation of Simulated Supercell Thunderstorms. *J Atmos Sci*. 42:271-292; 1985
- Rotunno, R.; Klemp, J.B.; Weisman, M.L. A Theory for Strong, Long-Lived Squall Lines. *J Atmos Sci*. 45:463-485; 1988
- Rowell, D.P.; Folland, C.K.; Maskell, K.; Ward, M.N. Variability of Summer Rainfall over Tropical North-Africa (1906-92) - Observations and Modeling. *Q J Roy Meteor Soc*. 121:669-704; 1995
- Rowell, D.P.; Milford, J.R. On the Generation of African Squall Lines. *J Climate*. 6:1181-1193; 1993
- Russell A, Vaughan G, Norton EG, Morcrette CJ, Browning KA, Blyth AM. 2008. Convective inhibition beneath an upper-level PV anomaly. *Q. J. R. Meteorol. Soc*. 134 : 371-383.
- Russell A, Vaughan G, Norton EG, Ricketts HMA, Morcrette CJ, Hewison TJ, Browning KA, Blyth AM. 2010. Convection forced by a descending dry layer and low-level moist convergence. *Tellus* 61A : 250-263.
- Ruti, P.M.; Williams, J.E.; Hourdin, F.; Guichard, F.; Boone, A.; van Velthoven, P.; Favot, F.; Musat, I.; Rummukainen, M.; Dominguez, M.; Gaertner, M.A.; Lafore, J.P.; Losada, T.; de Fonseca, M.B.R.; Polcher, J.; Giorgi, F.; Xue, Y.; Bouarar, I.; Law, K.; Josse, B.; Barret, B.; Yang, X.; Mari, C.; Traore, A.K. The West African climate system: a review of the AMMA model inter-comparison initiatives. *Atmos Sci Lett*. 12:116-122; 2011
- Rutledge, S.A.; Williams, E.R.; Keenan, T.D. The down under Doppler and Electricity Experiment (Dundee) - Overview and Preliminary-Results. *B Am Meteorol Soc*. 73:3-16; 1992
- Salack, S.; Giannini, A.; Diakhate, M.; Gaye, A.T.; Muller, B. Oceanic influence on the sub-seasonal to interannual timing and frequency of extreme dry spells over the West African Sahel. *Clim Dynam*. 42:189-201; 2014
- Sassen, K. Laser Depolarization Bright Band from Melting Snowflakes. *Nature*. 255:316-318; 1975
- Saxen, T.R.; Rutledge, S.A. Surface fluxes and boundary layer recovery in TOGA COARE: Sensitivity to convective organization. *J Atmos Sci*. 55:2763-2781; 1998
- Schrage, J.M.; Fink, A.H.; Ermert, V.; Ahlonsou, E.D. Three MCS cases occurring in different synoptic environments in the sub-Saharan wet zone during the 2002 West African monsoon. *J Atmos Sci*. 63:2369-2382; 2006
- Schwendike, J.; Kalthoff, N.; Kohler, M. The impact of mesoscale convective systems on the surface and boundary-layer structure in West Africa: Case-studies from the AMMA campaign 2006. *Q J Roy Meteor Soc*. 136:566-582; 2010
- Segal, M.; Arritt, R.W. Nonclassical Mesoscale Circulations Caused by Surface Sensible Heat-Flux Gradients. *B Am Meteorol Soc*. 73:1593-1604; 1992
- Sijkumar, S.; Roucou, P.; Fontaine, B. Monsoon onset over Sudan-Sahel: Simulation by the regional scale model MM5. *Geophys Res Lett*. 33; 2006
- Slingo, A.; Bharmal, N.A.; Robinson, G.J.; Settle, J.J.; Allan, R.P.; White, H.E.;

- Lamb, P.J.; Lele, M.I.; Turner, D.D.; McFarlane, S.; Kassianov, E.; Barnard, J.; Flynn, C.; Miller, M. Overview of observations from the RADAGAST experiment in Niamey, Niger: Meteorology and thermodynamic variables. *J Geophys Res-Atmos.* 113; 2008
- Smull, B.F.; Houze, R.A. Rear Inflow in Squall Lines with Trailing Stratiform Precipitation. *Mon Weather Rev.* 115:2869-2889; 1987
- Staniforth, A.; Wood, N. Analysis of the response to orographic forcing of a time-staggered semi-Lagrangian discretization of the rotating shallow-water equations. *Q J Roy Meteor Soc.* 132:3117-3126; 2006
- Stein, T.H.M.; Parker, D.J.; Hogan, R.J.; Birch, C.E.; Holloway, C.E.; Lister, G.M.S.; Marsham, J.H.; Woolnough, S.J. The representation of the West African monsoon vertical cloud structure in the Met Office Unified Model: an evaluation with CloudSat. *Q J Roy Meteor Soc.* 141:3312-3324; 2015
- Stensrud, D.J.; Coniglio, M.C.; Davies-Jones, R.P.; Evans, J.S. Comments on "A theory for strong long-lived squall lines' revisited". *J Atmos Sci.* 62:2989-2996; 2005
- Stensrud, D.J.; Fritsch, J.M. Mesoscale Convective Systems in Weakly Forced Large-Scale Environments .1. Observations. *Mon Weather Rev.* 121:3326-3344; 1993
- Stensrud, D.J.; Fritsch, J.M. Mesoscale Convective Systems in Weakly Forced Large-Scale Environments .2. Generation of a Mesoscale Initial Condition. *Mon Weather Rev.* 122:2068-2083; 1994
- Stensrud, D.J.; Fritsch, J.M. Mesoscale Convective Systems in Weakly Forced Large-Scale Environments .3. Numerical Simulations and Implications for Operational Forecasting. *Mon Weather Rev.* 122:2084-2104; 1994
- Stolzenburg, M.; Marshall, T.C.; Rust, W.D.; Smull, B.F. Horizontal Distribution of Electrical and Meteorological Conditions across the Stratiform Region of a Mesoscale Convective System. *Mon Weather Rev.* 122:1777-1797; 1994
- Sultan, B.; Janicot, S. The West African monsoon dynamics. Part II: The "preonset" and "onset" of the summer monsoon. *J Climate.* 16:3407-3427; 2003
- Sultan, B.; Janicot, S.; Diedhiou, A. The West African monsoon dynamics. Part I: Documentation of intraseasonal variability. *J Climate.* 16:3389-3406; 2003
- Sutton, L.J. Haboobs. *Q J Roy Meteor Soc.* 51:25-30; 1925
- Szeto, K.K.; Cho, H.R. A Numerical Investigation of Squall Lines .1. The Control Experiment. *J Atmos Sci.* 51:414-424; 1994
- Szeto, K.K.; Cho, H.R. A Numerical Investigation of Squall Lines .2. The Mechanics of Evolution. *J Atmos Sci.* 51:425-433; 1994
- Taylor, C.M. Detecting soil moisture impacts on convective initiation in Europe. *Geophys Res Lett.* 42:4631-4638; 2015
- Taylor, C.M.; Birch, C.E.; Parker, D.J.; Dixon, N.; Guichard, F.; Nikulin, G.; Lister, G.M.S. Modeling soil moisture-precipitation feedback in the Sahel: Importance of spatial scale versus convective parameterization. *Geophys Res Lett.* 40:6213-6218; 2013
- Taylor, C.M.; Clark, D.B. The diurnal cycle and African easterly waves: A land surface perspective. *Q J Roy Meteor Soc.* 127:845-867; 2001
- Taylor, C.M.; de Jeu, R.A.M.; Guichard, F.; Harris, P.P.; Dorigo, W.A.

- Afternoon rain more likely over drier soils. *Nature*. 489:423-426; 2012
- Taylor, C.M.; Ellis, R.J. Satellite detection of soil moisture impacts on convection at the mesoscale. *Geophys Res Lett*. 33; 2006
- Taylor, C.M.; Ellis, R.J.; Parker, D.J.; Burton, R.R.; Thorncroft, C.D. Linking boundary-layer variability with convection: A case-study from JET2000. *Q J Roy Meteor Soc*. 129:2233-2253; 2003
- Taylor, C.M.; Gounou, A.; Guichard, F.; Harris, P.P.; Ellis, R.J.; Couvreur, F.; De Kauwe, M. Frequency of Sahelian storm initiation enhanced over mesoscale soil-moisture patterns. *Nat Geosci*. 4:430-433; 2011
- Taylor, C.M.; Harris, P.P.; Parker, D.J. Impact of soil moisture on the development of a Sahelian mesoscale convective system: A case-study from the AMMA Special Observing Period. *Q J Roy Meteor Soc*. 136:456-470; 2010
- Taylor, C.M.; Lebel, T. Observational evidence of persistent convective-scale rainfall patterns. *Mon Weather Rev*. 126:1597-1607; 1998
- Taylor, C.M.; Parker, D.J.; Harris, P.P. An observational case study of mesoscale atmospheric circulations induced by soil moisture. *Geophys Res Lett*. 34; 2007
- Taylor, C.M.; Said, F.; Lebel, T. Interactions between the land surface and mesoscale rainfall variability during HAPEX-Sahel. *Mon Weather Rev*. 125:2211-2227; 1997
- Thorncroft, C.; Hodges, K. African easterly wave variability and its relationship to Atlantic tropical cyclone activity. *J Climate*. 14:1166-1179; 2001
- Thorncroft, C.D. An Idealized Study of African Easterly Waves .3. More Realistic Basic States. *Q J Roy Meteor Soc*. 121:1589-1614; 1995
- Thorncroft, C.D.; Blackburn, M. Maintenance of the African easterly jet. *Q J Roy Meteor Soc*. 125:763-786; 1999
- Thorncroft, C.D.; Haile, M. The Mean Dynamic and Thermodynamic Fields for July 1989 over Tropical North-Africa and Their Relationship to Convective Storm Activity. *Mon Weather Rev*. 123:3016-3031; 1995
- Thorncroft, C.D.; Hall, N.M.J.; Kiladis, G.N. Three-Dimensional Structure and Dynamics of African Easterly Waves. Part III: Genesis. *J Atmos Sci*. 65:3596-3607; 2008
- Thorncroft, C.D.; Hoskins, B.J. An Idealized Study of African Easterly Waves .1. A Linear View. *Q J Roy Meteor Soc*. 120:953-982; 1994
- Thorncroft, C.D.; Hoskins, B.J. An Idealized Study of African Easterly Waves .2. A Nonlinear View. *Q J Roy Meteor Soc*. 120:983-1015; 1994
- Thorncroft, C.D.; Parker, D.J.; Burton, R.R.; Diop, M.; Ayers, J.H.; Barjat, H.; Devereau, S.; Diongue, A.; Dumelow, R.; Kindred, D.R.; Price, N.M.; Saloum, M.; Taylor, C.M.; Tompkins, A.M. The JET2000 project - Aircraft observations of the African easterly jet and African easterly waves. *B Am Meteorol Soc*. 84:337-351; 2003
- Thorpe, A.J.; Miller, M.J.; Moncrieff, M.W. Two-Dimensional Convection in Non-Constant Shear - a Model of Mid-Latitude Squall Lines. *Q J Roy Meteor Soc*. 108:739-762; 1982
- Tiedtke, M. A Comprehensive Mass Flux Scheme for Cumulus Parameterization in Large-Scale Models. *Mon Weather Rev*. 117:1779-1800; 1989
- Tompkins, A.M. On the relationship between tropical convection and sea surface temperature. *J Climate*. 14:633-637; 2001

- Tompkins, A.M. Organization of tropical convection in low vertical wind shears: The role of cold pools. *J Atmos Sci.* 58:1650-1672; 2001
- Tompkins, A.M.; Diongue-Niang, A.; Parker, D.J.; Thorncroft, C.D. The African easterly jet in the ECMWF Integrated Forecast System: 4D-Var analysis. *Q J Roy Meteor Soc.* 131:2861-2885; 2005
- Torri, G.; Kuang, Z.M.; Tian, Y. Mechanisms for convection triggering by cold pools. *Geophys Res Lett.* 42:1943-1950; 2015
- Tratt, D.M.; Hecht, M.H.; Catling, D.C.; Samulon, E.C.; Smith, P.H. In situ measurement of dust devil dynamics: Toward a strategy for Mars. *J Geophys Res-Planet.* 108; 2003
- Vanvyve, E.; Hall, N.; Messenger, C.; Leroux, S.; van Ypersele, J.P. Internal variability in a regional climate model over West Africa. *Clim Dynam.* 30:191-202; 2008
- Vila, D.A.; Machado, L.A.T.; Laurent, H.; Velasco, I. Forecast and Tracking the Evolution of Cloud Clusters (ForTraCC) using satellite infrared imagery: Methodology and validation. *Weather Forecast.* 23:233-245; 2008
- Wakimoto, R.M. The Life-Cycle of Thunderstorm Gust Fronts as Viewed with Doppler Radar and Rawinsonde Data. *Mon Weather Rev.* 110:1060-1082; 1982
- Walters, D.N.; Best, M.J.; Bushell, A.C.; Copsey, D.; Edwards, J.M.; Falloon, P.D.; Harris, C.M.; Lock, A.P.; Manners, J.C.; Morcrette, C.J.; Roberts, M.J.; Stratton, R.A.; Webster, S.; Wilkinson, J.M.; Willett, M.R.; Boutle, I.A.; Earnshaw, P.D.; Hill, P.G.; MacLachlan, C.; Martin, G.M.; Moufouma-Okia, W.; Palmer, M.D.; Petch, J.C.; Rooney, G.G.; Scaife, A.A.; Williams, K.D. The Met Office Unified Model Global Atmosphere 3.0/3.1 and JULES Global Land 3.0/3.1 configurations. *Geosci Model Dev.* 4:919-941; 2011
- Weckwerth, T.M.; Murphey, H.V.; Flamant, C.; Goldstein, J.; Pettet, C.R. An observational study of convection initiation on 12 June 2002 during IHOP\_2002. *Mon Weather Rev.* 136:2283-2304; 2008
- Weckwerth, T.M.; Parsons, D.B. A review of convection initiation and motivation for IHOP\_2002. *Mon Weather Rev.* 134:5-22; 2006
- Weckwerth, T.M.; Parsons, D.B.; Koch, S.E.; Moore, J.A.; LeMone, M.A.; Demoz, B.B.; Flamant, C.; Geerts, B.; Wang, J.H.; Feltz, W.F. An overview of the International H2O Project (IHOP\_2002) and some preliminary highlights. *B Am Meteorol Soc.* 85:253-+; 2004
- Weisman, M.L. The Role of Convectively Generated Rear-Inflow Jets in the Evolution of Long-Lived Mesoconvective Systems. *J Atmos Sci.* 49:1826-1847; 1992
- Weisman, M.L. The Genesis of Severe, Long-Lived Bow Echoes. *J Atmos Sci.* 50:645-670; 1993
- Weisman, M.L.; Klemp, J.B. The Structure and Classification of Numerically Simulated Convective Storms in Directionally Varying Wind Shears. *Mon Weather Rev.* 112:2479-2498; 1984
- Weisman, M.L.; Klemp, J.B.; Rotunno, R. Structure and Evolution of Numerically Simulated Squall Lines. *J Atmos Sci.* 45:1990-2013; 1988
- Weisman, M.L.; Rotunno, R. "A theory for strong long-lived squall lines" revisited. *J Atmos Sci.* 61:361-382; 2004
- Weisman, M.L.; Rotunno, R. A theory for strong long-lived squall lines'

- revisited - Reply. *J Atmos Sci.* 62:2997-3002; 2005
- Williams, E.; Renno, N. An Analysis of the Conditional Instability of the Tropical Atmosphere. *Mon Weather Rev.* 121:21-36; 1993
- Wilson, D.R.; Ballard, S.P. A microphysically based precipitation scheme for the UK Meteorological Office Unified Model. *Q J Roy Meteor Soc.* 125:1607-1636; 1999
- Wilson, J.W.; Foote, G.B.; Crook, N.A.; Fankhauser, J.C.; Wade, C.G.; Tuttle, J.D.; Mueller, C.K.; Krueger, S.K. The Role of Boundary-Layer Convergence Zones and Horizontal Rolls in the Initiation of Thunderstorms - a Case-Study. *Mon Weather Rev.* 120:1785-1815; 1992
- Wilson, J.W.; Schreiber, W.E. Initiation of Convective Storms at Radar-Observed Boundary-Layer Convergence Lines. *Mon Weather Rev.* 114:2516-2536; 1986
- Yang, G.Y.; Slingo, J. The diurnal cycle in the Tropics. *Mon Weather Rev.* 129:784-801; 2001
- Yoneyama, K.; Fujitani, T. The Behavior of Dry Westerly Air Associated with Convection Observed during the Toga-Coare R/V Natsushima Cruise. *J Meteorol Soc Jpn.* 73:291-304; 1995
- Yoneyama, K.; Parsons, D.B. A proposed mechanism for the intrusion of dry air into the Tropical Western Pacific region. *J Atmos Sci.* 56:1524-1546; 1999
- Yuan, W.H. Diurnal cycles of precipitation over subtropical China in IPCC AR5 AMIP simulations. *Adv Atmos Sci.* 30:1679-1694; 2013
- Yuter, S.E.; Houze, R.A. The 1997 Pan American Climate Studies Tropical Eastern Pacific Process Study. Part I: ITCZ region. *B Am Meteorol Soc.* 81:451-481; 2000
- Zawadzki, I.; Torlaschi, E.; Sauvageau, R. The Relationship between Mesoscale Thermodynamic Variables and Convective Precipitation. *J Atmos Sci.* 38:1535-1540; 1981
- Zhang, G.J. Effects of entrainment on convective available potential energy and closure assumptions in convection parameterization. *J Geophys Res-Atmos.* 114; 2009
- Zipser, E.J. Role of Squall Systems in Tropical Disturbances. *B Am Meteorol Soc.* 50:767-&; 1969
- Zipser, E.J. Mesoscale and Convective-Scale Downdrafts as Distinct Components of Squall-Line Structure. *Mon Weather Rev.* 105:1568-1589; 1977